

Investigation on Friction Stir Welding of Dissimilar AA5083-AA6061 Aluminium Alloys for Improving Mechanical and Corrosion Properties

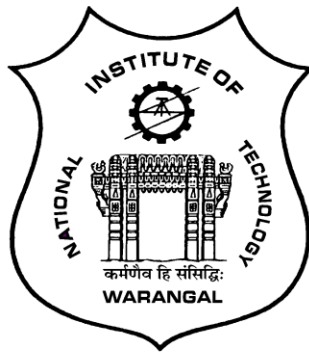
A thesis submitted in the partial fulfilment of the requirement
for the award of the degree of

DOCTOR OF PHILOSOPHY

by

KETHAVATH KRANTHI KUMAR

Roll No: 716131



**DEPARTMENT OF MECHANICAL ENGINEERING
NATIONAL INSTITUTE OF TECHNOLOGY
WARANGAL-506004, TELANGANA, INDIA.**

OCTOBER 2021

Investigation on Friction Stir Welding of Dissimilar AA5083-AA6061 Aluminium Alloys for Improving Mechanical and Corrosion Properties

A thesis submitted in the partial fulfilment of the requirement
for the award of the degree of

DOCTOR OF PHILOSOPHY

by

KETHAVATH KRANTHI KUMAR

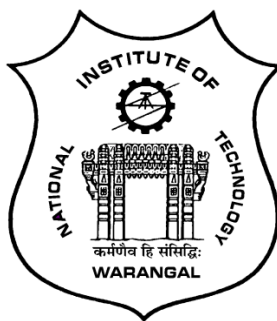
Roll No: 716131

under the Supervision of

Dr. ADEPU KUMAR

Professor, MED

Department of Mechanical Engineering



**DEPARTMENT OF MECHANICAL ENGINEERING
NATIONAL INSTITUTE OF TECHNOLOGY
WARANGAL-506004, TELANGANA, INDIA.**

OCTOBER 2021

THESIS APPROVAL FOR Ph.D.

This thesis entitled "**Investigation on Friction stir welding of dissimilar AA5083-AA6061 aluminium alloys for improving mechanical and corrosion properties**" by **Mr. Kethavath Kranthi Kumar** is approved for the degree of Doctor of Philosophy.

Examiner

Dr. Adepu Kumar
Professor, Department of Mechanical Engineering, NIT Warangal
Supervisor

Dr. Adepu Kumar
Head, Department of Mechanical Engineering, NIT Warangal
Chairman



NATIONAL INSTITUTE OF TECHNOLOGY

WARANGAL – 506 004, Telangana State, INDIA

CERTIFICATE

This is to certify that the work presented in the thesis entitled "**Investigation on friction stir welding of dissimilar AA5083-AA6061 aluminium alloys for improving mechanical and corrosion properties**" which is being submitted by Mr. Kethavath Kranthi Kumar (Roll No. 716131), is a bonafide work submitted to National Institute of Technology, Warangal in partial fulfillment of the requirement for the award of the degree of Doctor of Philosophy in Mechanical Engineering. To the best of our knowledge, the work incorporated in the thesis has not been submitted to any other university or institute for the award of any degree or diploma.

Dr. Adepu Kumar
Thesis Supervisor
Professor
Department of Mechanical Engineering
National Institute of Technology
Warangal-506 004, Telangana, India

Dr. Adepu Kumar
Chairman –DSC
Professor and Head
Department of Mechanical Engineering
National Institute of Technology
Warangal-506 004, Telangana, India



NATIONAL INSTITUTE OF TECHNOLOGY

WARANGAL – 506 004, Telangana State, INDIA

DECLARATION

This is to certify that the work presented in the thesis entitled "**Investigation on friction stir welding of dissimilar AA5083-AA6061 aluminium alloys for improving mechanical and corrosion properties**", is a bonafide work done by me under the supervision of Dr. Adepu Kumar and was not submitted elsewhere for the award of any degree.

I declare that this written submission represents my idea in my own words and where other's ideas or words have not been included. I have adequately cited and referenced the original sources. I also declare that I have adhered to all principles of academic honesty and integrity and have not misinterpreted or fabricated or falsified any idea/data/fact/source in my submission. I understand that any violation of the above will be a cause for disciplinary action by the Institute and can also evoke penal action from the sources which have thus not been properly cited or from whom proper permission has not taken when needed.

Date:

(Mr. Kethavath Kranthi Kumar)

Place:

Research Scholar

Roll No. 716131

ACKNOWLEDGEMENT

Firstly, I would like to express my sincere gratitude and thanks to my advisor Prof. Adepu Kumar, Department of Mechanical Engineering, National Institute of Technology, Warangal for the continuous support of my Ph.D. study, for his patience and motivation. His guidance, support and encouragement helped me in all the time of research and writing of this thesis.

Besides my advisor, I would like to thank the Doctoral scrutiny committee (DSC) members Prof. Adepu Kumar (Chairman and Head, Dept. of Mechanical Engineering), Prof. K V Sai Srinadh (Dept. of Mechanical Engineering), Prof. V. Suresh Babu (Dept. of Mechanical Engineering), Assistant Prof. G. Brahmaraju (Dept. of Metallurgical and Materials Engineering), for their valuable suggestions and comments at each and every stage during my Ph.D. progress.

I would like to thank Dr. shivraman (Dept. of Mechanical Engineering, NIT-Warangal) and Dr. Raja vishwanatham (Department of Humanities & Social Science, NIT-Warangal) for their support. The authors heartily thank the Dr. CH. Raj Mohan (Department of Chemical Engineering, NIT-Warangal, India for providing with research facilities to carry out the electrochemical study. The authors are grateful to Dr. I. Samajdar, Professor (Department of Metallurgical & Materials Science, IIT Bombay) for providing with an OIM and Texture facility.

My heartfelt thanks to my beloved parents, my younger brother Dr. Kethavath Srinivas, sister Boda Shobha, wife Maloth Deepa and other family members M. Rupa, M. Vikash, for their encouragement, constant support, and motivation. Their role is immeasurable, without which it would have been impossible for me to complete this project work and thesis.

My sincere thanks also goes to my seniors and well-wishers Dr. M. Krishna kishore, Dr. P Naresh, Mr B. Ambadas and Dr. Rajendra Prasad for their valuable suggestions and encouragement. I would be very delighted and happy to express my sincere thanks to my Labmates K Nagu, M V Satyanarayana, I Karthikeya sharma and Sarvana Sundar. and my friend S. Chandrashekhar for their sharing, caring and co-operation during my entire Ph.D stay.

Last but not least, I would like to thank the non-teaching staff Mr. Yellaswamy and many other at NIT Warangal for their help in many occasions during my experimental work.

- Kethavath Kranthi Kumar

**Dedicated
To
My beloved parents
Sri Kethavath Mangthya
Smt Kethavath Samani bai
Wife Maloth Deepa
Daughter Kethavath Pranshi**

ABSTRACT

Aluminium alloys can be used for structural parts because of their many unique qualities, such as light weight and high structural strength. Aluminium alloys meet the requirement for lightweight materials in the aerospace, automobile, and ship-building industries. The aluminum alloys AA6xxx and AA5xxx are widely employed in aviation and other structural applications. AA6061-T6 (Al-Mg-Si) alloys are readily weldable, they suffer from severe softening in the Heat Affected Zone (HAZ) due to dissolution of Mg₂Si strengthening precipitates during weld thermal cycle. AA5083-H111 (Al-Mg) series aluminium alloy with high Mg content impose poor weldability by fusion welding process due to its increased susceptibility to stress corrosion cracking behavior. Dissimilar welding of these two alloys is frequently faced in those structures.

The conventional fusion welding of aluminium and its alloys is a great challenge for designers and technologists due to numerous welding defects which includes voids, hot cracking, distortion, precipitates dissolution, loss of work hardening, hot cracking and lack of penetration in the joint. Furthermore, traditional fusion welding of aluminum alloys causes the fusion zone to melt and re-solidify, resulting in the production of brittle inter-dendritic structure and eutectic phases. The brittle structure that forms at the weld zone causes a significant reduction in mechanical characteristics and corrosion resistance.

Joining of aluminum alloys, was more promising with the latest friction based processes named friction stir welding which comes under the category of solid-state joining processes. It has compatibility to any alloy composition, and produces the welded joints by eliminating the defects with improved mechanical properties. Development of the Friction Stir welding (FSW) has provided an alternative improved way of producing dissimilar aluminium joints, in a faster and reliable manner. The formation and strength of bond in friction stir welding depends on selecting appropriate selecting base materials position, tool process parameters and cooling conditions. The above considerations formed the background of the present investigation in which dissimilar aluminium alloy AA6061-T6 and AA5083-H111 is joined using FSW.

In this present investigation, effect of changing the base material locations (advancing side and retreating side), varying process conditions (traverse speed and rotational speed) and applying different cooling environments (air, water and liquid nitrogen) was studied to understand the

material flow, mechanical properties and corrosion resistance of friction stir welded AA5083-AA6061 aluminium alloys.

A preliminary study investigates mechanical and corrosion properties of dissimilar friction stir welded joints by changing material location (AA5083-AA6061 and AA6061-AA5083) and also compared with similar joints of the two base materials. The materials were more properly mixed with better mechanical properties when the AA5083-H111 was on the advancing side and the AA6061-T6 was on the retreating side. According to the results of polarization curves and EIS plots, the corrosion resistance of SZs is similar to that of the base material on the advancing side, which should be attributed to the fact that the majority of SZs are composed of the AS base material.

With the goal to reduce the weld softening and improving the weld joint efficiency, in the second phase of work, for dissimilar FSWed joints by varying process conditions, the onion ring sub-layer width measured at the stir zone was significantly modified, according to microstructural study. Higher rotational speeds were thought to produce greater intermixing and improved mechanical characteristics. The onion ring sub-layer width measured at the stir zone was significantly modified, according to microstructural study. Higher rotational speeds were thought to produce greater intermixing and improved mechanical characteristics. Based on the results of the PDP and EIS test, the corrosion resistance of welded joints was found to be lower than that of base materials. The corrosion resistance decreased with the increase in traverse speed from 40 mm/min to 80 mm/min and the corrosion resistance increased with increase in rotational speed from 800 rpm to 1400 rpm. A remarkable degree of material intermixing and fragmentation of intermetallics at higher rotational speeds resulted in better corrosion resistance.

Dissimilar friction stir welding (FSW) of AA5083-AA6061 alloys in various cooling conditions (air, liquid nitrogen, and water) was successfully used as an alternate way to improve corrosion resistance and mechanical characteristics in the following phase. From Tafel and EIS results, it was observed that the corrosion resistance of FSWed joints was lower than that of base materials. The corrosion resistance of FSWed joint prepared using a water-cooling environment improved significantly compared to that of ACFSW and NCFSW joints. Intermetallics produced in joints employing cooling medium were finer and more corrosion resistant. Maximum yield

strength was achieved with a joint efficiency of 96 % to the AA5083 base material for the water-cooled joint.

In the final phase of the work, microstructure analysis (Such as pole figures, ODF) is studied along with mechanical properties such as strength, work hardening rate, strain hardening exponent, etc. of transverse and longitudinal tensile samples of all dissimilar aluminium alloys welds made using air and water cooling environments. The Cube [$\{112\} <111>$], Copper [$\{112\} <111>$] in ACFSW and Copper [$\{112\} <111>$] and Brass [$\{110\} <112>$] components in WCFSW joint were formed. Different types of shear textures are formed at SZ as a result of severe plastic deformation, which varied with cooling conditions during FSW. The strain hardening exponent and strain hardening rate enhanced, while ductility decreased using water cooling of FSW. Stage III and IV hardening occurred after yielding in both base metal and FSWed samples. Lower elongation was obtained in WCFSW than ACFSW joint due to the presence of flat surfaces, while high strength attained was resulted to smaller size dimples of WCFSW joint fracture surface.

Overall the present study identified the exact base material location, process conditions and cooling environment, which facilitates the efficient material flow and microstructure evolution, which resulted in improved mechanical strength and corrosion resistance. Moreover, the combination of optimized process conditions and cooling environment conditions showed the maximum joint efficiency and corrosion resistance of dissimilar FSWed joints.

TABLE OF CONTENTS

Certificate	i
Declaration	ii
Acknowledgements	iii
Abstract	v
Table of Contents	viii
List of Figures	xiii
List of Tables	xx
List of Abbreviations	xxii
List of Symbols	xxiv

CHAPTER 1	INTRODUCTION	Page No.
1.1 Background		1
1.2 Welding/joining		2
1.2.1 Fusion welding		3
1.2.2 Solid state welding		4
1.3 Friction stir welding		5
1.3.1 Working principle		5
1.3.2 Basic terminology		5
1.3.3 Different types of process parameters in FSW process		7
1.3.3.1 Tool rotation and traverse speed		7
1.3.3.2 Tool design		8
1.3.3.3 Tool tilt and plunge depth		10
1.3.4 Tool materials		11
1.3.5 Microstructure evolution in FSW		12
1.3.6 Advantages		13
1.3.7 Limitations		13
1.3.9 Applications		14
1.4 Aluminium alloys		14

1.4.1 Classification of aluminium alloys	15
1.4.2 Wrought alloys	15
1.4.3 Cast alloys	16
1.4.4 Welding of aluminium alloys	17
1.4.5 Characteristics of aluminium alloys	18
1.5 Definition of problem	19
1.6 Objectives and scope of research work	20
1.7 Methodology	20
1.8 Organization of thesis	21
CHAPTER 2 LITERATURE SURVEY	
2.1 Friction stir welding in aluminium alloys	22
2.1.1 FSW in non-heat treatable aluminium alloys	23
2.1.2 FSW in heat-treatable aluminium alloys	24
2.2 Material flow aspects in FSW	26
2.3 Heat generation and control in FSW	30
2.4 Corrosion behavior in FSW	36
2.5 Microstructure, Texture evolution and work hardening behavior in FSW	38
2.6 Summary	43
CHAPTER 3 EXPERIMENTAL PROCEDURES	
3.1 Introduction	44
3.2 Experimental Plan	44
3.3 Selection of workpiece	44
3.4 Selection of tool material and design	46
3.5 Friction stir welding machine	47
3.5.1 Cooling environment condition	48
3.6 Microstructure study	49
3.6.1 Sample cutting, mounting and polishing	49
3.6.2 Optical microscope	50
3.6.3 Scanning electron microscope	51
3.6.4 X-ray diffraction	51

3.6.5 Electron back scattered diffraction (EBSD)	52
3.7 Mechanical study	53
3.7.1 Microhardness tester	53
3.7.2 Tensile test	54
3.8 Corrosion study	55

CHAPTER 4

RESULTS AND DISCUSSION

4.1 Mechanical and corrosion behavior of friction stir welded 5083-6061 aluminium alloy joints: Effect of base material position	57
4.1.1 Introduction	57
4.1.2 Experimental Methodology	58
4.1.3 Microstructure characterization	59
4.1.3.1 Optical microscopy	59
4.1.3.2 Electron back scattered diffraction	62
4.1.3.3 Scanning electron microscopy	64
4.1.4 Phase analysis	67
4.1.5 Mechanical properties	68
4.1.5.1 Hardness	68
4.1.5.2 Tensile	70
4.1.6 Corrosion studies	72
4.1.7 Summary	75
4.2 Effect of friction stir welding parameters on the material flow, mechanical properties and corrosion behavior of dissimilar AA5083-AA6061 joints	76
4.2.1 Introduction	76
4.2.2 Experimental Methodology	77
4.2.3 Material flow	78
4.2.4 Microstructural characterization	81
4.2.5 Mechanical properties	86
4.2.5.1 Microhardness	86
4.2.5.2 Tensile properties	87
4.2.6 Corrosion studies	91
4.2.7 Summary	95

4.3 Enhancing corrosion resistance and mechanical properties of dissimilar friction stir welded 5083-6061 aluminium alloys using external cooling environment	96
4.3.1 Introduction	96
4.3.2 Experimental methodology	96
4.3.3 Microstructural characterization	97
4.3.3.1 Macrostructure	97
4.3.3.2 Microstructural analysis	98
4.3.3.3 Electron back scattered diffraction	101
4.3.3.4 Scanning electron microscopy	104
4.3.4 Phase analysis	107
4.3.5 Corrosion behaviour	108
4.3.5.1 Potentiodynamic polarization test	108
4.3.5.2 Electrochemical impedance spectroscopy test	110
4.3.6 Mechanical testing	112
4.3.6.1 Microhardness	112
4.3.6.2 Tensile properties	113
4.3.7 Summary	115
4.4 Analysing microstructure, texture evolution and tensile behavior of dissimilar 5083-6061 aluminium alloys welded using air and water cooled friction stir welding	116
4.4.1 Introduction	116
4.4.2 Experimental methodology	116
4.4.3 Microstructural observation	118
4.4.3.1 Optical microscopy	118
4.4.3.2 Electron back scattered diffraction	121
4.4.3.3 Scanning electron microscopy	123
4.4.3.4 Texture variation	124
4.4.4 Mechanical study	126
4.4.4.1 Tensile properties	126
4.4.4.2 Strain hardening behavior	128
4.4.4.3 Fractography	131

4.4.5 summary	132
CHAPTER 5	CONCLUSIONS
5.1 conclusions	134
5.2 Future scope of work	137
BIBLIOGRAPHY	139
LIST OF PUBLICATIONS	151
CURRICULUM VITAE	153

LIST OF FIGURES

Figure No.	Figure Caption	Page No.
Figure 1.1	An overview of the manufacturing processes and subset of joining processes for production of integrated systems or structures	2
Figure 1.2	An overview layout of the metallic material joining and the context of process-microstructure-properties-performance approach	3
Figure 1.3	Pressure characteristics in diffusion and/or deformation bonding	4
Figure 1.4	A schematic drawing of friction stir welding in a butt joint configuration	6
Figure 1.5	Diagrams showing the concept of (a) the 'processing window' for FSW, and (b) the overlapping of a processing window for welding dissimilar alloys	8
Figure 1.6	Parts of FSW tool	9
Figure 1.7	FSW tools with (a) Trivex, and (b) MX-Trivex pin designs	9
Figure 1.8	Schematic diagram of a 'Triflute' tool design	10
Figure 1.9	(a) Schematic of microstructural zones in FSW (b) Micrograph showing microstructural zones	12
Figure 2.1	Microhardness values across 5251 Al alloy friction stir welds in an H13 and annealed 'O' temper	24
Figure 2.2	Microhardness profiles across a friction stir weld of 7449 T7 Al alloy for two different welding speeds	25
Figure 2.3	Summary of material flow at different shoulder interaction in the transverse section of the weld (Y-Z plane)	27
Figure 2.4	Cross-section view of weld (b) Microstructural features of the FSW cross-section	28
Figure 2.5	Material flow around the tool during FSW	29
Figure 2.6	Defect prone region in the cross-section of FSW sample	30

Figure 2.7	Failure regions of dissimilar FS welded joints at (a) 36 mm/min, (b) 63 mm/min and (c) 60 mm/min	32
Figure 2.8	Vicker's microhardness profiles of the cross-section of dissimilar joints	32
Figure 2.9	Plots illustrating tensile strength vs. strain for both base materials and dissimilar weld joints	33
Figure 2.10	Fracture locations of different joints: (a) Normal FSW and (b) Underwater FSW	35
Figure 2.11	Microhardness profile of FSW joints	35
Figure 2.12	Engineering tensile stress-strain curves of the FSW joints under various parameters	37
Figure 2.13	Polarization curves of different positions of WNZ (a) varying traverse speed and (b) varying rotational speed	37
Figure 2.14	Optical image of friction stir weld of AA5083-O and AA6082-T6 alloys after 7 days immersion test in naturally aerated 3.5% NaCl solution	38
Figure 2.15	EIS plot of the three regions on AA5083, FSW and AA7023 surfaces in 3.5% NaCl electrolyte	38
Figure 2.16	Orientation distribution function (ODF, $\Phi_2 = 0^\circ, 45^\circ, 90^\circ$) of AA6061-T6 and AA5052-O alloy	40
Figure 2.17	{100}, {110}, and {111} pole figures of (a) center of stirred zone, (b) advancing, (c) and retreating sides	41
Figure 2.18	Strain hardening rate as a function of net flow stress of the base alloy and FSWed samples	42
Figure 2.19	strain hardening exponent, (b) strain hardening rate vs flow stress of FSWed joints at varying welding speeds	43
Figure 3.1	Work layout of the proposed work	45
Figure 3.2	FSW tool with schematic	46
Figure 3.3	Friction stir welding machine	48
Figure 3.4	(a) cooling environment set up and (b) water-cooling process.	49
Figure 3.5	Optical microscope used for microstructural studies.	50

Figure 3.6	Scanning electron microscopy	51
Figure 3.7	X-ray diffraction	52
Figure 3.8	Electron backscattered diffraction system	53
Figure 3.9	Hardness measuring line of the cross section sample	53
Figure 3.10	Vickers microhardness tester	54
Figure 3.11	ASTM E8 standard schematic specimen	54
Figure 3.12	Universal testing machine	55
Figure 3.13	Electrochemical work station	56
Figure 4.1	(a) FSW tool, (b) FSW schematic illustration, (c) Tensile specimen Schematic	59
Figure 4.2	Macrostructure images of: (a) AA5083-AA5083, (b) AA6061-AA6061, (c) AA5083-AA6061, and (d) AA6061-AA5083	60
Figure 4.3	Microstructure images of the AA5083-AA6061 sample condition: (a) AA5083-BM, (b) AS-HAZ, (c) AS-TMAZ, (d) SZ, (e) RS-HAZ and (f) AA6061-BM along with the macrostructure	61
Figure 4.4	The inverse pole figure in Z direction of (a) AA5083-BM, (b) AA6061-BM and (c) AA5083-AA6061-SZ	63
Figure 4.5	The distributions of misorientation angle distribution of: (a) AA5083-BM, (b) AA6061-BM, and (c) AA5083-AA6061-SZ	63
Figure 4.6	SEM picture and EDS spectrum of the FSWed AA5083-AA6061 joint's onion ring sub-layers	64
Figure 4.7	(a) SEM image of AA5083-H111, (b) EDS spectrum at location 1 and (c) EDS at location 2	66
Figure 4.8	(a) SEM of AA6061-T6, (b) EDS spectrum at location 1 and (c) EDS spectrum at location 2	66
Figure 4.9	SEM with EDS images at the SZ: (a) AA5083-AA5083, b) AA6061-AA6061, (c) AA5083-AA6061 and (d) AA6061-AA5083	67
Figure 4.10	Base materials and FSWed samples XRD peaks	68
Figure 4.11	Microhardness across the transverse cross section of FSWed joints: (a) AA5083-AA5083, (b) AA6061-AA6061, (c) AA5083-AA6061 and (d) AA6061-AA5083	69

Figure 4.12	strain-strain curves of the base material and FSWed samples	71
Figure 4.13	PDP curves of (a) as-received base materials (b) FSWed joints at different conditions (c) EIS plots of similar and dissimilar joints	73
Figure 4.14	Optical micrograph images of: (a) AA5083-BM (b) AA6061-BM, (c) AA5083-AA5083, (d) AA6061-AA6061, (e) AA5083-AA6061 and (f) AA6061-AA5083	74
Figure 4.15	(a) FSW schematic illustration, (b) FSW tool with dimensions, (c) Schematic of traverse tensile test specimen and (d) Schematic of notch tensile test specimen	77
Figure 4.16	Macrostructure images of the transverse cross-section of the dissimilar FSWed sample conditions: (a) 800-40, (b) 800-60, (c) 800-80, (d) 1100-60, (e) 1400-60 and (f) 1700-60	79
Figure 4.17	Microstructures at the SZ towards the advancing side of the dissimilar FSWed sample conditions: (a) AS-800-40, (b) AS-800-60, (c) AS-800-80, (d) AS-1100-60, (e) AS-1400-60 and (f) AS-1700-60	80
Figure 4.18	SEM image and EDS spectrum of the onion ring sub-layers of the dissimilar FSWed AA5083-AA6061 joint at 800-40 sample condition	81
Figure 4.19	Microstructure images of the dissimilar AA5083-AA6061 FSWed sample condition of 1400 rpm and 60 mm/min: (a) AA5083-BM, (b) AS-HAZ, (c) AS-TMAZ, (d) SZ, (e) RS-HAZ and (f) AA6061-BM along with the macrostructure	83
Figure 4.20	Microstructure images at the SZ of the dissimilar AA5083-AA6061 FSWed sample conditions: (a) 800-40, (b) 800-60, (c) 800-80, (d) 1100-60, (e) 1400-60 and (f) 1700-60	84
Figure 4.21	(a) SEM image of AA5083-H111, (b) EDS spectrum of Al(Fe, Mn, Mg/Si) and (c) EDS of Al-Mg	85
Figure 4.22	(a) SEM of AA6061-T6, (b) EDS spectrum of Al(Fe, Mg, Si) and (c) EDS of Mg-Si	85

Figure 4.23	SEM images at the SZ of the dissimilar AA5083-AA6061 FSWed sample conditions: (a) 800-40 (along with EDS analysis at location 1, location 2 and location 3), (b) 800-60, (c) 800-80, (d) 1100-60, (e) 1400-60 and (f) 1700-60	86
Figure 4.24	Microhardness profiles of the dissimilar AA5083-AA6061 FSWed joints: (a) varying traverse speeds and (b) varying rotational speeds	87
Figure 4.25	Tensile stress-strain graph of dissimilar AA5083-AA6061 FSWed joints: (a) Varying traverse speed and (b) Varying rotational speed along with the fractured specimens	89
Figure 4.26	Notch tensile stress-strain graph of dissimilar AA5083-AA6061 FSWed joints: (a) Varying traverse speed and (b) Varying rotational speed along with the fractured specimens	89
Figure 4.27	Fractography SEM images of the samples after the tensile test: a) AA5083-H111, b) AA6061-T6, c) 800-80 and d) 1400-60	90
Figure 4.28	PDP curves of dissimilar AA5083-AA6061 FSWed joints: (a) as-received base materials (b) varying traverse speed and (c) varying rotational speed	93
Figure 4.29	Corrosion morphologies at the dissimilar AA5083-AA6061 FSWed sample conditions: (a) 800-40, (b) 800-60 and (c) 800-80, (d) 1100-60, (e) 1400-60 and (f) 1700-60	94
Figure 4.30	EIS plots of the dissimilar AA5083-AA6061 FSWed joints: (a) varying traverse speed and (b) varying rotational speed	95
Figure 4.31	Photographs of dissimilar friction stir welded plates in (a) ACFSW, (b) NCFSW and (c) WCFSW	97
Figure 4.32	Macrostructure of dissimilar FSWed AA5083-6061 joints in (a) ACFSW, (b) NCFSW and (c) WCFSW conditions	98
Figure 4.33	Microstructure images of the dissimilar AA5083-AA6061 FSWed sample conditions: (a) AA5083-BM, (b) AS-HAZ, (c) AS-TMAZ, (d) SZ, (e) RS-HAZ and (f) AA6061-BM	100
Figure 4.34	Microstructure images at the HAZs of the dissimilar AA5083-AA6061 FSWed sample conditions: (a) AS-ACFSW, (b) RS-	101

ACFSW, (c) AS-NCFSW, (d) RS-NCFSW, (e) AS-WCFSW and (f) RS-WCFSW	
Figure 4.35 EBSD (IPF + Grain boundary) for the (a) AA5083-BM, (b) AA6061-BM, SZ of the (c) ACFSW, (d) NCFSW and (e) WCFSW	103
Figure 4.36 Misorientation angle distributions for the (a) AA5083-BM, (b) AA6061-BM, SZ of the (c) ACFSW, (d) NCFSW and (e) WCFSW	104
Figure 4.37 SEM-EDS images of as-received base materials (a) AA5083-H111 and (b) AA6061-T6	105
Figure 4.38 (a) SEM images of the dissimilar FSWed AA5083-AA6061 joints of (a) ACFSW (along with EDS analysis at location 1, location 2 and location 3), (b) NCFSW and (c) WCFSW	106
Figure 4.39 XRD results of base materials and FSWed samples	107
Figure 4.40 Tafel curves of BM and FSWed samples	109
Figure 4.41 Optical micrograph images of: (a) AA5083-BM (b) AA6061-BM, (c) ACFSW, (d) NCFSW and (e) WCFSW	110
Figure 4.42 (a) EIS plot of FSWed samples and (b) Equivalent circuit used for fitting of the curves obtained from EIS test	111
Figure 4.43 Hardness distribution across the FSWed joints	112
Figure 4.44 (a) Stress-strain curves of base materials and FSWed samples and (b) Appearance of the failed tensile samples	113
Figure 4.45 Fracture surfaces of the (a) AA5083-BM, (b) AA6061-BM, (c) ACFSW, (d) NCFSW and (e) WCFSW	115
Figure 4.46 (a) Schematic illustration of FSW process, (b) Pseudo-3D optical micrograph of AA5083-H111 (c) Pseudo-3D optical micrograph of AA6061-T6, (d) Schematic with dimensions of a tensile test specimen and (e) Schematic diagram for sample preparation	117
Figure 4.47 Optical images of ACFSW: (a) Macrostructure of ACFSW, (b) HAZ-AS, (c) HAZ-RS, (d) TMAZ-AS, and (e) SZ	119

Figure 4.48	Optical images of WCFSW: (a) Macrostructure of WCFSW, (b) HAZ-AS, (c) HAZ-RS, (d) TMAZ, and (e) SZ	120
Figure 4.49	EBSD images and Misorientation angle distributions: (a) 5083-BM, (b) 6061-BM, (c) ACFSW-SZ, and (d) WCFSW-SZ	122
Figure 4.50	SEM images with EDS analysis of (a) AA5083-BM and (b) AA6061-BM	123
Figure 4.51	SEM images with EDS analysis of joints: (a) ACFSW and (b) WCFSW	124
Figure 4.52	{100}, {101} and {111} PFs and ODFs: (a) 5083-BM, (b) 6061-BM, SZ of the (c) ACFSW and (d) WCFSW	126
Figure 4.53	Stress-strain plots of BMs and FSWed samples: (a) Transverse tensile specimens (b) Longitudinal tested specimens at SZ (c) Longitudinal tested specimen in advancing and retreating side	128
Figure 4.54	A typical plot to evaluate strain hardening exponent of FSWed samples: (a) Transverse tensile specimens (b) Transverse tested specimens (c) Longitudinal tested specimen and (d) Longitudinal at HAZ in advancing and retreating side tensile specimens	130
Figure 4.55	Strain hardening rate (θ) versus net flow stress ($\sigma - \sigma_y$) plots of (a) Transverse tested specimens, (b) Longitudinal tested specimen and (c) Longitudinal tested of HAZ in advancing and retreating side tensile specimens	131
Figure 4.56	SEM images of the fracture surfaces of (a) AA5083-H111, (b) AA6061-T6, (c) ACFSW-L and (d) WCFSW-L	132

LIST OF TABLES

Table No.	Table Caption	Page no.
Table 1.1	Tool materials used for FSW of monolithic alloys	11
Table 1.2	International designation system for Al wrought alloys	15
Table 1.3	Temper conditions of heat treatable wrought Al alloys	15
Table 1.4	Temper conditions of non-hetreatable wrought Al alloys	16
Table 1.5	Common tempering conditions of commercial cast Al alloys	16
Table 1.6	United State revised designation system for Al cast alloys	17
Table 3.1	Chemical composition of AA5083-H111 and AA6061-T6	45
Table 3.2	Mechanical properties of AA5083-H111 and AA6061-T6 aluminium alloys	45
Table 3.3	Chemical composition of AISI H13 tool steel	46
Table 3.4	FSW Machine specifications	47
Table 3.5	Specifications of 3D Optical microscopy	50
Table 3.6	Euler angles for different texture components of FCC materials	52
Table 4.1	EBSD results	62
Table 4.2	Similar and dissimilar FSWed sample conditions tensile characteristics	71
Table 4.3	Corrosion potential and corrosion current density of the base materials and FSWed samples	74

Table 4.4	Stir zone width and onion ring sub-layer width of the dissimilar AA5083-AA6061 FSWed sample conditions	80
Table 4.5	Tensile properties of the base materials and dissimilar AA5083-AA6061 FSWed sample conditions	91
Table 4.6	Corrosion potentials and corrosion current density of the base materials and dissimilar AA5083-AA6061 FSWed sample conditions	93
Table 4.7	Grain size at AS-HAZ and RS-HAZ of the dissimilar AA5083-6061 FSWed sample conditions	99
Table 4.8	EBSD results of the base materials and dissimilar FSWed AA5083-AA6061 sample conditions	103
Table 4.9	Corrosion potentials and corrosion current density of the base materials and dissimilar FSWed AA5083-AA6061 sample conditions	109
Table 4.10	The fitting results of the EIS data at SZ of dissimilar AA5083-AA6061 FSWed joints	111
Table 4.11	Tensile properties of the base materials and dissimilar FSWed AA5083-AA6061 sample conditions	114
Table 4.12	Average grain size at HAZ-AS, HAZ-RS and SZ of FSWed sample conditions	120
Table 4.13	Summary of tensile test results of the BMs and dissimilar FSWed samples	127
Table 4.14	Summary of strain hardening parameters	129

LIST OF ABBREVIATIONS

FSW	Friction stir welding
TWI	The Welding Institute
DRZ	Dynamic recrystallized zone
SZ	Stir zone
HAZ	Heat affected zone
TMAZ	Thermo-mechanically affected zone
AS	Advancing side
RS	Retreating side
WNZ	Weld nugget zone
BM	Base metal
OM	Optical microscope
SEM	Scanning electron microscope
EDS	Energy dispersion spectroscopy
XRD	X-ray diffraction
EBSD	Electron backscattered diffraction
PF	Pole figure
ODF	Orientation distribution functions
DRX	Dynamic recrystallization
ACFSW	Air-cooled friction stir welding
NCFSW	Liquid nitrogen-cooled friction stir welding
WCFSW	Water-cooled friction stir welding
SPD	Severe plastic deformation
FCC	Face centered cubic
LAGBs	Low angle boundaries
HAGBs	High angle boundaries
IPF	Inverse pole figure
AGG	Abnormal grain growth
UTM	Universal testing machine
UTS	Ultimate tensile strength

YS	Yield strength
TE	Tensile Elongation
NDT	Nondestructive testing
OCP	Open circuit potential
EIS	Electrical impedance spectroscopy
PDP	Potentiodynamic polarization
CPE	Constant phase elements
R_p	Polarization resistance
R_s	Solution resistance
Z_{im}	Imaginary component of impedance
Z_{re}	Real component of impedance
Y_o	admittance
SAZ	shoulder affected zone
PAZ	pin affected zone

LIST OF SYMBOLS

μm	micrometer
mm	millimeter
V	Linear speed or traverse speed
W	Rotational speed
Q	Activation energy
ϵ	Strain rate
R	Gas constant
T	Temperature
T_{MP}	Melting temperature
f_{HAGB}	Fraction of high angle boundaries
HV	Vickers hardness
Y_s	Yield strength
UTS	Ultimate tensile strength
TE	Tensile Elongation
Θ	strain hardening rate
Θ_0	strain hardening rate at yield stress
n	Strain hardening exponent
σ_s	Saturation stress
σ	Stress
$\sigma - \sigma_y$	net flow stress
E_{corr}	Corrosion potential
I_{corr}	Current density
R_s	Solution resistance
R_{CT}	Charge transfer resistance

CHAPTER 1

INTRODUCTION

This chapter explains the introductory nature and general introduction of the subject matter of thesis viz, history of welding, the concept of friction stir welding, essential characteristics of aluminium alloys, welding of aluminium alloys. The scope of the present research lies in an increasing demand for utilizing aluminium alloys in various engineering sectors. The thesis discusses the mechanical and corrosion properties of friction stir welded dissimilar AA5083-AA6061 aluminium alloys.

1.1 Background

Welding is a fabrication or artistic method that unites materials. Gold round containers likely to be produced around 2000 years ago by pressure welding have been discovered. Many tools and weapons were left behind, and bronze and iron artifacts showed forging and forge welding activities discovered in Egypt's pyramids. Many articles of iron were welded by hammering during the Middle Ages. The Iron Pillar located at Delhi in India was built almost 1700 years ago, is one of the most massive welds from this period. Professional welding, as we know it today, did not come until the nineteenth century. In the mid-nineteenth century, Englishman Sir Humphrey Davies discovered acetylene and used a battery to create an arc between two carbon electrodes. After the invention of the electric generator, arc welding became popular in the mid-nineteenth century. Gas cutting/welding and arc welding with carbon/metal electrodes were invented in the late 1800s and early 1900s respectively. Resistance welding has also evolved into a helpful method of joining materials.

The demand for metal materials production by welding was drastically increased as a servicing process during World War I, which led to inventing new welding and joining techniques to meet the demand in the US and Europe. After War in 1919, The American Welding Society (AWS) was founded to advance the allied processes of welding. In 1920, automatic welding and several grades of electrodes with and without coated were developed. In 1941, Heliarc welding (helium for shielding) was invented and patented by Meredith. The gas shielded metal arc welding was developed by Battelle Memorial Institute in 1948. The same principle was used in gas tungsten arc welding (GTAW) by replacing tungsten electrodes. Later many welding techniques were developed to improve its applications. Electron beam welding was developed by French Atomic Energy Commission in 1940.

1.2 Welding/joining

In the production of integrated systems, welding and connecting materials is a crucial stage. The majority of traditional welding procedures entail local melting along the joint line, followed by solidification, which results in the development of a joint. **Figure 1.1** depicts a broad classification of manufacturing processes, with metal welding and joining falling under consolidation processes. Joining and mechanical fastening are examples of consolidation/assembly processes. The joining technique chosen is determined by the size and design of the structures. Shipbuilding uses welding processes, whereas large airplanes use mechanical fastening. Automobiles employ a variety of processes, that includes joinig/welding and adhesive bonding. Role of joining process on the workpiece is a critical factor to consider. **Figure 1.2** depicts the relationship between joining and microstructural changes and reliability of metals. The inset in the illustration is a famous liberty ship that failed because of a faulty joining method. Design, materials, welding techniques and final inspection are all intertwined. Of course, a basic grasp of these is necessary to avoid sudden failures and enhance the structural efficiency of the systems.

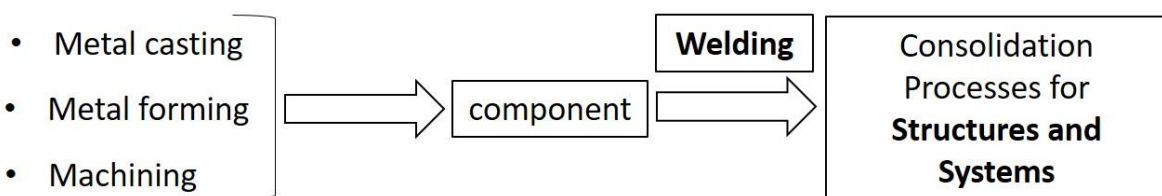


Figure 1.1: An overview of the manufacturing techniques.

Fusion welding, solid-state welding, brazing and soldering, and adhesive bonding are the four fundamental categories of metal joining methods. Melting of base metal and addition of a filler

metal with a continuous puddle of liquid metal joins the pieces of metals in fusion welding methods. The metal pieces are connected once the molten pool solidifies. Only the filler metal melts in the brazing and soldering instead of base metal; the filler metal is pulled into the area between the base metals and solidifies to form the link. The filler substance in adhesive bonding is glue rather than molten metal. Bond formation occurs via deformation or atom diffusion, and neither the base metal nor the filler metal is melted.

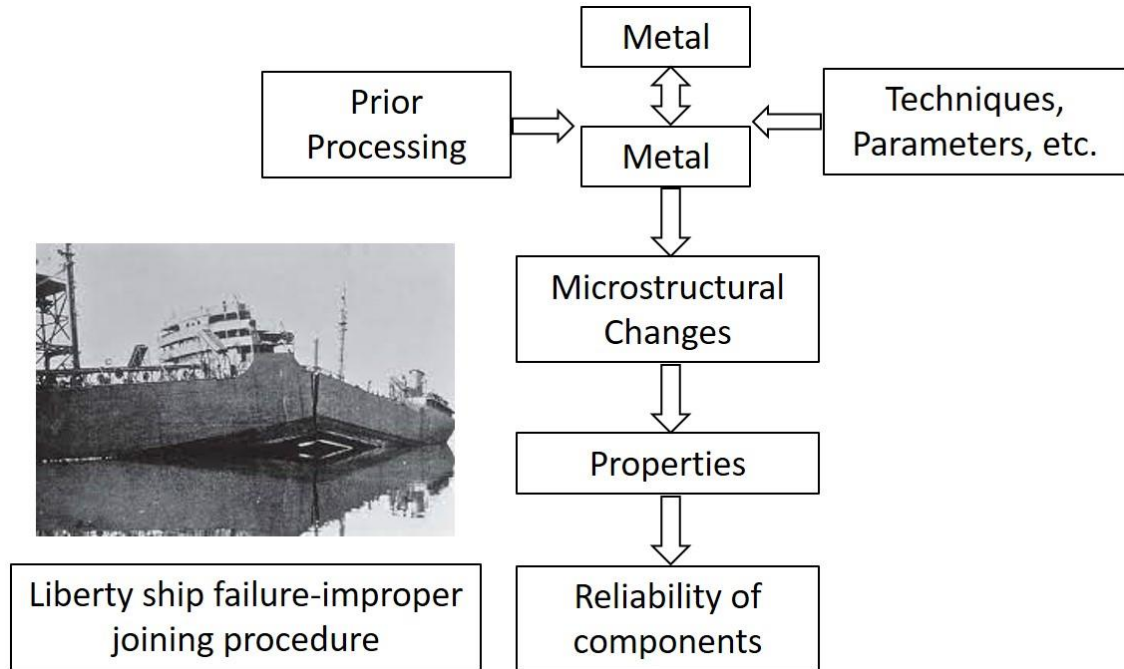


Figure 1.2: layout showing the metal joining with process-microstructure-properties-performance approach [Mishra et al., (2014)].

1.2.1 Fusion welding

Chemical bonding between metal pieces takes place in the molten state of fusion welding procedures, which may necessitate the use of a filler wire roll or a consumable electrode. The most common types of fusion welding are MIG, TIG, LBW, and EBW. Because all of these techniques involve melting metal and then solidifying it to produce the joint, fusion welding has several drawbacks. As a result, the finished weld has a casting structure, which reduces the weld mechanical qualities like fatigue strength, ultimate tensile strength, and ductility. Issues like porosity, hot cracking, micro-segregation, and other macro and microstructural problems are all drawbacks of the casting structure in the joint made by fusion welding.

Moreover, because different metals have different thermal conductivity and expansion, the fusion welding technique restricts combining dissimilar metals and alloys. Furthermore, the heat-affected zone (HAZ) in fusion welding procedures is significant, resulting in a reduction in the mechanical characteristics of the welds.

1.2.2 Solid-state welding

Pressure and deformation of material provide a large percentage of the bonding in these processes. In most cases, no filler material is required and melting of the base metal does not occur. Diffusion bonding uses a high enough pressure to distort the hills and valleys locally on the abutting surfaces. There is no significant distortion of the base metals. The atoms are then allowed to diffuse across the interface at temperatures just below the melting temperature of the base metals, filling up any residual voids and completing the process of joining. Deformation bonding techniques use applied pressures higher than the work piece yield strength, generating gross deformation and bringing atoms on one surface into close contact with atoms on the other. The joint is formed via atomic attraction. Cold welding, forge welding, explosive welding, friction welding, roll welding, ultrasonic welding, and friction stir welding (FSW) are all categorized under solid-state welding techniques. Because the materials move and combine to form the joint, FSW is unique among deformation-based solid-state procedures. It produces outstanding qualities when done correctly, which is why it has been used successfully in various aerospace, automotive, and shipbuilding applications. **Figure 1.3** depicts a configuration of pressure and time during solid-state welding. FSW causes significant plastic deformation and has a short weld cycle

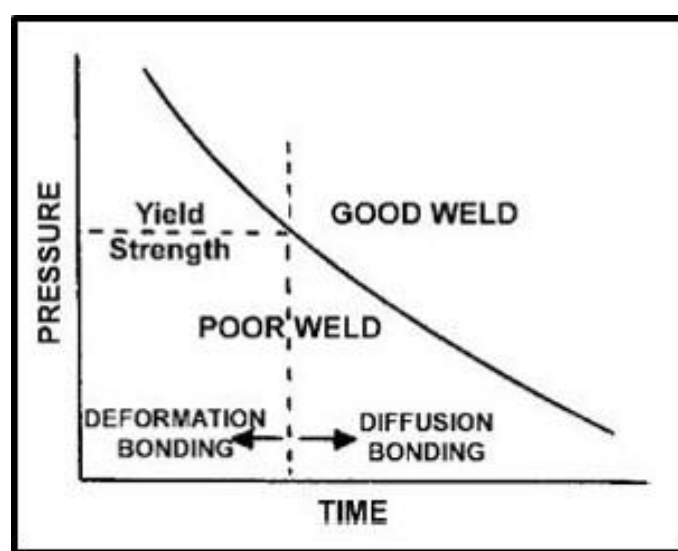


Figure 1.3: Pressure characteristics in diffusion or deformation bonding [Mishra et al., (2014)].

1.3 Friction stir welding

Friction stir welding (FSW) is a more advanced variant of traditional friction welding. The Welding Institute (TWI) invented it in 1991 [[\(Thomas and Nicholas 1997\)](#)]. It is the most recent and significant advancement in metal joining technology in the last two decades. FSW first gained popularity as a solid-state joining technique for similar aluminum alloys. Still, it is currently being used to combine different alloys and metals of more challenging metal and plastics.

1.3.1 Working principle

The FSW technique involves rotating and slowly plunging a profiled pin into the joint line between two rigidly secured substrates on a backing plate support. A cylindrical tool pin profile is shown in **Figure 1.4**, along with a schematic depiction of FSW and a developed fixture for clamping the plates. With force applied, the tool shoulder is in firm contact with the top surface of the workpiece. Frictional heat is produced between the workpieces and the welding tool (shoulder and pin). The tool shoulder is subjected to more heat than the pin surface.

On the other hand, rotation of the tool pin causes deformation or churning, resulting in more heat. The plasticized material surrounding the pin undergoes extreme deformation and a material flow from the tool's front edge to the trailing edge, forged into the joint. As a result, a solid-state link forms between the two plates. Due to the tool's combination of rotating and traverse motions, the velocities of two symmetrical spots on the advancing side (AS) and retreating side (RS) are not the same. As a result, the heat transfer and material flow of the two sides of the weld are asymmetric. In fact, in the AS, the rotational tool speed and traverse speed are the same; however, they are not in the RS.

1.3.2 Basic terminology

The basic terminology of the friction stir welding process was considered from the American standard: D17.3/D17.3:2016 specification for friction stir welding of aluminium alloys for aerospace applications.

- **Shoulder** – Part of the welding tool that deforms the top layers of the workpiece and accommodates the material deformed by the pin. Usually, the shoulder to pin diameter is in the ratio of 2-3.
- **Pin/probe** – Part at the end of the FSW tool that is inserted into the base material to make the weld.

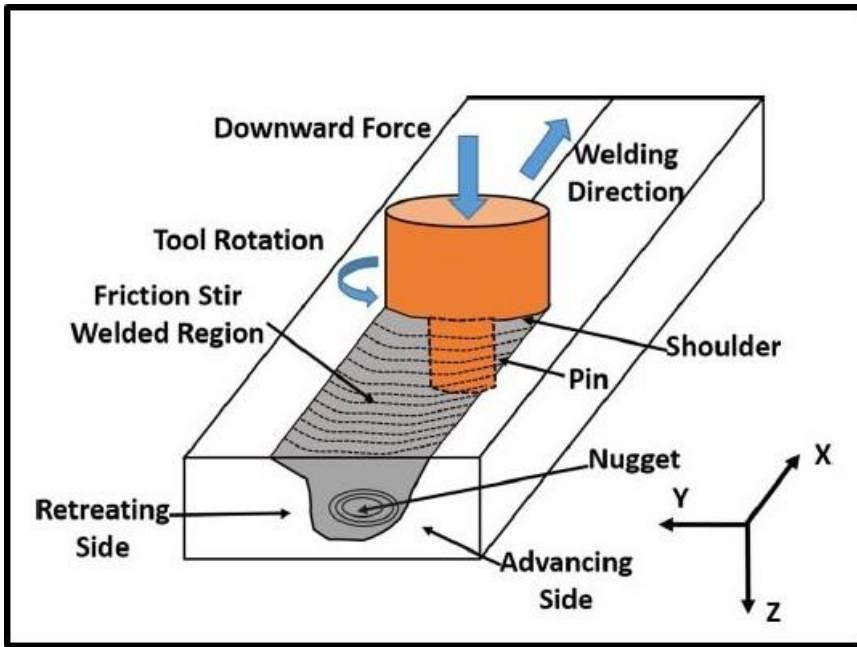


Figure 1.4: In a butt joint configuration, a schematic representation of friction stir welding [Wang et al., (2018)].

- **Tool rotational rate or speed** – The Angular speed of the welding tool in rpm.
- **Traverse speed** – Rate at which the welding operation progresses in the direction of welding.
- **Spindle head tilt** – Usually referred to as the tilt angle, it is the angle between the spindle axis and normal axis of the workpiece.
- **Advancing side (AS)** – Side of the joint where the tangential direction of tool rotation is the same as the welding direction.
- **Retreating side (RS)** – Side of the joint where the tangential direction of tool rotation is opposite to the welding direction.
- **Leading edge** – The un-welded region in front of the tool along the weld line.
- **Trailing edge** – The welded region back to the tool along the weld line.
- **Axial force** – Force applied to the work piece along the axis of tool rotation.
- **Cavity** – Void-type discontinuity within a solid-state weld.
- **Exit hole** – Hole remains at the end of a weld after the withdrawal of the tool.
- **Flash** – Material expelled along the weld toe during FSW.
- **Incomplete joint penetration** – Discontinuity where the total thickness of the joint has not been welded.

- **Linear mismatch across joint** – Misalignment between two welded pieces such that while their surfaces planes are parallel, they are not in the required plane.

1.3.3 Different types of process parameters in the FSW process

The fundamental goal of any welding process is to generate defect-free welds, with quality weld joints coming in second (generally strength and appearance). The bond formation determines the quality of the friction stir welding process (for the material flow). Most of the heat generated during friction stir welding is due to material deformation caused by the rotating tool effect [Rhodes et al., (1997)]. The tool's size, shape, rotational speed, and traverse speed determine the weld region's peak temperature. The quantity of heat input within the weld zone is controlled in part by the rotation, traverse speed, and axial force. The greater the tool diameter, the faster it rotates and the slower it traverses, the more heat it generates.

On the other hand, the lower the heat input within the weld is generated due to the higher traverse speed or the lower rotating speed. This lower heat may not be enough to soften the material sufficiently, resulting in incorrect material flow, pin damage, and defect formation [Zeng et al., (2018)]. The quantity of heat generated during joining has a significant impact on the mechanical and corrosion properties of the joined components. Grain coarsening occurs as a result of excessive heat, resulting in poorer mechanical and corrosion properties. Minimizing heat input may help to mitigate this risk. The temperature should not be reduced to the point where the material softening beneath the probe is prevented. As a result, correct welding parameters must be chosen to ensure that the temperature surrounding the tool is high enough to allow adequate material flow [Ren et al. (2007)]. The heat generated during the process alters the post-weld microstructure, resulting in distinct microstructures in different locations.

1.3.3.1 Tool rotation and traverse speed

The tool transverse and rotational speed will need to be appropriately selected to establish a satisfactory FSW joint. During welding, the material surrounding the tool must be heated to a temperature range where significant plastic deformation can quickly occur while minimizing the forces acting on the tool. In general, increasing rotation speed or reducing transverse speed increases heat input to the work piece [Peel et al., (2006)]. Inadequate heat generation can result in cavities and flaws inside the stir zone, and high processing forces can damage the friction stir tool. Too high a temperature, on the other hand, might cause the material's surface layer to melt, resulting in cavities or affecting the microstructure through re-

solidification [Peel et al., 2006]). Because these factors degrade the material's quality, the processing conditions must be chosen within the 'processing window' to achieve a high-quality weld (**Figure 1.5**). Unfortunately, the processing window varies depending on the alloy. As a result, when two incompatible materials or alloys are welded, the permissible processing parameters are further limited.

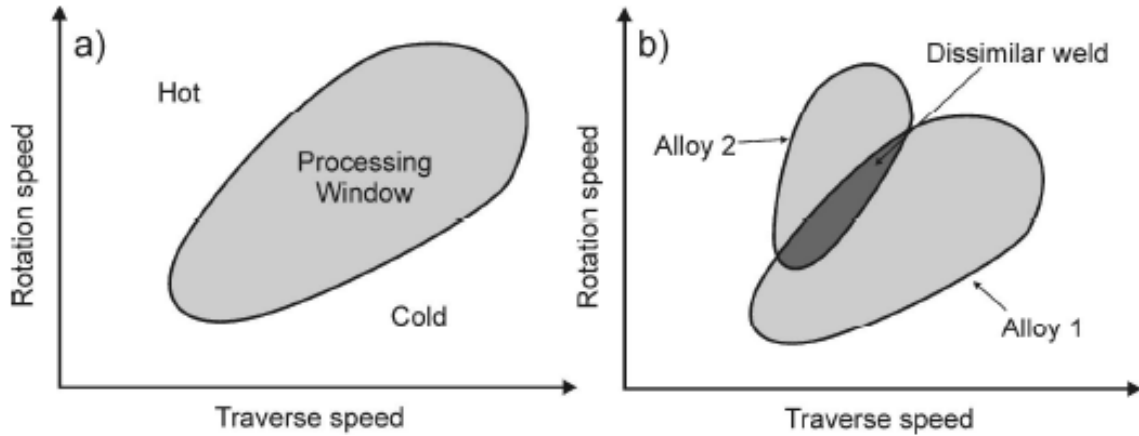


Figure 1.5: Images showing the concepts of (a) FSW 'processing window' and (b) overlapping of a processing window in case of dissimilar alloys welding [Peel et al., (2006)].

1.3.3.2 Tool design

In FSW, the tool design is exceptionally crucial. The quality of the weld, or processed track, can be enhanced and productivity can be increased by utilizing a correctly designed tool piece. As shown in **Figure 1.6**, an essential friction stir tool consists of two major parts: the tool shoulder and the tool pin. The tool shoulder's primary purpose is to keep the material under the tool from being lost as a flash. The shoulder generates the heat needed to raise the temperature of the material to a point where it can be plasticized easily. The tool pin's principal function is to transfer material up and down the SZ and around the pin by acting as a "small" solid-state extrusion pump. The pin also aids in breaking up and dispersing big particles, oxides, and contaminants present in the material. The pin and shoulder have undergone numerous improvements and adjustments, and each design is thought to have a somewhat different function.

The most common and first to be used was the 'Whorl' pin design [Mishra et al., (2016)]. This pin is either cylindrical or tapered, with a thread features on the pin surface. Additionally, the pins may have salient features with threads of varied pitches. These features are thought to increase the material downward flow ability and as a result, optimize the weld quality. The 'Trivex' design uses a triangle probe instead of a cylindrical or tapered pin, which is another regularly used pin geometry (**Figure 1.7**).

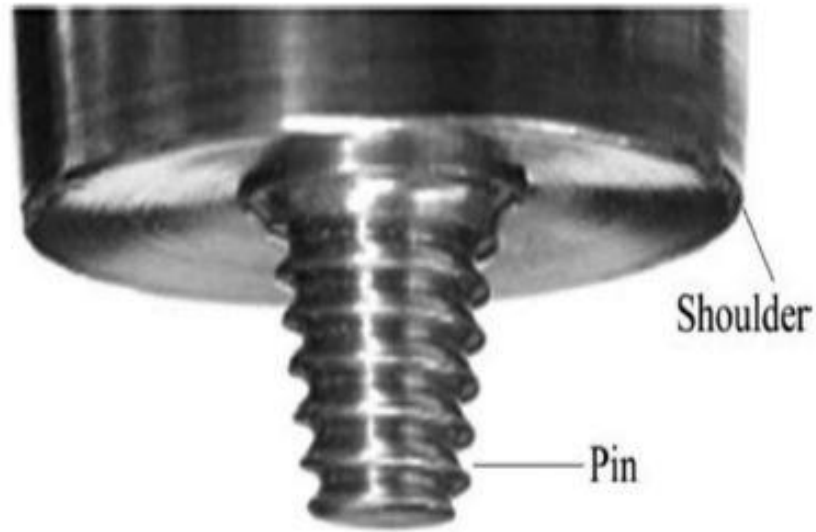


Figure 1.6: Parts of FSW tool [Meilinger et al., (2013)].

Pin with Flat surfaces have been discovered to lessen the forces acting on the tool, by lowering the danger of the tool or machine being damaged [Thomas et al., (2001)]. As a result, trivex tools are increasingly used to weld and treat materials with a thicker section. Threads can be added to the pin and the flats, which is thought to aid in the break-up of big second phase particles within the material. As a result, the final microstructure will have a finer particle dispersion, and the material's characteristics will be improved after processing.

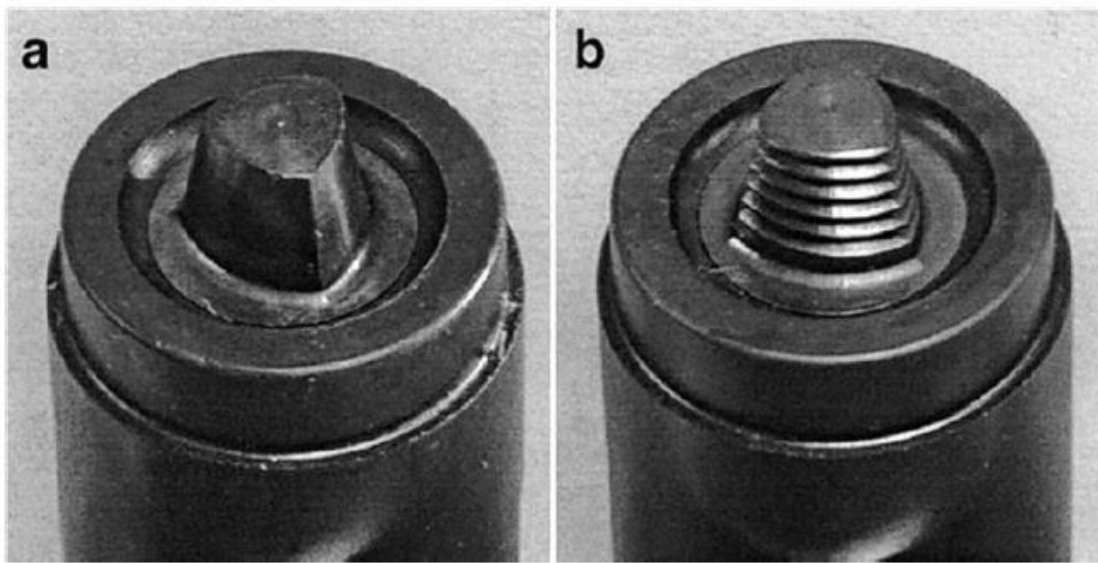


Figure 1.7: (a) Trivex and (b) MX-Trivex pin designs [Kumar et al., (2007)].

The 'Triflute' design (**Figure 1.8**) is also being researched and used more frequently. The triflute design is slightly more sophisticated than the whorl and trivex pins. The design consists of a tapered

and threaded pin with three revolving salient flutes. These features are thought to aid in distributing heat and oxide break up by increasing material mobility around the pin.

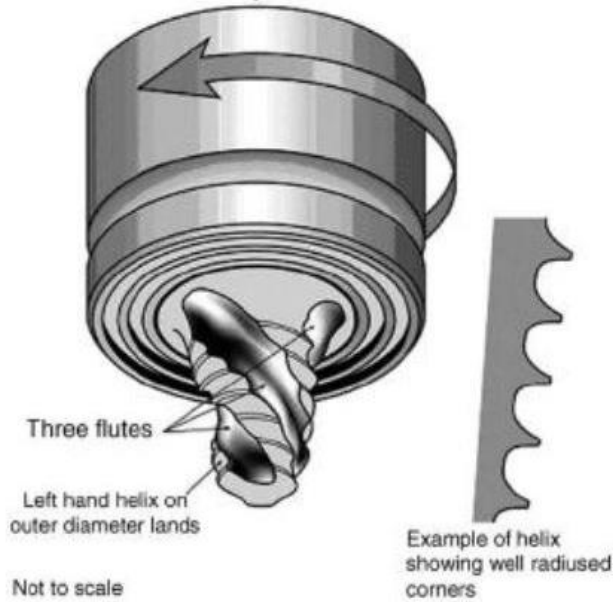


Figure 1.8: 'Triflute' tool design schematic [Thomas et al., (2001)].

Many scholars have analyzed alternative pin modifications; however, most were unsuccessful or are uncommon. A retractable pin feature, which allows the probe to change its length during processing, is a particularly fascinating design that NASA has examined. In this plunge depth may be readily adjusted during the operation. The pin can also be progressively retracted at the final exit position to avoid a material exit hole. This is especially crucial during repair welding and when material waste must be minimized.

Additionally, adjustments to the shoulder design can be made to improve the joining process. When the FSW process is carried out with zero tilt angle, scrolls or grooves are frequently used on the shoulder. This is thought to diminish flash and improve material mobility around the tool near the weld surface, improving a fine grain structure generation. However, as shown in **Figure 1.6**, the concave shoulder design is used when the tool is tilted. This configuration works as an hindrance to extruding materials coming out side of the shoulder and therefore maintaining downward force on the base metals to ensure excellent forging and avoiding flaws.

1.3.3.3 Tool tilt and plunge depth

The plunge depth is defined as the distance between the lowest surface of the shoulder and the surface of the material to be treated. This is required to generate pressure beneath the tool for the material to be suitably forged at the tool trailing edge. Inadequate plunge depth

can lead to erroneous welding or processing depths and the formation of cavities in the material. On the A high plunge depth can damage the tool by rubbing between the backing plate and the pin. Furthermore, if the plunge depth is set too high, a substantial amount of flash will be created, resulting in a significant variation in thickness at the welded zone and the unaffected material [Mishra et al., (2016)]. Moreover, a tool tilt by 2-4° can be given to the tool, making the front of the tool higher than the back. This is said to help with forging at the tool trailing edge and also increase the process quality. However, because the tool is at an angle, the surface contact between the material and the tool shoulder is reduced, resulting in less heat input. As a result, the tilt angle is typically limited to 4°, with 0.2-0.3 mm plunge depth is used to improve the contact area.

1.3.4 Tool materials

The tool material must be harder than the plate material to be welded. The heat generation between the tool shoulder and the surface of the plates depends on the coefficient of friction. If the coefficient of friction is higher, the heat generation will be higher. The hardness of the tool influences the coefficient of friction. The chemical composition of the tool material significantly affects the hardness of the tool [Padmanaban et al., (2009)]. A less hard tool will produce less heat generation and induce defects and vice versa. **Table 1.1** shows various tool materials commonly used for FSW of different monolithic alloys.

Table 1.1: Tool materials used for FSW of monolithic alloys

S.No	Work piece material	Tool material
1.	Aluminium and alloys	High-speed steel, High carbon steel, Tool steel, Mild steel, stainless steel.
2.	Magnesium and alloys	High-speed steel, High carbon steel, Tool steel, Mild steel, stainless steel
3.	Copper and alloys	Hot work steel, Ni-based super alloys, Tungsten.
4.	Steels, Nickel, Titanium and its alloys	Polycrystalline Cubic Boron Nitride (PCBN), Polycrystalline Diamond (PCD), Tungsten-25% rhenium alloy, Tungsten Carbide (WC), Tungsten, Mo-based alloys.

1.3.5 Microstructure evolution in FSW

As previously stated, produced heat and deformation cause the base metal (BM) to flow without melting, allowing the tool to be moved along the weld line. The distorted material is moved from the tool pin's AS to its RS, which is forged by the tool shoulder, producing a solid-state bond between the two plates. The weld zone's significant plastic deformation causes a widespread change in microstructural and, as a result, mechanical properties. FSW partitions the microstructure of joints into distinct zones. **Figure 1.9** depicts the typical macrostructure of an FSW-welded joint. The zones can be divided into the following categories:

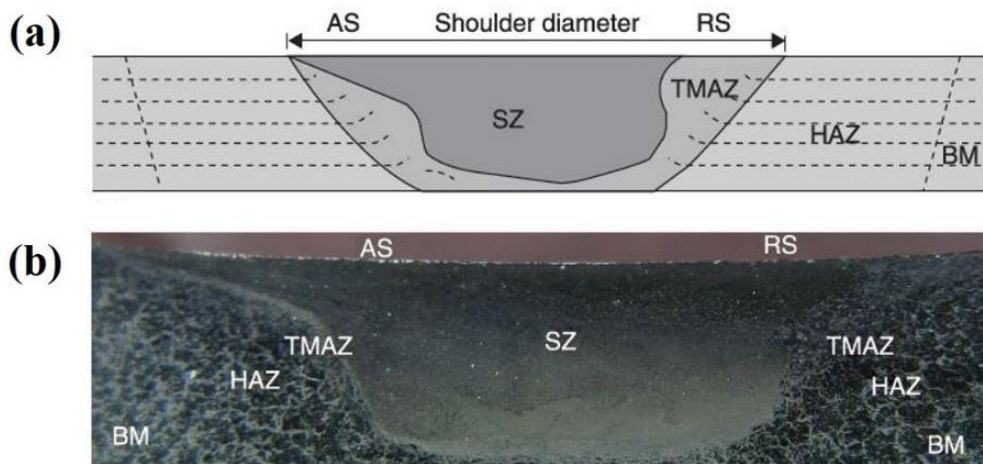


Figure 1.9: (a) Schematic of different microstructural zones in FSW (b) Typical micrograph showing microstructural zones [P. Asadi., (2014)].

- a) Unaffected material or BM: This material that has not been deformed and, although having gone through a thermal cycle with the weld, has not been affected by the heat in terms of microstructure or mechanical qualities.
- b) Heat-affected zone (HAZ): The material has undergone a thermal cycle in this region, which is visibly closer to the weld center, altering the microstructure or mechanical properties. However, there has been no plastic deformation in this location. Grain growth, solubilization, and coarsening of strengthening precipitates are the most prevalent metallurgical phenomena in this domain.
- c) Nugget zone (NZ) or Stir Zone (SZ): This area is made of equiaxed grains and is located in the weld center (the location of the pin during welding). During FSW, the combination of heat and high plastic deformation causes dynamic recrystallization at the weld's center. This region's geometry is determined by welding factors, including rotating speed, traverse speed, and axial

force. The grains in the nugget zone are frequently smaller than those in the BM. The widespread presence of numerous concentric rings, which have been likened to an onion ring structure, is a unique feature of NZ. Although changes in particle number density, grain size, and texture have all been hypothesized, the specific cause of these rings has yet to be identified.

d) Thermomechanically affected zone (TMAZ): The FSW tool has plastically deformed the material in this region, and the heat generated has had some effect on the substance. Elongated or twisted grains are a frequent feature of this region, and recrystallization does not occur due to insufficient heat and plastic deformation.

1.3.6 Advantages

FSW has various advantages over fusion welding procedures due to its solid-state nature, eliminating any potential flaws in cooling from the liquid phase. During FSW, problems including porosity, solute redistribution, and solidification cracking do not arise. FSW has been discovered to create minimal concentrations of faults and be remarkably tolerant to general changes in parameters and materials. FSW, as a relatively new welding method, has several significant advantages over fusion welding: energy efficient;

- No fumes or gases generated as the process is solid state therefore it is termed as Green technology,
- Most promising technique for un-weldable aluminium alloys because it avoids many problems (for example solidification cracking) arises with fusion welding.
- With grain refinement, the final welds are having excellent mechanical properties compared to fusion welding techniques.
- Plate or sheet distortion (residual stresses) is less with improved fatigue life due to fine grain size.
- Many dissimilar combinations of materials can be joined (for example different grades of aluminium alloys, aluminium to steel, aluminium to titanium etc.)

1.3.7 Limitations:

- When the tool is withdrawn at the end of the process, a exit hole left behind.
- Generally tool forces are high, heavy-duty clamping is necessary.
- The maximum thickness of the material to be joined is limited to 50 mm with conventional tools (in single side welds) and 100 mm with bobbin tools (in double side welds).
- Tool wear is a usual phenomenon during FSW while welding hard materials.

1.3.8 Applications

FSW has been used in several commercial applications, as listed below

Marine Industry:

- Aluminum Super structures of cruise ships (Seven Seas Navigator)
- Japanese Fast Ferry (Ogasawara) in 2004
- Honeycomb panels
- Hulls

Automobiles:

- Long low distortion (25 m welds) double skin extrusions for railways
- Suspension parts, Crash boxes, and wheels
- Engine cradles
- Mazda Rx-8 sports car (bonnet and rear doors).

Aerospace Industry:

- Fuel tanks for un-manned Delta II and Delta IV rockets
- Eclipse 500 business jet frame
- Monolithic metal wings
- Metallic fuselages

1.4 Aluminium alloys

Aluminium is a soft, robust, light-weight, malleable metal having a silvery look, but changes to dull grey depending on the surface roughness. The density and rigidity of aluminum are about one-third that of steel. It shows high ductility and can be easily machined, cast, drawn, or extruded with ease because these alloys have melting temperatures ranging from 482 - 660° C. Resistance to corrosion in normal environmental conditions can be high because a thin aluminum oxide coating accumulates on the metal's surface when exposed to air, thus preventing further oxidation.

The high strength-to-weight ratio, corrosion resistance to environmental conditions, high thermal and electrical conductivity, non-toxicity, reflectivity, appearance, ease of formability, machinability, and nonmagnetic nature of aluminium and its alloys are all essential criteria in their selection. Steel has a thermal conductivity of six times aluminum. In contrast, aluminum has a thermal expansion of two times that of steel.

1.4.1 Classification of aluminium alloys

Pure aluminum can be easily alloyed with a variety of other metals to produce a variety of physical and mechanical properties. The alloys are divided into two categories: wrought alloys and cast alloys, with the following designations.

1.4.2 Wrought Alloys

Although certain alloys are regularly utilized as castings, Al alloys are primarily manufactured as wrought plates or sheets, widely used in structural and aerospace applications. An international identification system proposed by the American Al Association, as illustrated in **Table 1.2** [Callister e al., (2003)], has now been approved to characterize wrought Al alloys further. Each wrought Al alloy is identified by a four-digit code and letters and numbers indicating the tempering condition. The first digit, which classifies the primary alloying element, is the most important. The remaining digits usually refer to the alloy's purity or the number of additions present.

Table 1.2: International designation system for Al wrought alloys [Polmear et al., 1995].

Code	Major Alloying Element(s)	Heat-Treatable
1xxx	Pure	
2xxx	Cu	Yes
3xxx	Mn	No
4xxx	Si	No
5xxx	Mg	No
6xxx	Si & Mg	Yes
7xxx	Zn	Yes
8xxx	Other	

A suffix, which comes after the four digits number, describes the tempered condition of heat-treatable wrought Al alloys. **Table 1.3** shows how an alloy's condition is usually denoted by a letter and a number. The tempered condition for non-heat-treatable alloys is represented separately in **Table 1.4**.

Table 1.3: Temper conditions of heat-treatable wrought Al alloys [Polmear et al., 1995].

Tempers	Description
T3	Solution annealing, cold working followed by naturally ageing

T4	Solution annealing followed by naturally ageing
T5	Cooled down from high-temperature shaping followed by artificially ageing
T6	Solution annealing followed artificially ageing
T7	Solution annealing followed by artificially over-ageing
T8	Solution annealing, cold working followed by artificially ageing

Table 1.4: Temper conditions of non-heat-treatable wrought Al alloys [Polmear et al., 1995].

Tempers	Description
F	As-fabricated
O	Annealed
H	Work hardened (wrought components)
H1	Work hardened only
H2	Work hardened and partially annealed
H3	Work hardened and stabilized

1.4.3 Cast alloys

Complex geometries are typically cast in a near-net shape. Cast aluminum alloys are utilized to make a large variety of components in the automotive sector. Engine blocks, automotive pistons, gearbox casings, and car steering knuckles are just a few examples. Cast Al alloys, unlike wrought Al alloys, do not have a globally recognized categorization system. The temper conditions of cast alloys is shown in **Table 1.5**. The Aluminum Association of the United States, on the other hand, has established a revised approach that is comparable to that used for wrought alloys and is now more widely used (**Table 1.6**).

Table 1.5: Common tempering conditions of commercial cast Aluminium alloys [Polmear et al., 1995].

Tempers	Description
M	As cast
TB	Solution annealing followed by naturally ageing
TB7	Solution annealing and stabilized
TE	Artificially ageing after casting

TF	Solution annealing followed by artificially ageing
TF7	Solution annealing, artificially ageing and stabilized
TS	Thermally stress relieved

Table 1.6: The United States revised designation system for Aluminium cast alloys [Polmear et al., 1995].

Code	Major alloying elements	Heat treatable
1xxx	Pure	
2xxx	Cu	Yes
3xxx	Si with added Cu and/or Mg	Yes
4xxx	Si	No
5xxx	Mg	No
6xxx	Unused series	
7xxx	Zn	Yes
8xxx	Ti	No
9xxx	other	

1.5 Welding of aluminium alloys

Gas tungsten arc welding (GTAW), gas metal arc welding (GMAW), variable polarity plasma arc (VPPA), and electron beam welding (EBW) are the most used joining methods for aluminum alloys. Due to the high intensity of heat generated by these processes, these techniques allow us to acquire optimal mechanical properties with minimum deformation. GMAW is used to join somewhat thicker sections. In contrast, GTAW is used to join thin sheets. Aluminum alloys are difficult to weld due to their high conductivity, reactivity, and coefficient of expansion. Due to the high thermal conductivity and high expansion coefficient (about twice steel), parts may be severely distorted by high heat input generated during welding. To produce a good weld with aluminum alloys, you must carefully regulate the welding parameters.

Gas tungsten arc welding of aluminum alloys can be done with or without filler wire. Filler wire is selected based on its ease of welding, mechanical strength, ductility, and corrosion resistance. Shielding gas like argon is typically used in the GTAW of aluminium alloys. Helium is also employed for a variety of purposes. Helium produces a higher arc voltage while emitting

the same amount of heat at a lower current. Because aluminum is a powerful heat conductor, using helium for primary shielding can result in a more uniform weld bead and improved penetration. However, due to the more expense of helium gas and the difficulty of initiating an arc, a mixture of helium and argon was used as a shielding gas for aluminum welding. Sometimes, the filler material composition does not match the base metal in welding aluminum alloys, and the cleanliness of the filler metal is another factor to be considered. This is also true for the matched filler 2319, which has a slightly higher Ti and Zr concentration. The material loses strength due to melting and rapid solidification, which causes all of the strengthening precipitates to dissolve and renders the material as good as cast [Ghaffarpour et al., (2017) and Sharma et al., (2015)].

Weld solidification cracking is one of the most common issues in the fusion welding of aluminum alloys. Solidification cracking is particularly sensitive to the weld metal composition, filler metal composition, base metal composition, and dilution amount in aluminum alloys. As a result, the filler metal composition and/or welding parameters must be carefully chosen such that the resulting weld composition is not prone to solidification cracking. There are filler metal selection guidelines for various classes and types of aluminum alloys.

On the other hand, there are no filler metals that can create crack-free welding for many dissimilar aluminum alloy combinations. Even when a suitable filler metal is available, excellent joint efficiencies are impossible to achieve. Moreover, the selection of filler metal and process variables to avoid solidification cracking is sometimes easily done in similar alloys. Still, the problem is with dissimilar aluminium alloy combinations since very few prescribed filler materials are mentioned. However, the requirement of multiple filler materials and lower joint efficiency are the drawbacks of joining dissimilar aluminium alloys. Therefore, fusion welding of dissimilar aluminum alloys is often avoided in industries for these reasons.

1.5.1 Characteristics of aluminium alloys

Due to their high strength-to-weight ratio, better ductility, and good corrosive resistance, aluminum alloys have a wide range of applications, particularly in the fabrication industries, aircraft production, vehicle body building, and other structural applications. Wrought aluminium alloys are of two types, non-heat-treatable (1xxx, 3xxx, 4xxx, and 5xxx series) and heat treatable (2xxx, 6xxx, and 7xxx series).

The 6xxx are heat treatable aluminium alloys containing magnesium and silicon as major alloying elements. They are widely used for automotive, shipbuilding and aerospace structures due to their excellent extrudability, weldability and excellent corrosion resistance [Lumley et al., (2010)]. These alloys are also aged hardenable and usually heat treated to T6 condition (solution treatment and artificially aging) to develop adequate strength. Although Al-Mg-Si alloys are readily weldable, they suffer from severe softening in the Heat Affected Zone (HAZ) because of the dissolution of Mg₂Si precipitates due to the weld thermal cycle during welding. It will be more convenient to overcome or reduce the HAZ softening to improve the mechanical properties of weldments [Elangovan et al., (2008)].

The 5xxx are non-heat-treatable aluminium alloys containing magnesium as major alloying element. They are extensively used as structural materials in ship-building, automobile sector, aviation industries and cryogenic applications due to their medium strength, excellent corrosion resistance and high ductility [Lumley et al., (2010)]. The AA5xxx-H111 group of non-heat-treatable aluminium alloys is annealed, subjected to cold working (H111), and exhibits Portevin-Le Chatelier behaviour under plastic deformation. Due to the various applications and formability characteristics of these two different alloys, their joining as dissimilar aluminium alloy is very interesting. However, it is notable that the AA5xxx (Al-Mg) and the AA6xxx (Al-Mg-Si) alloys show peculiar characteristics when joined in compatible welds by FSW.

The aluminium alloy (AA) has a high strength-to-weight ratio, a leading factor for considering these materials in engineering design [Ratchev et al., (1995)]. AA5xxx and AA6xxx aluminium alloys, including AA5083 and AA6061, have become widely used in automotive [Burger et al., (1995)] and marine industries [Ishii et al., (2007)]. The increasing number of applications has posed new problems for welding process development. FSW (friction stir welding) is a well-known technique for connecting aluminum alloys and other materials. For aluminium alloys and other engineering materials, the procedure was developed as an alternative for fusion joining. This friction stir welding method significantly reduces porosity and hot cracking faults, which are frequently caused by fusion welding, resulting in better mechanical and corrosion properties.

1.5.2 Definition of problem

The problem title is “Investigation on friction stir welding of dissimilar AA5083-AA6061 aluminium alloys for improving mechanical and corrosion properties”. Based on the

Literature survey, Alumiminium alloys are lighter in weight, have high strength to weight ratio, full recyclability will make them in good demand as a replacement with steels. The present study improves joint strength and corrosion resistance of friction stir welding without degrading weld quality and was challenging to compete with advanced fusion and hybrid welding technologies such as Plasma-MIG hybrid welding, fiber laser-MIG hybrid welding and laser beam welding, etc. The welded joints showed poor mechanical and corrosion properties, but significantly less work has been done on improving these properties. It is possible to investigate and understand the material flow and microstructure evolution during friction stir welding since two different grade alloys are being joined. Understanding the corrosion behavior of the welded joint, particularly the stir zone where two distinct aluminum alloys are intensely mixed, is also of importance. Hence, the main present study aimed to extensively identify a suitable location for placing base material position, process parameters and cooling environment conditions to improve mechanical and corrosion properties. This is done by understanding the material flow, conducting the metallurgical characterization and mechanical testing of different weld zones of the friction stir welded AA5083-AA6061 dissimilar aluminium alloys.

1.6 Objectives and scope of research work

The main objectives of the thesis are to study the,

Objective 1: Mechanical and corrosion behavior of friction stir welded 5083-6061 aluminium alloy joints: Effect of base material position.

Objective 2: Effect of friction stir welding parameters on the material flow, mechanical properties and corrosion behavior of dissimilar AA5083-AA6061 joints.

Objective 3: Enhancing corrosion resistance and mechanical properties of dissimilar friction stir welded 5083-6061 aluminium alloys using an external cooling environment.

Objective 4: Analysing microstructure, texture evolution and tensile behavior of dissimilar 5083-6061 aluminium alloys welded using air and water-cooled friction stir welding.

1.7 Methodology

- The trails were conducted to select process parameter values such as tool rotational speed, traverse speed, and tilt angle with an objective of defect-free welds.
- Conduct the experiments by changing tool traverse speed at constant rotational speed to improve the mechanical properties of friction stir welded joint

- Conduct the experiments by varying tool rotational speed at constant traverse speed to improve mechanical and corrosion properties of the FSWed joint
- Determine the appropriate cooling environment (like air, water and liquid nitrogen) on mechanical and corrosion properties.
- Perform the material flow, microstructure, texture studies to analyze the welded joints and compare them with base materials.
- Perform the microhardness, tensile test for analyzing the tensile strength, strain hardening exponent and strain hardening rate of the final welds and compare them with base materials.

1.8 Organization of thesis

The whole thesis was organized into five chapters.

Chapter-1: This chapter briefly introduces conventional joining techniques, solid-state welding, and the working principle of the friction stir welding process and applications.

Chapter-2: This chapter gives a comprehensive review of the existing literature on various aspects of the friction stir welding process related to the present research problem.

Chapter-3: This chapter outlines the experimental procedures followed for performing the experiments to reach the objectives of the present research work.

Chapter-4: This chapter explains the results and a discussion was explained for each objective under separate headings.

Chapter-5: This chapter summarizes the conclusions of the present research work with possible remarks and the scope for future work.

Bibliography

List of Publication

CHAPTER 2

LITERATURE SURVEY

This chapter briefly outlines the literature review in various aspects of friction stir welding such as FSW in aluminium alloys, heat generation in FSW, Material flow aspects of FSW, Microstructure characteristics, texture evolution, mechanical properties and corrosion behavior of FSW dissimilar aluminium alloys, etc., and the summary of literature work was presented at the end of the chapter.

2.1 Friction stir welding in aluminium alloys

[Thomas et al., \(1991\)](#) invented and patented the friction stir welding (FSW) technology at The Welding Institute (TWI), United Kingdom. They described friction stir welding as a continuous solid-state joining process where a non-consumable rotating having shoulder and probe of a harder material than material to be welded. The FSW process produces a low distortion of final plates with a good appearance and relatively low cost. FSW is the most prominent and promising joining technique for welding aluminium and aluminium alloys. FSW has also proven its capability to weld copper, copper alloys, steels, titanium, magnesium, polymers, and various dissimilar combinations.

They also summarized the use of friction stir welding in transportation industries. They listed several applications of friction stir welding such as cryogenic fuel tanks, airframes, Sheet bodywork, thin alloy skins in the aerospace, automotive engine support frames, hull frame in ship building, coachwork and railway wagon for railways, etc. [\[Thomas et al., \(1997\)\]](#).

Friction stir welding develops a complex thermo-mechanical interaction of parameters, affecting the thermal cycles, severe plastic deformation of the material, dynamic recrystallization, and finally, the weld integrity in the structure. FSW allows welding a wide

range of metals such as magnesium, copper, steel, titanium, and various dissimilar combinations of metals, etc. [Nandan et al., (2008)].

2.1.1 FSW in non-heat-treatable aluminium alloys

In the heat affected zone, very minimal changes in the microstructure of a non-heat-treatable alloy can be seen. This is especially possible if the base material is subjected to annealing prior to welding [Etter et al., (2007)]. The deformation experienced during FSW is the primary driver of alterations inside the thermo-mechanically affected zone (TMAZ) and Dynamic recrystallized zone (DRZ) or stir zone (SZ) in this scenario. Grain shearing and significant dislocations are induced into the TMAZ microstructure, with the effect being more at the weld center. The DRZ is also dominated by extreme plastic deformation, which causes the grains to recrystallize and refine. The hardness at TMAZ and DRZ is typically raised slightly following FSW due to these changes in the microstructure. (**Figure 2.1**).

Suppose the strain hardening (H-temper) material was welded. In that case, however, the original microstructure across the weld may recover and recrystallize due to the increased temperature during welding [Etter et al., (2007)]. This has been observed to diminish the material's hardness from its cold-worked state in general (**Figure 2.1**). Despite the fact that the grains are refined within the DRZ, the softening effect caused by dislocation recovery has a greater impact on the mechanical properties.

Sato et al., (2001) investigated the factors governing hardness, such as grain size, dislocation structure, and particles, in friction stir welds of solid solution-hardened alloy (5083-O) and welds of Al alloy 1080-O. In an Al alloy 1080 that did not contain any second-phase particles, the effect of grain boundary on hardness was investigated. The FSWed Al alloy 1080 has smaller grains at the SZ than that in the base material. Relatively low dislocation densities are observed in the SZ and BM locations compared to TMAZ. The hardness profile in the FSWed joint of AA5083 is homogeneous because there is no difference in the dislocation densities between the SZ, TMAZ and unaffected region due to the distribution of small particles.

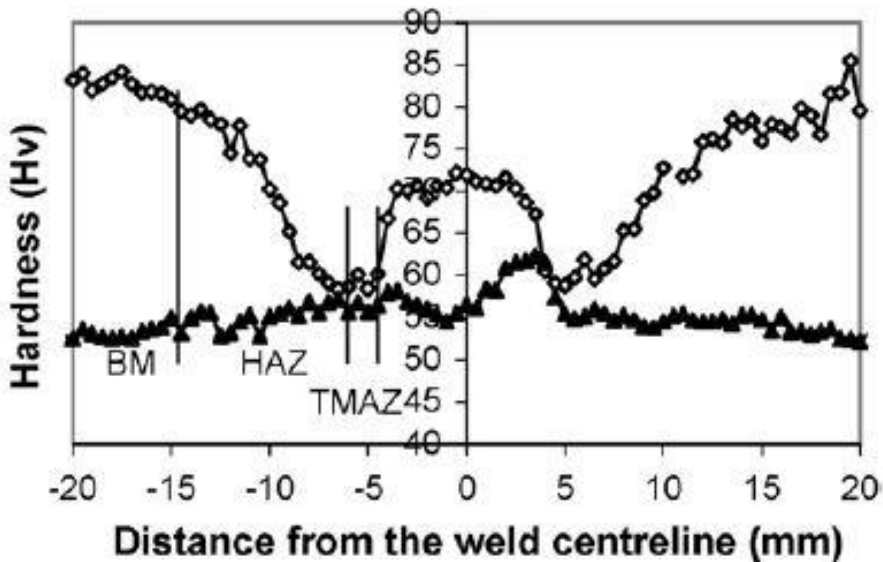


Figure 2.1: Microhardness values for friction stir welds made of 5xxx Al alloy in an strain hardened ‘H’ and annealed ‘O’ temper [Etter et al., (2007)].

Leitao et al., (2009) studied the microstructure and mechanical behavior of AA5182-H111 and AA6016-T4 thin friction stir welds that were similar and distinct. The mechanical behavior of the AA5182-H111 comparable welds was found to be substantially similar to the base material. Similar welds in alloy AA6016-T4 showed a 15% reduction in hardness and a 20% reduction in strength. Due to the plastic flow localization of the weakest TMAZ, this strength decline was followed by a significant loss in ductility. The hardness variance between AA6016-T4 and AA5182-H111 welds is consistent with the microstructure progression across the TMAZ. Unlike the AA6016-T4 identical welds, the dissimilar welds showed no appreciable drop in hardness and had a strength efficiency of roughly 90%. However, due to the previously described heterogeneous features of these welds, their ductility drops dramatically compared to the base materials.

2.1.2 FSW in heat-treatable aluminium alloys

The heat generated during welding is relatively high, and the solidus temperature of the metastable transition phases of the material can be achieved nearer the weld center in most situations. Small metastable strengthening phases can dissolve back into solid solution or convert within the HAZ and TMAZ in heat-treatable alloys containing second phase particles, causing over aging by nucleation of coarser equilibrium phase. The hardness of the precipitates will diminish due to coarsening and transformation, as well as partial dissolution [Dumont et al., (2006)].

The microstructure of the DRZ is driven to fully recrystallize due to high-temperature thermal cycles and significant plastic deformation during welding [Su et al., (2003)]. After welding, the grains are very fine (usually 2-6 μm) and equiaxed. However, dislocations can still be seen

within these grains, implying that plastic deformation and recovery occur after recrystallization. The dislocation concentrations of the new grains vary a lot from one grain to the next, regardless of where they are in the microstructure. The hardness of the DRZ will initially be low after welding due to a decrease in precipitation density caused by the high temperature in this region, which dissolves most precipitates back into a solid solution. Re-precipitation of Guinier-Preston Zones (GPZs) will increase the hardness of the DRZ if the weld is allowed to age naturally after welding [Dumont et al., (2006)]. The hardness of the DRZ will typically stay lower than that of the parent material even after natural aging has stabilized. This is because the strengthening precipitation phases dominate the microstructure of the original T6/T7 tempered alloy, but the softer GPZs replace them after welding. The material within the DRZ will be subjected to the most plastic deformation (strains significantly greater than 100 have been projected) and the highest temperature during welding [Colegrove et al., (2004)]. As a result, any precipitates formed inside a heat treatable alloy will usually dissolve back into a solid solution. This produces a super-saturated solid solution, and if the cooling rate is slow enough, some re-precipitation may occur as the material cools after the welding operation (Figure 2.2). Note that the welding parameters and temperature determine the volume proportion of precipitates that is re-solutionized. It was also discovered that the dislocation density of the recrystallized grains considerably influences the distribution of freshly produced precipitates [Su et al., (2003)].

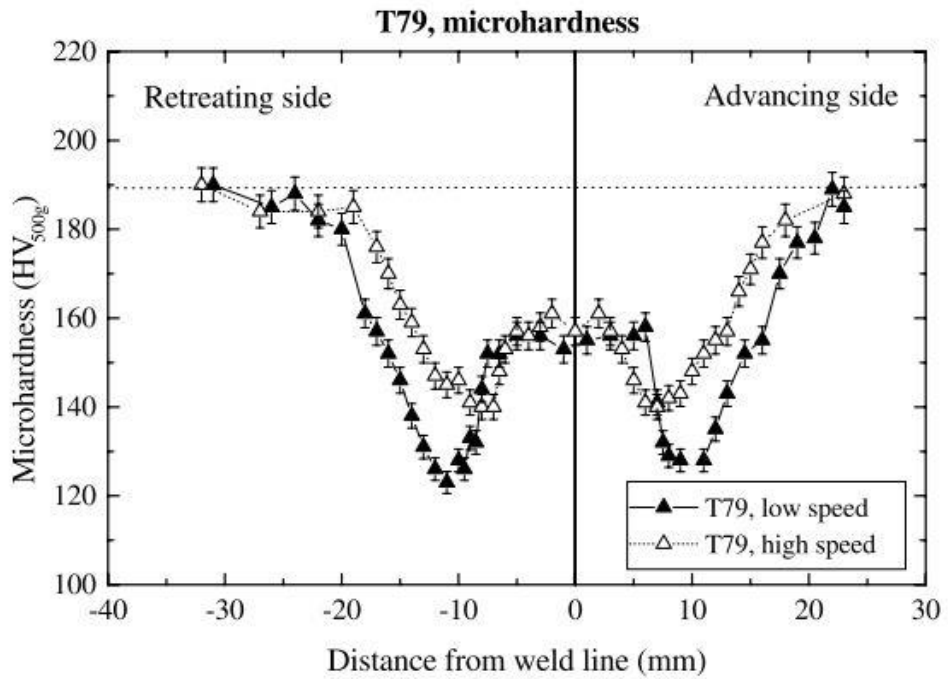


Figure 2.2: Hardness profiles across a friction stir weld of AA7xxx-T79 [Dumont et al., (2006)].

Liu et al., (1997) investigated the microstructural characteristics of the FSWed AA6061-T6. Optical Microscopy (OM) and Transmission electron microscopy (TEM) were used to

characterize the welded zone, and the microstructures were compared along with the original 6061-T6 aluminium alloy. A dynamic recrystallized zone characterizes the weld zone of the FSWed AA6061-T6 joint. Second phase particles in the workpiece are stirred and fine precipitates are converted into large precipitates, containing a considerable amount of iron along with the AlSi. They also observed that more lathe-type precipitates were seen, usually seen as homogeneously distributed precipitates like BM, except they usually contained copper in roughly the same proportion as magnesium and silicon ($Al_xMgSiCu$). (Svensson et al. 2000) investigated microstructure characteristics and mechanical properties of the Friction stir welded (FSWed) AA5083 and AA6082. They observed that AA5083 fractured near the center of the weld, whereas the fracture location of AA6082 was mainly observed in the heat-affected zone (HAZ). The hardness was constant across the weld zone in AA5083. In contrast, in the zone of lowest hardness at HAZ, the hardening precipitates ($\beta'' Mg_5Si_6$) had dissolved or transformed to non-hardening precipitates and stated this is the reason for minimum hardness and decreased tensile strength in AA6082 welds.

2.2 Material flow aspects in FSW

The extrusion process influences material flow in the weld zone, in which the applied axial force (F) and tool pin motion propel the material after it has undergone plastic deformation. The plunge depth of the tool pin into the work piece is directly influenced by the shoulder force. Hydrostatic pressure beneath the shoulder and temperature in the stir zone will both rise as the axial force rises [Elangovan et al., (2008)]. Both the hydrostatic pressure beneath the shoulder and the temperature in the stir zone will rise as the axial force rises. The hydrostatic pressure should be essentially higher than the flow stress of the materials of the mating surfaces [Kumar et al., (2008)].

Schmidt et al., (2008) developed a thermal pseudo-mechanical model in which temperature-dependent material's yield stress controls heat generation. The basic parameters like tool rotational speed rate, welding speed and axial force in FSW are selected with the minimum criteria of plasticizing the workpiece material, thereby deforming around the tool pin and beneath the tool shoulder and flowing towards the trailing edge. The mechanism of weld occurs due to plastic deformation and frictional contact, which is complex. Therefore, unlike many other thermomechanical processes, FSW is fully coupled, which means a pure thermal model cannot be sufficient. During FSW, the material is plasticized within a temperature range from room temperature ($T_{ambient}$) to solidus temperature ($T_{solidus}$) of material and the strain rates of the order of 1000 s^{-1} [Schmidt et al., (2008)]. The formation of the bond during the FSW process depends on key aspects developed by the tool, such as frictional contact heat and shear

deformation heat which plays a vital role in the quality of the joint. Thus the process parameters and tool design were the crucial part of the FSW technique. The primary requirement of the tool was to produce a sufficient amount of heat under the shoulder, which helps in plasticizing the material leading to the joining of plates [Schmidt et al., (2008)].

Kumar et al., (2008) clarified the flow regions such as pin driven and shoulder driven and analyzed the interaction of the shoulder with the workpiece. They regarded the FSW tool interaction as a third body interface, which generates heat due to frictional and shearing action, bonds the two materials without melting them in a solid-state condition. The key for bond formation is clearly understood when the role of the tool is clarified. They observed that the weld's material was diverted back to the weld region with the increase of shoulder interaction. The onion ring formation mechanism is explained from the schematic of material flow explained in **Figure 2.3**, initially the creation of weld cavity during plunging occurs (**Figure 2.3a**). The flow observed in **Figure 2.3b** is created due to pin-driven flow. Further, in **Figure 2.3c**, the pin-driven flow and shoulder-driven flow merge. Finally, **Figure 2.3d** shows the drawing of base material into the weld nugget occurs. This material flow process of the formation of onion rings is a continuous process.

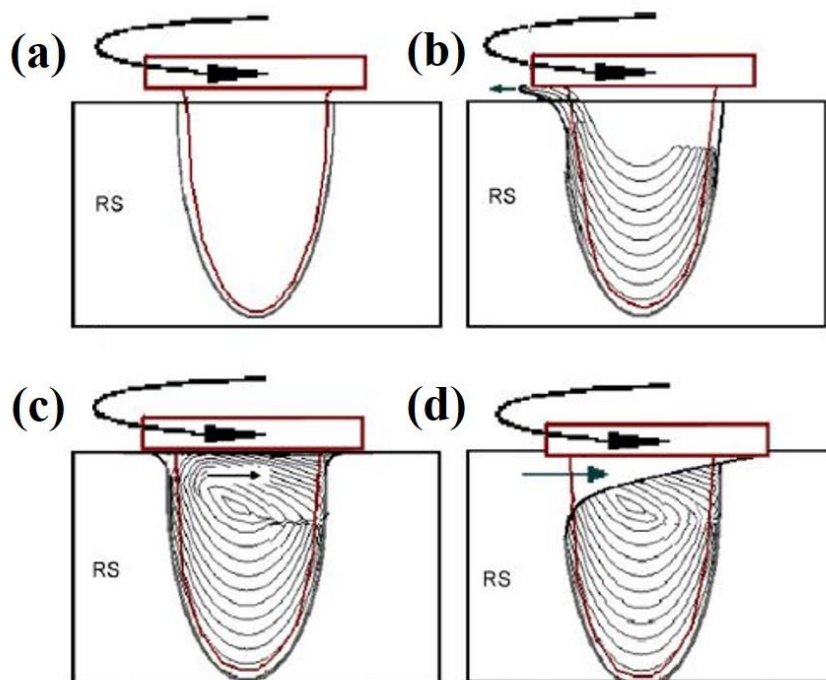


Figure 2.3: Summary of material flow at different shoulder interaction in the transverse section of the weld (Y-Z plane) [Kumar et al., (2008)].

Zhang et al., (2008) developed a thermo-mechanical model fully coupled for studying friction stir welding and understood that the rotation of the tool shoulder accelerated the material

flow near the top surface. They observed that the microstructural evolution in FSW is directly linked to the thermal history and material flow behavior. Due to the severe plastic deformation of material at the shoulder/workpiece interface, temperature generation at top layers is higher than the bottom layers of the workpiece.

[Krishnan et al., \(2002\)](#) explained the formation of onion rings as a geometric effect as the material is extruded during each rotation as cylindrical sheets. It is also proposed that the tool is subjected to a brief period for producing the frictional heat and the material under the tool extrudes cylindrically shaped marks. The samples were sliced in the middle of the XZ plane to observe the formation of the onion rings, as shown in **Figure 2.4a and b**. The FSW is a method of extrusion. The metal in front of the tool is heated by friction during each turn, and the forward motion extrudes the metal to the back of the tool. There should be a cavity at the back of the tool if the material is to be extruded there. If there is a cavity, air will almost definitely fill it, causing the clean extruded metal to oxidize. Short-term air contact is anticipated to result in only minor oxidation, with the oxidized material most likely to be found on the surface of each semi-cylinder.

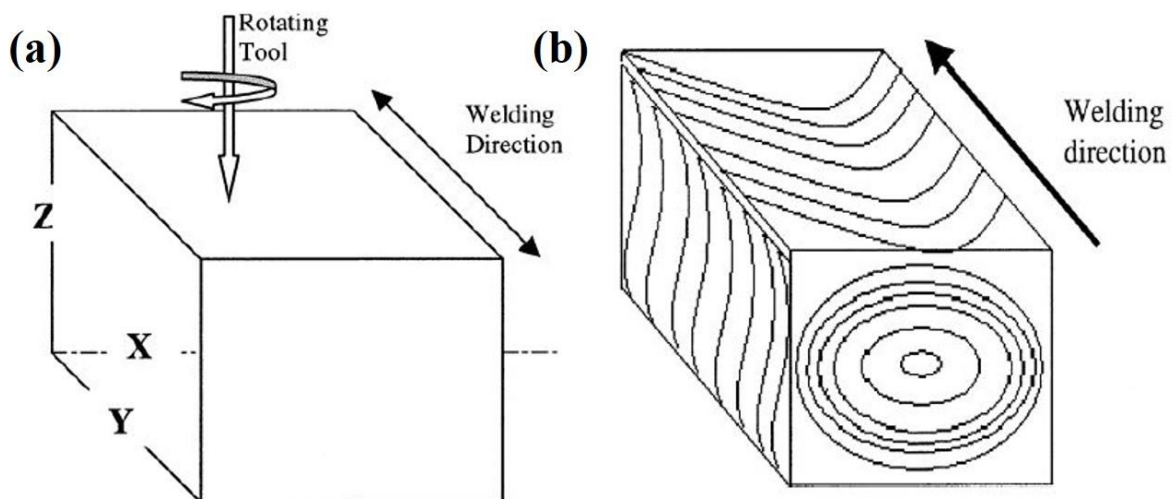


Figure 2.4: Cross-section view of a weld (b) Microstructural features of the FSW cross-section [[Krishnan et al., \(2002\)](#)].

Using a fully coupled thermomechanical model, [Zhang et al., \(2008\)](#) investigated the effect of transverse speed in FSW. It was discovered that when the transverse speed increases, the welding tool's stirring action weakens, resulting in the appearance of weld flaws. It was also discovered that in the FSW process, friction contributes the most to temperature rise. As the transverse speed is raised, the contribution of plastic deformation to temperature rise increases.

Using Arbitrary Lagrangian-Eulerian (ALE) Formulation in DEFORM 3D, [Pashazadeh et al., \(2014\)](#) developed a numerical model to predict temperature distribution, effective plastic strain, and material flow of FSWed copper sheets. For performing the metal-forming processes

simulations, the computational solid mechanics (CSM) approach was generally used where the material is assumed as a rigid-visco plastic material, which means the total strain equals the viscoplastic strain. They observed a slightly higher temperature at the advancing side (AS) than the retreating side (RS) because of the more severe plastic deformation on AS. Plasticizing material, thereby generating the maximum temperature, will affect the material and softens the HAZ zone.

[Zhang et al., \(2014\)](#) utilized FLUENT and simulated FSW of 6061-T6 aluminum alloy and proposed a detailed method for calculating heat generation. They observed that a significant portion of heat is generated close to the shoulder region and decreases while moving downwards. They identified the three stages of the material flow as shown in **Figure 2.5a** before the tool advances. The material is plasticized by the shoulder contact in the dwelling stage **Figure 2.5b** softened material is subjected to multiple rotations around the tool surface before final deposition **Figure 2.5c** as the tool moves in steps of weld pitch, a moon-like cavity is formed backside to the tool, under the function of the rotation the plasticized material that sticks will be extruded to deviate.

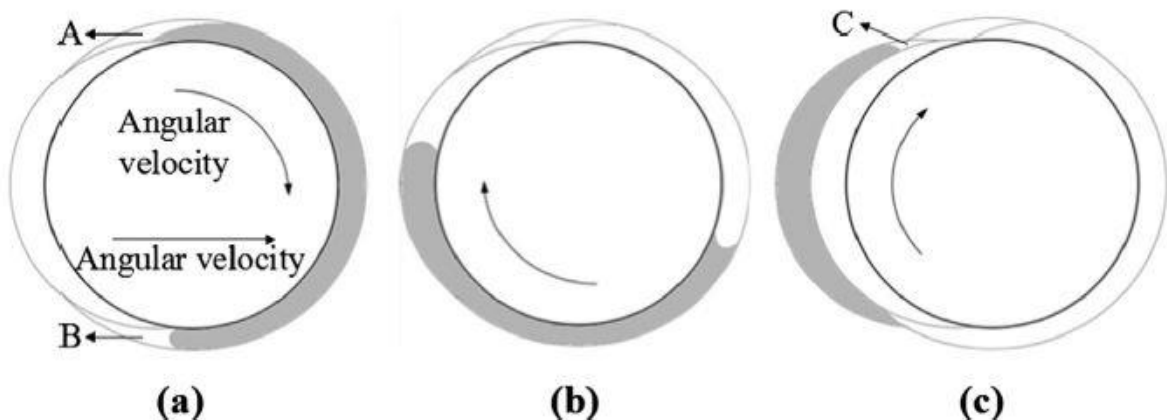


Figure 2.5: Material flow around the tool during FSW [[Zhang et al., \(2014\)](#)].

The flow of material in region A is poor since the tool does not affect this zone. Region B suggests that some traces of material at AS were dragged and transported to RS through extrusion around the tool during this process. Depending on the process condition, excess material (flash) may be noticed. When the plasticized material flows towards the cavity, it will be subjected to two different forces: axial tool force and the parent material's resisting force, which results in textural variations. During that process, if the material flow is not stable, groove and pore defects were noticed in region C (generally termed defect prone region (DPR)). Generally, the flow of material near the bottom of the pin is weakest. Thus defects appear as shown in **Figure 2.6**.

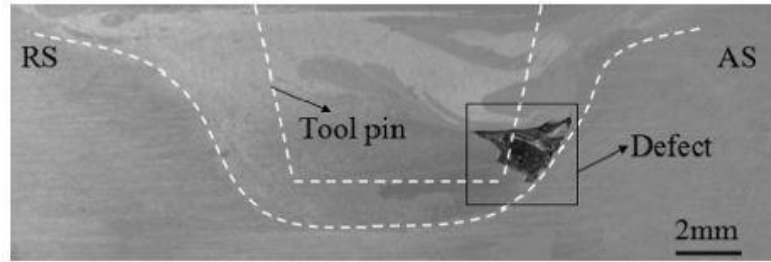


Figure 2.6: Defect prone region in the cross-section of FSW sample [Zhang et al., (2014)].

2.3 Heat generation and control in FSW

The tool rotational speed (RS) is one of the most important factors influencing the formation of frictional heat. If the rotational speed is too slow, the frictional heat is insufficient to create plasticized flow resulting in weld flaws. The plasticized layer grows from the top to the bottom by increasing rotational speed, resulting in fewer flaws in the weld zone. Another critical factor is traverse speed. When the traverse speed is low, the temperature rises due to friction heat. Because the heat input to a given volume of material occurs over a long time when the traverse speed is low, the temperature rise will be higher. However, when the traverse speed is too high, the frictional heat generated is insufficient to plasticize the materials beneath the tool shoulder and surround the probe, resulting in incorrect welding [Hassan et al., (2003) and Ma et al., (2005)].

Peel et al., (2003) discussed the results of microstructural, mechanical property, and residual stress examinations of four aluminum AA5083 friction stir welds made under various conditions. The weld properties were found to be dominated by the thermal input rather than the tool's mechanical deformation. The microstructure of the weld zone is dominated by recrystallized grains and by increasing the traverse speed, the width of the weld zone narrowed. This recrystallized zone resulted in considerably lower hardness and yield strength than the parent material.

Peel et al., (2006) analyzed the relationship between microstructure characteristics and the local mechanical behavior of Friction stir welded (FSWed) AA5083-AA6082 using a range of rotational and traverse speeds. The use of higher rotational speed has been shown to affect grain size and the natural aging process strongly. They concluded that the temperature near the weld nugget can be significantly altered by varying rotational speed rather than traverse speed.

Cavaliere et al., (2008) Looked at the mechanical and microstructural properties of AA6082-T6 joints made by friction stir welding at a constant rotating speed and traverse rates ranging from 40 to 460 mm/min. When the advancing speed was increased from 40 to 165 mm/min, a considerable change in the nugget mean grain size was noticed, followed by a

plateau with no further variations when the speed was increased to 460mm/min. The yield strength of the material was observed to increase substantially from lower speeds to 115 mm/min, then begin to decline when the advancing speed was increased. The material's ductility followed the same pattern but resumed to increase after the advancing speed was increased.

[Sakthivel et al., \(2009\)](#) studied that the welding speed causes the tool to translate, which pushes the stirred material from the front to the back of the tool pin, completing the welding. Frictional heat is generated when the tool shoulder and pin rub against the workpiece. The welding speed affects grain growth by determining the exposure period of this frictional heat per unit length of a weld. The welding speed has a significant impact on the rate of heating in a thermal cycle during FSW. Increased welding speed reduces frictional heat generation and results in a lack of stirring. The welding speed also influences the width of the stir zone.

[Jayaraman et al., \(2010\)](#) analyzed that the rotation of the tool results in stirring and mixing of material around the rotating pin. The rotational speed is a significant process variable since it influences the transitional velocity. Higher tool rotation generates higher temperature because of high frictional heating, resulting in more intense stirring and mixing of material. The production of flaws is determined by the pace at which plasticized material is stirred. Tunnel defects will occur from excessive churning of plasticized material. Bonding will be compromised if there isn't enough stirring. With increased tool rotating speed, [Azimzadegan et al., \(2010\)](#) found an increase in the width of the stir zone. The temperature in the stir zone and subsequent grain development influence the tool rotating speed [[Karthikeyan et al., \(2010\)](#)].

[Palanivel et al., \(2014\)](#) studied the effect of rotational tool speed on the microstructure and tensile strength of the dissimilar aluminium alloys AA5083-H111 and AA6351-T6 joints. Dissimilar joints were made using three different tool rotational speeds of 600 rpm, 950 rpm and 1300 rpm. In the weld zone, three distinct zones were observed: unmixed, mechanically mixed, and mixed flow, with rotational speed having a significant impact on the microstructure and tensile strength of the joints. Due to changes in material flow behavior, loss of cold work in the HAZ of the AA5083 side, dissolution and over the aging of precipitates on the AA6351 side, and creation of macroscopic defects in the weld zone, the two process parameters influenced joint strength. Figure 2.7 depicts the failure location of different joints.



Figure 2.7: Failure regions of dissimilar FS welded joints at (a) 36 mm/min, (b) 63 mm/min and (c) 60 mm/min [Palanivel et al., (2014)].

Palanivel et al., (2014) investigated the microstructure and tensile strength of FSWed AA5083-AA6351 dissimilar alloys by varying tool traverse speed. They found that distinct regions of the unmixed region, mixed flow and mechanically mixed region were formed in the stir zone. They concluded that there was no mixed-flow area formation following a higher traverse speed. [Guo et al., (2014)] carried out studies by varying process parameters of FSWed AA6061-AA7075 Al alloys. They observed that the highest tensile strength was obtained at very high welding speeds while minimum hardness values were found at HAZ of AA6061 regardless of process parameters. Regardless of the relative materials location or the applied process parameters, the hardness minima are seen in the HAZ on the AA6061 side in all cases, as indicated by the arrows in **Figure 2.8**. In reality, at tensile testing, all joints on the AA6061 side failed in HAZ regions extremely close to the TMAZ, where the minimum hardness is located.

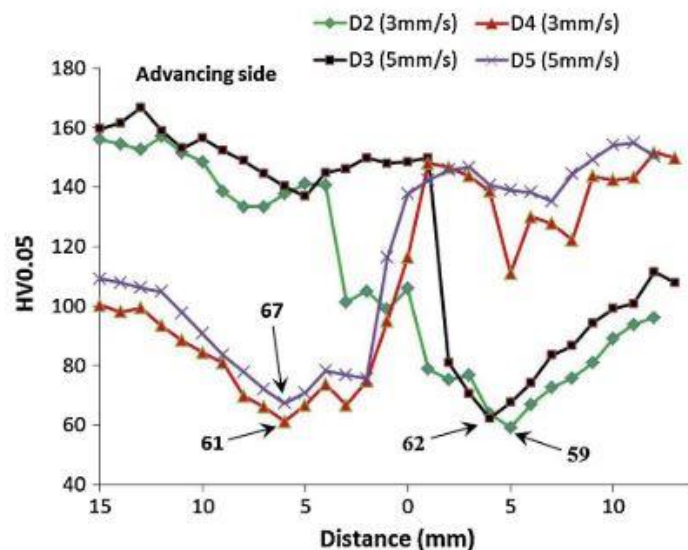


Figure 2.8: microhardness profiles at the cross-section of dissimilar joints [Guo et al., (2014)].

Moshwan et al., (2015) investigated FSW between 3 mm thick AA5052-O aluminium plates to characterize the microstructure and mechanical properties using 800-3000 rpm rotational speed and a traverse speed of 120 mm/min. Except for the rotating tool speed of 3000 rpm, all other rotational speeds generated sound welded joints with smooth surfaces, according to the appearances of the weld joints. The greatest tensile strength of the joint generated at 1000 rpm was 132 MPa, which was 74% of the base material.

Mastanaiah et al., (2016) analysed AA5083-AA2219 FSWed joints to obtain defect-free welds by varying tool traverse and rotational speeds. They reported that the mixing patterns in the SZ were affected by welding parameters, and the values of tensile strength were associated with the degree of material intermixing. **Figure 2.9** shows that the thoroughly mixed dissimilar weld joint has tensile strength and percent elongation comparable to those of both base materials.

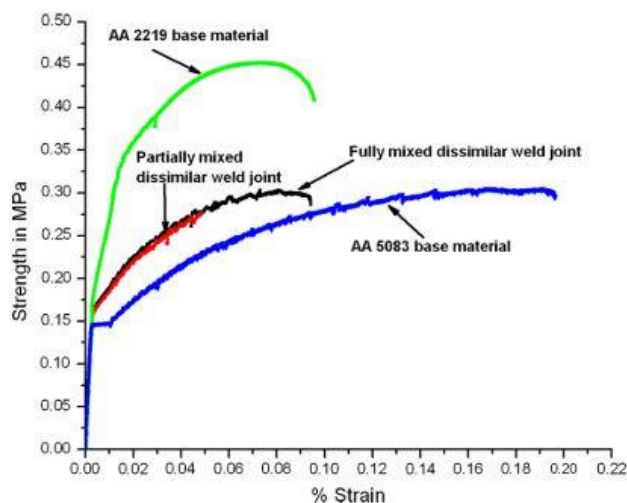


Figure 2.9: Plots illustrating tensile strength vs. strain for both base materials and dissimilar weld joints [Mastanaiah et al., (2016)].

Cetkin et al., (2019) also studied the mechanical properties of FSWed AA7075-AA5182 using different rotational speeds (980, 1325 and 1800 rpm) and traverse speed (108 and 233 mm/min). They concluded that better mechanical properties were obtained using low rotational speed (980 rpm) and traverse speed (108 mm/min).

Zhang et al., (2019) studied the microstructure and mechanical properties of AA7075-2024 similar and dissimilar joints. They found that the TMAZ on the RS of the joints has a broader width than the TMAZ on the AS. The width of the TMAZ on the AS and RS is increased as the rotating speeds are increased. They discovered that the mixing degrees of dissimilar materials in AA7075-2024 are influenced by rotational speed and base materials position

Although the minimal heat input created during FSW does not cause the base metal to melt, thermal cycles applied to the samples cause the mechanical characteristics of the joints to deteriorate. Controlling the temperature level appears intriguing and possible to improve the strength of typical friction stir welded joints. Several solid-state joining techniques have used external liquid cooling to improve joint performance [Liu et al., (2010)].

The aim of Fratini et al., (2009) was to see if in-process heat treatments may improve joint performance. To accomplish this, the AA7075-T6 weld joints were tested in three different environments: free air, forced air, and water flowing over the joint's surface. When external cooling is used during the FSW process, the mechanical resistance of the produced joints improves in terms of UTS. Water cooling ensured a more durable cooling medium, and using the in-process cooling treatment allowed for more robust mechanical resistance outcomes. The external cooling provided to the joint during the FSW process allows the thermal flow near the tool to be limited as much as possible, reducing conduction phenomena to the following material. The softened zone is narrower when water is used than when normal process conditions are used, and the parent material's hardness value is attained closer to the welding line, at least on the retreating side. With increasing the efficacy of the cooling medium used, the width of the welded zones, notably HAZ and TMAZ, is significantly reduced. This decrease in the welded zones indicates less material softening due to the welding process, which explains the improved mechanical performance of the FSW joints.

Underwater friction stir welding of 2219 aluminum alloy was carried out by Liu et al., (2010) to improve joint performance by altering welding temperature history. The results showed that by using external water cooling, the joint's tensile strength could be increased from 324 MPa to 341 MPa. The joint's elongation, on the other hand, has worsened. During tensile testing, the underwater FSW joint fractures at the interface between WNZ and TMAZ on the AS, as illustrated in Figure 2.10, whereas normal joints fracture in the HAZ on the AS. The underwater FSW joint has a lower hardness in the WNZ and higher hardness in the TMAZ and HAZ than the regular FSW joint.

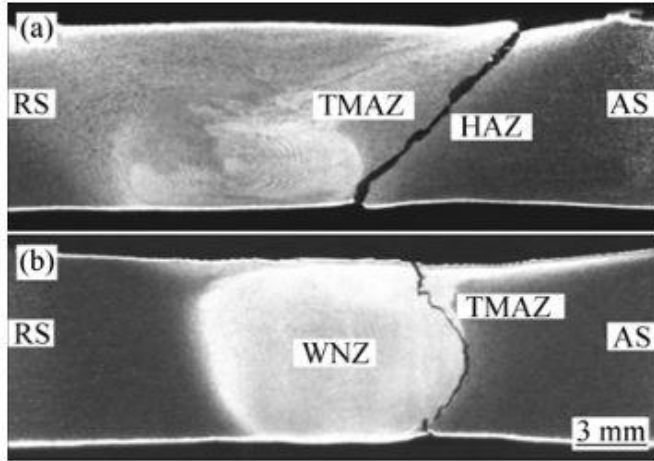


Figure 2.10: Fracture locations of different joints: (a) Normal FSW and (b) Underwater FSW [Liu et al., (2010)].

Sharma et al., (2012) investigated the effect of in-process cooling such as compressed air, liquid nitrogen and water cooling on the microstructure characteristics and mechanical behaviour of friction stir welded AA7039 aluminium alloy. They discovered that water cooling improves the mechanical properties of the joint more effectively. In-process cooling decreases the size of HAZ and reduces the extent of weld joint softening. The higher hardness of HAZ of in-process cooled joints than regular joints, as shown in **Figure 2.11**, is due to a reduction in the degree of coarsening.

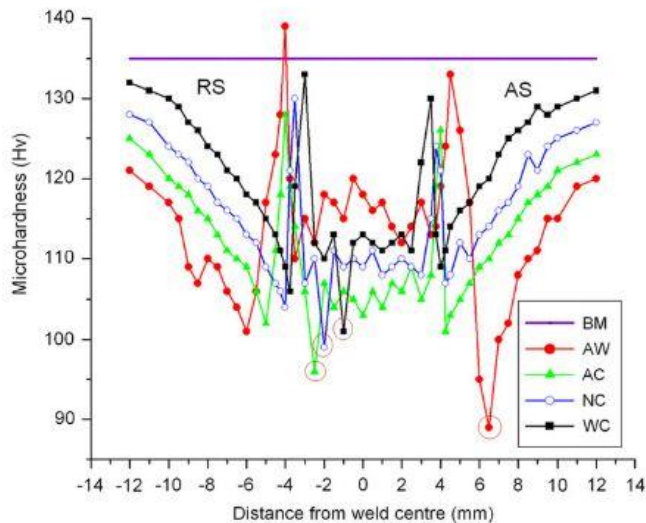


Figure 2.11: Microhardness profile of FSW joints [Sharma et al., (2012)].

Cho et al., (2016) they investigated FSW combined with a cooling system to overcome the strength loss for Al-Mg-Si (AA6082) aluminium alloys. They found that by using a coolant, both the yield strength and ultimate tensile strength of the joint increased, which could be attributed to the presence of fine strengthening precipitates after welding. Wang et al., (2017)

studied the effect of softening behavior of FSWed AA5083-H19 with and without additional water cooling. They concluded that by applying water cooling, softening in FSW was significantly reduced due to narrowed low hardness zone. At the same time, high tensile strength was obtained, which was almost equal to that of the base material, as shown in Figure 2.12.

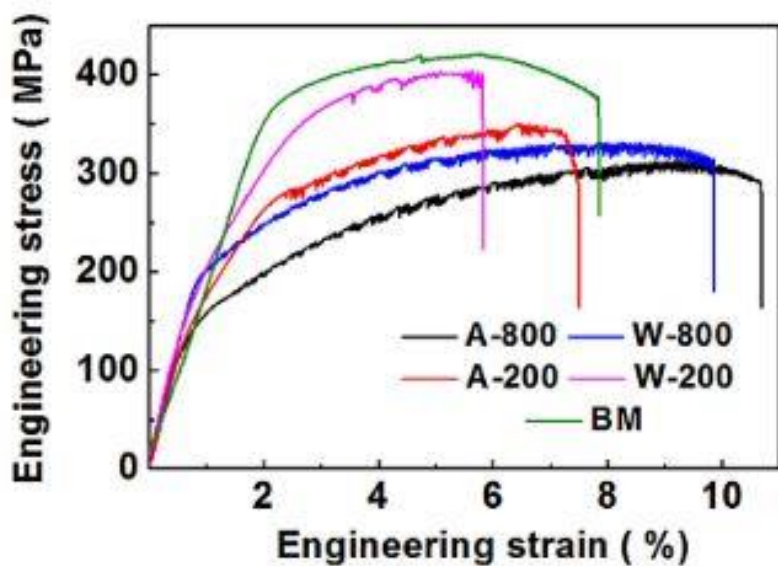


Figure 2.12: Engineering tensile stress-strain curves of the FSW joints under various parameters [Wang et al., (2017)].

Dong et al., (2019) produced AA7003-AA6061 FSWed joint using water as cooling media to improve joint efficiency and obtained 90.4% joint efficiency to the 6061 base material. The microstructural zone width such as HAZ is reduced in the case of water-cooled joints than an air-cooled joint.

2.4 Corrosion behavior in FSW

Because of the different phenomena on the formation of grain microstructure and the occurrence of dynamic recrystallization during the FSW process, FSWed aluminium alloys is prone to severe corrosion in welded zone regions.

W. Xu et al., (2009) investigated the pitting corrosion of the weld nugget zone along the plate thickness in friction stir welded 2219-O aluminum alloy in alkaline chloride solution at three different sites (Top, Middle, and Bottom). The base material was more prone to pitting corrosion, resulting in severe pitting corrosion on the groove surface. Compared to the base material in alkaline chloride solution, the corrosion resistance improves dramatically at the weld nugget zone. With the reduction in traverse speed from 100 to 60 mm/min or the tool rotational

speed from 600 to 500 rpm, the Ecorr, Epit, and Erp improved and the current density moved upwards as shown in **Figure 2.13**.

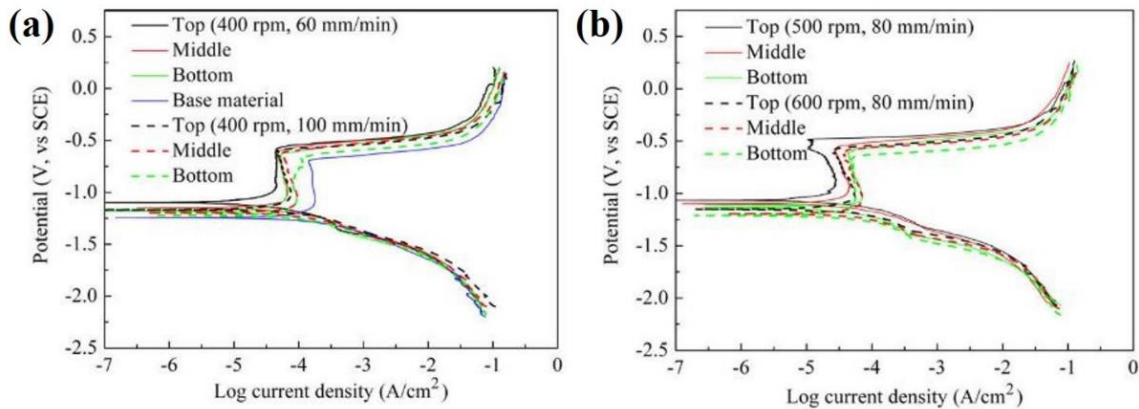


Figure 2.13: Polarization curves of different positions of WNZ (a) varying traverse speed and (b) varying rotational speed [W. Xu et al., (2009)].

The best conditions in sea water for corrosion prevention of friction stir-welded 5083-O aluminum alloy were determined by electrochemical experiments. As determined by polarization studies, the limiting potential for avoiding the effects of hydrogen embrittlement was -1.6 V, which corresponded to the crossover point between concentration and activation polarization. Because the current density in the potentiostatic tests was low at these values, the best protective potential lies between -1.5 and -0.7 V. When a galvanic cell is produced in seawater, the welds show electrochemically stable trends. In galvanic testing, welded sections with varying area ratios were stable and showed outstanding anticorrosion properties [PARK et al., 2009]. Fahimpour et al., (2012) Studied the corrosion behavior of FSWed 6061 aluminium alloy joints and stated that poor corrosion resistance was observed at the weld nugget of FSWed joints than BM. It was observed that the corrosion potential of a secondary phase was not the same as the parent phase and this difference resulted in the formation of a galvanic cell. Bagheri et al., (2013) studied the effects of varying welding parameters (rotational and traverse speed) on the corrosion behaviour of FSWed AA5052 alloy. They established an optimum tool rotational and traverse speed combination for the best corrosion resistance. This was due to the additional fine grain structure that accelerated the passive film nucleation.

Donatus et al., (2015) examined the corrosion-sensitive regions of dissimilar AA5083-AA6082 FSWed joints. They found that zonal heterogeneities formed in the SZ of dissimilar alloys were prone to corrosion attack and these zones showed additional corrosion attacks with higher welding speed. This was due to decreased rotation rate of the tool per weld length

required for heat generation and material mixing. The most corrosion-prone areas in the friction stir weld are shown in **Figure 2.14**.

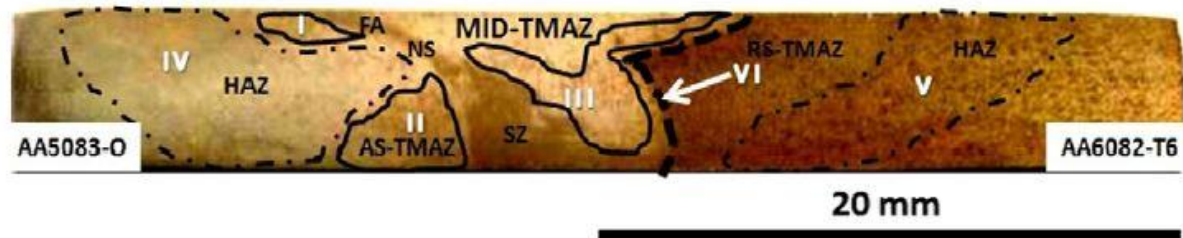


Figure 2.14: Optical picture of FSWed AA5083-AA6082 after a 7-day immersion test in 3.5 percent NaCl solution [Donatus et al., (2015)].

Davoodi et al., (2016) investigated the corrosion behavior of an AA5083-AA7023 dissimilar FSWed joint. The EIS plot of the base materials and FSWed joints is shown in **Figure 2.15**. They reported that the corrosion susceptibility of AA5083-AA7023 dissimilar joint depends on Cu and Si-based intermetallic particles present in both AA5083 and AA7023, thereby creating a potential galvanic cell.

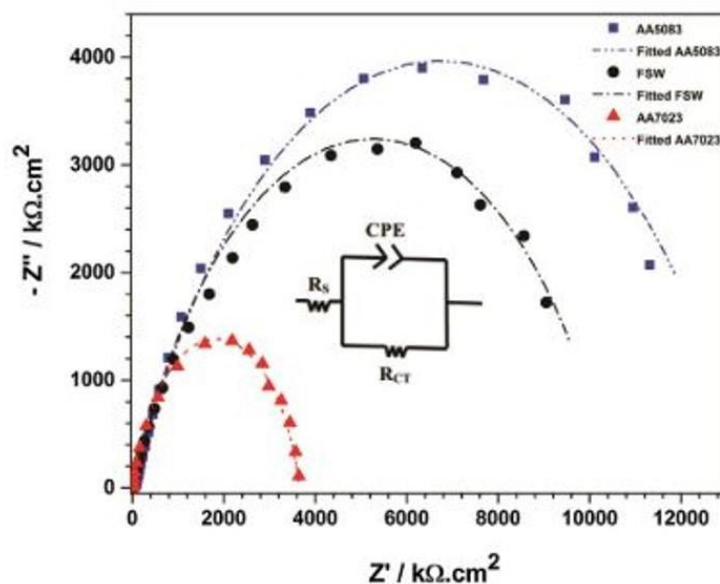


Figure 2.15: EIS plot of the three regions on AA5083, FSW and AA7023 surfaces in 3.5% NaCl electrolyte [Davoodi et al., (2016)].

2.5 Microstructure, Texture evolution and work hardening behavior in FSW

Yutaka et al., (2001) studied the micro-texture of 4mm thick, friction stir welded 6063 aluminum alloy. The base-material plate has a Goss orientation. They reported that the presence

of shear texture component in the weld nugget region with a pair of [$\{111\} <110>$] orientations parallel to the cylindrical pin surface and along the direction of the plate.

[Schneider et al., \(2004\)](#) studied the plastic flow of the friction stir welding and analysed the bands or formation of the onion ring structure using orientation image mapping. They found that parent material has a [$\{110\} <112>$] rolling texture and the joints which were made along the rolling direction has two regions, one with finely recrystallized equiaxed grains comprised with the bulk mechanically deformed zone of the weld region and the other with the finely recrystallized equiaxed grains with an apparent shear fiber orientation texture with $\{111\}$ poles aligned with the axis of the rotation of the tool.

The works carried by [Fonda et al., \(2007\)](#) have determined the banding in friction stir welded associated with different microstructural features in 2195 aluminum alloy. They noticed that and components of shear textures (standard) were present in the weld. [\[Xu et al., \(2008\)\]](#) studied the texture patterns of the friction stir welded components in transverse, longitudinal and horizontal cross-sections of 6061 aluminum alloy. Their conclusions revealed that the banded texture pattern exists on the advancing side of welds. They also reported that the mechanical strength of friction stir welded joints depends highly on the interface of the deformed material. [Xu et al., \(2008\)](#) identified that during friction stir welding of 6061 aluminum alloy, the texture development at the circumference of the pin, the material flow led to the formation of [$\{112\} <110>$] simple shear texture component.

[Cho et al., \(2008\)](#) modeled the crystallographic texture evolutions during friction stir welding of 6061 aluminum alloy. They analyzed that the plastic anisotropy present in the yield surface due to texture is assumed to have little effect on the overall flow field. Major texture components during two-dimensional modeling of FSW were pure and straightforward shear components due to severe shearing deformation were found in both the predictions and experiments.

[Chen et al., \(2014\)](#) studied the texture evolution during friction stir welding of 2219 aluminum alloy. They found different texture components in the welding, Cube [$\{001\} <100>$], Goss [$\{011\} <100>$], Brass [$\{011\} <211>$] and cube ND [$\{001\} <110>$] in thermos-mechanically affected zone, the heat-affected zone, and the weld zone. This clarifies that a more suitable coordinate system to define the textures in FSW should be using a shear plane and shear direction.

[Wang et al., \(2015\)](#) performed the EBSD analysis of dissimilar joints made of 5052 and 6061 aluminum alloys. They identified that the grain refinement of the weld nugget zone was achieved by dynamic recrystallization. They also observed that the deformation texture component

of $\{001\} <100>$ C cube texture, $\{123\} <634>$ S texture in base material as shown in **Figure 2.16** are gradually transformed into the shear texture components.

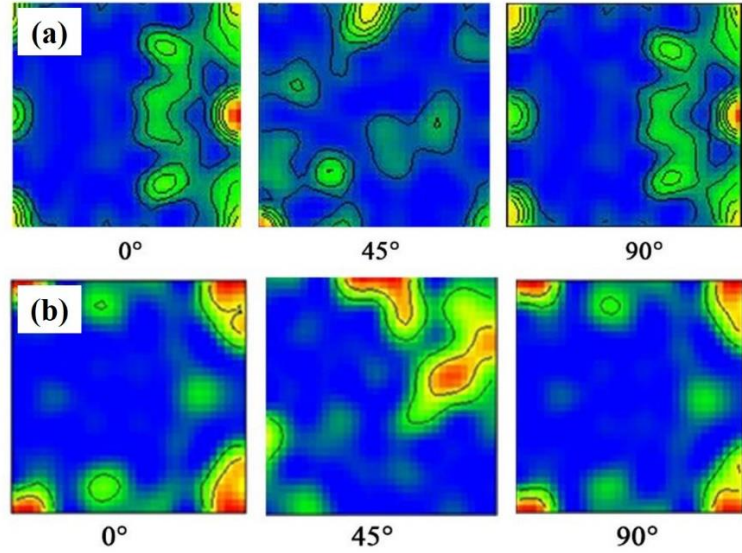


Figure 2.16: Orientation distribution function (ODF, $\Phi_2 = 0^\circ, 45^\circ, 90^\circ$) of AA6061-T6 and AA5052-O alloy (Wang et al. 2015).

[Moradi et al., \(2019\)](#) reported the texture at the SZ of AA5083-AA6082 dissimilar joint. The main orientations characterized are Rotated Cube $\{001\} <100>$ component and Rotated Goss $\{011\} <011>$ component. Compared to the as-received sheets, the results showed a poorer texture in all three regions after FSW. Because of the non-uniform plastic deformation of FSW, the textures of the stirred zone's center, advancing side, and retreating side are entirely asymmetric, as shown in **Figure 2.17**.

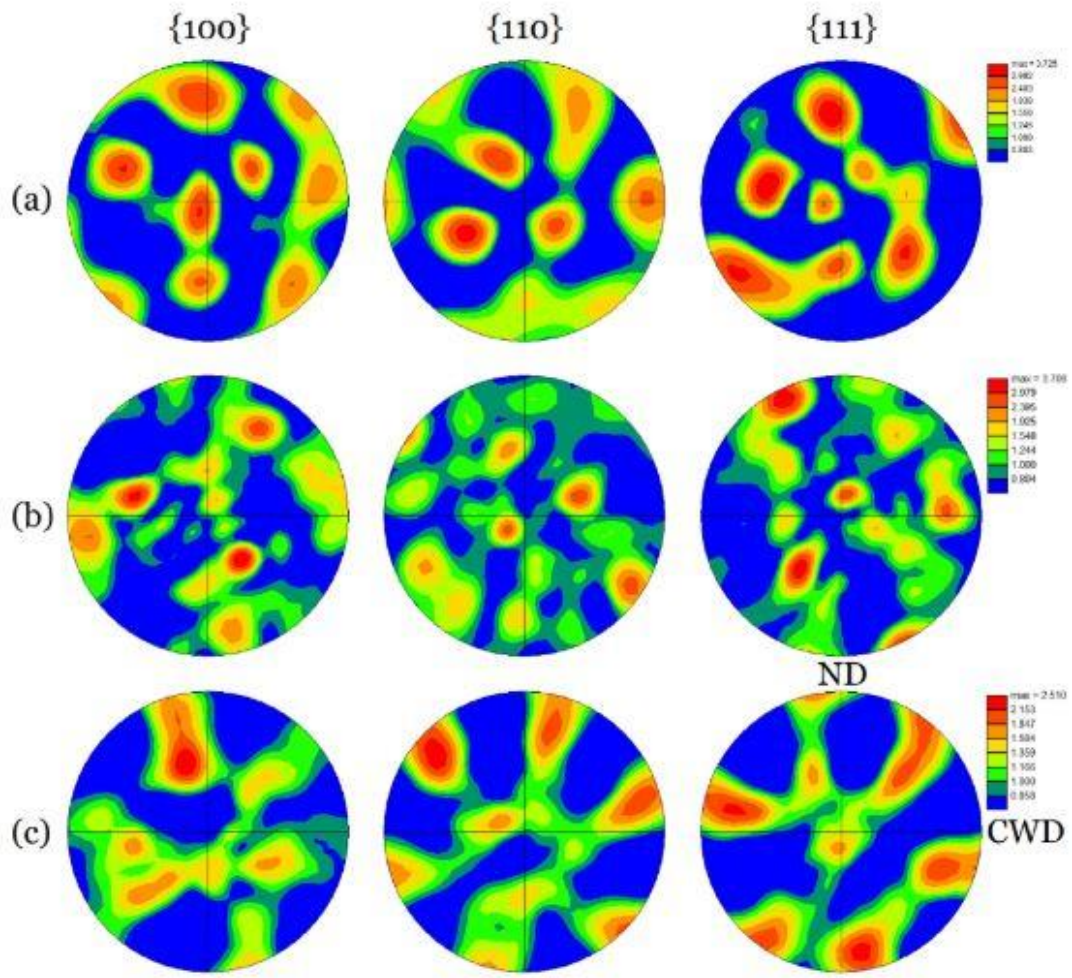


Figure 2.17: {100}, {110}, and {111} pole figures of (a) center of stirred zone, (b) advancing, (c) and retreating sides [Moradi et al., (2019)].

As-received base materials AA5083 and AA6061 have varying mechanical properties (strength/hardness, ductility and deformation) and thermophysical properties. Moreover, very little attention was given to tensile behavior (strain hardening behavior and strain hardening rate) of the FSWed joints.

[Sinclair et al., \(2006\)](#) Proposed a model for the low-temperature tensile response of copper polycrystals with grain size in the range of 2-50 μm . The initial work hardening behavior is strongly grain size-dependent and is considered to arise from a combination of kinematic and isotropic hardening due to dislocation-grain boundary interactions. [Afrin et al., \(2007\)](#) used two modified equations of hardening capacity and strain hardening exponent to estimate the work hardening parameters of a friction stir welded magnesium alloy, excluding the elastic deformation stage. **Figure 2.18** shows Kocks-Mecking type plots illustrating different stages of strain hardening. When compared to the base alloy, the flow stress of FSWed samples was lower. While FSW produced about half the yield strength of the base alloy, the ultimate tensile strength after FSW was roughly two-thirds that of the base alloy. As a result, the FSWed

samples had a hardening capability roughly double that of the primary alloy. Following yielding, the base alloy displayed a high initial and almost constant strain hardening rate, equivalent to stage II linear hardening, followed by stage III linear hardening with a linearly declining hardening rate, and finally stage IV hardening. Stage II hardening did not occur after FSW, while stage III hardening did occur shortly after yielding. In almost every case, the strain hardening exponent of the FSWed samples was three times higher than that of the base alloy.

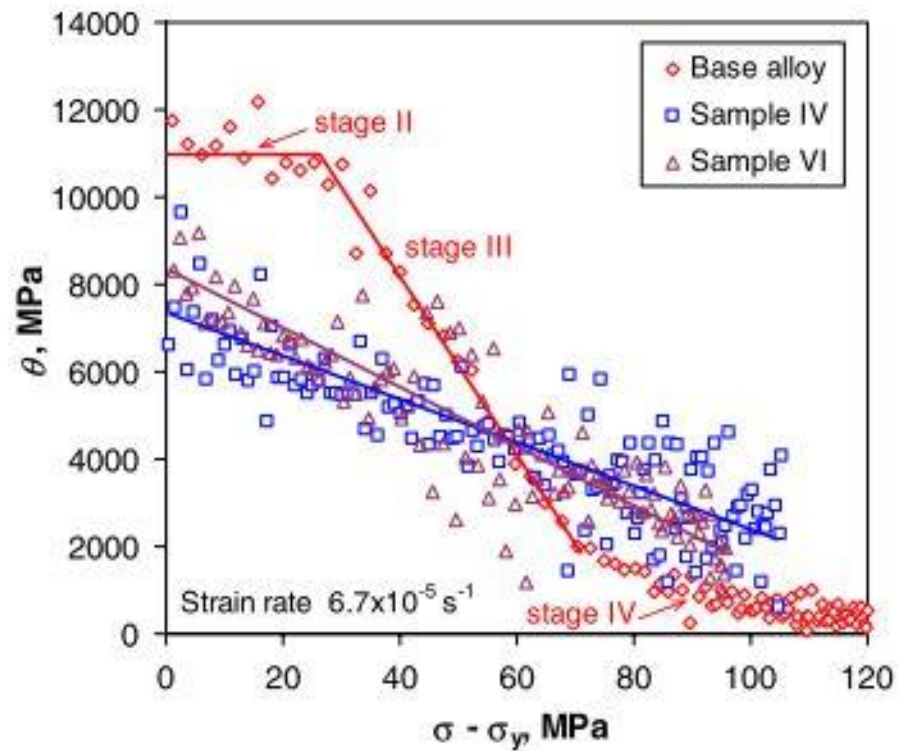


Figure 2.18: Strain hardening rate as a function of net flow stress of the base alloy and FSWed samples [Afrin et al., (2007)].

Ni et al., (2014) studied the strain hardening behavior of FSWed 2009 aluminium alloy. They found that strain hardening exponent of the BM and FSWed samples had little effect on strain rate. They showed that FSWed joints showed only stage III and stage IV hardening behavior in the Kocks-Mecking plots of strain hardening rate. Moreover, a higher strain hardening rate was obtained in FSWed joints than in base metal. Feng et al., (2014) also examined the strain hardening behavior in addition to the microstructural evolution of FSWed AA7075 alloy. They explained that the strain hardening exponent and strain hardening rate improved after FSW, as shown in **Figure 2.19**.

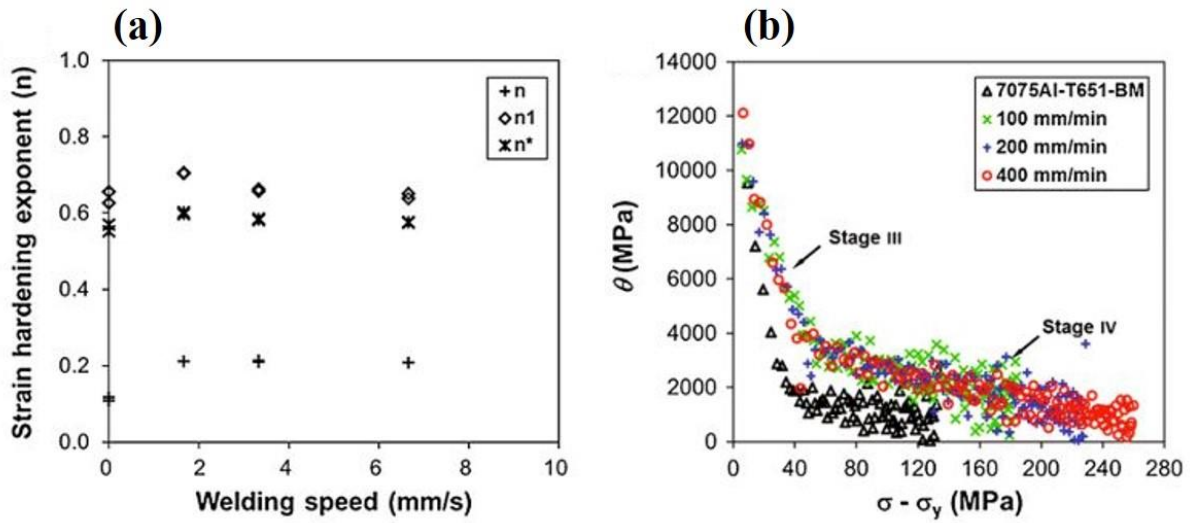


Figure 2.19: (a) strain hardening exponent, (b) strain hardening rate vs. flow stress of FSWed joints at varying welding speeds [Feng et al., (2014)].

2.6 Summary

From the literature review, considerable work has been carried out on enhancing the joint properties of FSWed dissimilar alloys by varying process parameters and changing tool geometry. However, in the aspect of material flow, microstructure and texture characteristics were scarce in dissimilar welding of non-heat-treatable and heat-treatable aluminium alloys. Therefore in this study, our main aim is to improve the mechanical properties and corrosion resistance of AA5083-AA6061 FSWed joints using various techniques like optimizing the process conditions (traverse speed and rotational speed) and applying a cooling environment. An attempt has been made to study the mechanical properties by detailed microstructural analysis by Optical Microscopy, SEM with EDS, EBSD. Grain size measurements, microhardness measurements and tensile tests were performed for all conditions and compared with the as-received base materials. The corrosion behavior of FSWed joints and the as-received base metals using the electrochemical workstation was also investigated. An attempt was also made to study the tensile properties (ultimate tensile strength, strain hardening exponent and strain hardening rate) of FSWed joints.

CHAPTER 3

EXPERIMENTAL PROCEDURES

3.1 Introduction

In the present work, an FSW machine was used to join AA5083-AA6061 dissimilar aluminum alloys to analyze the mechanical and corrosion properties of the joint. The effect of base material position, process parameters, and in-process cooling environment on mechanical and corrosion behavior of FSWed AA5083-AA6061 dissimilar aluminium alloys was studied. This chapter presents the details of base material, FSW process conditions, cooling environment conditions, metallographic studies, mechanical testing, and corrosion test.

This section outlines the experimental techniques used to join and characterize the microstructure, mechanical, microhardness and corrosion properties described in the results section in this study. Most of the techniques are well known, so will be described briefly.

3.2 Experimental plan

The overall experimental plan is shown in **Figure 3.1**. The experimental and analysis work was majorly divided into five parts: selection of workpiece materials, Friction stir welding, Microstructure study, Mechanical properties, and corrosion behavior.

3.3 Selection of workpiece

In this study, as-received base materials AA5083-H111 and AA6061-T6 aluminium alloys with 300 mm x 70mm x 6mm dimensions were butt joined along the rolling direction using a numerically controlled FSW machine. The elemental composition of the base materials was determined using Optical Emission Spectrometer (BAIRD, DV6) and the composition of each element is given in **Table 3.1**. The Mechanical Properties of the as-received base material are shown in **Table 3.2**.

Table 3.1: Chemical composition of AA5083-H111 and AA6061-T6 (in %wt.).

Material	Si	Cu	Mn	Mg	Cr	Zn	Fe	Ti	Al
5083-H111	0.12	0.06	0.55	4.07	0.07	0.11	0.23	0.01	Bal.
6061-T6	0.63	0.25	0.09	0.66	0.19	0.15	0.3	0.02	Bal.

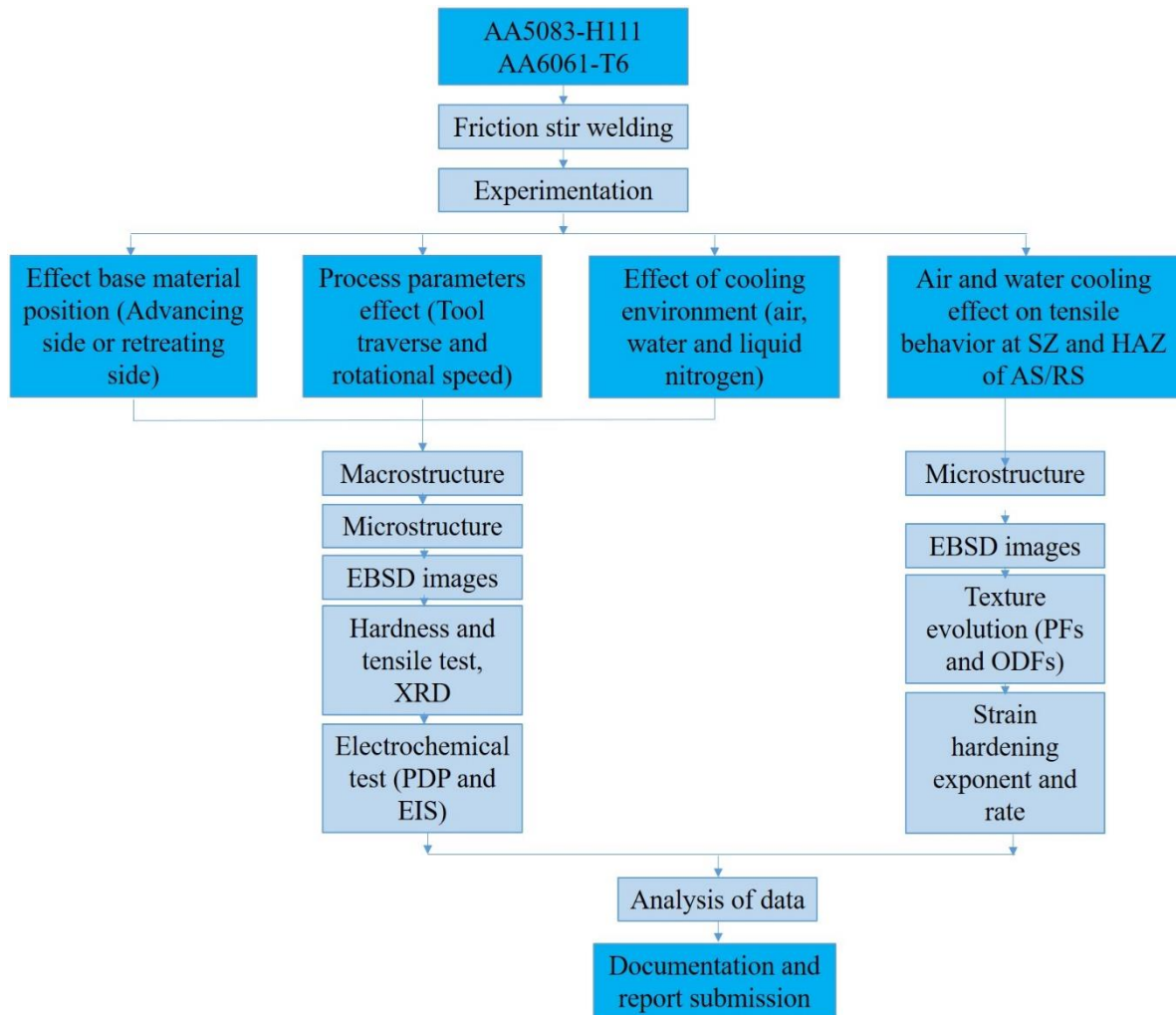


Figure 3.1: Detailed layout of the proposed work

Table 3.2: Mechanical properties of AA5083-H111 and AA6061-T6 aluminium alloys (as-received condition).

Material	Microhardness	Yield strength	Ultimate Tensile	Elongation
	(HV)	(MPa)	strength (MPa)	
AA5083-H111	87.6	175	315	11.7
AA6061-T6	84.5	226	294	10.1

3.4 Selection of tool material and design

Friction stirring is a thermomechanical deformation technique in which the tool temperature approaches the solidus temperature of the work piece. The proper tool material selection for the desired application is required to produce a high-quality friction stir zone. The tool material used in this experiment is AISI H13 tool steel. This is owing to tool steel's high-temperature strength and stability, as well as its wear resistance, thermal fatigue strength, ease of friction stirring, machinability, and low cost. The typical chemical composition of H13 tool steel is presented in **Table 3.3**. A conical tapered threaded pin profile with a diameter of 6mm at the root and 4 mm at the tip, length of 5.5 mm and tool shoulder diameter of 18 mm with 3° concavity was used as shown in **Figure 3.2**.

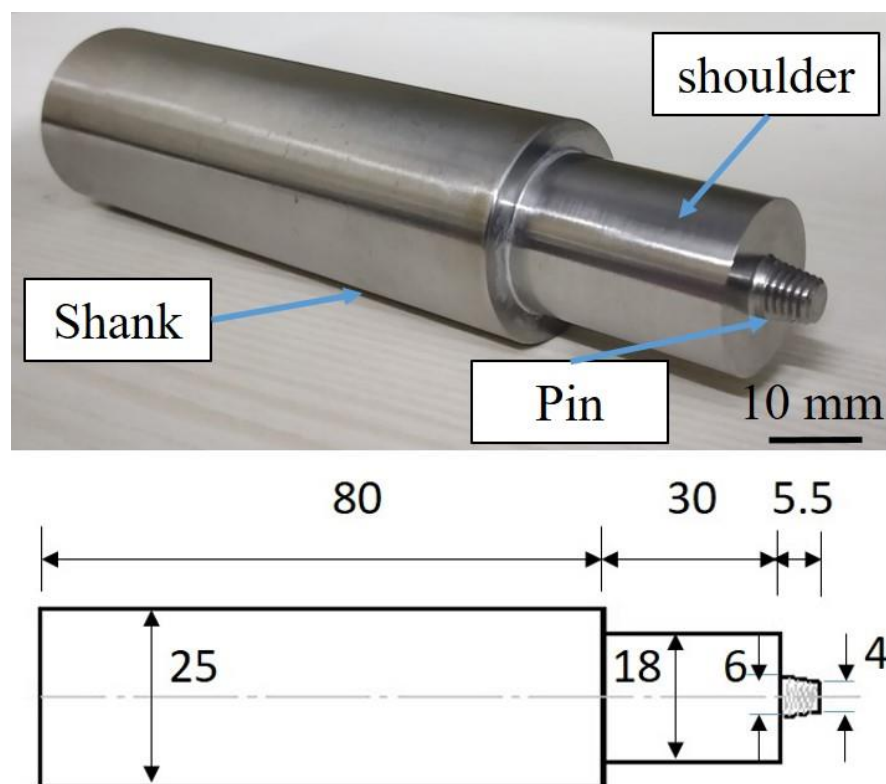


Figure 3.2: FSW tool with the schematic.

Table 3.3: Chemical composition of AISI H13 tool steel

Element	C	Mn	P	S	Si	Cr	V	Mo	Fe
Wt. %	0.42	0.28	0.015	0.003	1.00	5.20	1.05	1.45	Balance

3.5 Friction stir welding machine

The experiments were performed on the numerically controlled 3-Ton friction stir welding machine (RV Machine tools, FSW-3T-NC, India) with inbuilt data acquisition system as shown in **Figure 3.3**. The specifications of the machine are shown in **Table 3.4**.

Table 3.4: FSW Machine specifications

S.No	Details	Specifications	S.No	Details	Specifications
1	Spindle Motor	AC Induction motor with VFD drive	11	Control Modes	Force Control and position control
2	Spindle rotational speed	0-3000 rpm	12	Load cell	Z and X-axis
3	X-axis rapid traverse (welding speed)	0-1000 mm/min	13	Spindle Head	Up to $\pm 5^\circ$ (manual) tilting
4	X-axis stroke	400 mm	14	X-axis Thrust	15 kN
5	Y-axis stroke	200 mm	15	Y-axis Thrust	Manual
6	Z-axis stroke	300 mm	16	Z-axis Thrust	30 kN
7	Spindle Torque	75 N-m @ 1400 rpm	17	Spindle Motor	11 kW/1400 RPM/440V Capacity
8	Z-axis Drive rapid traverse	0-1000 mm/min (automatic)	18	X-axis drive	Servo with gear box
9	Tool Holder	ISO 40 Arbor	19	Data acquisition and analysis	Spindle speed, axis velocity against time, and force
10	Centralized lubricating system	Manual	20	Table size	400 x 300 mm with threaded Holes

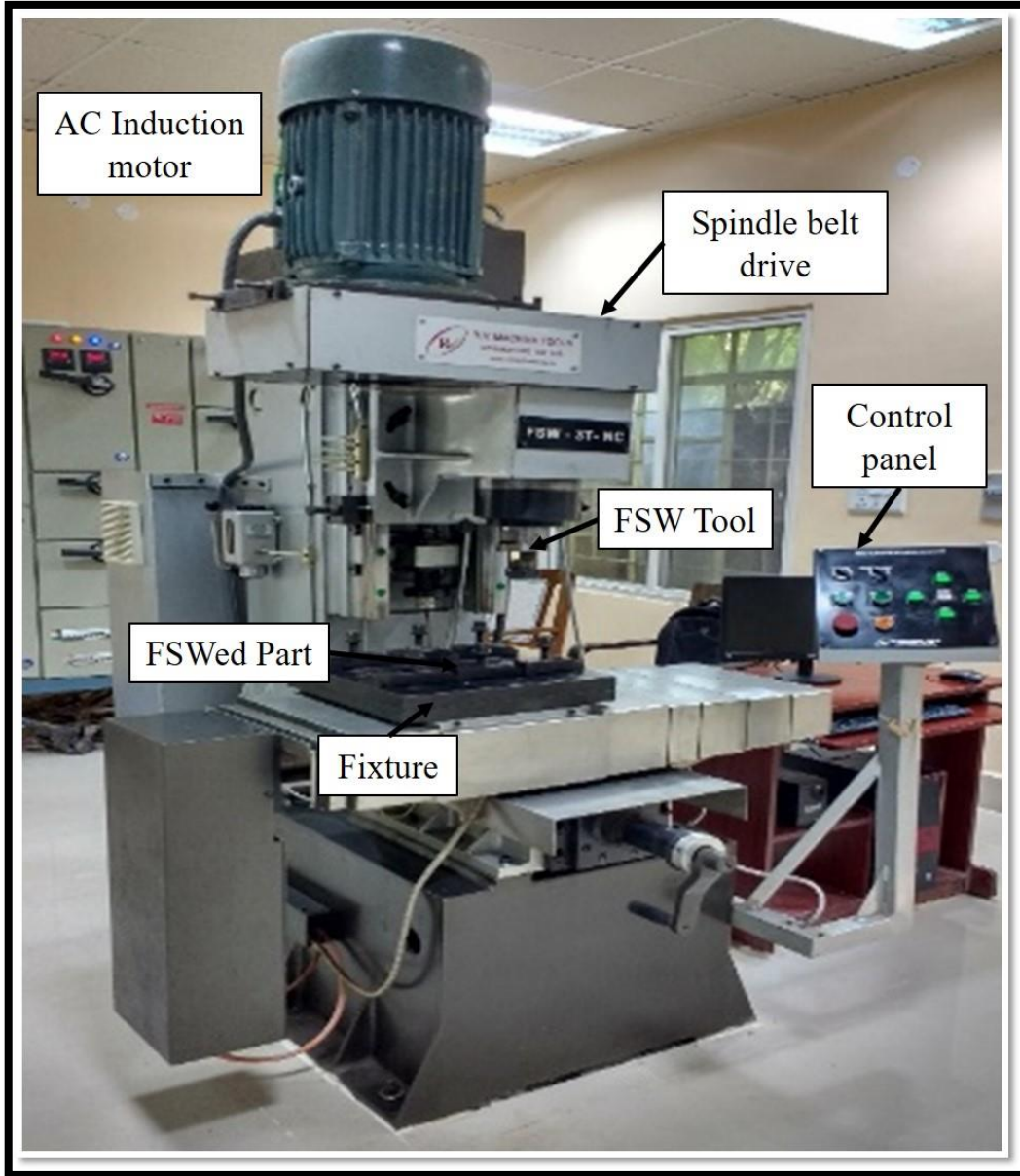


Figure 3.3: Friction stir welding machine

3.5.1 Cooling environment condition

Friction stir welding was done in three different cooling environments: ambient environment or air-cooled (ACFSW), liquid nitrogen-cooled (NCFSW) and water-cooled (WCFSW). During liquid nitrogen and water-cooled FSW, coolants were supplied immediately at a distance of 25 mm behind the tool with a flow rate of 0.3 l/min and 1.8 l/min, respectively to maintain a constant temperature throughout the process. A cooling environment set-up was designed in a box-type model made of transparent glass fiber sheets and fixed to the table of the FSW machine to store the coolant to ensure efficient cooling is shown in **Figure 3.4**.

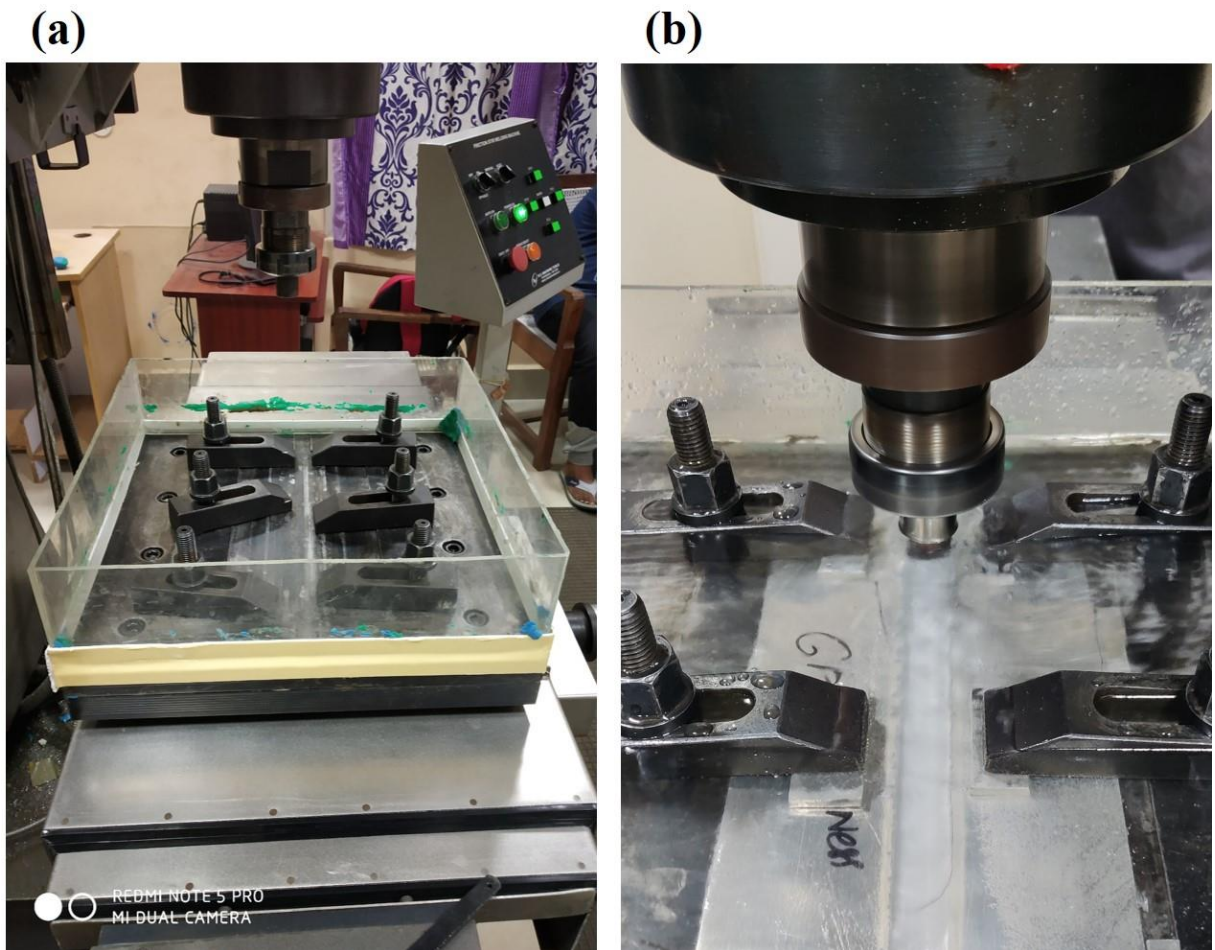


Figure 3.4: (a) cooling environment set up and (b) water-cooling process.

3.6 Microstructure study

3.6.1 Sample cutting, mounting and polishing

The samples were sliced perpendicular to the weld direction for tensile, hardness and metallography; for easy handling, metallography samples were mounted on Bakelite powder using the hot mounting press. For the optical microscopic study, the cross-section of metallography sample was polished with various grades of emery papers (200, 400, 600, 800, 1000, Grade 1, Grade 2, Grade 3 and Grade 4) and fine disc polished with a diamond paste of 0.25 μm . The samples were prepared by conventional metallographic techniques and etched using Keller's reagent (190ml distilled water + 2ml HF + 3ml HCl + 5ml HNO_3) to reveal the microstructural features.

Microstructural characterization was then carried out using optical microscopy (OM) (Huvitz co Ltd, HRM300, South Korea), Scanning Electron Microscope (SEM) with energy dispersion spectroscopy (EDS), X-ray diffraction technique (XRD) and Electron Back Scattered Diffraction (EBSD).

3.6.2 Optical microscope

The polished and etched weld cross-section samples were subjected to macro and microstructural characterization using optical microscopy (OM) (Huvitz co Ltd, HRM300, South Korea). The corroded surface analysis was also carried out using OM. The optical microscope is shown in **Figure 3.5** and the specifications are given in **Table 3.5**.

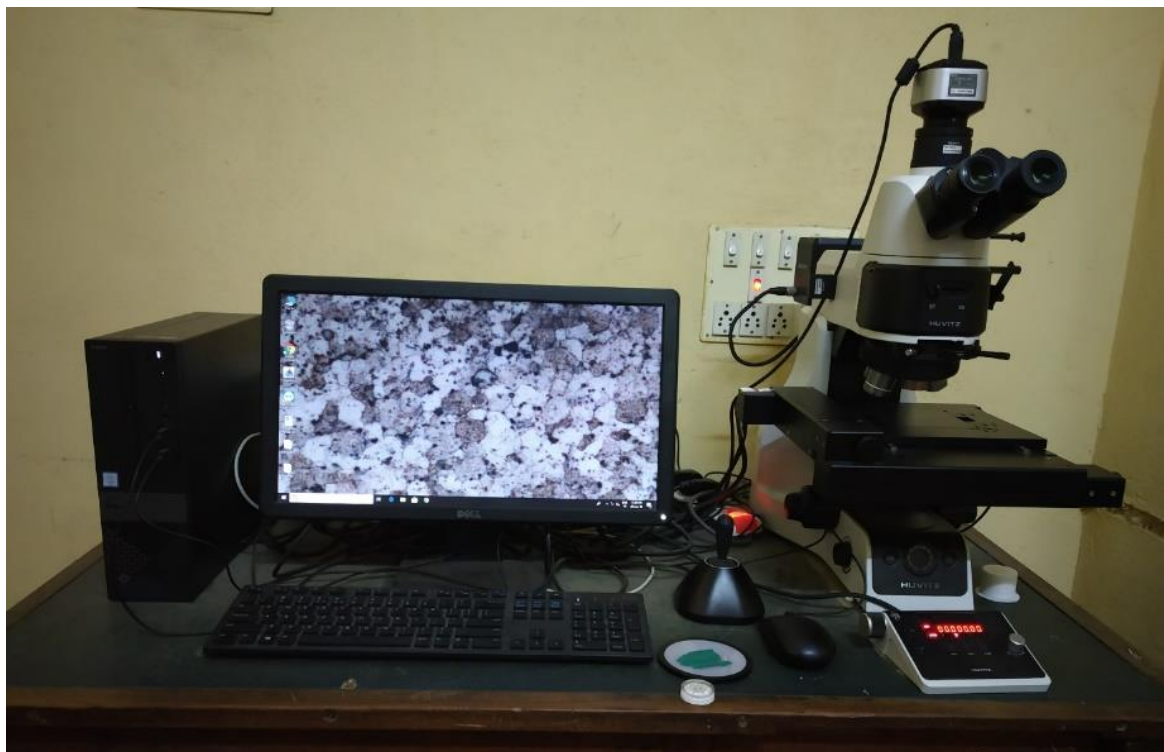


Figure 3.5: Optical microscope used for microstructural studies

Table 3.5: Specifications of 3D Optical microscopy

S.No	Detail	Specifications
1	Eye piece	10x Wide Field, Diapler Adjustable
2	Observation Tube	Trinocular Erect
3	Mountable Objective Lens	Plan Flou EPI 5X, 10X, 20X, 50X and 100X
4	Accuracy and repeatability	Accuracy of Magnification \pm 15 - \pm 20 μm , Repeatability of magnification \pm 10 - \pm 15 μm
5	Lump Halogen	12V, 100W halogen Lamp
6	camera	Image Sensor, $\frac{1}{2}$ inch, 3 megapixels
7	Illumination	Reflected bright field/dark filed/polarized
8	Filter	Neutral Density Filter Differential Interference contrast filter

9	Focussing unit	Stroke 30-45 mm, Resolution 0.01-0.05 μm , maximum sample height 15—25 mm.
10	3D Imaging and Panasis professional measurement software	

3.6.3 Scanning electron microscope

Scanning Electron Microscope (SEM) (Vega 3 LMU, Tescan, France) with tungsten filament and an accelerating voltage of 20 kV was used for studying the microstructure analysis (Grain structure, precipitates and intermetallics evolved) and fractography of the tensile specimens. The photograph of the scanning electron microscope is shown in **Figure 3.6**.



Figure 3.6: Scanning electron microscopy

3.6.4 X-ray diffraction

X-ray diffractometer (PANalytical, X'Pert Powder XRD, Netherlands) was used to study the phase formation in the stir/nugget zone and base material of the welded sample at the cross-section. Scan angle kept constant during the analysis was from 20° to 100° . The obtained result is further kept in the ICSD software to obtain the variation of the peak. The photograph of the X-ray diffraction setup is shown in **Figure 3.7**.



Figure 3.7: X-ray diffraction

3.6.5 Electron back scattered diffraction (EBSD)

The EBSD data acquisition was carried out in an FEI Quanta (FEI, Quanta 3D-FEGTM) SEM equipped with TSL OIM software v 7.12 operating at 30kV. Orientation mapping was then performed in square 54 regions of area 400 x 400 on advancing side, nugget zone and retreating side of the weld with a step size of 0.5 and the initial processing of the data was done using ATEX software. The texture components were found at possible Euler angles of different texture components of FCC materials, as shown in **Table 3.6**. The photograph of the electron backscattered microscope is shown in **Figure 3.8**.

Table 3.6: Euler angles for different texture components of FCC materials

Name	Representation	$\Psi 1$ (in °)	Ψ (in °)	$\Psi 2$ (in °)
Brass	{110} <112>	55	90	45
Goss	{110} <001>	90	90	45
Cube	{001} <100>	45	0	45
R-cube	{001} <110>	0/90	0	45
Copper	{112} <111>	90	35	45
S	{123} <346>	59	37	63
A	{110} <111>	35	90	45
R-goss	{011} <011>	0	90	45



Figure 3.8: Electron backscattered diffraction system

3.7 Mechanical study

3.7.1 Microhardness tester

The photograph of the microhardness measuring line is shown in **Figure 3.9**. The Vickers microhardness was measured at the midplane of weld cross-section at each 0.5mm using a Vickers indenter of model ECONOMET VH-1 manufactured by Chennai Metco Pvt Ltd, Chennai, with 100gf load and 10s dwell time as shown in **Figure 3.10**. Tests were carried out for FSWed 5083-6061 Aluminium alloys and compared with untreated AA5083-AA6061 base alloys.

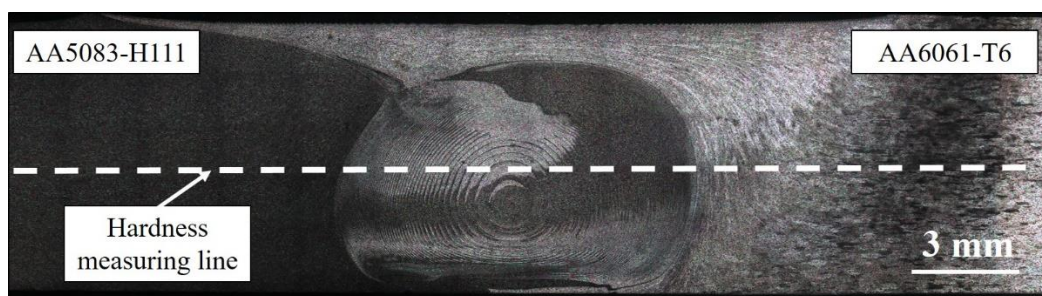


Figure 3.9: Hardness measuring line of the cross-section sample.



Figure 3.10: Vickers microhardness tester

3.7.2 Tensile test

Transverse tensile tests of gauge length 25 mm, radius 6 mm and web 10 mm were sectioned as per ASTM E8 standard using a wire-cut electrical discharge machine (WEDM), as shown in **Figure 3.11**. The tests were performed at room temperature to evaluate the joint's mechanical properties using (M50, S.M.Engineers, Pune, India) as shown in **Figure 3.12**.

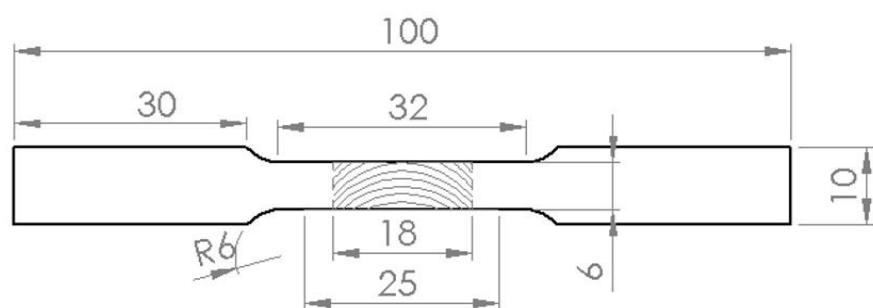


Figure 3.11: ASTM E8 standard schematic specimen.

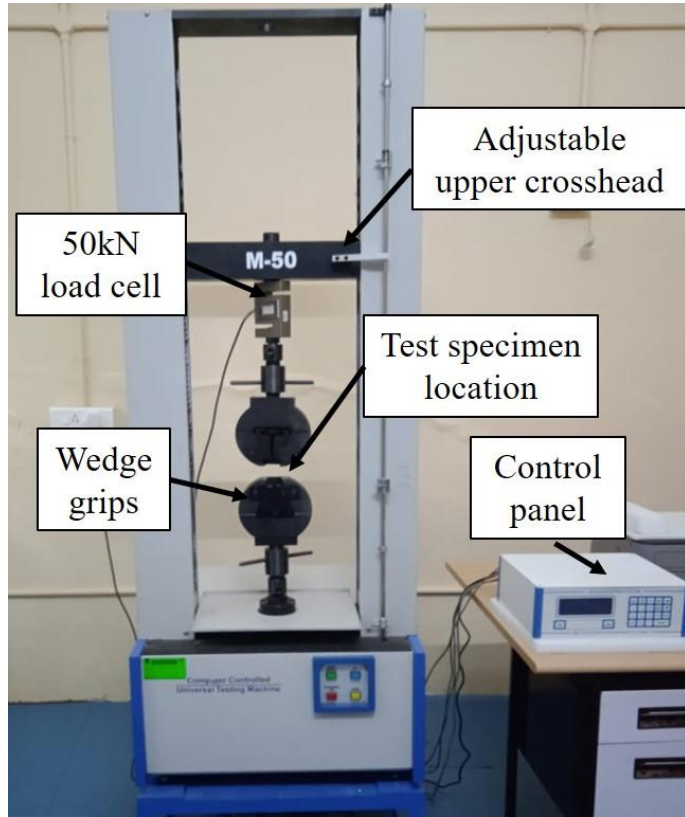


Figure 3.12: Universal testing machine

3.8 Corrosion study

Potentiodynamic measurements are commonly used to generate polarization Tafel curves, calculating the corrosion potential (E_{corr}) and corrosion current density (i_{corr}). The only approach indicating the relative anodic and cathodic contributions is potentiodynamic polarization, which displays the corrosion process kinetics. The approach is destructive and cannot be used to anticipate the material's long-term corrosion rates. A potentiodynamic test was carried out at Chemical Engineering Department, NIT Warangal, (CH Instruments, USA, 604e), as shown in **Figure 3.13**. Before the corrosion test, specimens were wet ground to grade P1200 grit for smooth surface finish followed by drying in warm air. In all cases, the tests were performed in duplicate to guarantee the reliability of the results. The Potentio-dynamic polarization (PDP) test was carried out according to the ASTM G3 standard using a three-electrode cell potentiostat. The three electrodes used were a test sample, platinum mesh, and a saturated calomel electrode (SCE), treated as working, counter, and reference electrodes. Open circuit potential (OCP) was initially performed at the SZ of the FSWed joint for 30 minutes to get an equilibrium potential. PDP tests were done at a scanning rate of 0.167 mV/s and a scanning range of ± 0.5 V to OCP values of each sample. The electrochemical measurements were performed with a working area of 0.2826 cm^2 exposed to 3.5 wt% NaCl solution at room temperature (25° C).

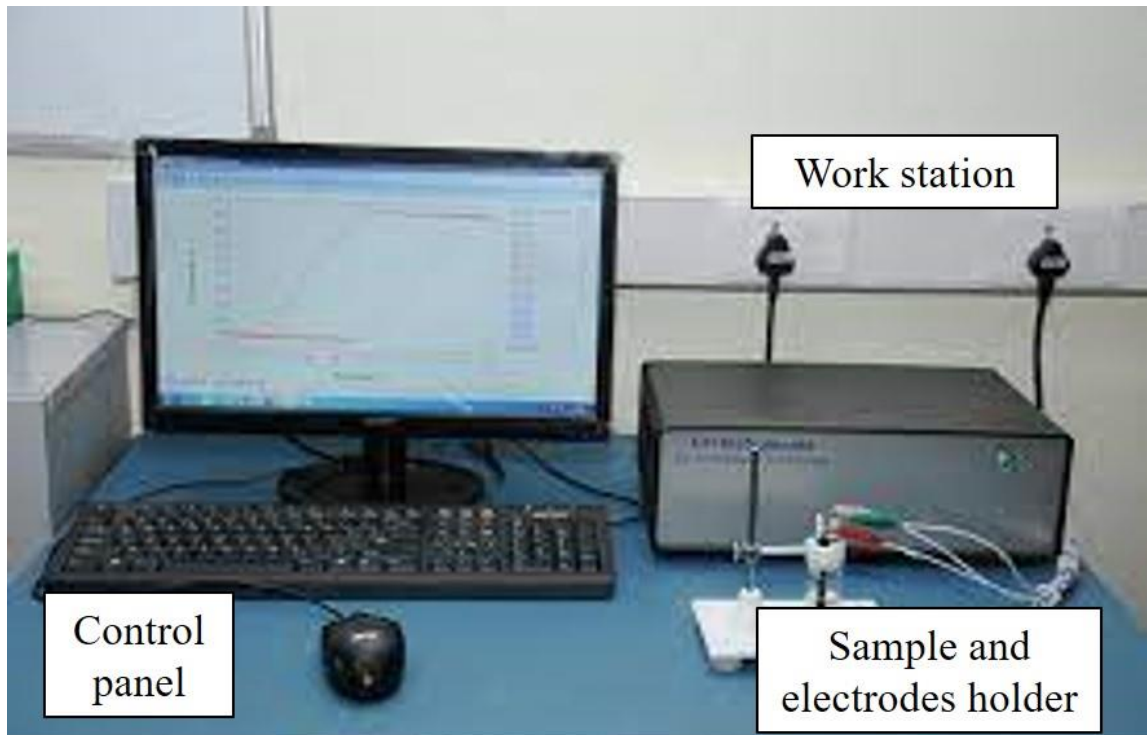


Figure 3.13: Electrochemical workstation

Electrochemical impedance spectroscopy was performed according to ASTM G 106 for all specimens to support Polarization Tafel curves. EIS technique is used to evaluate as-received base materials (AA5083-BM and AA6061-BM) and FSWed AA5083-AA6061 joints corrosion resistance in corrosive environments. EIS measures the impedance of the specimens at different frequencies. Electrochemical impedance spectroscopy (EIS) test was conducted at frequencies ranging from 0.01 Hz to 100 kHz and at an amplitude of 0.005 V. The test surfaces were analyzed using OM after the PDP test on every specimen correlating with potentiodynamic curves as well as corrosion rate measurements.

CHAPTER 4

RESULTS AND DISCUSSION

4.1 Mechanical and corrosion behavior of friction stir welded 5083-6061 aluminium alloy joints: Effect of base material position

4.1.1 Introduction

The main objective of the work is to improve the mechanical and corrosion properties of the dissimilar FSWed AA5083-6061 aluminium alloys by understanding the effect of using different techniques. This chapter investigates microstructure characteristics, mechanical and corrosion properties of friction stir welded dissimilar AA5083-AA6061 joints by changing base material location (AA5083-AA6061 and AA6061-AA5083) and these joints were also compared with similar joints of the two base materials (AA6061-AA6061 and AA5083-AA5083). There were quite a few studies in FSW of aluminium alloys; both AA5083-H111 and AA6061-T6 were studied extensively as similar alloys, very few studies were on dissimilar alloy joints. The placements of base materials of dissimilar FSWed joints on the advancing (AS) or retreating side (RS) may affect the material flow and micro-structural homogeneity in the joint because of their varying mechanical qualities (such as strength/hardness, ductility and deformation) and thermophysical properties (specific heat and thermal conductivity). Therefore the location of the material has a significant effect on the material flow, microstructure and joint properties (such as hardness, tensile strength and corrosion resistance) during the FSW process. We attempted to fill the gap in knowledge about these alloys as dissimilar FSWed joints by contributing knowledge on similar and dissimilar joints of AA5083-H111 and AA6061-T6. However, in the open literature, the effect of the position of base materials on mechanical and corrosion behavior, to the best of the author's knowledge, has not been noticed. The microhardness, mechanical properties and corrosion behavior of the similar and dissimilar AA5083-AA6061 FSWed joints were evaluated for completeness of the study.

4.1.2 Experimental Methodology

A numerically controlled FSW machine (RV Machine tools, FSW-3T-NC, India) was used to butt weld AA5083-H111 and AA6061-T6 of 300 mm x 70mm x 6mm dimensions along the rolling direction as shown in **Figure 4.1b**. The tool rotational speed of 800 rpm and traverse speed of 40 mm/min of the FSW process were kept constant. As illustrated in **Figure 4.1a**, a tool made up of H13 tool steel of tapered threaded conical pin profile with shown dimensions and with 3° concavity at the shoulder is utilized. Throughout the experiments, the tool plunge depth of 0.2 mm and 1° tilt angle were maintained. The samples were labeled according to the position of the material. For example, AA5083-AA5083 represents a sample with a similar joint of AA5083 and AA5083-AA6061 represents a sample with a dissimilar joint with AA5083 on AS and AA6061 on RS. The microstructural samples were sliced in the perpendicular direction of the weld direction. Microstructure testing was conducted using optical (OM) (Huvitz co Ltd, HRM300, South Korea), scanning microscope electron (SEM) with energy dispersion spectroscopy (EDS) (Vega 3 LMU, Tescan, France) and scattered electron back diffraction (EBSD) (FEI, Quanta 3D-FEGTM). To confirm the existence of intermetallic phases, the X-ray diffraction (XRD) (PANalytical, X'Pert Powder XRD, Netherlands) technique was also used. The Vickers microhardness (Chennai metco, Economet VH-1, India) of the welded specimens was measured in the mid thickness of the joint transverse cross-section. The transverse tensile specimens were prepared as per ASTM E8M-04 standard as shown in **Figure 4.1c**. Tensile tests were performed using a 100 kN capacity universal testing machine (UTM) (Fine spray, M-100, India) in a displacement-controlled mode with a 0.5 mm/min crosshead speed. SEM was used to examine the fracture characteristics. OCP, PDP and EIS tests were conducted for electrochemical corrosion measurement (CH Instruments, 604e, USA).

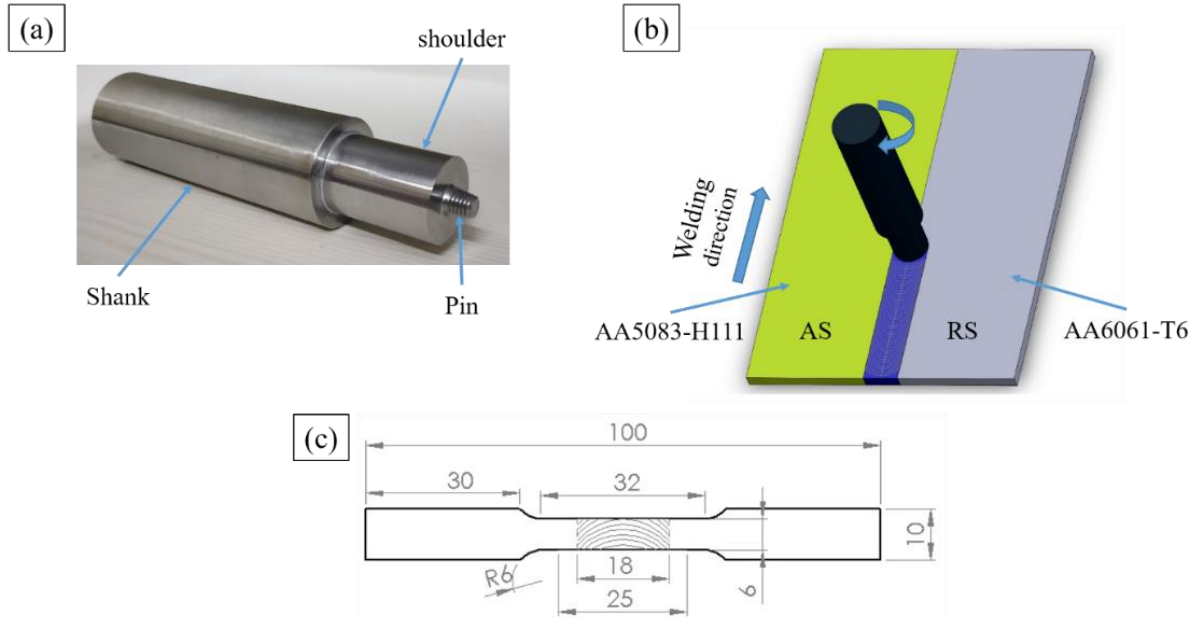


Figure 4.1: (a) FSW tool, (b) FSW schematic illustration, (c) Tensile specimen Schematic.

4.1.3 Microstructure characterization

4.1.3.1 Optical Microscopy

FSW successfully joined the different combinations of AA5083 and AA6061. Figure 4.2 shows the cross-sectional images of the different combinations of FSWed joints showing different zones across the joint. All of the joints formed at the given process settings are defect-free, as shown in Figure 4.2. This implies that chosen FSW process conditions resulted in satisfactory heat output. Defective joints can be caused by high heat input generated using a faster rotational rate and a slow welding speed. The nugget zone of a friction stir welded AA5083-AA5083 joints has a complicated form and ring pattern, as shown in **Figure 4.2a**. The ring pattern is well developed in the stir zone's core, whereas the boundary between SZ and TMAZ is better defined on AS of the weld (to the left in **Figure 4.2**). This is due to the tool's movement and rotational direction. Whereas, AA6061-AA6061 joint showed clear areas of TMAZ on both AS and RS (**Figure 4.2b**).

Furthermore, the dissimilar AA5083-AA6061 welded joint SZ consists of two types of materials, the major among them is one from AA5083 of the AS (**Figure 4.2c**). This is primarily due to FSW material flow from AS to RS. In the stir zone, AA5083 looked darker colored than AA6061 due to the difference in etching responses of each material. More light-colored patches are believed to be AA6061, resulting in a significant fraction in the stir zone when AA6061 was fixed on the AS (**Figure 4.2d**). When AA5083 was placed on the AS, the stir zones microstructure was mostly made up of AA5083. As a result, the macrostructure of the stir zone was determined mainly by the material placed on the AS and some of the material on the RS.

The mechanical and corrosion characteristics of the FSWed AA5083-AA6061 dissimilar joints are significantly different due to this, as will be explained in the following sections.

The microstructures of AA5083-AA6061 FSWed joint at different locations are shown in Figure 4.3. Microstructural pictures of the base materials are shown in **Figure 4.3a** and **f**. The grains in both base materials are elongated with average grain size for AA5083 and AA6061 of $30\pm25\ \mu\text{m}$ and $103\pm35\ \mu\text{m}$ respectively, along the rolling direction. The FSWed joints HAZ of AS and RS are shown in **Figure 4.3b** and **e**, respectively. Grain coarsening occurred throughout the FSW process in both base materials, with grain sizes of $39\pm13\ \mu\text{m}$ and $121\pm15\ \mu\text{m}$, respectively, attributable to the thermal cycle at HAZ. TMAZ was formed due to mechanical deformation and frictional heating, with the grains appearing refined slightly and extended upwards, as illustrated in **Figure 4.3c**. Due to intense plastic deformation, the stir zones of welded joints have more refined grain structures (**Figure 4.3d**).

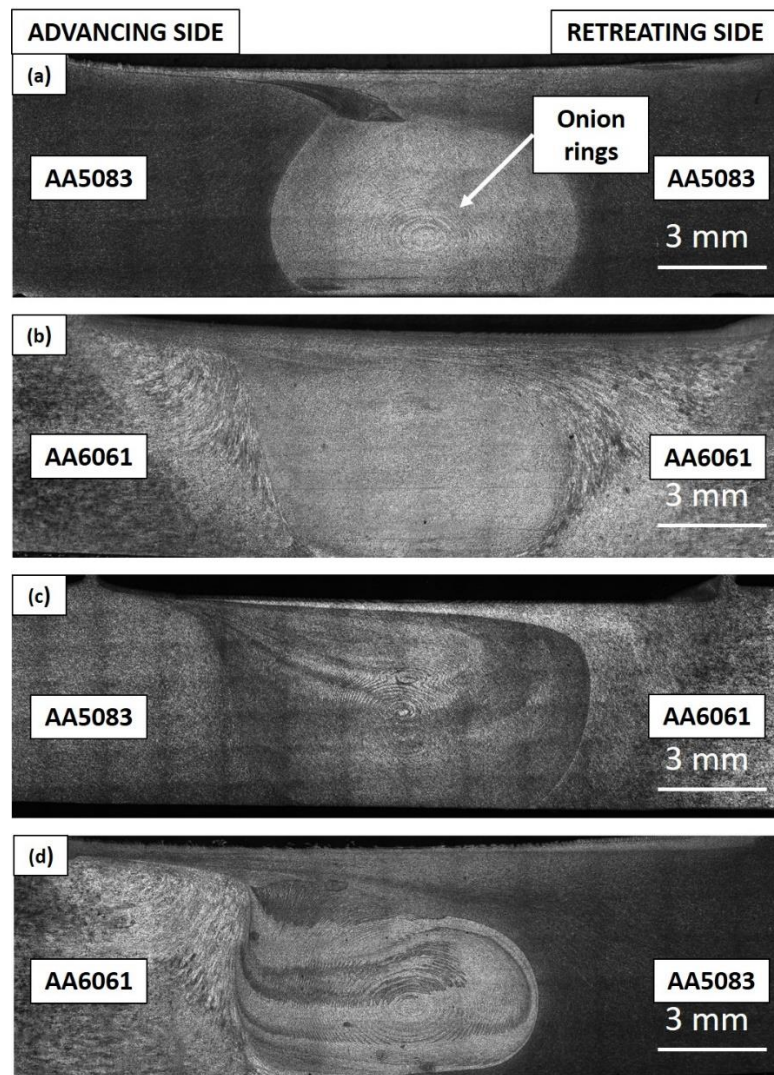


Figure 4.2: Macrostructure images of: (a) AA5083-AA5083, (b) AA6061-AA6061, (c) AA5083-AA6061, and (d) AA6061-AA5083.

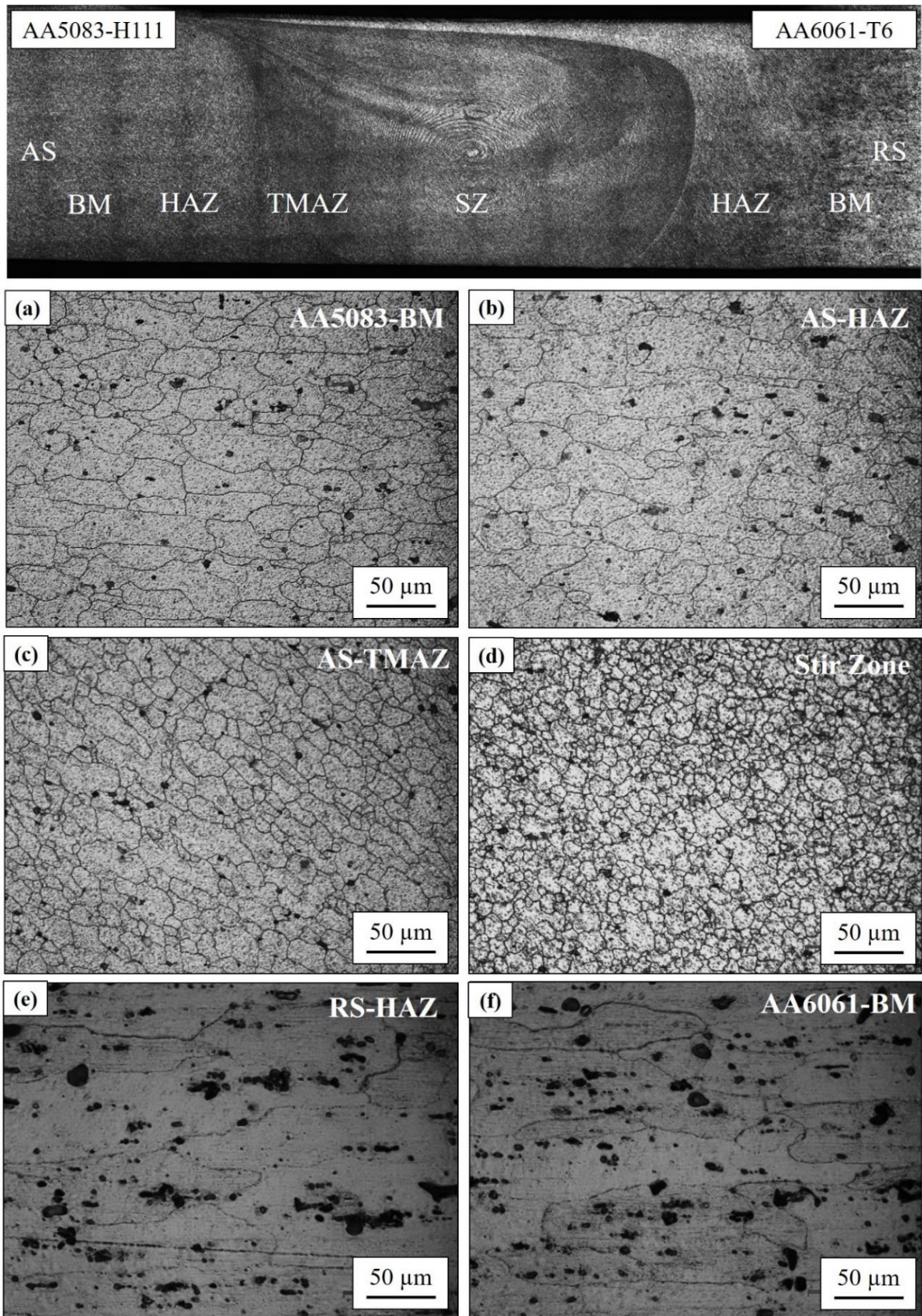


Figure 4.3: Microstructure images of the AA5083-AA6061 sample condition: (a) AA5083-BM, (b) AS-HAZ, (c) AS-TMAZ, (d) SZ, (e) RS-HAZ and (f) AA6061-BM along with the macrostructure.

4.1.3.2 Electron back scattered diffraction

The grain structure maps and distribution of the misorientation angle of BMs and AA5083-AA6061 joint are shown in **Figure 4.4** and **Figure 4.5**. The statistical data from the EBSD results are shown in **Table 4.1**. The rolling process results in lath-shaped grains in AA5083 and AA6061 BM (**Figure 4.4a** and **b**). Grain refinement was attained in all FSWed joints because grain refining was exclusively due to dynamic recrystallization [[Kumar et al., \(2021\)](#)]. The EBSD image of the AA5083-AA6061dissimilar joint is shown in **Figure 4.4c**. Both BMs have a high percentage of Low angle grain boundaries (LAGBS), indicating that they are substantially deformed in as-received conditions (**Figure 4.5a and b**). The volume proportion of HAGBs increases following FSW, based on the misorientation angle distribution (**Figure 4.5c**). In newly formed grains with a substantial number of HAGBs, a process of significant grain rotation and severe deformation ensues, as seen in **Figure 4.5c**.

Table 4.1: EBSD results

Sample condition	Grain size (μm)	Fraction of grain boundaries (%)	
		LABs	HABs
AA5083-BM	27.5±10.5	91.8	8.2
AA6061-BM	103.9±23.5	86.0	14.0
AA5083-AA6061	7.1±4.2	37.9	62.1

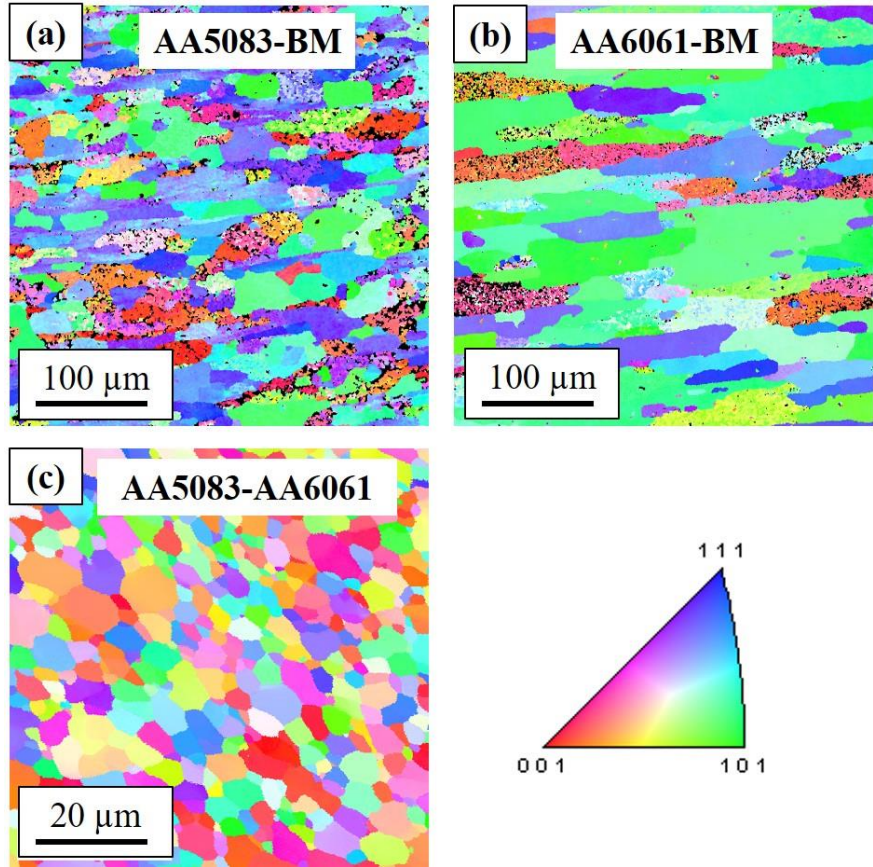


Figure 4.4: The inverse pole figure in Z direction of (a) AA5083-BM, (b) AA6061-BM and (c) AA5083-AA6061-SZ.

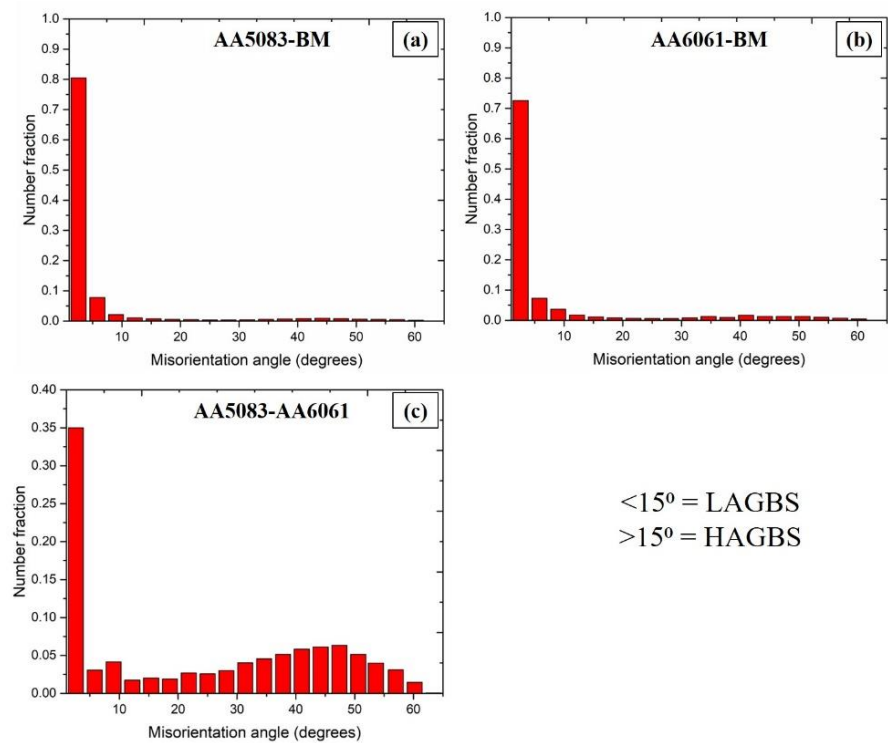


Figure 4.5: The distributions of misorientation angle distribution of: (a) AA5083-BM, (b) AA6061-BM, and (c) AA5083-AA6061-SZ.

4.1.3.3 Scanning electron microscopy

The onion ring sub-layer in **Figure 4.6** is seen as a dark and bright color, attributed to Keller's reagent's differential etching response of two base materials. According to the EDS, as shown in Figures c and d, the AA5083 alloy has a dark color, whereas the AA6061 alloy has a bright color. Furthermore, the onion ring sub-layer forms three different regions consisting of AA6061 sub-layer, AA5083 sub-layer, and mixed sub-layer. The production of the AA5083 and AA6061 sub-layers is rather frequent, however, the formation of the mixed zone is owing to the vigorous stirring induced using selected pin profile, which allows for intense mixing.

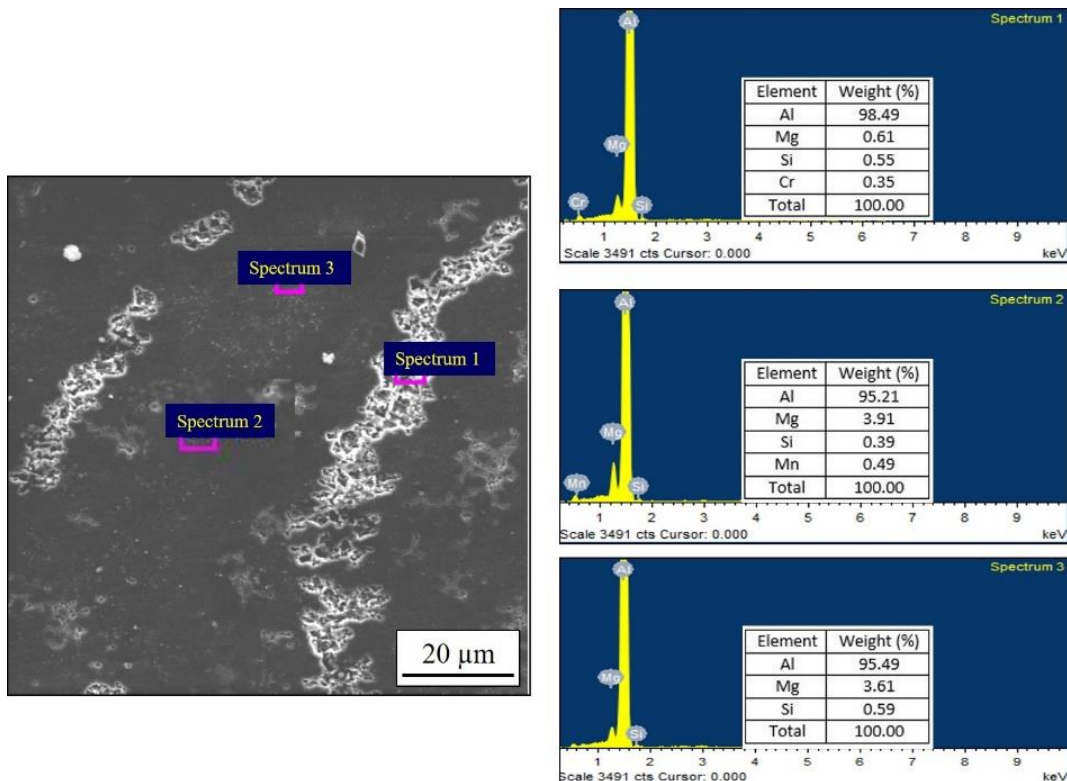


Figure 4.6: SEM picture and EDS spectrum of the FSWed AA5083-AA6061 joint's onion ring sub-layers.

SEM pictures of the as-received base materials and FSWed joints at various process settings are shown in **Figure 4.7**, **Figure 4.8** and **Figure 4.9**, along with the EDS analyses. AA5083-H111 contains two main intermetallics in terms of constituent elements (**Figure 4.7a**). As demonstrated in the EDS spectrum, the intermetallics in BM comprise Al (Fe, Mn, Mg/Si) phase and Al-Mg phase (**Figure 4.7b** and **c**). Al (Fe, Mn, Si) and Mg-Si are the most prevalent precipitates of AA6061-T6 alloy (Figure 4.8a-c) [Kartsonakis et al., (2016)]. SEM images of AA5083-AA5083, AA6061-AA6061, AA5083-A6061 and AA6061-AA5083 conditions are shown in Figure 4.9a-d. At temperatures 175 to 250 °C, the phase (Al_3Mg_2) will precipitate from the AA5083 matrix during the welding process [Choi et al., (2013)]. During normal FSW

of Al alloys, the peak temperature in the NZ has been reported to reach above 450 °C. As a result, due to elevated temperature and severe plastic deformation, phase particles precipitated from the matrix (Al_3Mg_2) are majorly dissolved and very little are precipitated in the grain boundaries. The production of precipitate particles in AA5xxx series Al alloys, which are solution-strengthened, will result in a slight loss of strength after FSW. Meanwhile, because of the substantial annealing impact during the FSW thermal cycle, the high density of dislocations were also mostly eliminated. Furthermore, the stirring action of a pin in the SZ causes the fragmentation of coarse $\text{Al}_6(\text{Mn, Fe})$ intermetallics present in AA5083-BM into the very smaller particles distributed over the SZ (**Figure 4.9a**).

In the AA6061-AA6061 joint, the size of iron and silicon particles in the SZ is smaller in the BM region, according to **Figure 4.9b**. The pin collided with the intermetallic particles in the SZ region and spread them across the Al matrix. The SZ of the AA6061-AA6061 joint has a higher number of intermetallics particles (such as Al-Fe-Si) than the BM region but a lower volume proportion. The corrosion resistance of weldments is primarily influenced by the composition density and distribution of these intermetallic particles.

Comparison of **Figure 4.9c** and **d** shows that the AA5083 distribution in the stir zone of the AA6061-AA5083 joint is non-uniform, whereas it is uniformly spread in the AA5083-AA6061 joint. The AA5083 distribution in the stir zone of the AA5083-AA6061 joint conforms to the continuous onion ring. The EDS examination of the AA5083-AA6061 sample reveals that the intermetallic phases in positions 1, 2, and 3 are Al (Fe, Mn), Al-Fe-Si, and Al-Mg (Donatus et al. 2015). The AA5083 content of the dark-colored onion ring is much higher than that of the light-colored onion ring, as shown in **Figure 4.9c**. Therefore, the significant intermetallic spread over the SZ in AA5083-AA6061 is observed to $\text{Al}_6(\text{Mn, Fe})$ and Al-Fe-Si in case of the AA6061-AA5083 dissimilarity joint.

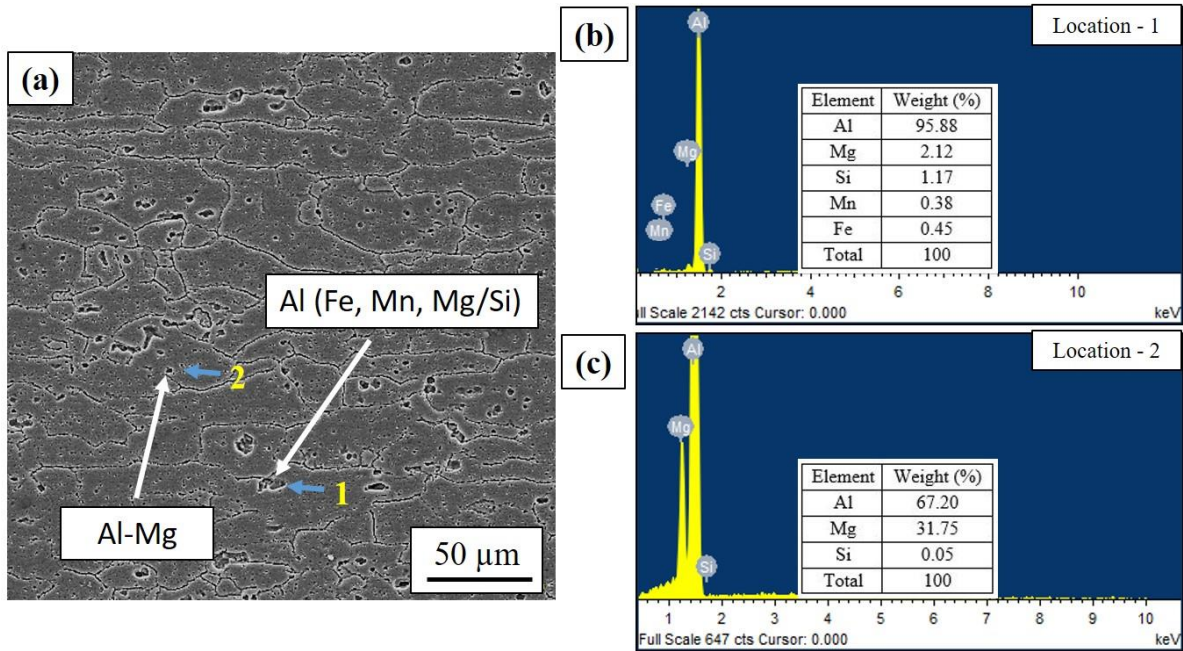


Figure 4.7: (a) SEM image of AA5083-H111, (b) EDS spectrum at location 1 and (c) EDS at location 2.

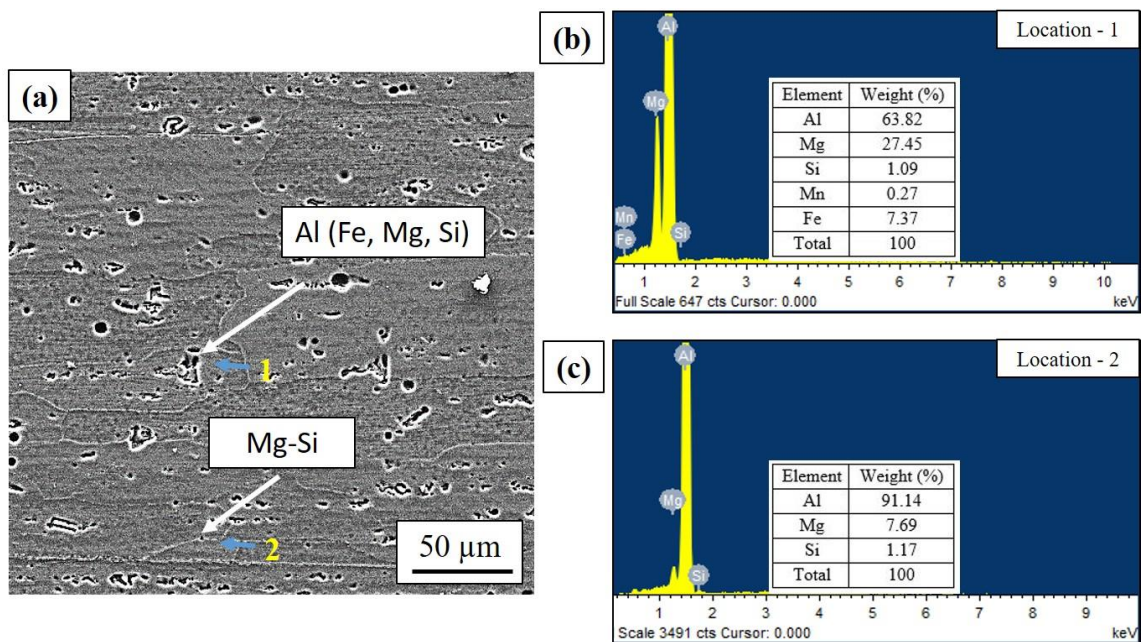


Figure 4.8: (a) SEM of AA6061-T6, (b) EDS spectrum at location 1 and (c) EDS spectrum at location 2.

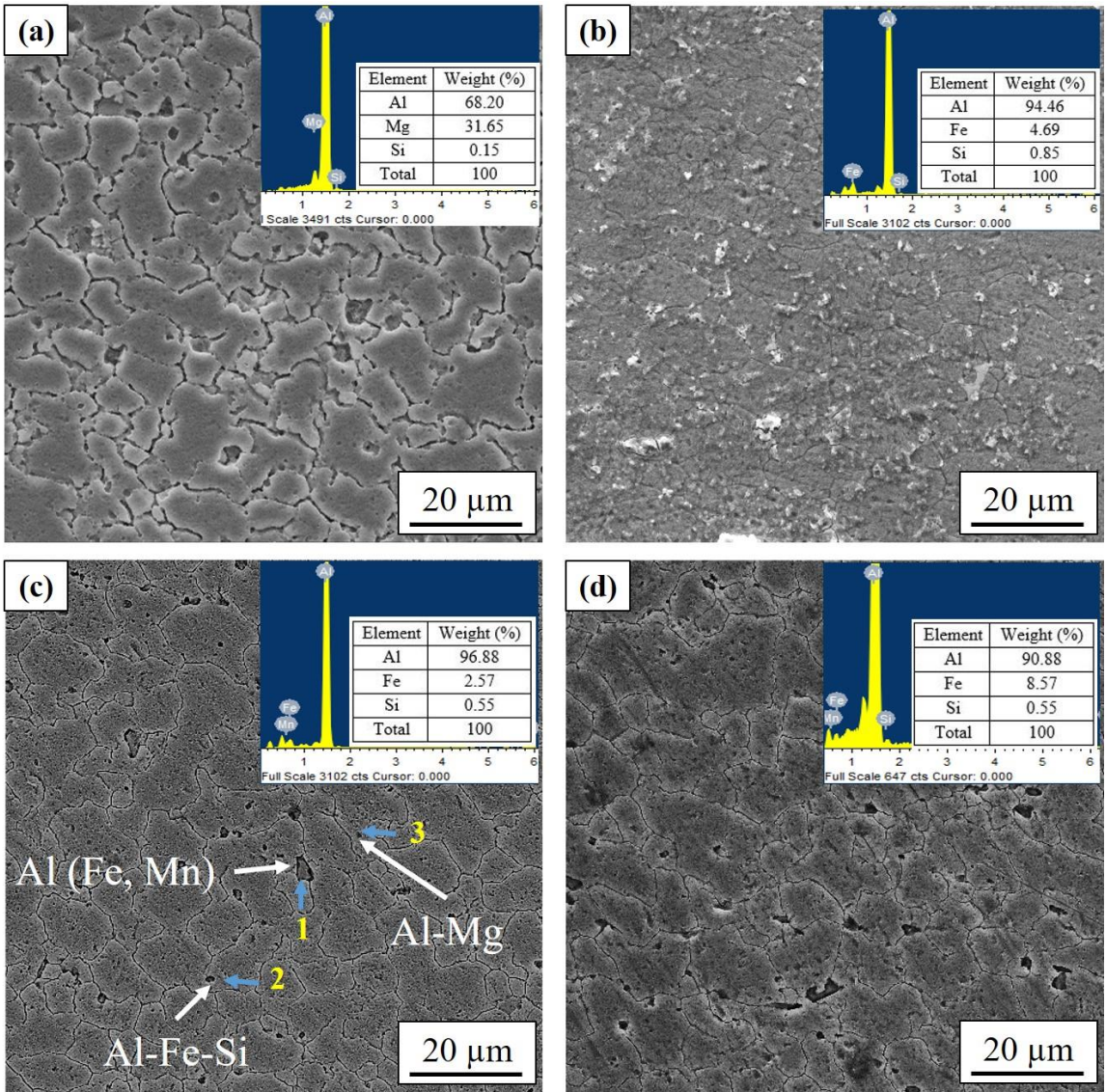


Figure 4.9: SEM with EDS images at the SZ: (a) AA5083-AA5083, b) AA6061-AA6061, (c) AA5083-AA6061 and (d) AA6061-AA5083.

4.1.4 Phase analysis

X-ray diffraction (XRD) patterns of each sample are shown in **Figure 4.10**. The intermetallics detected in AA5083 were AlFe_2Mn and Al_3Mg_2 . Similarly, Mg_2Si and $\text{Al}_{19}\text{Fe}_4\text{MnSi}$ are detected in AA6061. After FSW, both the number and the intensity of Al_6FeMn diffraction peaks decrease. Furthermore, the intensity of $\beta\text{-Al}_3\text{Mg}_2$ diffraction peaks in FSW of AA5083-AA5083 is lower compared with the AA5083-BM. The intermetallic phase identified in the AA6061-AA6061 joint is a $\beta\text{-Mg}_2\text{Si}$ and the second one is identified as $\text{Al}_{19}\text{Fe}_4\text{MnSi}$ particles. The heat generated in the FSW process promotes diffusion between the base alloys, allowing unique intermetallic compounds to develop in the dissimilar FSWed joints. The four phases were detected at SZ, including Al_3Mg_2 , Mg_2Si , $\text{Al}_6(\text{Mn, Fe})$ and

$\text{Al}_2\text{Fe}_3\text{Si}_4$. The strengthening precipitate Mg_2Si which was not detected in SEM of the dissimilar joint was also observed here.

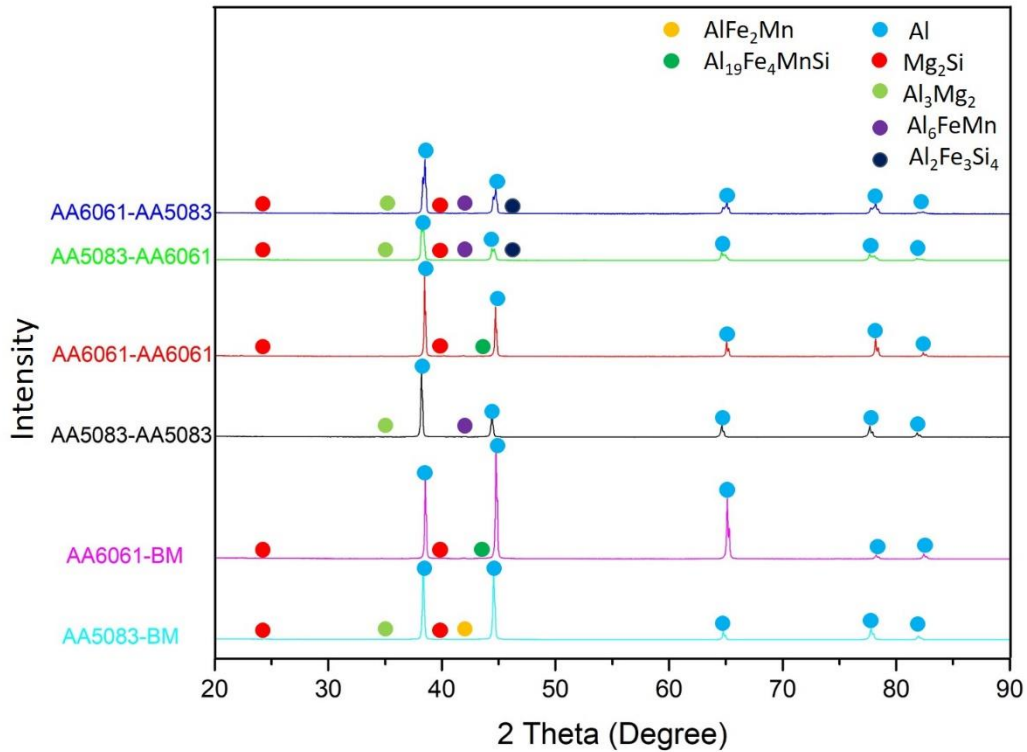


Figure 4.10: Base materials and FSWed samples XRD peaks.

4.1.5 Mechanical properties

4.1.5.1 Hardness

Microhardness tests transverse to the weld direction were done to assess the mechanical property heterogeneity across the welds, as shown in **Figure 4.11**. The average microhardness values of 87.6 HV and 84.5 HV have been obtained for the as-received AA5083 and AA6061 base alloy. The rapid strain rate deformation and high temperatures during the welding process can generate significant microstructural changes that alter the material's hardness profile (**Figure 4.11a**). The weld (the SZ, The TMAZ, and the HAZ) had a lower hardness than the base material (average hardness of about 87.6 HV); the SZ had an average hardness of around 83.5 HV. The minimum hardness zone was found at the SZ, not at the HAZ, as determined by examining the hardness profile and comparing it to the observed microstructure (**Figure 4.3**).

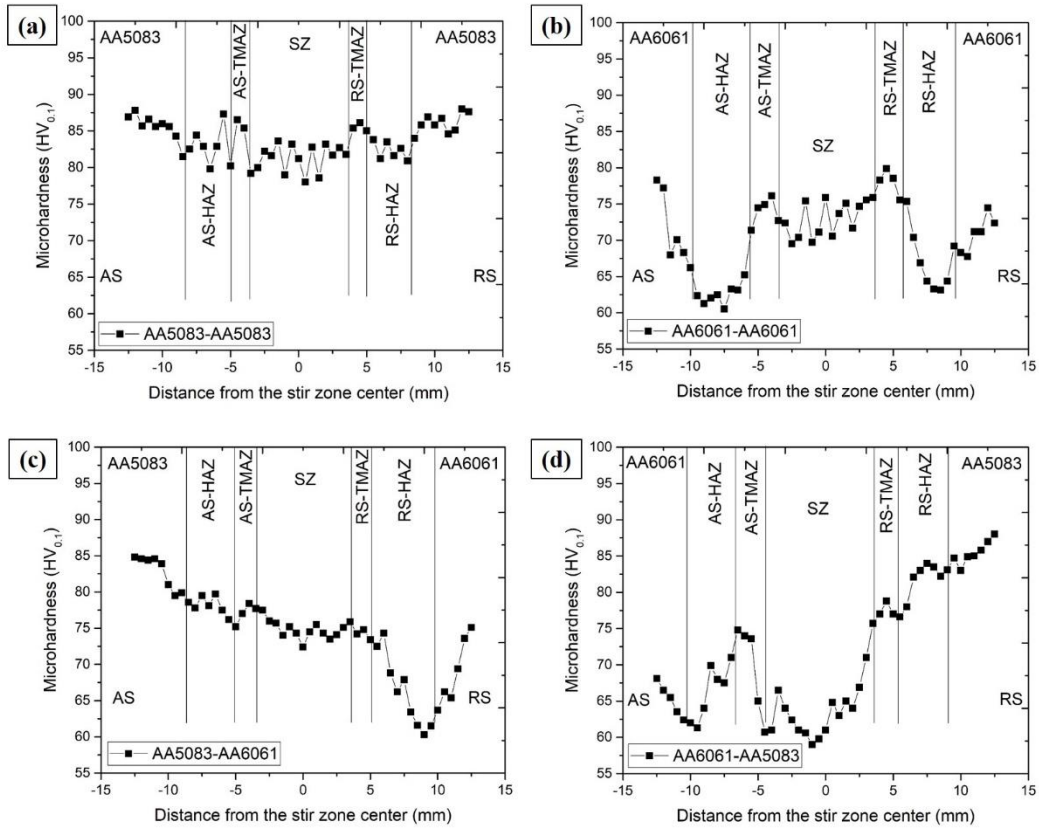


Figure 4.11: Microhardness across the transverse cross section of FSWed joints: (a) AA5083-AA5083, (b) AA6061-AA6061, (c) AA5083-AA6061 and (d) AA6061-AA5083

The hardness distribution of the AA6061-AA6061 joint is as shown in **Figure 4.11b**. Softening was seen in both SZ and HAZ, with SZ (~72HV) having lower hardness than BM (~84.5 HV) and HAZ (59 HV) having the lowest hardness. The finer the grains, the higher the hardness, according to the Hall-Petch formula. However, in SZ, although the smaller grain size, the hardness was lower than that of BM. On the one hand, welding defects in SZ cause poor conduct; on the other hand, it was discovered that the temperature field primarily determines the severity of thermal softening in HAZ and SZ and due to which the dissolution or partial dissolution of hardening precipitates occurs in SZ and HAZ [Malopheyev et al., (2016)]. This could be due to the disintegration of Mg_2Si precipitates during the welding process, which reduces hardness and strength. AA6061-T6 are heat treatable Al-Mg-Si alloys that form Mg-Si typed hardening precipitates after T6 heat treatment. During FSW, the temperature in SZ is reached around 500 °C. Mg_2Si dissolve at this temperature, and hardness reduces as a result.

In the case of both AA5083-AA6061 (**Figure 4.11c**) and AA6061-AA5083 (**Figure 4.11d**) joints, the HAZ of the AA6061-T6 side was found to have the lowest microhardness value due to the dissolution or partial dissolution of hardening precipitates caused by the weld thermal cycle. For the AA6061-AA5083 joint, according to the results of the microhardness

analysis of the AA6061-AA6061 joint, the asymmetry of the hardness values along the SZ has been substantial, most likely due to insignificant inter-mixing of materials from the AS in the SZ during FSW, as also discussed in **section 4.1.3.1**.

4.1.5.2 Tensile

The tensile stress-strain curves of the samples obtained in transverse and longitudinal cross-sections under different conditions are shown in **Figure 4.12**. The tensile properties of the BM and various FSW samples are shown in **Table 4.2**. Very high UTS of 311 MPa together with a relatively high elongation of 11.7% were achieved in the AA5083-BM, attributable to severe work hardening. Under welding conditions, the UTS of the AA5083-AA5083 sample obtained is 190 MPa, with an elongation of 4.72% due to the weld softening caused by the weld thermal cycle in the SZ.

In AA6061-AA6061, a minimum in hardness was noted at 9 ± 2 mm from the weld centerline. The UTS dropped from 296 to 188 MPa, and the TE of the joint reduced noticeably. As demonstrated in **Figure 4.3**, the microstructure of the base material was relatively homogeneous, but the microstructure and hardness of the FSW joint varied across the welded zone. As a result, during deformation, the weak HAZ local strain tends to accumulate, resulting in a decrease in total specimen elongation. That is why the UTS and YS of FSW joints were much below those of the base materials.

The deformation during the tensile test of dissimilar welded joints (AA5083-AA6061 and AA6061-AA5083) was focused at the HAZ of the AA6061 side, which corresponds to the weakest zone among all zones of welded joints. At this zone, the failure occurred in both cases of a dissimilar joint. Tensile strength in dissimilar aluminium alloys is governed by defect-free welding, intermixing, and dissolution of precipitates. The highest value of UTS (~183 MPa) was obtained in AA5083-AA6061 compared to the other AA6061-AA5083 dissimilar joint. To find the effect of the mixing behavior of two alloys at the SZ on tensile properties. The tensile test was conducted in the longitudinal FSW direction for all the joints and plotted as shown in **Figure 4.12b**. It was observed that the UTS measured was higher than the YS and UTS measured transverse to the FSW directions as listed in **Table 4.2**, due to the fine grain structure at the SZ covering the whole gauge length as discussed in **Section 4.1.3**.

Table 4.2: Similar and dissimilar FSWed sample conditions tensile characteristics

Sample condition	Yield strength (MPa)	Ultimate tensile strength (MPa)	Tensile elongation (%)	Joint efficiency (%)	Fracture Location
AA5083-BM	175 \pm 4	325 \pm 5	11.7 \pm 0.4	-	-
AA6061-BM	226 \pm 5	294 \pm 3	10.1 \pm 0.5	-	-
AA5083-AA5083-T	154 \pm 2	190 \pm 2	4.0 \pm 0.2	61.24	RS (HAZ)
AA6061-AA6061-T	157 \pm 1	188 \pm 1	3.9 \pm 0.2	63.94	AS (HAZ)
AA5083-AA6061-T	156 \pm 3	183 \pm 2	3.8 \pm 0.3	62.24	SZ
AA6061-AA5083-T	159 \pm 3	175 \pm 2	4.2 \pm 0.3	59.52	RS (HAZ)
AA5083-AA5083-L	158 \pm 1	309 \pm 1	12.2 \pm 0.3	91.38	-
AA6061-AA6061-L	157 \pm 1	220 \pm 3	9.4 \pm 0.2	74.07	-
AA5083-AA6061-L	156 \pm 2	247 \pm 2	9.7 \pm 0.2	83.16	-
AA6061-AA5083-L	155 \pm 3	231 \pm 1	8.7 \pm 0.3	77.77	-

The AA5083-AA6061 joint showed the YS and UTS higher than that of the AA6061-AA5083 joint for the longitudinal FSW samples. For transverse tensile specimens, the AA5083-AA6061 joint showed almost the same tensile strength as the AA6061-AA5083 joint, as shown in **Table 4.2**. Also, for the transverse tensile FSW samples, the TE of the AA5083-AA6061 and AA6061-AA5083 joints were entirely compatible with each other. Moreover, when a longitudinal test of the FSW joint is done, the tensile elongations of the samples almost reach that of base materials. It is observed that the longitudinal strength of the dissimilar joints is more significant in the case of the similar joint having high strength that was placed to the advancing side (AA5083-AA6061) during the FSW.

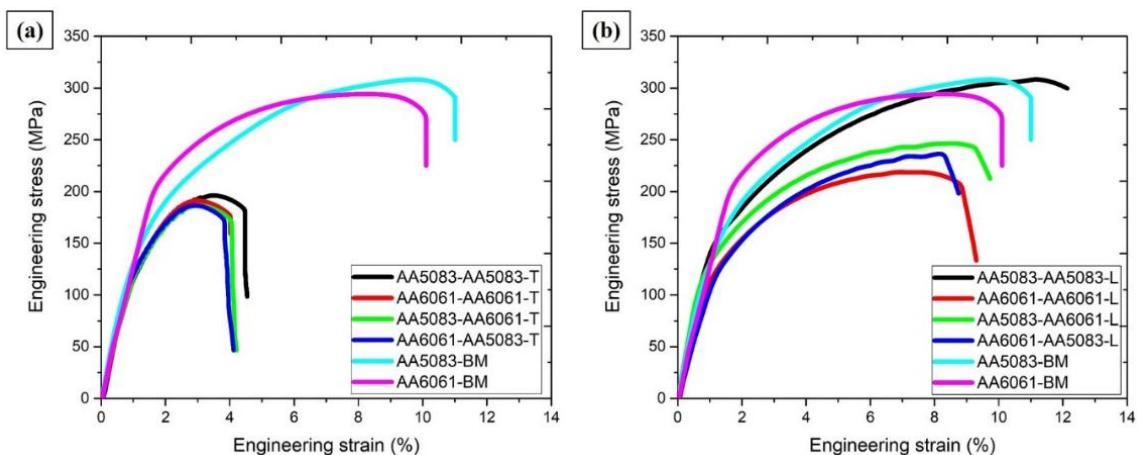


Figure 4.12: strain-strain curves of the base material and FSWed samples.

4.1.6 Corrosion studies

Figure 4.13a and **b** show the PDP plots of the as-received base materials and FSWed samples of similar and dissimilar combinations. **Table 4.3** shows the test's corrosion potential (E_{corr}) and corrosion current density (i_{corr}) output values derived from PDP curves. In general, E_{corr} represents the sample's corrosion tendency, while i_{corr} values represent the corrosion rate. It is observed that the two base materials E_{corr} variation was approximately 144 mV, implying that galvanic corrosion could occur in the event of dissimilar FSWed joints [Schneider et al., (2014)].

On the one hand, the Al-Mg phase intermetallic present in as received AA5083-BM cause corrosion [Goswami et al., (2010)]. On the other hand, the more refined grains at SZ and dissolution of Al_3Mg_2 precipitates at elevated temperature leads to better corrosion resistance in the AA5083-AA5083 joint than BM (**Figure 4.13**). The cathodic current density of the base alloys was double that of the AA5083-AA5083 weld, indicating a higher corrosion rate. The corrosion in 6XXX alloys is mainly due to Fe-enriched phases and Mg-Si particles [Blanc et al., (1997)] and [Mehdizade et al., (2020)]. The influence of microstructure on corrosion rate is substantial and a secondary phase's corrosion potential differs from that of its parent phase. These differential potential values cause the creation of a galvanic cell. Precipitates rich in Fe and Si are prominent examples. Corrosion cells arise due to their potential differences with the matrix, as detailed in **Section 4.1.3**. More cathodic reactions occur when these precipitates are present in larger quantities. Therefore the corrosion resistance of the AA6061-AA6061 FSWed joint was lower than AA6061-BM, as also observed in the study by Fahimpour et al., (2012).

Al (Fe, Mn), Al-Fe-Si, and Al-Mg are the intermetallic phases that form in the FSW of dissimilar AA5083-AA6061. Since the SZ is a mixture of AA5083 and AA6061, as discussed in section 4.1.3. Because the AA6061-T6 rich zones are cathodic to the AA5083-H111 rich zones, the corrosion attack begins galvanically at the borders and spreads into AA5083 rich zones. The attack is more localized in the region where Fe is present, acting as a cathode with aluminium matrix and causing galvanic corrosion with the surrounding matrix. The Fe-based intermetallic in AA5083-AA6061 is lower than compared to AA6061-AA5083 and because of which less galvanic corrosion occurrence in this joint. **Figure 4.14** shows the corroded surface of base materials and FSWed samples following the PDP test. Based on the images displayed in **Figure 4.14a** and **b**, it was found that the surface of the AA6061-T6 base material had the least number of pits. **Figures 4.14c** and **d** illustrated that the AA6061-AA6061 joint had a more severe corrosion attack than the AA5083-AA5083 joints. This corrosion attack was decreased and turned into uniform corrosion with the AA5083-base material on the advancing side

(Figure 4.14e). The AA6061-AA5083 joint had extensive corrosion attacks throughout the SZ **(Figure 4.14f).** According to the corrosion current density values, the PDP test surfaces showed a similar level of corrosion attack to the weld samples. In contrast, the base materials surfaces showed a lower level of corrosion attack. The corrosion susceptibility obtained at different combinations was also analyzed using Nyquist plots of different conditions, as shown in **Figure 4.13c.** On the x-axis, the Nyquist plot shows a real part of impedance (Z_{re}) and an imaginary component of impedance (Z_{im}) on the y-axis. The Nyquist plots of all samples have similar shapes, indicating a similar process with the only variance in impedance magnitude. Corrosion resistance is proportional to the size of the semi-circle obtained after the EIS test, with more giant diameter loops indicating stronger corrosion resistance. The AA5083-AA6061 condition had superior corrosion resistance than the AA6061-AA5083 junction, based on the PDP and EIS data. EIS validated the results of the PDP test in this investigation.

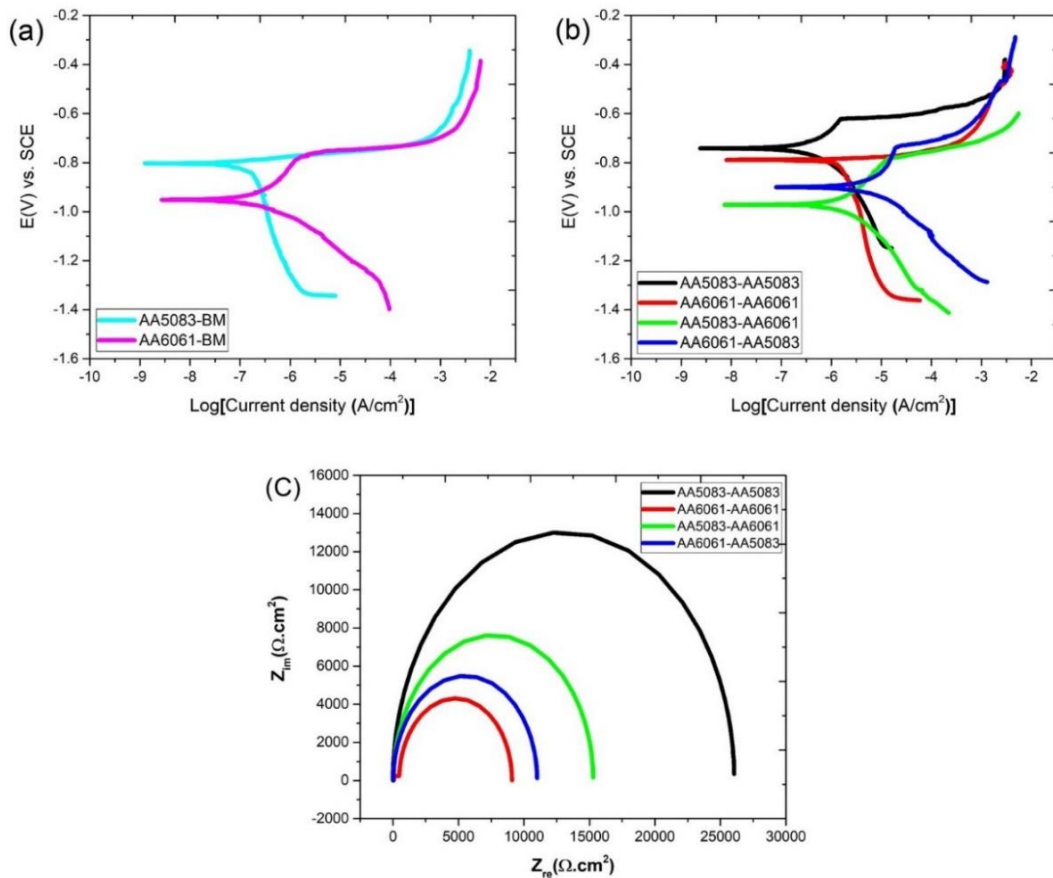


Figure 4.13: PDP curves of (a) as-received base materials (b) FSWed joints at different conditions (c) EIS plots of similar and dissimilar joints.

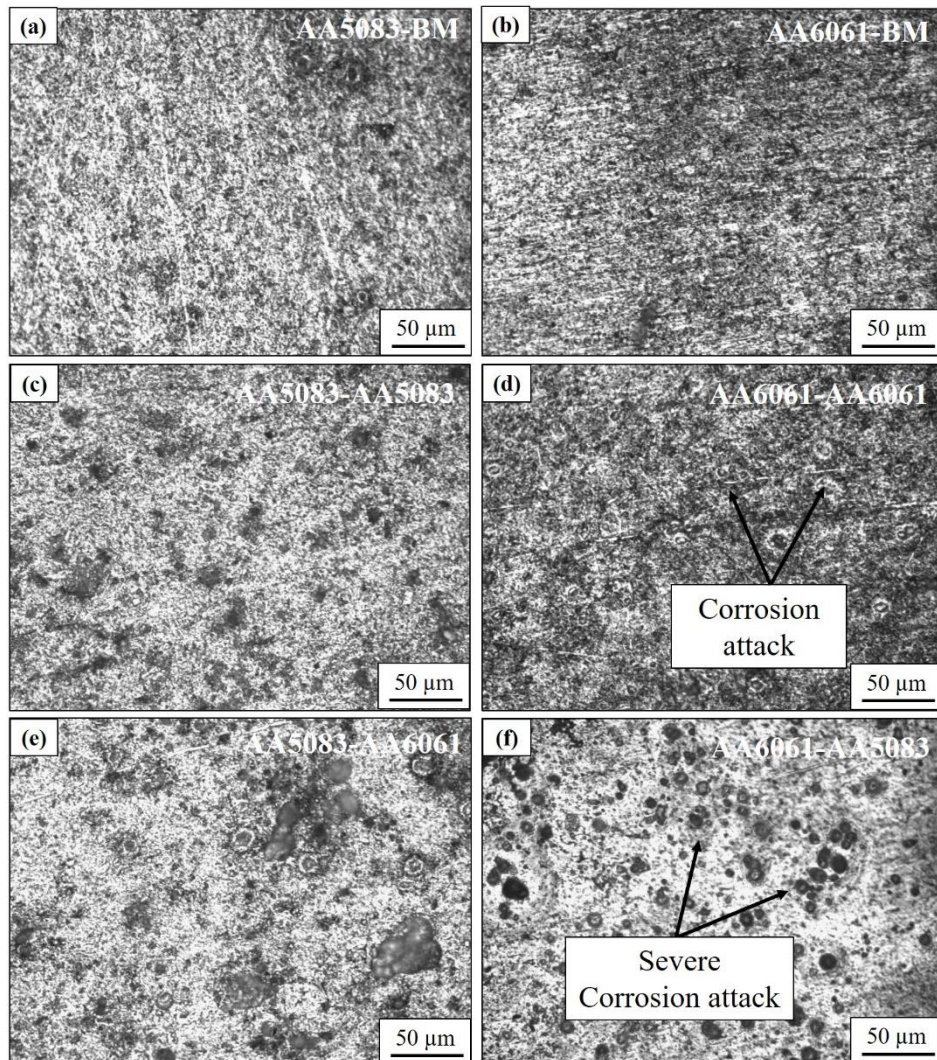


Figure 4.14: Optical micrograph images of: (a) AA5083-BM (b) AA6061-BM, (c) AA5083-AA5083, (d) AA6061-AA6061, (e) AA5083-AA6061 and (f) AA6061-AA5083.

Table 4.3: Corrosion potential and corrosion current density of the base materials and FSWed samples.

Sample conditions	Corrosion potential E_{corr} (mV (SCE))	Current density i_{corr} ($\mu A/cm^2$)
AA5083-BM	-804	0.12
AA6061-BM	-948	0.76
AA5083-AA5083	-739	0.06
AA6061-AA6061	-788	1.15
AA5083-AA6061	-970	1.36
AA6061-AA5083	-901	1.86

4.1.7 Summary

Similar and dissimilar joints of aluminum alloys were tested for the microstructural, mechanical and electrochemical properties of friction stir 5083-H111 to 6061-T6. The mechanical effects and corrosion resistance of the dissimilar joints of the base material position were examined.

During the welding process, significant microstructural changes contributed to the formation of different microstructural zones. EBSD at SZ showed that sub grain boundaries in grains collected misorientation and turned into LABs, subsequently transformed into HAB by continuous dynamic recrystallization, resulting in a fine and equiaxed microstructure. The materials were correctly mixed in the AA5083-AA6061 joint from AS and RS. In contrast, the bulk of the base metal in the AS was drawn into the stir zone and the materials were not adequately mixed in the AA6061-AA5083 joint for dissimilar aluminum alloys. The joint efficiency obtained by AA5083-AA5083 and AA6061-AA6061 is 61.24% and 63.94% respectively. The dissimilar joints exhibited UTS ranged between 183 and 175 MPa, with joint efficiency ranging between 62.24 and 59.54% relative to the strength of AA6061-BM. It should be noted that the longitudinal strength of the dissimilar joints is comparable to the strength of the similar joint that was placed to the advancing side during the FSW. According to the results of polarization curves and EIS plots, the corrosion resistance of SZs is similar to that of the base material on the advancing side, which should be attributed to the fact that the majority of SZs are composed of the AS base material.

4.2 Effect of friction stir welding parameters on the material flow, mechanical properties and corrosion behavior of dissimilar AA5083-AA6061 joints

4.2.1 Introduction

Further to the previous study demonstrating mechanical effects and corrosion resistance of the dissimilar joints by changing the base material position, the next step was to explore the role of process parameters on material flow, mechanical properties and corrosion behavior of dissimilar friction stir welds of AA5083-AA6061. Analysing the discussed literature, high tool rotational speed was contemplated to raise the strain rate to impact the recrystallization process. Higher traverse speeds were selected to reduce heat input to the weld and enhance the joint's cooling rates. This resulted in reduced intermixing and, lower microstructural transformation (such as re-precipitation, coarsening of precipitates, and intermetallics formation). Usually, welding parameters (rotational speed and traverse speed) are considered a key factor is impacting the flow of material during FSW. Local microstructural changes and modification of material characteristics locally are attributed to intense plastic flow at high thermal exposure during FSW. Thus, a good understanding of the process parameters of the friction stir welding process is of vital importance. Although the relationship between material flow and welding parameters has been stated in literature studies, the effect of material flow patterns obtained by using different welding parameters on joint performance has not been accounted for.

Furthermore, In general, while understanding the behaviour of FSWed joints, it is a common practice to analyse the quality of joints through tensile tests and hardness values measured across the transverse cross-section of the joints. However, to avoid catastrophic failure, it is also essential to understand the effects of welding parameters on both mechanical and corrosion behaviour of FSWed joints. Furthermore, limited research is available on the impact of process parameters on mechanical and corrosion behaviour of dissimilar friction stir welding of aluminium alloys. And, there is no literature available on material flow, mechanical properties and corrosion behaviour of dissimilar AA5083-AA6061 FSWed joint by varying process parameters to the best of the authors' knowledge. Therefore, a systematic study on enhancing mechanical properties and corrosion resistance at different FSW process parameters were essential. Hence, the present investigation aimed to study the effect of tool rotational speed and traverse speed on material flow, mechanical properties and corrosion behaviour. Thereby obtaining the optimized process parameters to determine the best mechanical properties and corrosion resistance of FSWed AA5083 -AA6061 dissimilar aluminium alloys.

4.2.2 Experimental Methodology

FSW joints were made by placing AA5083, AA6061 on the advancing side (AS), and retreating side (RS), respectively, using six different combinations of welding parameters (tool traverse and rotational speed). Initially, the joints were made using FSW at varying traverse speeds of 40, 60, and 80 mm/min by keeping rotational speed constant at 800 rpm. Later, joints were made at the different rotational speeds of 1100, 1400, and 1700 rpm, keeping traverse speed constant at 60 mm/min. The samples were named based on the process parameters selected. For example, 800-40 represents a sample at a rotational speed of 800 rpm rotational speed and 40 mm/min of traverse speed. A schematic representation of the FSW experiment, FSW tool with dimensions is shown in

Figure 4.15a and b. The samples for microstructural characterization were carried out using OM (optical microscopy), scanning electron microscope (SEM), with energy dispersion spectroscopy (EDS). The grain size was determined by image analysis using Image ‘J’ software. The transverse tensile and notch tensile samples were prepared as per ASTM E8M-04 standard and a schematic diagram of the dimensions is shown in **Figure 4.15c and d**. The notch tensile test was carried out for failure at the SZ to analyze the notch tensile strength behavior of FSWed joints. The corrosion behavior of FSWed joints at different process parameters was compared with that of base materials. The Potentio-dynamic polarization (PDP) test was carried out according to ASTM G3 standard using a three-electrode cell potentiostat. Electrochemical impedance spectroscopy (EIS) test was conducted at frequencies ranging from 0.01 Hz to 100 kHz and at an amplitude of 0.005 V.

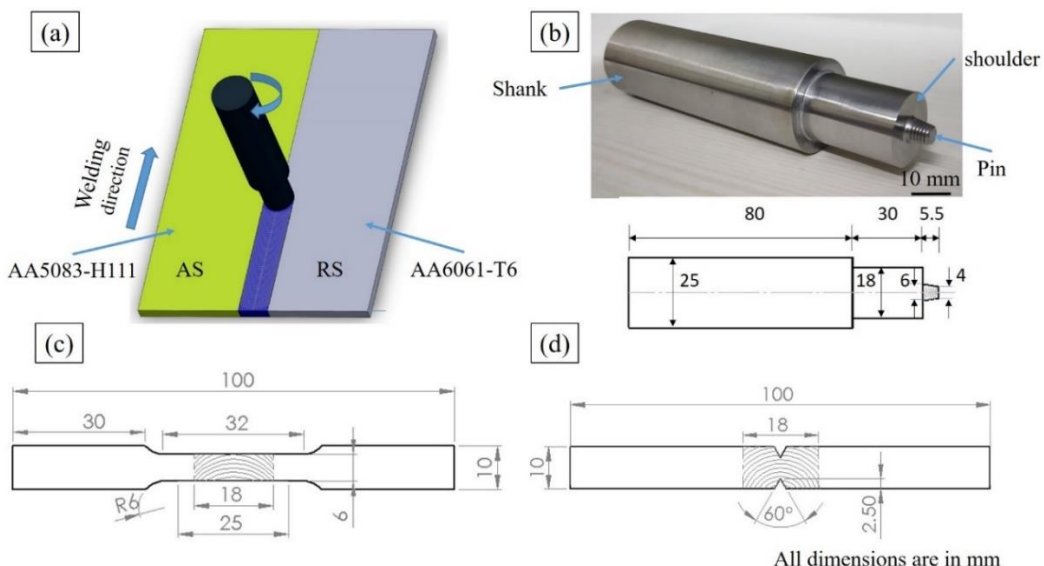


Figure 4.15: (a) FSW schematic illustration, (b) FSW tool with dimensions, (c) Schematic of traverse tensile test specimen and (d) Schematic of notch tensile test specimen.

4.2.3 Material flow

The cross-sectional macrographs of FSWed joints produced at different conditions are illustrated in Figure 4.16. From the macrographs, it is observed that the heat generated by varying different welding parameters (transverse and rotational speed) during FSW has a significant effect on SZ modification. The width of SZ is measured at three different locations of mid-section using OM with an accuracy of 0.01 mm and the mean values of the measurements are recorded in Table 4.4. The heat produced at the joint at low tool traverse speed is higher, leading to an increase in temperature, making the material soften and increasing the width at SZ. Accordingly, SZ width reduced due to lower heat generation and higher cooling rate with an increase in traverse speed (**Figure 4.16a-c**). On the other side, the increase in rotational speed caused high heat generation and strain rate at the SZ by intense stirring action, which resulted in enlarged SZ (**Figure 4.16d-f**). As shown in Figure 4.16, onion ring structure formation typically seen in FSW was evident in all the joints. The small part of the onion ring structure called sub-layer was analyzed to understand the impact of process parameters on intermixing as shown in **Figure 4.17a-h**. These images were captured at a distance of 2 mm from the center of the SZ location towards the advancing side as shown in **Figure 4.16c** for all the process conditions. It is observed clearly from **Figure 4.17c** that the onion ring sub-layer consists of dark color and light color-banded onion ring sub-layers attributed to differential etching response by two base materials using Keller's reagent. The EDS elemental mapping of the sub-layer of the 800-40 (800rpm and 40 mm/min) condition as shown in Figure 4.18 states that AA5083 alloy is featured as dark color, while the AA6061 is featured as having light color. Moreover, three different kinds of regions are formed in the onion ring sub-layer; (i) Spectrum 1 is the lighter region comprising major alloying elements of Mg and Si i.e. (AA6061 sub-layer), (ii) Spectrum 2 is a darker region consisting of a major alloying element of Mg i.e. (AA5083 sub-layer) and (iii) Spectrum 3 consists of a mixed layer of two alloys i.e. (mixed sub-layer). The formation of AA5083 and AA6061 sub-layer is quite common but the formation of the mixed region is due to intense stirring action caused by the threaded pin profile, giving an opportunity for inter-mixing around the threads of the pin profile before it is forged back. It is a curious observation that the onion ring sub-layer width changes with different welding parameters (traverse speed and rotational speed) with the width of each sample condition onion ring sub-layer determined shown in **Table 4.4**. The onion rings are symmetric from the center towards both the advancing and retreating sides. Hence, only the images observed on the advancing side were considered for material flow analysis. The increase in traverse speed from 40 to 80 mm/min led to an increase in sub-layer width as shown in **Figure 4.17a-c**, and the image shows a clear layer of zig-zag interface separating both base materials. This may be

because of the lower heat input to the weld, which results in lower flowability of AA5083 base material compared to that of AA6061 [Fujii et al., (2006)]. It was discovered from the microstructure in **Figure 4.17d-f** that intermixing of both base materials was more with an increase in tool rotational speed from 800 rpm to 1400 rpm. This is due to the intense stirring action at higher rotational speed because of which the low flow strength material acquires sufficient flowability under high temperature at the weld, giving rise to extensive material mixing and leading to a reduction in the onion ring sub-layer width (**Figure 4.17d-f**). During the plunging or initial deforming phase the material sticks to the tool and attains the velocity of the tool, as the deformation progresses with respect to time the temperature increases and slipping condition occurs. Partially sticking/slipping of the material occurs as a result of the tool translation motion. However, the sudden increase in sub-layer width is due to a change in contact conditions from partial sticking/slipping mode to slipping dominated of the base material with the tool pin at high rotational speeds (1700 rpm). This was also explained by [Kumar et al., (2008)] and [Schmidt et al., (2006)]. Therefore, the width of the onion ring sub-layer signifies the intermixing degree between the two base materials and the larger width denotes lower intermixing. The effect of process conditions on the intermixing can be noticed on the mechanical properties and corrosion behavior discussed in the sections to follow.

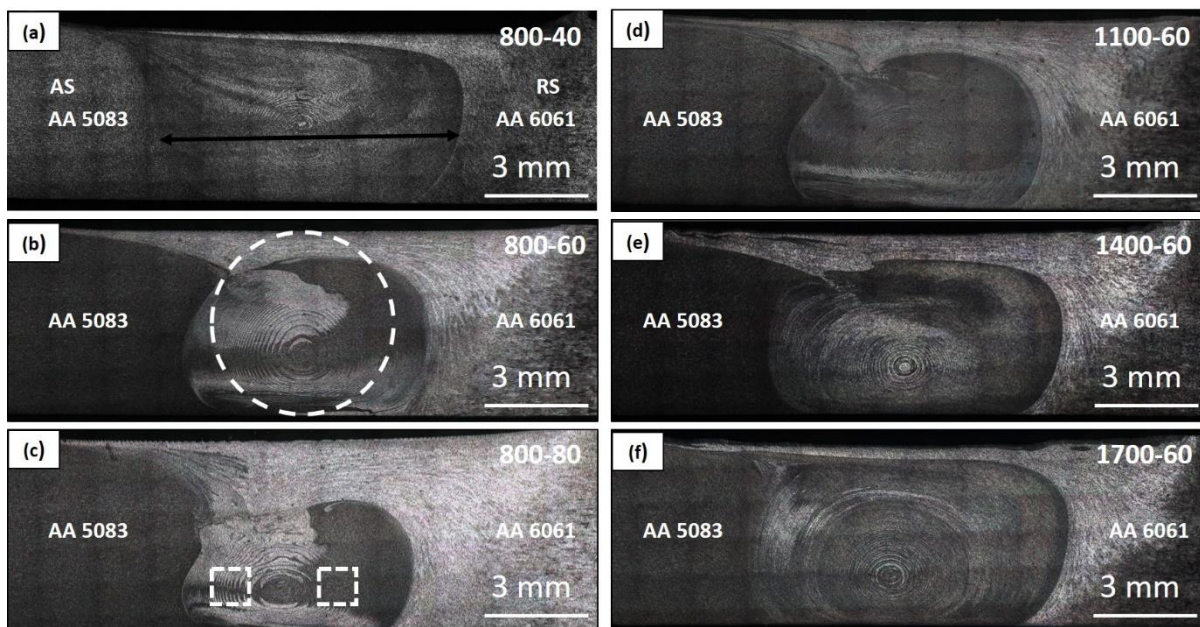


Figure 4.16: Macrostructure images of the transverse cross-section of the dissimilar FSWed sample conditions: (a) 800-40, (b) 800-60, (c) 800-80, (d) 1100-60, (e) 1400-60 and (f) 1700-60.

Table 4.4: Stir zone width and onion ring sub-layer width of the dissimilar AA5083-AA6061 FSWed sample conditions.

Sample conditions	Stir zone width	Onion rings sub-layer width
	(mm)	(μm)
800-40	9.02 \pm 0.05	26 \pm 4
800-60	7.95 \pm 0.07	52 \pm 2
800-80	7.08 \pm 0.02	70 \pm 5
1100-60	8.26 \pm 0.05	34 \pm 8
1400-60	8.78 \pm 0.03	23 \pm 5
1700-60	9.63 \pm 0.08	38 \pm 3

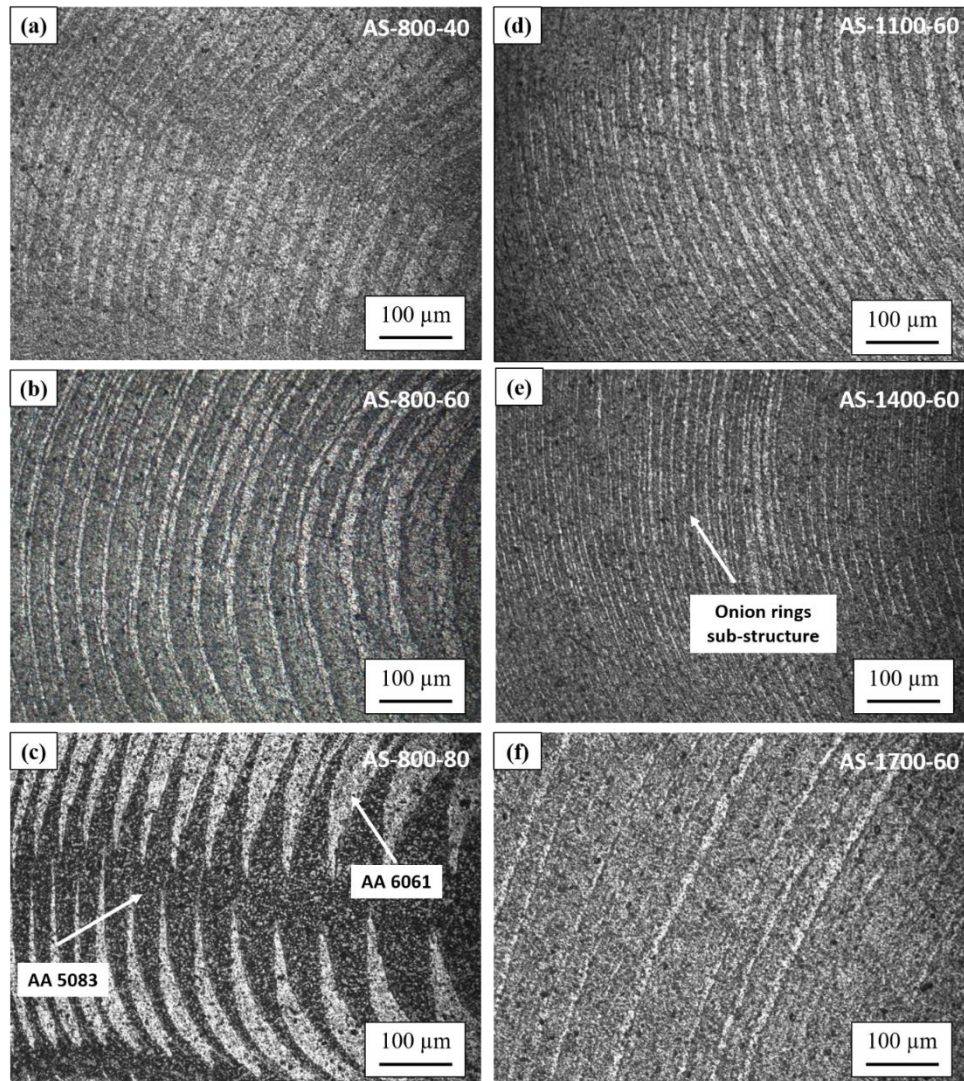


Figure 4.17: Microstructures at the SZ towards the advancing side of the dissimilar FSWed sample conditions: (a) AS-800-40, (b) AS-800-60, (c) AS-800-80, (d) AS-1100-60, (e) AS-1400-60 and (f) AS-1700-60

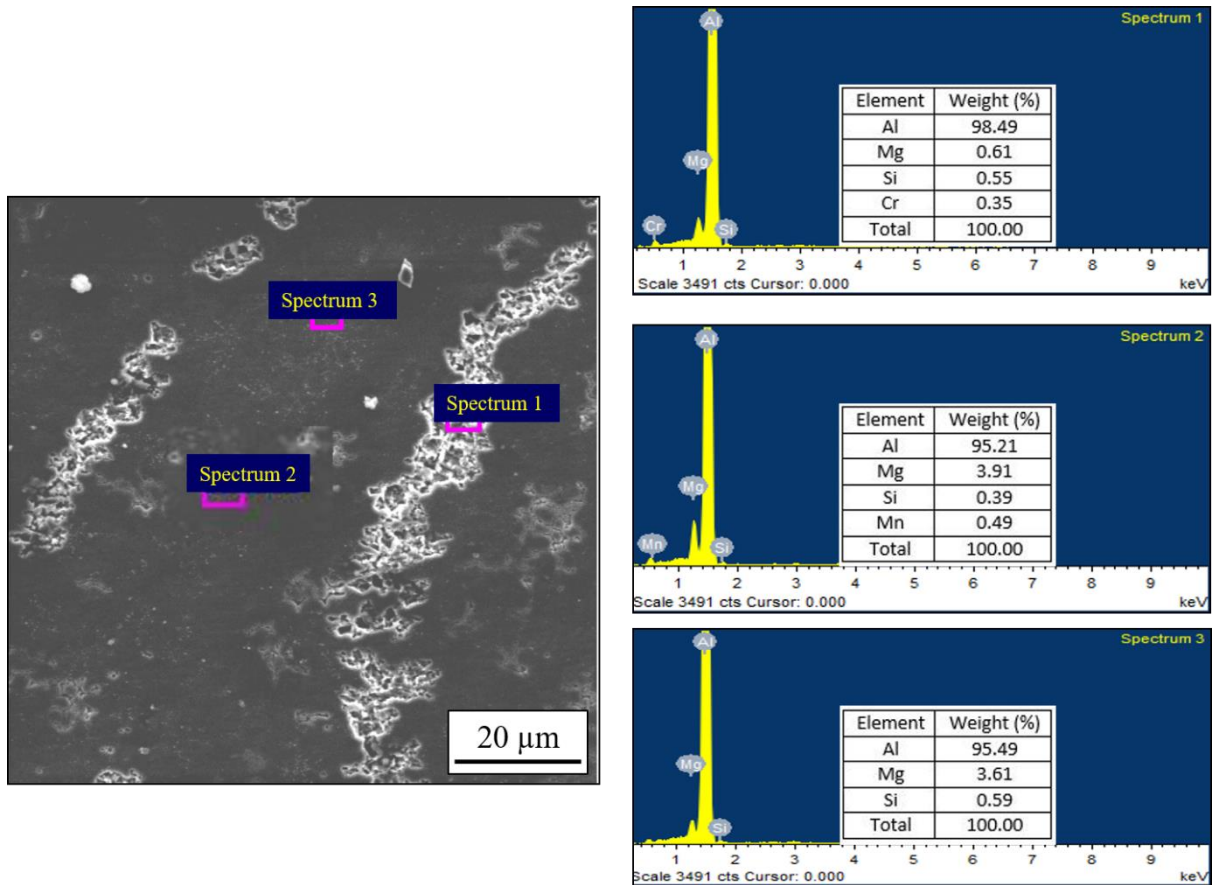


Figure 4.18: SEM image and EDS spectrum of the onion ring sub-layers of the dissimilar FSWed AA5083-AA6061 joint at 800-40 sample condition.

4.2.4 Microstructural characterization

Figure 4.19 shows the typical microstructures obtained at different locations of the FSWed joint at 1400-60 process conditions. Figure 4.19a and f show the microstructural images of the as-received AA5083-H111 and AA6061-T6 base materials respectively. Both the base materials consist of elongated grains along the rolling direction with an average grain size of 30 ± 25 μm for AA5083 and 103 ± 35 μm for AA6061. **Figure 4.19b** and e exhibit the HAZ corresponding to AS and RS of dissimilar FSWed joint respectively. During the FSW process, grain coarsening occurred in both AA5083-H111 and AA6061-T6 with an average grain size of 39 ± 15 μm and 121 ± 18 μm respectively, which is attributed to the thermal cycle experienced at HAZ. Simultaneously, TMAZ was formed due to frictional heating and mechanical deformation, where the grains were seen to be slightly refined and elongated upwards as shown in **Figure 4.19c** [Zhou et al., (2018)]. The stir zone of dissimilar weld joint displays a refined grain structure owing to severe plastic deformation (**Figure 4.19d**). The microstructural images at the stir zone of each condition are shown in **Figure 4.20a-f**. These images depict an increase in the refinement in grain size with an increase in the traverse speed as a consequence of varied heat input [Farahmand et al., 2016]. The average grain size measured in the SZ of the joints at

a traverse speed of 40, 60, and 80 mm/min were found to be 7.4 ± 4.3 , 6.7 ± 3.5 , and 6.5 ± 4.2 μm respectively. However, an increase in the rotational speed resulted in an increase in the grain size owing to higher heat generation [Chen et al., (2018)]. The average grain size measured at the center of the stir zone was found to be 7.1 ± 4.2 μm , 7.6 ± 5.3 μm , and 8.8 ± 6.3 μm at a rotational speed of 1100, 1400, and 1700 rpm respectively.

SEM images of the as-received base materials and the SZ of the FSWed joints at different process conditions are illustrated in **Figure 4.21**, **Figure 4.22** and **Figure 4.23** along with EDS analysis. In terms of constituent elements, AA5083-H111 has two main intermetallics (**Figure 4.21a**). The intermetallics in BM include Al (Fe, Mn, Mg/Si) phase and Al-Mg phase as shown in the EDS spectrum (**Figure 4.21b and c**). The most common precipitates of AA6061-T6 alloy are Al (Fe, Mn, Si) and Mg-Si (**Figure 4.22a-c**), also reported by Kartsonakis et al., (2016). SEM images at the SZ of dissimilar AA5083-AA6061 FSWed specimens at the conditions 800-40, 800-60, and 800-80 respectively are shown in **Figure 4.23a-c**. With increase in traverse speed, the material mixing in SZ was lowered which resulted in an agglomeration of intermetallic particles as shown in Figure 4.23b and c. The SEM images of dissimilar AA5083-AA6061 FSWed joints at SZ of 1100-60, 1400-60, and 1700-60 specimens respectively are shown in Figure 4.23d-f. The fragmentation and distribution of intermetallic particles are affected by an increase in rotational speed. An increase in rotational speed from 800 rpm to 1400 rpm improves the distribution of intermetallic particles (**Figure 4.23b, d and e**). However, a further increase in the rotational speed to 1700 rpm exhibited slight coarsening of intermetallics particles due to higher peak temperature generated at a very high tool rotational speed (**Figure 4.23f**). The microstructure observed in SEM shows three distinct intermetallic phases of different sizes and morphology (**Figure 4.23a**). The EDS analysis done at three locations of the 800-40 sample suggests that Al (Fe, Mn), Al-Fe-Si, and Al-Mg are among the intermetallic phases in locations 1, 2, and 3, respectively [Donatus et al., (2015)]. From the EDS analysis for base materials and the SZ of the FSWed joint, it was confirmed that precipitation, dissolution, and re-precipitation occurred during the joining of dissimilar AA5083-AA6061 FSWed joints.

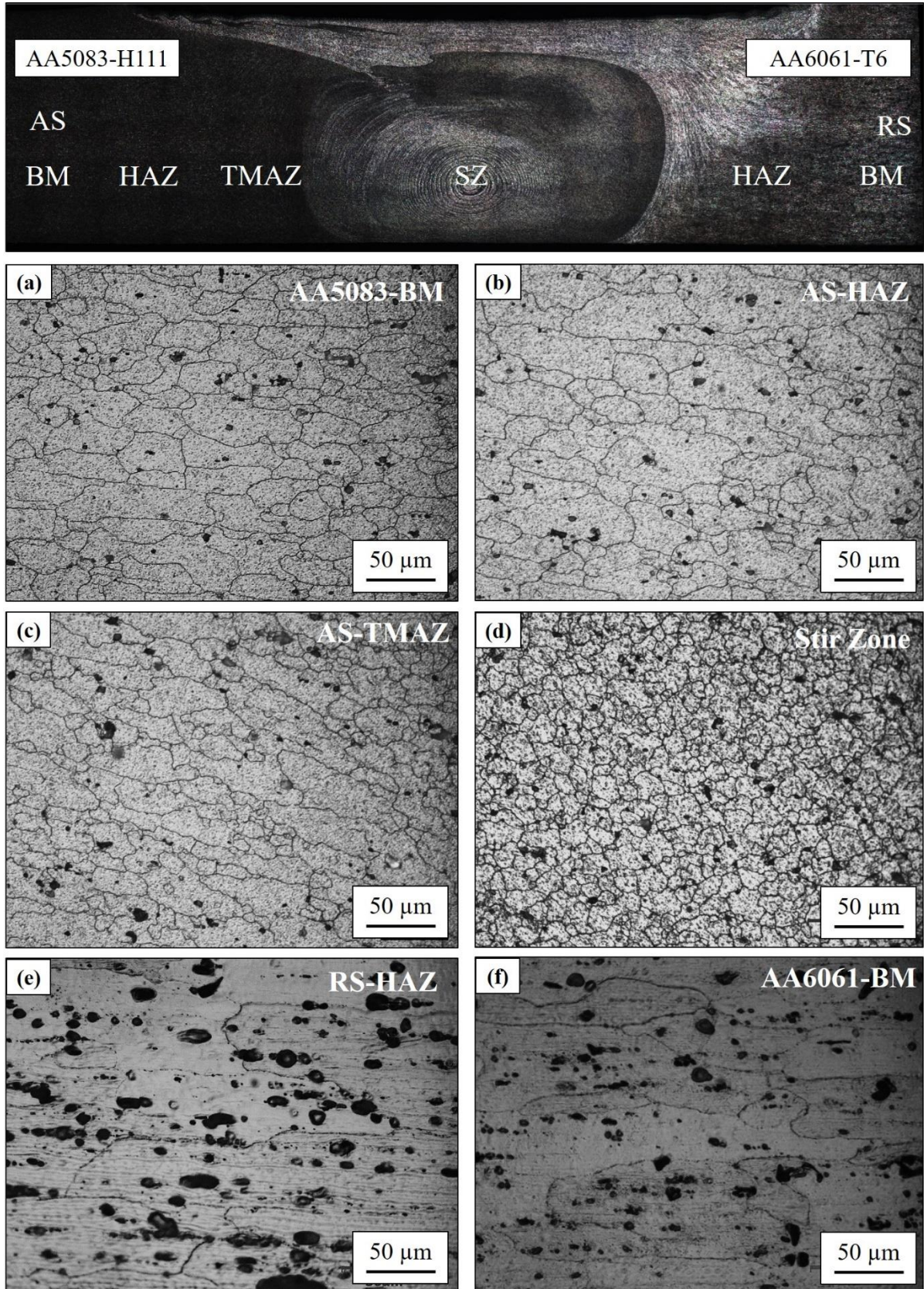


Figure 4.19: Microstructure images of the dissimilar AA5083-AA6061 FSWed sample condition of 1400 rpm and 60 mm/min: (a) AA5083-BM, (b) AS-HAZ, (c) AS-TMAZ, (d) SZ, (e) RS-HAZ and (f) AA6061-BM along with the macrostructure.

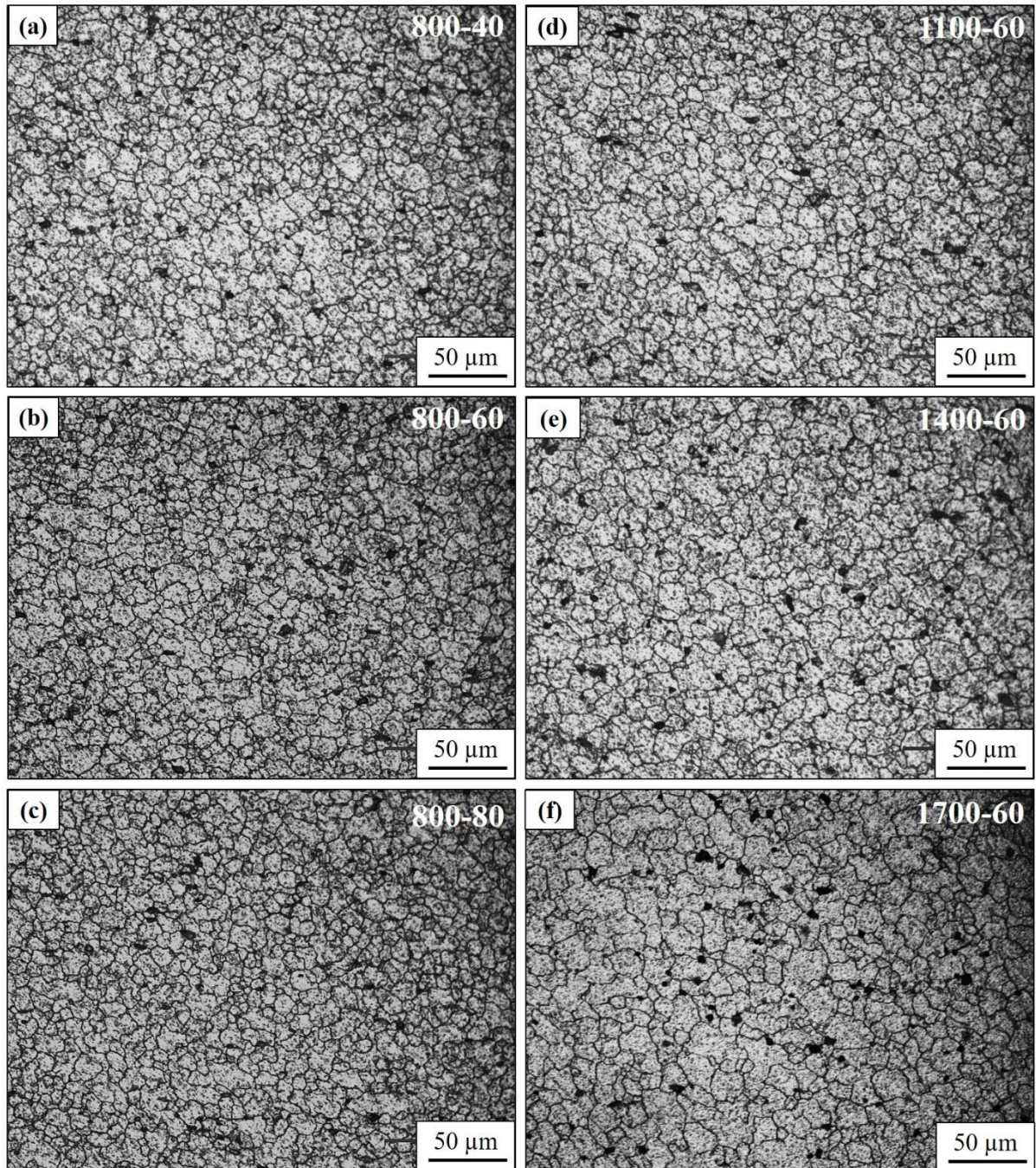


Figure 4.20: Microstructure images at the SZ of the dissimilar AA5083-AA6061 FSWed sample conditions: (a) 800-40, (b) 800-60, (c) 800-80, (d) 1100-60, (e) 1400-60 and (f) 1700-60.

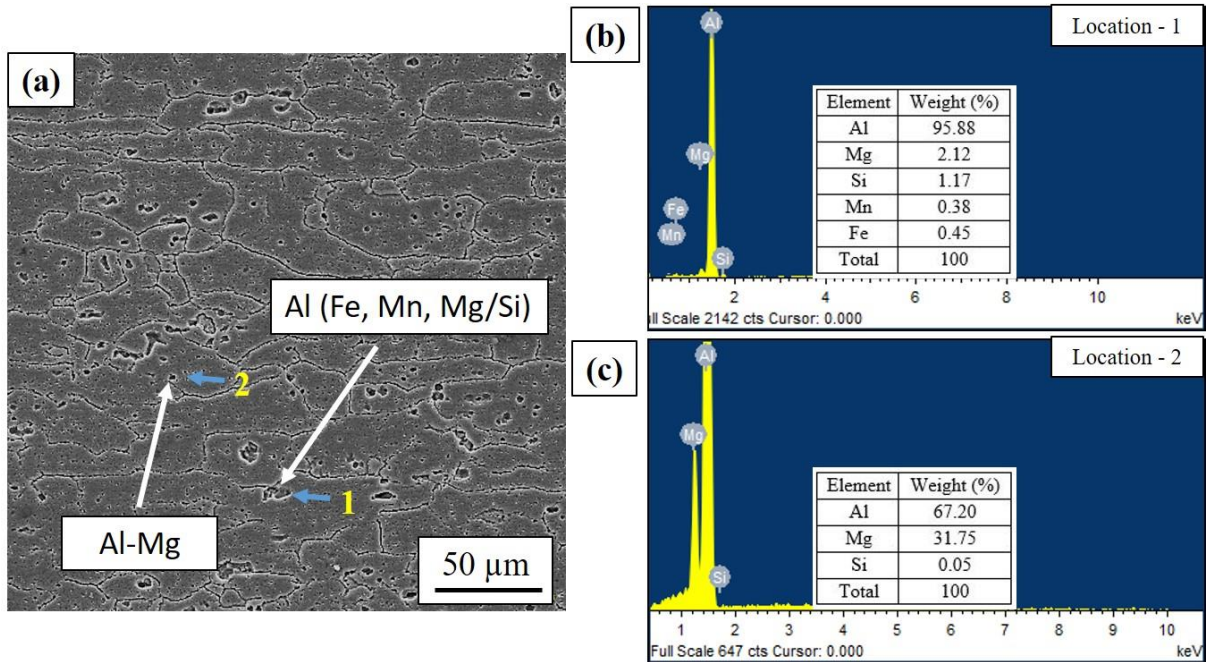


Figure 4.21: (a) SEM image of AA5083-H111, (b) EDS spectrum of Al(Fe, Mn, Mg/Si) and (c) EDS of Al-Mg

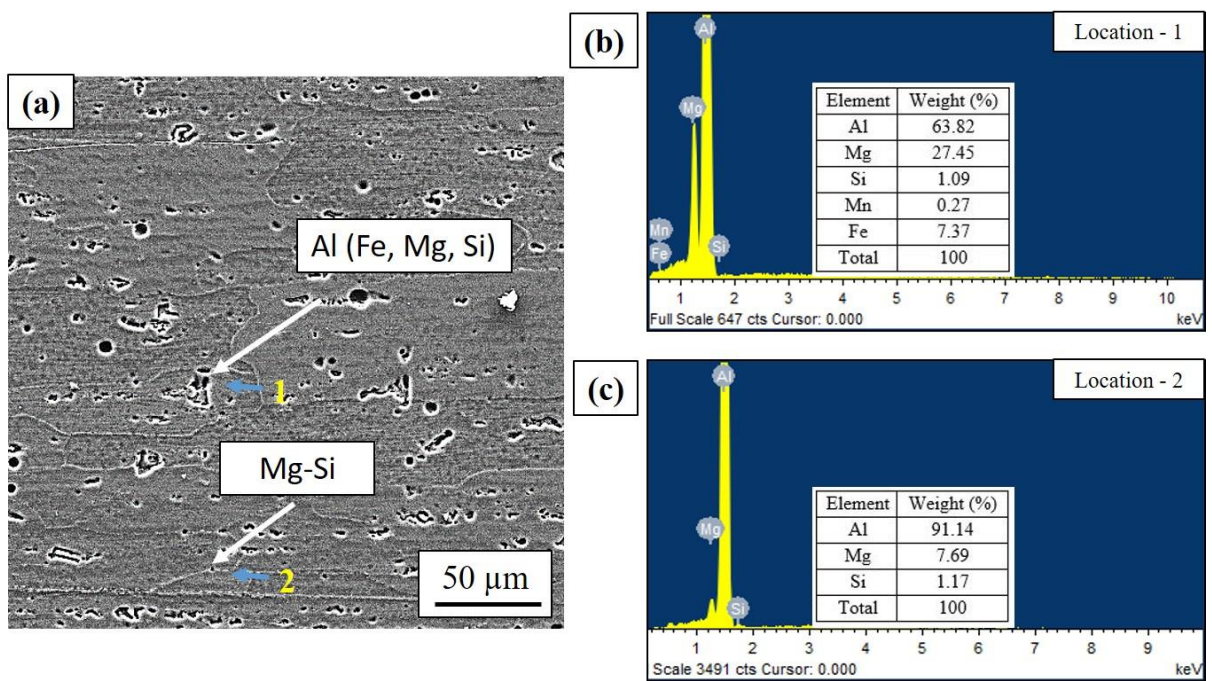


Figure 4.22: (a) SEM of AA6061-T6, (b) EDS spectrum of Al(Fe, Mg, Si) and (c) EDS of Mg-Si.

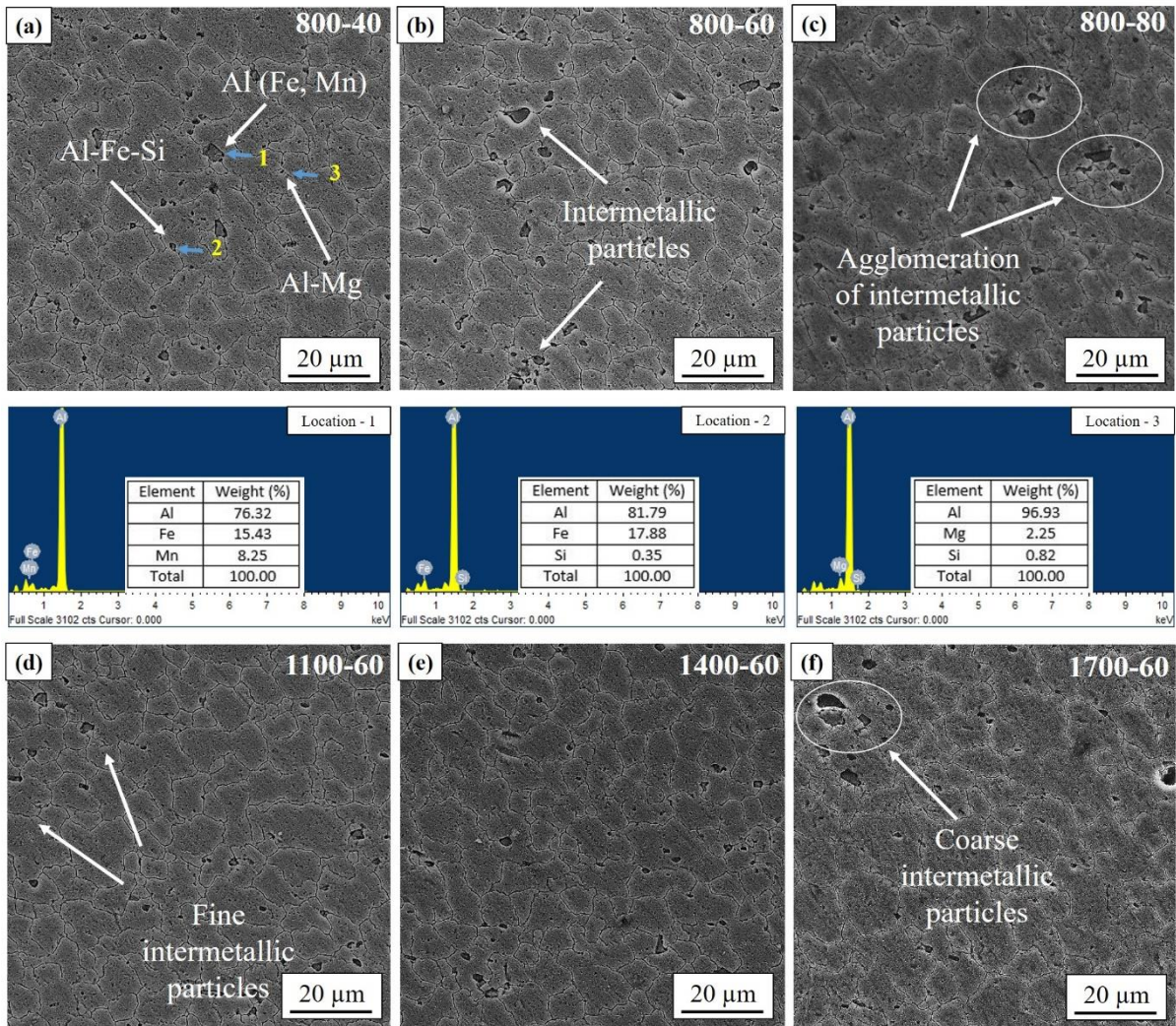


Figure 4.23: SEM images at the SZ of the dissimilar AA5083-AA6061 FSWed sample conditions: (a) 800-40 (along with EDS analysis at location 1, location 2 and location 3), (b) 800-60, (c) 800-80, (d) 1100-60, (e) 1400-60 and (f) 1700-60.

4.2.5 Mechanical properties

4.2.5.1 Microhardness

The Vickers microhardness values were measured at the mid-section of the traverse cross-sectioned FSWed specimens. Microhardness profiles developed under varying traverse speed (40-80 mm/min) and rotational speed (1100-1700 rpm) are shown in **Figure 4.24a** and **b**. The average hardness value of as-received AA5083-H111 and AA6061-T6 was estimated to be about 84.3 ± 3.6 HV and 87.8 ± 2.5 HV respectively. The fluctuation in the hardness values across different zones of the welded region is characterized by different microstructural zones as explained in **Section 3.2**. Due to the grain coarsening and dissolution of the second phase strengthening precipitates present in AA6061-BM and those present in the retreating side HAZ region exhibited minimum hardness [Guo et al., (2014)]. The microhardness trend at the SZ of FSWed joint at higher traverse speed (80 mm/min) exhibited greater average hardness than that

developed at lower traverse speed (40 mm/min), which could be attributed to the refinement of grain structure. Despite welding at higher traverse speed, the hardness values at the SZ were below that of both base materials. This was due to the loss of work hardening behavior of AA5083 and dissolution of strengthening precipitates caused in AA6061. The average hardness values at the SZ at higher rotational speed of 1700 rpm showed lower hardness values. This was attributed to an increase in grain size and prolonged thermal exposure. The higher traverse and lower rotational speeds led to an increase in cooling rate, thereby rendering the stir zone microstructure finer at higher traverse speeds while lower rotational speed caused higher microhardness profile at the SZ. Due to almost equal initial hardness values of as-received base materials, the banded structure formed at the stir zone did not show much variation in hardness trend at the SZ.

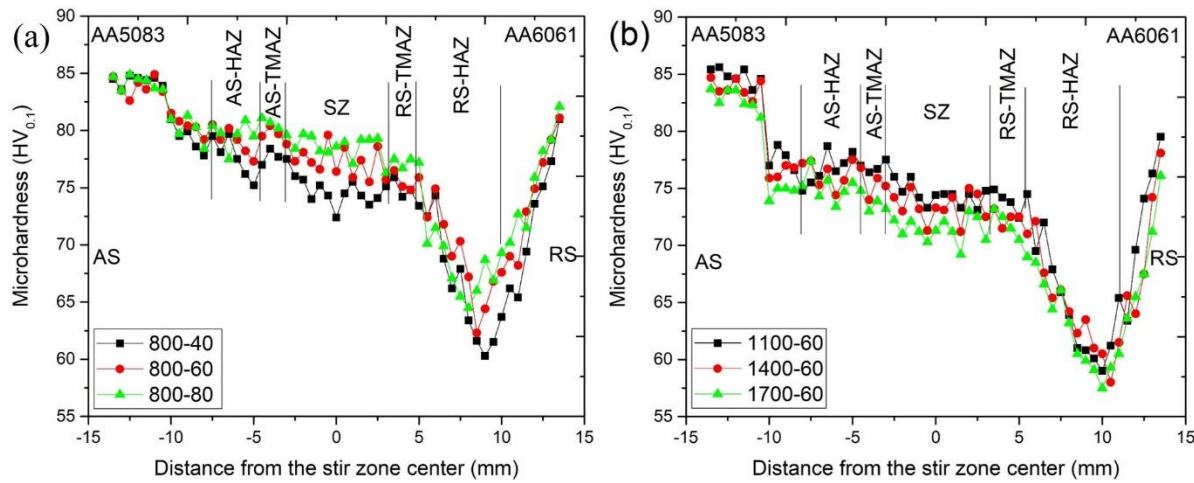


Figure 4.24: Microhardness profiles of the dissimilar AA5083-AA6061 FSWed joints: (a) varying traverse speeds and (b) varying rotational speeds

4.2.5.2 Tensile properties

The effect of tool process conditions on the transverse tensile behavior of FSWed dissimilar aluminium alloys with stress-strain curves along with fractured tensile tested specimens is shown in **Figure 4.25a** and **b**. The tensile properties of the welded joints along with that of base materials are summarized in **Table 4.5**. All the samples showed lower mechanical properties than that of base material. During tensile testing, the deformation of dissimilar welded joint was concentrated in the HAZ of AA6061 as it corresponds to the weakest zone among different zones of welded joints and in almost all cases failure is occurred within this region. The only exception was in the joint made by 800-80 condition which failed at the SZ (shown with arrow in **Fig. 11a**) due to insufficient intermixing of AA5083-AA6061 to create a bond for mechanical loading, as discussed in **Section 3.1**. From the experiments conducted at a constant tool rotational speed of 800 rpm and varying traverse speeds of 40, 60

and 80 mm/min, maximum UTS of $\sim 191 \pm 1$ MPa was recorded at 60 mm/min. It was found that with increase in the traverse speed from 40 mm/min to 60 mm/min, the heat input to the weld decreased which resulted in reduction of softening effect at HAZ. Upon increasing the traverse speed from 60 mm/min to 80 mm/min, the intermixing was lowered at the SZ causing difficulty in flow of the material to create intermixing, resulting in a weak bond. This caused failure at the SZ following reduced tensile strength. Similar results were also obtained by [Sabari et al., (2016)] and [Karthikeyan et al., (2011)]. Defect-free weld, amount of intermixing, and dissolution of precipitates govern tensile strength in dissimilar FSWed aluminium alloys. The highest value of tensile strength for the joints (~ 197 MPa) was obtained at 1100-60 conditions with a joint efficiency of 67% relative to AA6061 base material strength with failure location at HAZ. With a change in rotational speed from 800 rpm to 1100 rpm at a constant traverse speed of 60 mm/min, the onion ring sub-layer width reduced in SZ showing a good sign of intermixing of both base materials and making a way for higher tensile strength. Although good intermixing was obtained at 1400 rpm, the tensile strength began to decrease after 1100 rpm due to prolonged thermal exposure causing softening at HAZ. The tensile strength results of the present findings were also similar to those investigated by [Li et al., (2018)] and [Liu et al., (2017)]. From the tensile test, it was clear that a joint made at a very high traverse speed without any defect failed at SZ due to lower intermixing between two dissimilar base materials. Therefore, to achieve higher tensile strength in FSWed dissimilar aluminium alloys, rotational speed also needs to be varied for proper intermixing in the SZ.

In the tensile test, the highest UTS was obtained at 1100-60 condition with the failure location shifting to HAZ for all the joints welded at different rotational speeds to 800-80 condition. Though the material mixing was better in the case of 1400-60 and 1700-60 conditions, as discussed in section 3.1, the tensile strength reduced in these joints because of failure location at HAZ. Therefore, to correlate material flow behavior with tensile strength, a notch tensile test was conducted with a notch made at the center of SZ. The effect of tool process conditions on the notch tensile behavior of FSWed dissimilar aluminium alloys with stress-strain curves along with fractured tensile tested specimens is shown in the **Figure 4.26a and b**. The notch tensile strength is shown to be higher than normal tensile strength due to the failure at SZ instead of at weak HAZ. Higher notch tensile strength was observed in the joint fabricated at 1400 rpm rotational speed and 60 mm/min traverse speed because of better material mixing. The findings of notch tensile strength are in line with the onion ring sub-layer width of dissimilar AA5083-AA6061 FSWed joints.

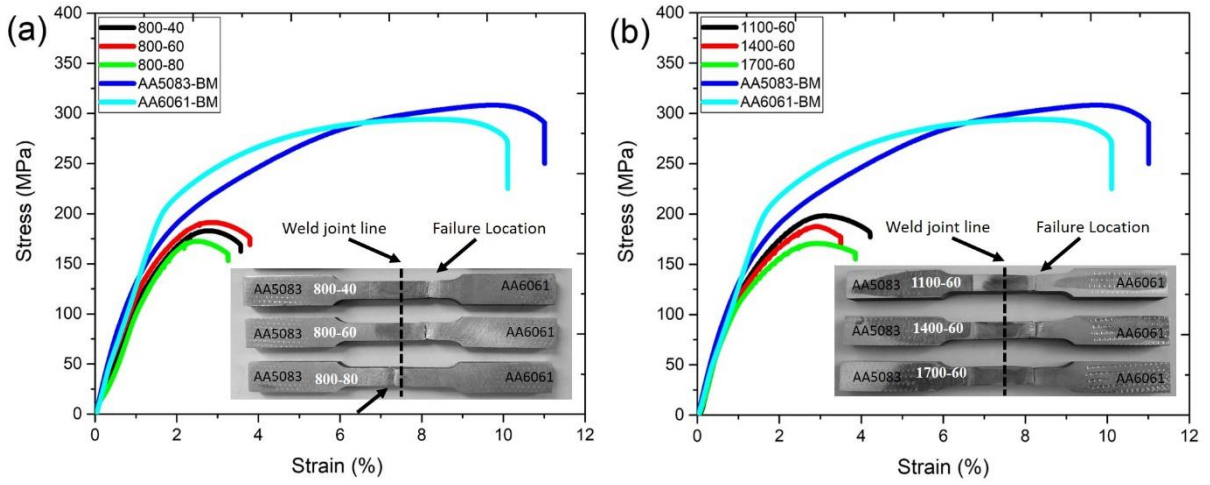


Figure 4.25: Tensile stress-strain graph of dissimilar AA5083-AA6061 FSWed joints: (a) Varying traverse speed and (b) Varying rotational speed along with the fractured specimens.

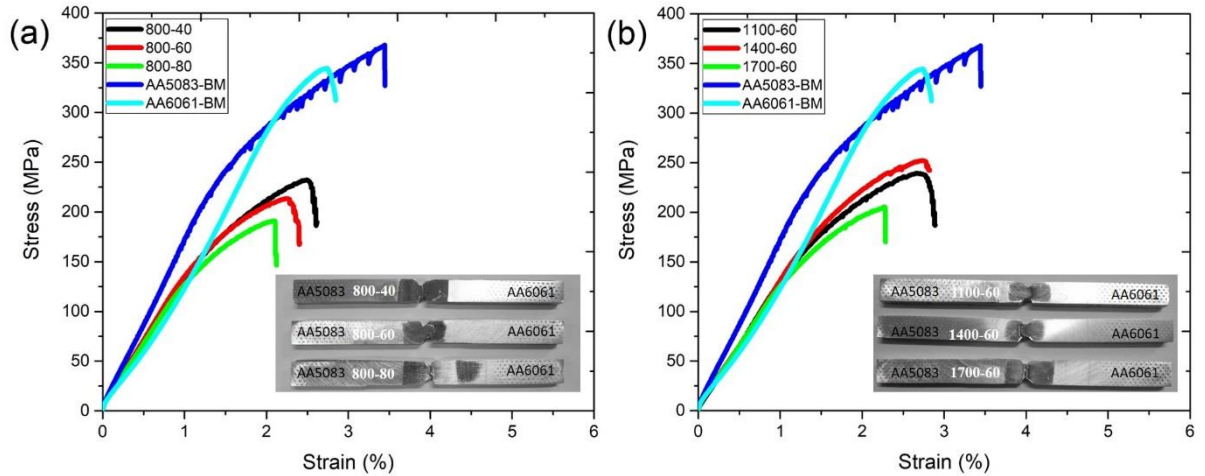


Figure 4.26: Notch tensile stress-strain graph of dissimilar AA5083-AA6061 FSWed joints: (a) Varying traverse speed and (b) Varying rotational speed along with the fractured specimens.

The tensile fracture surfaces of as-received base material and dissimilar FSWed AA5083-AA6061 joints failed at SZ (800-80) and HAZ (1400-60) (**Figure 4.27**). SEM micrographs of the as-received AA5083 and AA6061 failed specimen surface (Figure 4.27a and b) displays a large number of shallow dimples indicating a ductile fracture mode. The fractured surfaces of the sample which failed at SZ (800-80) has both smaller size dimples and flat surfaces, indicating a mixture of ductile and brittle fracture (**Figure 4.27c**). The smaller size dimples is attributed to refined grain structure while flat surfaces are formed due to insufficient material mixing as discussed in **Section 4.2.3**. Similarly, the fractured surfaces of the sample which failed at HAZ (1400-60) consist of non-uniform dispersion of dimples with different sizes and flat surfaces (**Figure 4.27d**). As compared to AA6061 base material, the shallowness

of dimples decreased in 1400-60 sample. As HAZ is the weakest zone in the FSWed joint there is no time to deform during tensile loading, leading to formation of depthless dimples and reduced elongation of 10% of the base metal to 4% for FSWed sample. On the other hand, coarsening of precipitates in HAZ fracture occurred without any deformation at some areas and resulted in the formation of flat surfaces.

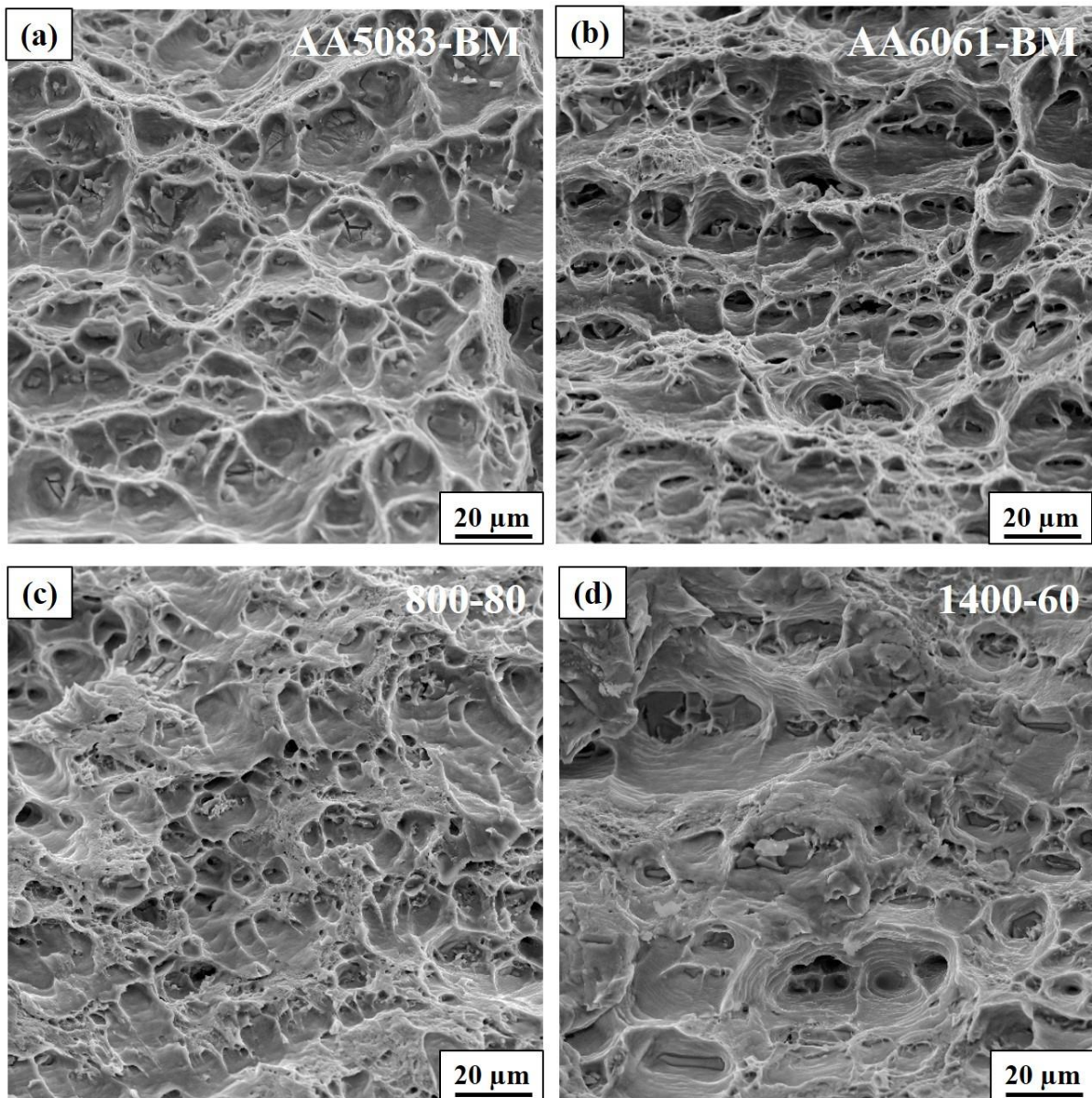


Figure 4.27: Fractography SEM images of the samples after the tensile test: a) AA5083-H111, b) AA6061-T6, c) 800-80 and d) 1400-60.

Table 4.5: Tensile properties of the base materials and dissimilar AA5083-AA6061 FSWed sample conditions.

Sample condition	Yield strength (MPa)	Ultimate tensile strength (MPa)	Notch tensile strength (MPa)	Tensile elongation (%)	Joint efficiency (%)	Fracture Location
AA5083-BM	175±4	311±5	367±6	11.7±0.4	-	-
AA6061-BM	226±5	294±3	346±4	10.1±0.5	-	-
800-40	154±2	183±2	228±3	4.0±0.2	62.24	RS (HAZ)
800-60	157±1	191±1	213±1	3.9±0.2	64.96	RS (HAZ)
800-80	152±3	172±2	190±5	3.8±0.3	58.50	SZ
1100-60	159±3	197±2	238±4	4.2±0.3	67.00	RS (HAZ)
1400-60	155±2	188±2	252±1	3.7±0.4	63.94	RS (HAZ)
1700-60	154±3	170±3	205±3	3.8±0.2	57.82	RS (HAZ)

4.2.6 Corrosion studies

The PDP curves of the as-received base materials, FSWed samples at varying tool traverse speeds and rotational speed conditions are shown in **Figure 4.28**. The output values of corrosion potential (E_{corr}) and corrosion current density (i_{corr}) of the test obtained from PDP curves are shown in **Table 4.6**. In general, E_{corr} signifies the corrosion tendency of the sample, and i_{corr} values quantify the corrosion rate. From **Table 4.6**, it is observed that base material has lower i_{corr} values than FSWed samples and lower i_{corr} signifies better corrosion resistance. It was also observed that the E_{corr} difference between the two base materials was about 144 mV, which results in the possibility of galvanic corrosion [Schneider et al., (2014)].

In general, the corrosion mechanism in 6xxx alloys is related to Fe-enriched phases and Mg-Si particles [Blanc et al., (1997)] and [Mehdizade et al., (2020)]. On the other hand, corrosion is caused due to the precipitation of Al-Mg intermetallic particles in AA5xxx [Goswami et al., (2010)]. As discussed earlier, the intermetallic phases precipitated in FSW of dissimilar AA5083-AA6061 include Al (Fe, Mn), Al-Fe-Si, and Al-Mg. The corrosion attack is primarily concentrated in Fe-enriched region, which behaves like a cathode to the matrix and the galvanic corrosion occurs in the material surrounding it. While, the Al-Mg phase which is anodic to the matrix is precipitated at the grain boundaries, if the density is sufficient enough at grain boundaries, then there is a serious risk of intergranular corrosion. The joints welded at various traverse speeds (800-40, 800-60, and 800-80) showed lower corrosion resistance with

increase in traverse speed. This is because the intermetallic particles precipitated in AA5083-AA6061 dissimilar joints agglomerated at higher traverse speed and thus created a site for galvanic corrosion (Figure 4.23b-c). A similar problem was also reported by [Donatus et al., (2015)]. The decrease in corrosion resistance was in proportion to increased onion ring sub-layer width formed because of insufficient intermixing caused at higher traverse speed as discussed in section 3.1. The degree of material intermixing in the SZ improved with increase in rotational speed from 800 rpm to 1400 rpm, resulting in increased corrosion resistance. These results indicate that fragmentation and distribution of intermetallic particles at higher rotational speed is an important process parameter that lowers corrosion resistance by minimizing galvanic corrosion sites. Despite the higher rotational speed at 1700 rpm, the corrosion resistance of 1700-60 condition decreased due to inadequate material mixing. [Li et al., (2018)] and [Zhang et al., (2020)] also found that the intermetallic phases in the NZ affect the corrosion resistance of dissimilar FSWed joints.

The corroded surface after the PDP test of base materials and FSWed samples are shown in **Figure 4.29**. The severity of the corrosion attack increased with increase in traverse speed from 40mm/min to 80mm/min as shown in **Figure 4.29a-c**, and this corrosion attack was reduced and converted into uniform corrosion with the increase in rotational speed from 800rpm to 1700 rpm as shown in **Figure 4.29d-f**. The corrosion attack intensity of the PDP test surfaces was in line with the corrosion current density values and base materials surfaces showed lower corrosion attack than the welded samples **Figure 4.29g and h**.

The corrosion behavior of weld joints obtained at different traverse speed and rotational speed specimens was further analysed by EIS test and the obtained Nyquist plots obtained for different conditions are shown in **Figure 4.30**. In this study, EIS confirmed the results of the PDP test. The Nyquist plot indicates a real part of impedance (Z_{re}) on x-axis and an imaginary part of the impedance (Z_{im}) on y axis. All the Nyquist plots of the EIS tested samples are of similar shapes, depicting a similar mechanism with difference only in the magnitude of impedance. The diameter of the semi-circle generated in the Nyquist plot relates to corrosion resistance and the larger size diameter loops indicate better corrosion resistance. Considering the results of the PDP and EIS results, the 1400-60 condition exhibited excellent corrosion resistance.

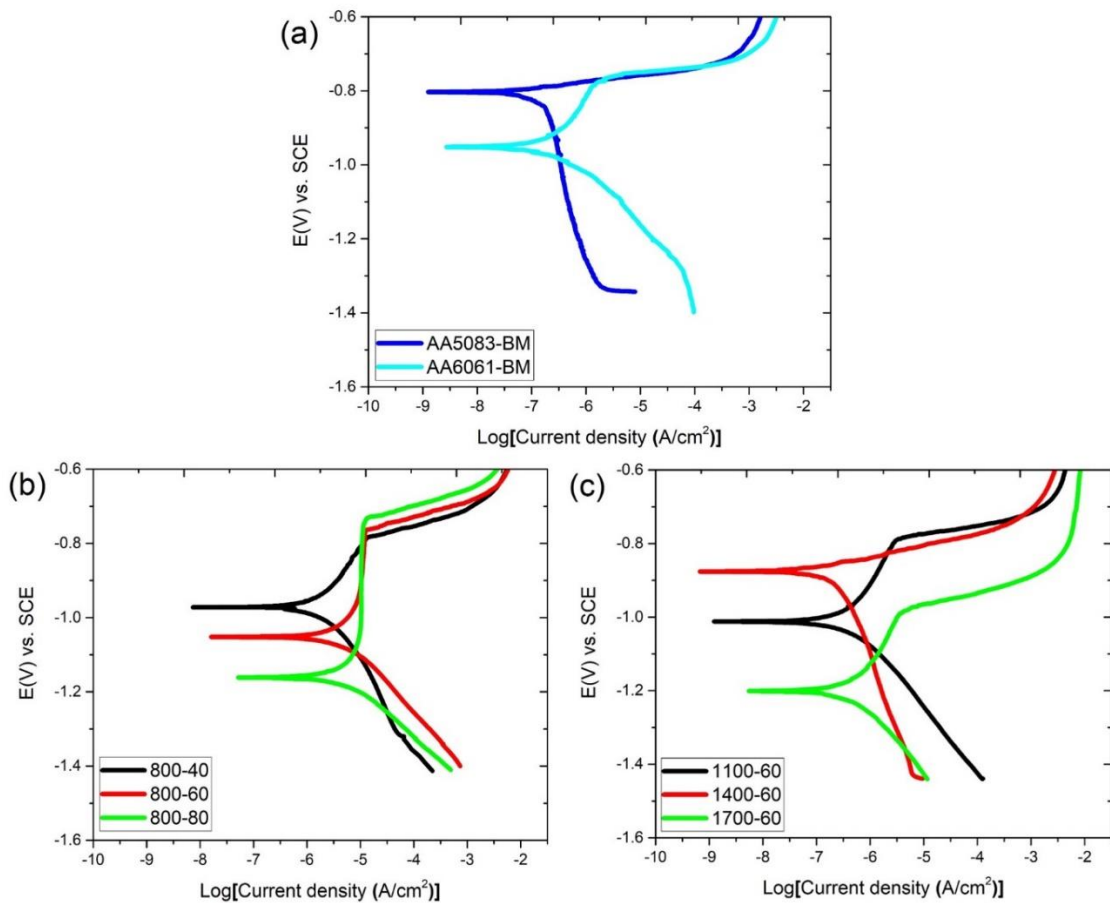


Figure 4.28: PDP curves of dissimilar AA5083-AA6061 FSWed joints: (a) as-received base materials (b) varying traverse speed and (c) varying rotational speed.

Table 4.6: Corrosion potentials and corrosion current density of the base materials and dissimilar AA5083-AA6061 FSWed sample conditions.

Sample conditions	Corrosion potential E_{corr} (mV (SCE))	Current density i_{corr} ($\mu A/cm^2$)
AA5083-BM	-804	0.12
AA6061-BM	-948	0.76
800-40	-970	1.36
800-60	-1052	1.87
800-80	-1161	2.11
1100-60	-1013	1.15
1400-60	-874	0.94
1700-60	-1203	1.21

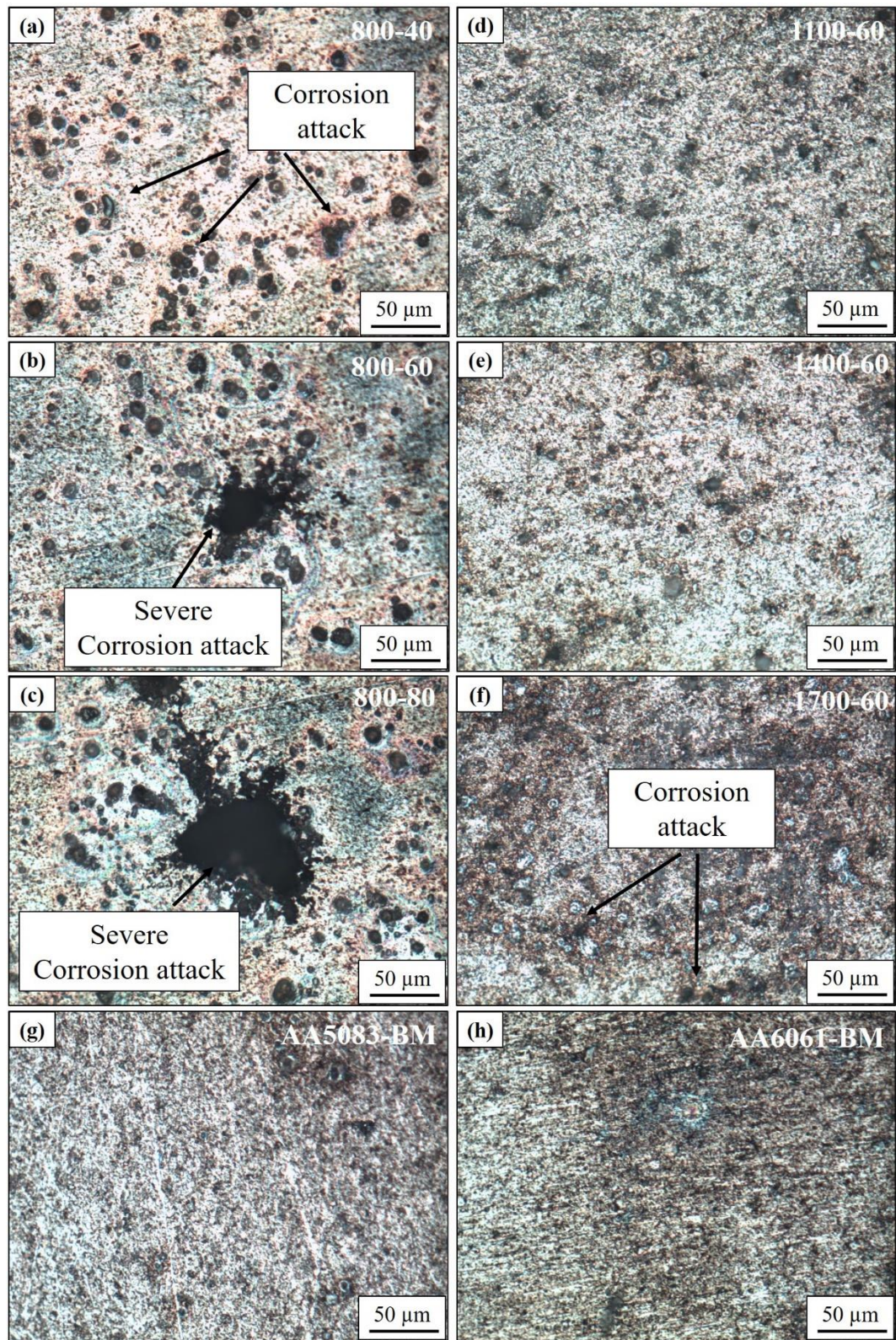


Figure 4.29: Corrosion morphologies at the dissimilar AA5083-AA6061 FSWed sample conditions: (a) 800-40, (b) 800-60 and (c) 800-80, (d) 1100-60, (e) 1400-60 and (f) 1700-60.

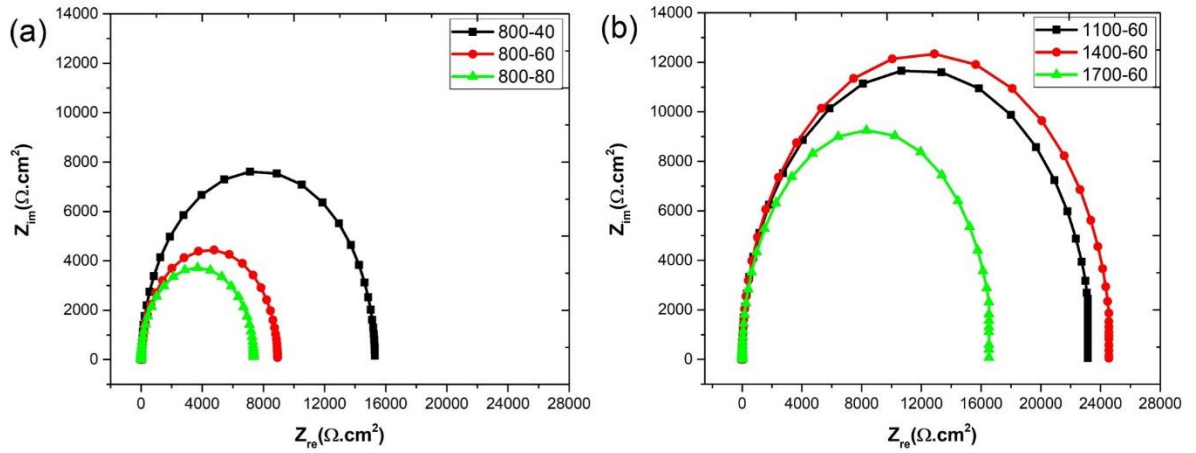


Figure 4.30: EIS plots of the dissimilar AA5083-AA6061 FSWed joints: (a) varying traverse speed and (b) varying rotational speed.

4.2.7 Summary

In this study, AA5083-H111/AA6061-T6 dissimilar friction stir butt welds of 6 mm thickness were prepared using different process conditions. The material flow, mechanical properties and corrosion behavior were analyzed and correlated. The stir zone microstructure of all the joints resulted in refined grains from the existing elongated microstructures of as-received base materials. Process parameters influenced the SZ and onion ring sub-structure width. The intimate intermixing of two base materials during FSW was observed at lower traverse speeds and higher rotational speeds. Superior tensile strength was achieved at the intermediate process conditions of 1100 rpm and 60 mm/min of ultimate tensile strength (UTS) of around 197 MPa, with a joint efficiency of 67 % during the normal tensile test. The notch tensile strength test showed higher mechanical resistance at rotational speed of 1400 rpm and traverse speed of 60 mm/min process conditions. Based on the results of the PDP and EIS test, the corrosion resistance of welded joints was found to be lower than that of base materials. The corrosion resistance decreased with the increase in traverse speed from 40 mm/min to 80 mm/min and the corrosion resistance increased with increase in rotational speed from 800 rpm to 1400 rpm. The onion ring sub-structure width reduced at higher rotational speed and interestingly corrosion resistance also improved with increase in rotational speed. Tool rotational speed of 1400 rpm showed better corrosion resistance due to fragmentation and distribution of intermetallics phases, creating fewer sites for corrosion attack.

4.3 Enhancing corrosion resistance and mechanical properties of dissimilar friction stir welded 5083-6061 aluminium alloys using external cooling environment

4.3.1 Introduction

The previous work on the effect of process parameters showed higher tensile strength and corrosion resistance at rotational speed of 1400 rpm and traverse speed of 60 mm/min process conditions. During FSW, there is a lot of heat generation and mechanical deformation, due to which metallurgical changes occur in the stir zone and nearby regions. Although melting does not occur from heat generated during FSW, but the mechanical properties are degraded. To minimize the degradation of mechanical properties, it is important to decrease heat input to the weld. Controlling heat input is possible by adjusting welding process parameters and using an external coolant to minimize heat input during friction stir welding. As a result of the knowledge gap, it was essential to investigate the impact of the cooling environment on various metallurgical characteristics that can be linked to corrosion behavior and mechanical properties of the FSWed joint. However, the corrosion behavior and mechanical properties of FSWed AA5083-AA6061 joints with the cooling environment has not been investigated till now. Hence, the present work focuses on enhancing the corrosion behavior and mechanical properties of dissimilar friction stir welded AA5083-6061 aluminium alloys using an external cooling environment.

4.3.2 Experimental methodology

In this study, as-received base materials AA5083-H111 and AA6061-T6 aluminium alloys with 300 mm x 70mm x 6mm dimensions were butt joined along the rolling direction using a 3-Ton capacity numerically controlled FSW machine. The process parameters of FSW, such as tool rotational speed and traverse speed were maintained at 1400 rpm and 60 mm/min respectively. A conical tapered threaded pin profile made of H13 tool steel with a diameter of 6mm at the root and 4 mm at the tip, length of 5.5 mm and tool shoulder diameter of 18 mm with 3° concavity was used. FSW joints were made by placing AA5083 on the advancing side (AS) and AA6061 on the retreating side (RS) respectively. Friction stir welding was done in three different cooling environments: ambient environment or air-cooled (ACFSW), liquid nitrogen-cooled (NCFSW) and water-cooled (WCFSW). During liquid nitrogen and water-cooled FSW, coolants were supplied immediately at a distance of 25 mm behind the tool with a flow rate of 0.3 l/min and 1.8 l/min respectively to maintain a constant temperature throughout the process. A cooling environment set-up was designed in a box-type model made of transparent glass fiber sheets and fixed to the table of the FSW machine to store the coolant to

ensure efficient cooling. The welded plates in ACFSW, NCFSW and WCFSW conditions are shown in **Figure 4.31**.

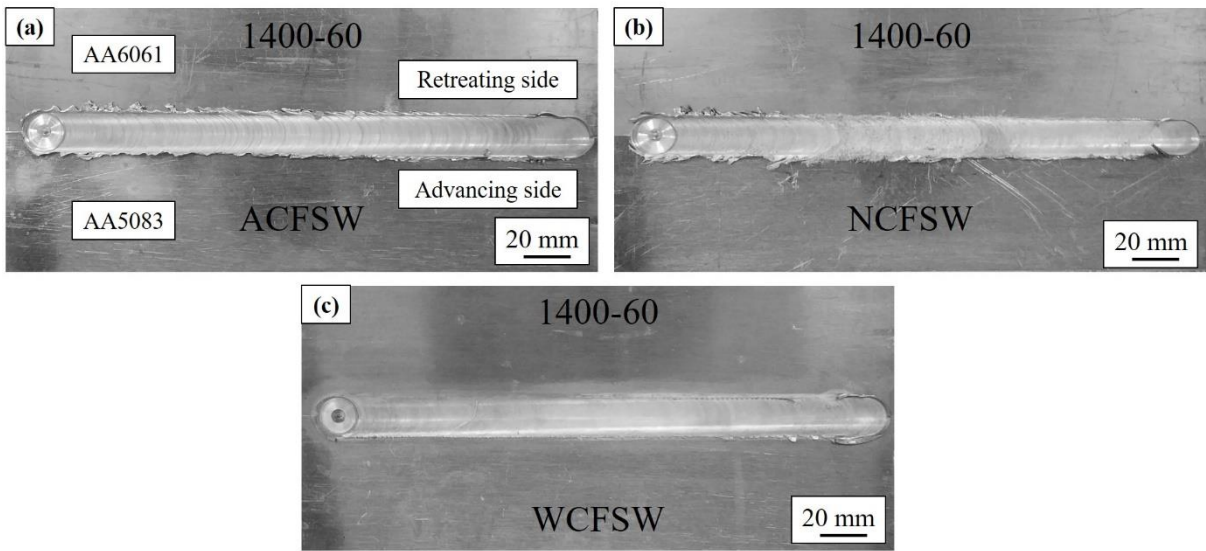


Figure 4.31: Photographs of dissimilar friction stir welded plates in (a) ACFSW, (b) NCFSW and (c) WCFSW.

4.3.3 Microstructure characterization

4.3.3.1 Macrostructure

The macrostructures of weld cross-section of dissimilar AA5083-AA6061 joints done under ACFSW, NCFSW and WCFSW are shown in **Figure 4.32**. The macrostructure revealed no defects in any of the FSWed joints, confirming that the process parameters selected were suitable to generate sufficient heat input and plastic deformation to produce a non-defective joint. From **Figure 4.32**, it is observed that the width of the stir zone narrowed because of cooling conditions comparable to air-cooled FSW. The availability of cooling media reduces the width of the SZ in NCFSW and WCFSW joints relative to the ACFSW joint due to rapid heat dissipation (**Figure 4.32a**). However, both NCFSW and WCFSW joints showed lower SZ width attributed to rapid heat transfer as a result of complete submergence of the base plates in coolants during FSW (**Figure 4.32b and c**). An important feature observed from the macrostructure is that material flow at the SZ is also influenced by the cooling conditions of the joint. The SZ of FSW is further classified into shoulder affected zone (SAZ) and pin affected zone (PAZ). Furthermore, the pin affected zone had an onion ring shaped structure that resulted from the periodic deposition of flow material whereas the shoulder affected area was very smooth [[Liu et al., \(2019\)](#)]. During NCFSW, the plate to be joined initially was subjected to cryogenic cooling before the welding progressed; and with this, the heat input to the weld was not sufficient enough to plastically deform the material to ensure sufficient flowability of material. Hence, a cryogenic

cooling environment restricted the capability of the material to flow to the joint, resulting in a reduced intermixing at PAZ.

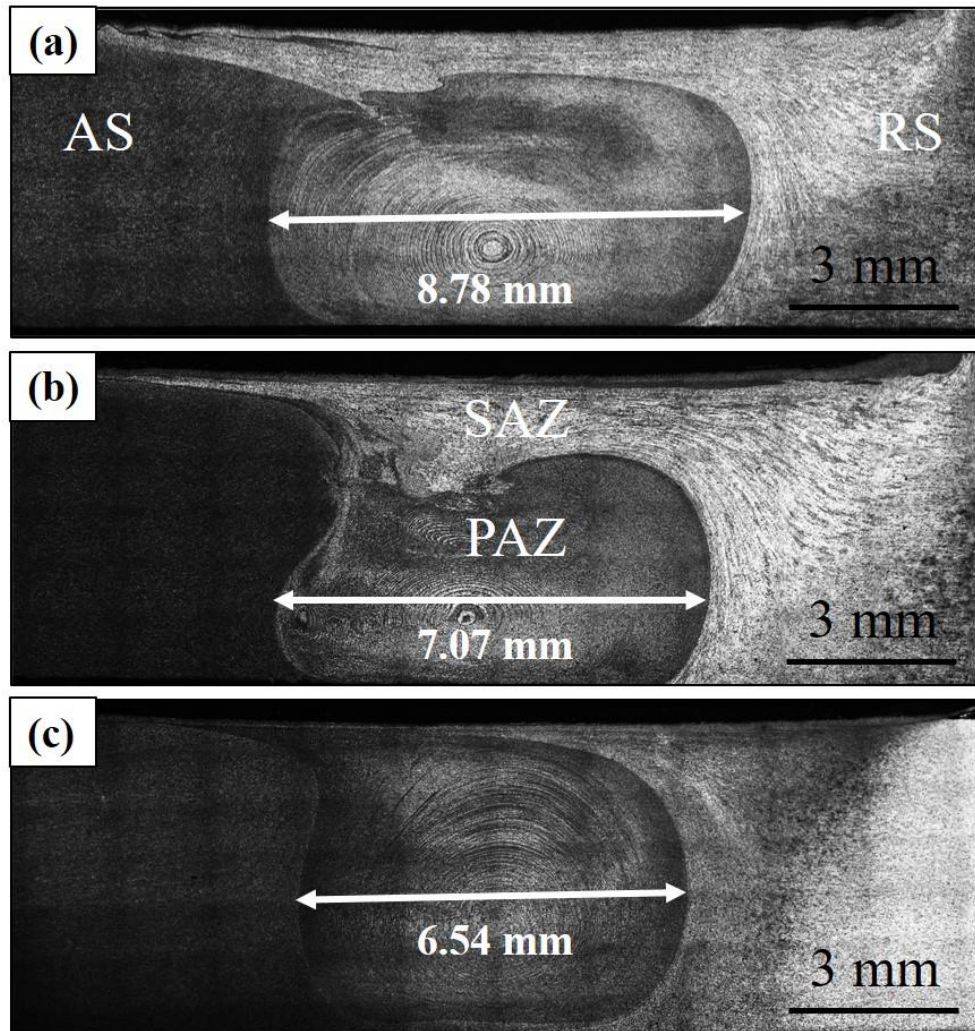


Figure 4.32: Macrostructure of dissimilar FSWed AA5083-6061 joints in (a) ACFSW, (b) NCFSW and (c) WCFSW conditions.

4.3.3.2 Microstructure analysis

Figure 4.33 shows the microstructures obtained at different locations of the ACFSW joint. **Figure 4.33a** and **f** show the microstructural images of the as-received AA5083-H111 and AA6061-T6 base materials consisting of elongated coarse grains. The stir zone of the dissimilar weld joint displays a refined grain structure owing to dynamic recrystallization (DRX) caused by severe plastic deformation (SPD) (**Figure 4.33d**). The in-depth microstructure analysis at the SZ is explained in a later section using EBSD. Figure 4.33b and e exhibit the HAZ corresponding to AS and RS of dissimilar FSWed joints respectively. Grain coarsening occurred at HAZ due to the thermal cycle produced during FSW process in both AA5083-H111 and AA6061-T6 [Park et al., (2010)] and [Peel et al., (2006)]. Simultaneously,

TMAZ was formed due to frictional heating and mechanical deformation, where the grains were slightly refined and elongated upwards (**Figure 4.33c**).

Grain size in HAZ is determined by heat input, which is controlled by cooling media used during FSW. **Figure 4.34** shows the images of microstructural zones such as HAZ of the advancing side (HAZ-AS) and HAZ of the retreating side (HAZ-RS) produced with ACFSW, NCFSW and WCFSW conditions of dissimilar AA5083-AA6061 FSWed joints. Changes in cooling rates cause grain size variation (**Figure 4.34a-d**). The average grain size measured at the AS-HAZ and RS-HAZ of the joints welded with three different cooling media is shown in Table 4.7. The grain size was found to be the lowest in both AS-HAZ and RS-HAZ in the case of WCFSW, shown in **Figure 4.34e** and **f**. Following the application of external coolant, the cooling rate increases, resulting in a shorter period to maintain the peak temperature after the weld. The maximum temperature generated during welding is affected by external coolant, which has an impact on grain development after post-weld recovery, resulting in grain size changes.

Table 4.7: Grain size at AS-HAZ and RS-HAZ of the dissimilar AA5083-6061 FSWed sample conditions.

Sample conditions	AS-HAZ	RS-HAZ
	(μm)	(μm)
ACFSW	39.1 ± 03	121 ± 18
NCFSW	33.5 ± 05	113 ± 15
WCFSW	31.7 ± 04	108 ± 17

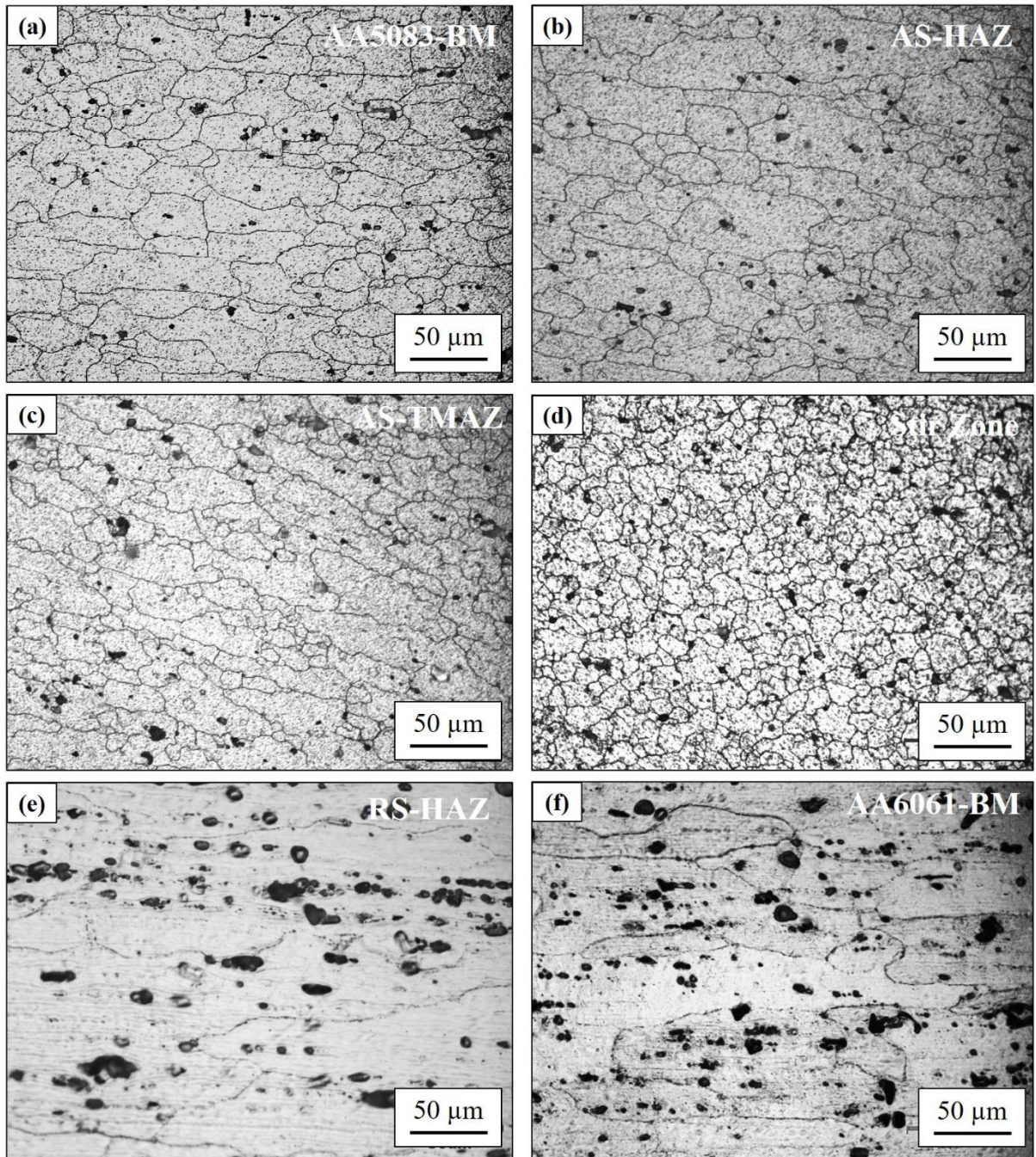


Figure 4.33: Microstructure images of the dissimilar AA5083-AA6061 FSWed sample conditions: (a) AA5083-BM, (b) AS-HAZ, (c) AS-TMAZ, (d) SZ, (e) RS-HAZ and (f) AA6061-BM.

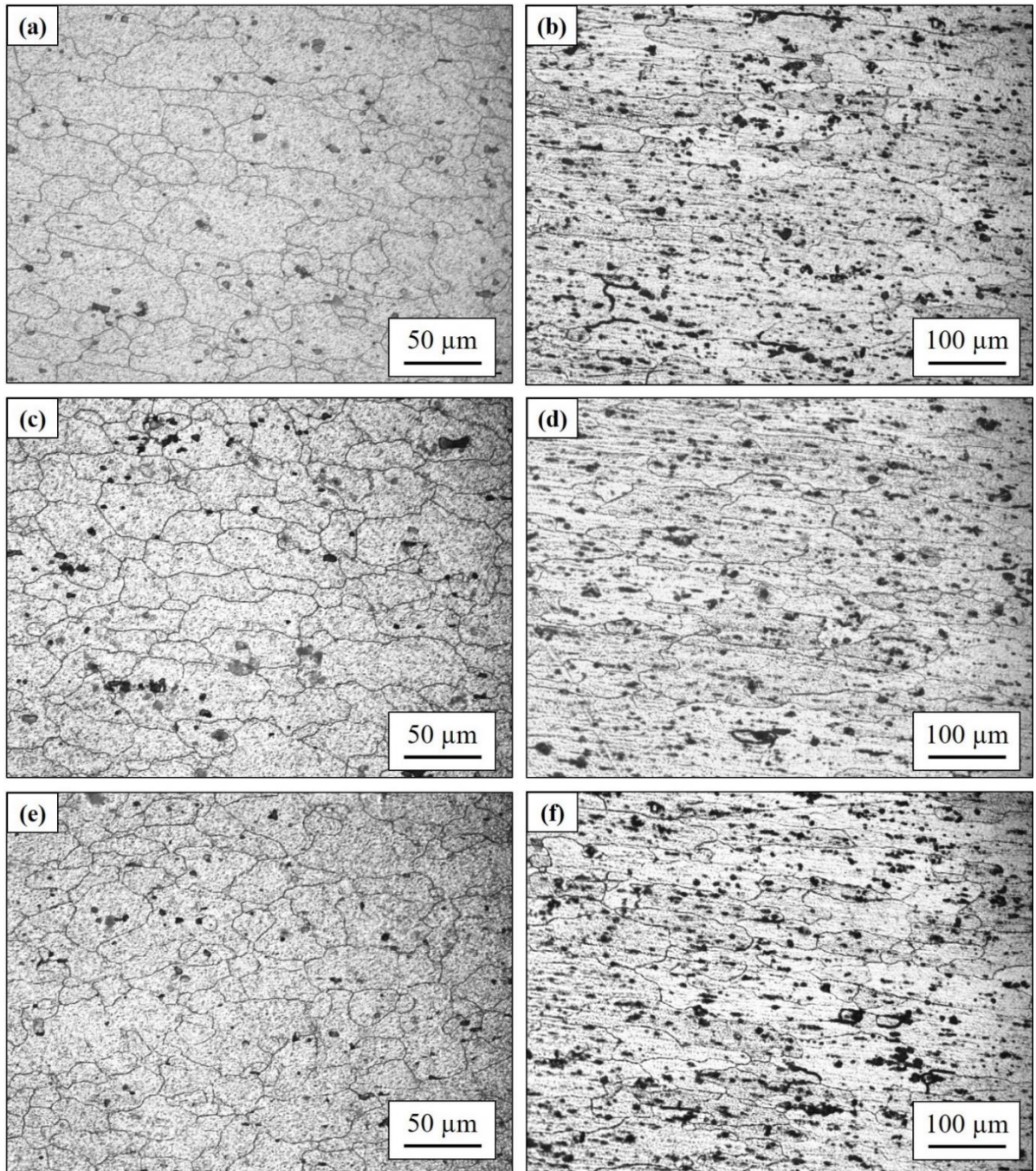


Figure 4.34: Microstructure images at the HAZs of the dissimilar AA5083-AA6061 FSWed sample conditions: (a) AS-ACFSW, (b) RS-ACFSW, (c) AS-NCFSW, (d) RS-NCFSW, (e) AS-WCFSW and (f) RS-WCFSW.

4.3.3.3 Electron back scattered diffraction

The microstructure evolution at the SZ of FSWed joints is further explained using EBSD analysis. The EBSD (IPF + grain boundary) maps and grain boundary misorientation of base materials and FSWed joints are shown in **Figure 4.35** and **Figure 4.36**. **Table 4.8** shows the statistical data of EBSD results. As with images in optical microscopy, EBSD maps of AA5083 and AA6061 base materials showed significantly elongated grains as a result of the rolling process. During FSW, SZ was subjected to large heat input with intense mechanical stirring

resulted in fine recrystallized grains with a high fraction of high angle grain boundaries (HAGBs). The mechanism behind the formation of fine grains with HAGBs is explained as follows. The heat generated is sufficient enough to cause thermal annealing and due to this, three different mechanisms operate at the SZ during FSW; dynamic recovery, dynamic recrystallization and grain growth. Dynamic recovery occurs immediately after thermal annealing. During this, the point defect (such as vacancies) created during the rolling process were eliminated due to the annihilation of dislocations by dislocation climb, which resulted in a reduction in vacancies. When dislocations move together, the opposite sign dislocations annihilate themselves, while the same sign dislocation annihilation did not occur and sub-grain boundary or low angle grain boundaries developed from dislocation rearrangement. The dislocations which were not annihilated acted as a driving force or nucleation sites for recrystallization to happen. Recrystallization occurs until the maximum refining or critical grain size is reached and this continuous process of nucleation and development of new grains is called dynamic recrystallization. Once the critical size of the grain is reached, they rotate and begin to migrate to form high-angle grain boundaries [Wang et al., (2015)].

The EBSD results of the strongly inhomogeneous microstructures around the joint cross-section are shown in Figure 4.36. The grains were given different colours depending on their crystallographic orientation. The grains of AA5083 and AA6061 BM are in lath-shape, which is attributed to the rolling process (**Figure 4.35a and b**). Due to the availability of excess heat after recrystallization, grain growth occurs. However, to remove excess heat after recrystallization a cooling environment is used during FSW. Since the refinement of grain occurred solely due to dynamic recrystallization, the maximum grain size was obtained in ACFSW. This is due to the unrestricted grain growth phenomenon (**Figure 4.35c**). The uniform heat dissipation from the welded zone due to total submergence in the cooling medium is attributable to the minimum grain size in WCFSW (**Figure 4.35e**). The heat supplied to NCFSW (**Figure 4.35d**) was significantly low and the heat at the stir zone was not sufficient enough to create plastic deformation, resulting in coarser grains than WCFSW.

It can be observed that both base materials consist of a high fraction of Low angle grain boundaries (LAGBS) which indicates that the as-received base materials are in a highly deformed state (**Figure 4.36a and b**). In addition to the development of recrystallized fine grains during FSW, the grain boundary misorientation is also controlled by heat input. Based on the misorientation angle distribution (**Figure 4.36c-e**), the volume fraction of HAGBs increases with the addition of cooling media. This is because lower heat input that resulted from

using cooling media eliminated the occurrence of more dislocations and substructure, thereby increasing the volume fraction of HAGBs.

Table 4.8: EBSD results of the base materials and dissimilar FSWed AA5083-AA6061 sample conditions

Sample condition	Grain size (μm)	Fraction of grain boundaries (%)	
		LABs	HABs
5083-BM	27.5 ± 10.5	91.8	8.2
6061-BM	103.9 ± 23.5	86.0	14.0
ACFSW	7.6 ± 2.9	35.7	64.3
NCFSW	4.5 ± 0.7	23.2	76.8
WCFSW	3.2 ± 0.5	20.2	79.8

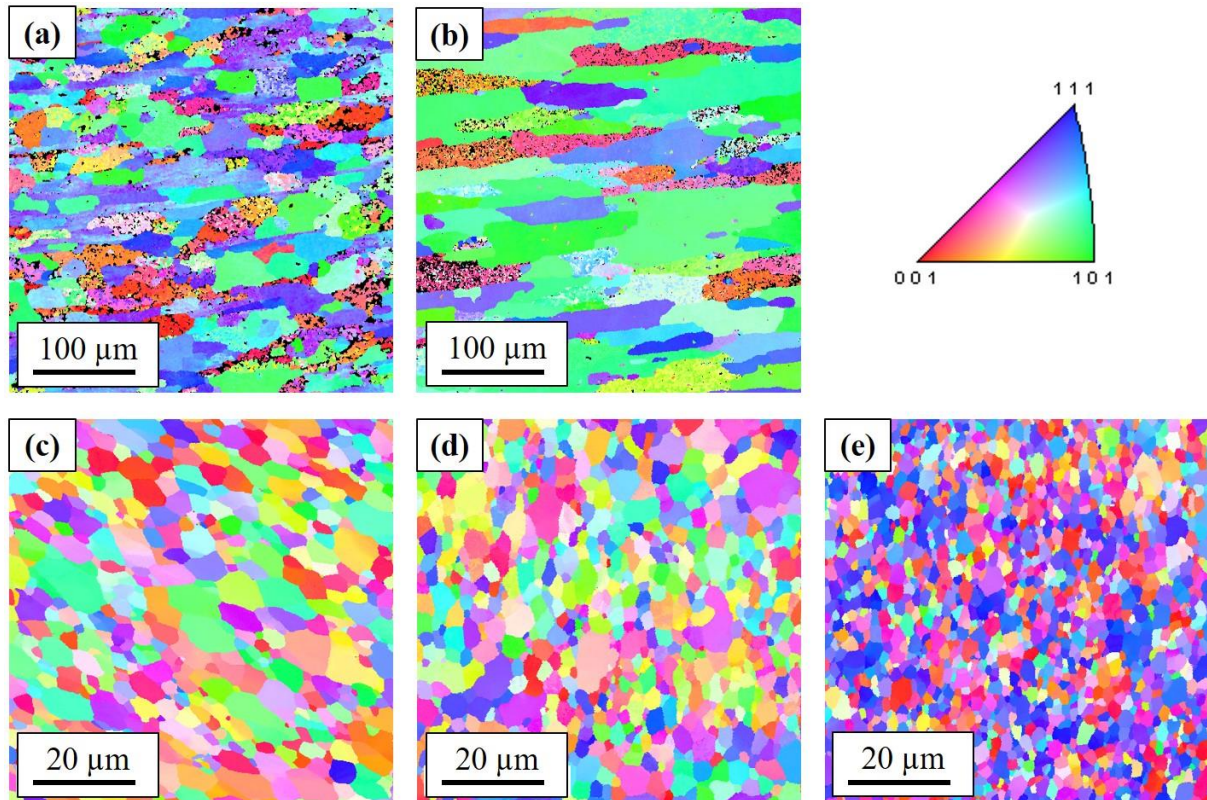


Figure 4.35: EBSD (IPF + Grain boundary) for the (a) AA5083-BM, (b) AA6061-BM, SZ of the (c) ACFSW, (d) NCFSW and (e) WCFSW.

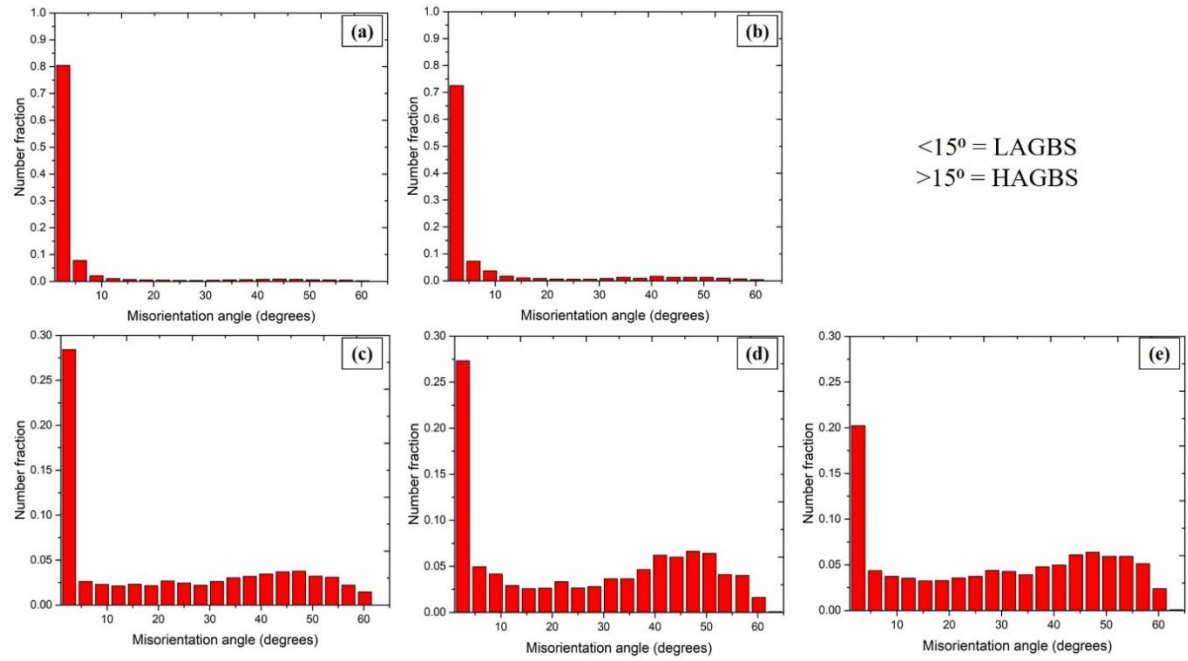


Figure 4.36: Misorientation angle distributions for the (a) AA5083-BM, (b) AA6061-BM, SZ of the (c) ACFSW, (d) NCFSW and (e) WCFSW.

4.3.3.4 Scanning electron microscope

SEM images of the as-received base materials and SZ of the FSWed joints at various cooling conditions are discussed in **Figure 4.37** and **Figure 4.38** along with EDS analysis. In terms of constituent elements, AA5083-H111 has two main intermetallics. The intermetallics in BM include the Al (Fe, Mn, Mg/Si) phase and Al-Mg phase as shown in location 1 and location 2 of the EDS spectrum (**Figure 4.37a**). The most common intermetallics of AA6061-T6 alloy are Al (Fe, Mn, Si) and Mg-Si as shown in **Figure 4.37b** along with the corresponding EDS spectrum shown in location 1 and location 2 [Kartsonakis et al., (2016)]. To get a clear picture of the impact of the cooling environment on dissimilar FSWed AA5083-6061 joints, the precipitation behavior of each sample was examined as shown in **Figure 4.38**. EDS analysis was performed at the SZ of the ACFSW joint and the corresponding EDS spectrum of the distinct intermetallics evolved are also shown above the SEM image (**Figure 4.38a**). Three distinct particle locations of the ACFSW sample suggest that Al (Fe, Mn), Al-Fe-Si, and Al-Mg are among the intermetallic phases precipitated as shown in locations 1, 2, and 3, respectively. The coarser intermetallics present in both the base materials of AA5083 and AA6061 were disintegrated into fine particles and were distributed in the SZ due to the intense stirring action of the FSW tool (**Figure 4.38a**). From the EDS analysis carried out for base materials and the SZ of the FSWed joint, it is confirmed that precipitation, dissolution, and re-precipitation occurred during the joining of dissimilar AA5083-6061 FSWed joints.

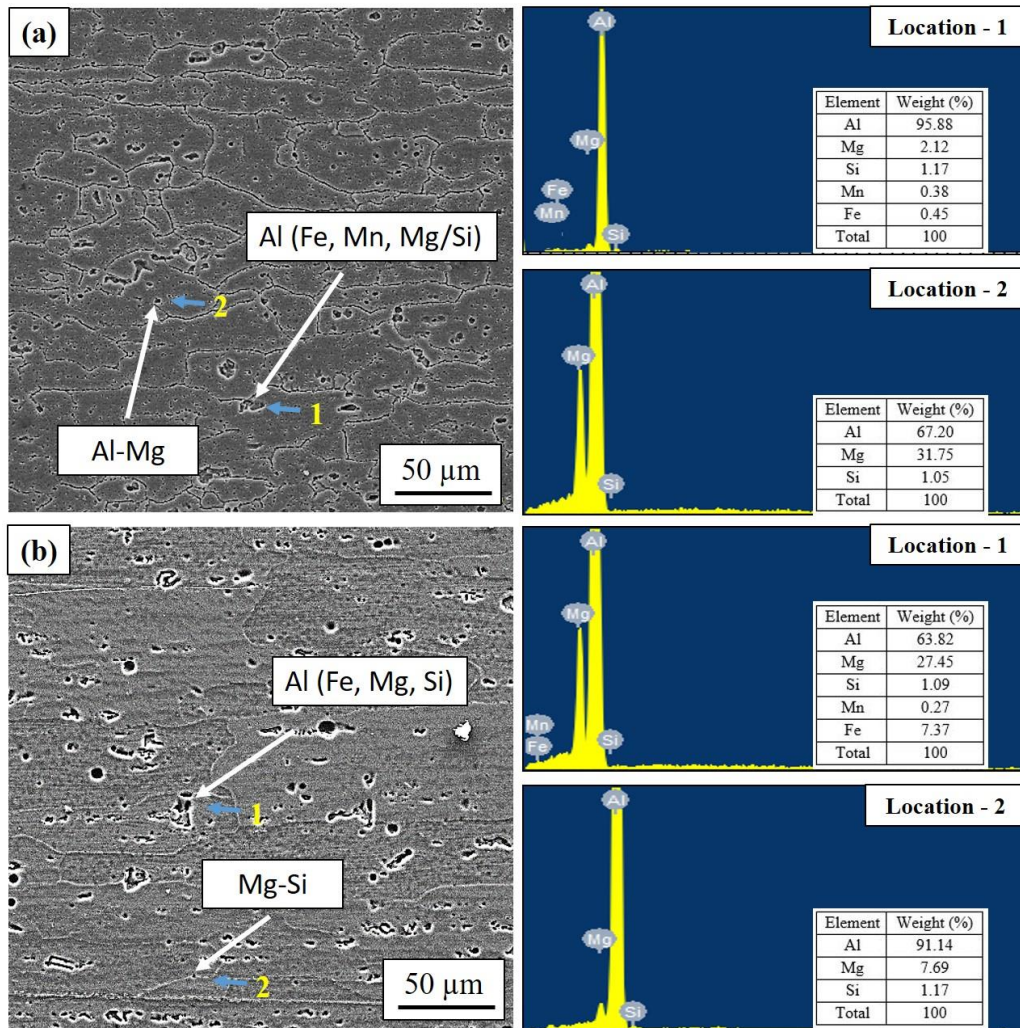


Figure 4.37: SEM-EDS images of as-received base materials (a) AA5083-H111 and (b) AA6061-T6

The intermetallics Al-Fe-Mn and Al-Mg were precipitated from the AA5083 matrix and fragmentation or aggregation of these particles occurred as a result of stirring during FSW. On the other hand, the second phase precipitated out of AA6061 was mainly Al-Fe-Mn-Si. The main phase responsible for the strengthening of 6061 alloys was the β'' phase (Mg_2Si), which was very small and could not be detected by SEM and was partially or completely dissolved [Salih et al., (2020)]. Furthermore, during the thermal cycle of FSW, the increased temperature in the weld can cause pre-existing intermetallic particles to develop or new intermetallic particles to precipitate [Guo et al., (2014)]. Moreover, the reduction in the size of larger particles thereby restricting the coarsening of smaller ones during FSW could be explained by a combination of factors stirring and involving external cooling. In the case of NCFSW and WCFSW samples, very fine intermetallics (Al-Fe-Mn) and (Al-Fe-Si) were seen in the SZ (Figure 4.38b-c). Additional cooling with NCFSW and WCFSW prevents the growth of intermetallics which resulted in the distribution of fine intermetallics (Figure 4.38c). This

confirms that the heat generation and cooling environment are critical factors for precipitation, dissolution, and coarsening of intermetallic particles. So, the intermetallic particle coarsening is avoided due to lower peak temperature generation by using an externally used cooling environment in the welded zone.

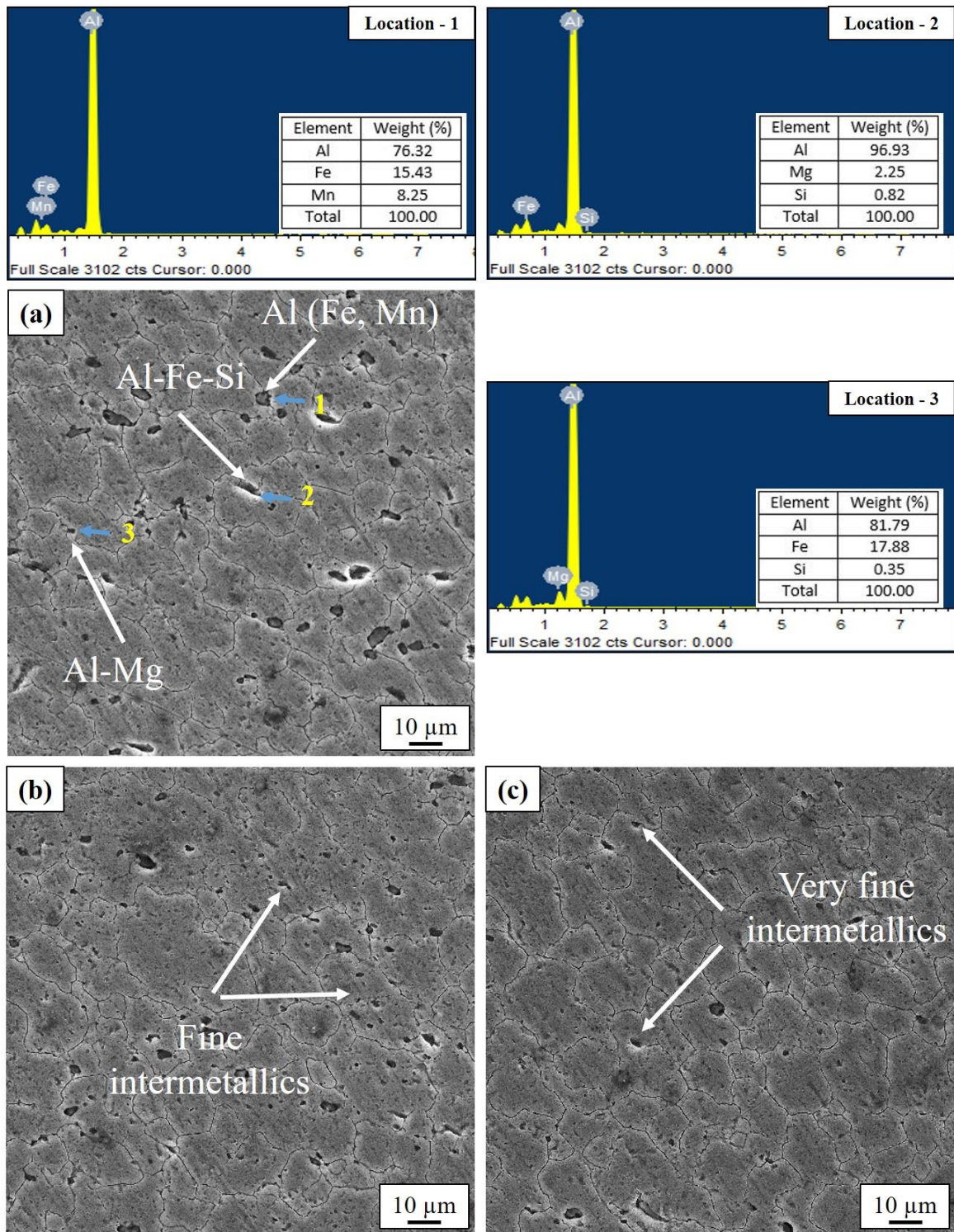


Figure 4.38: (a) SEM images of the dissimilar FSWed AA5083-AA6061 joints of (a) ACFSW (along with EDS analysis at location 1, location 2 and location 3), (b) NCFSW and (c) WCFSW

4.3.4 Phase analysis

Figure 4.39 shows the XRD patterns taken from base materials and the stir zone of FSWed joints to determine the phase composition. While EDS analysis revealed the composition of intermetallic phases, XRD analysis was done to confirm their presence. The intermetallics detected in AA5083 base material were Al_3Mg_2 and Al_6FeMn . Similarly, Mg_2Si and $\text{Al}_{19}\text{Fe}_4\text{MnSi}$ were detected in AA6061. Heat produced during the FSW process appeared to increase diffusion between the stirred AA5083 and AA6061 alloys, allowing distinct Al-Mg, Al-Fe-Si and Al(Fe, Mn) intermetallic compounds to form. Due to this, four phases were detected at SZ, which include Al_3Mg_2 , Mg_2Si , AlFe_2Mn and $\text{Al}_2\text{Fe}_3\text{Si}_4$. The strengthening precipitate Mg_2Si which was sensitive to heat input and not detected in SEM images of FSWed joints was detected at this juncture. The low intensity of aluminium in all the welded samples compared to base materials is due to refinement of the grain structure. The intensity of the intermetallics formed by ACFSW was slightly higher than that of NCFSW and WCFSW joints. Compared with NCFSW and WCFSW joints, the higher heat input of FSW in ACFSW joint has modified the part and sizes of intermetallic phases. The minimum peak intensities of the WCFSW joint suggest the formation of the intermetallic formation of minimum size and in line with the results of the SEM study.

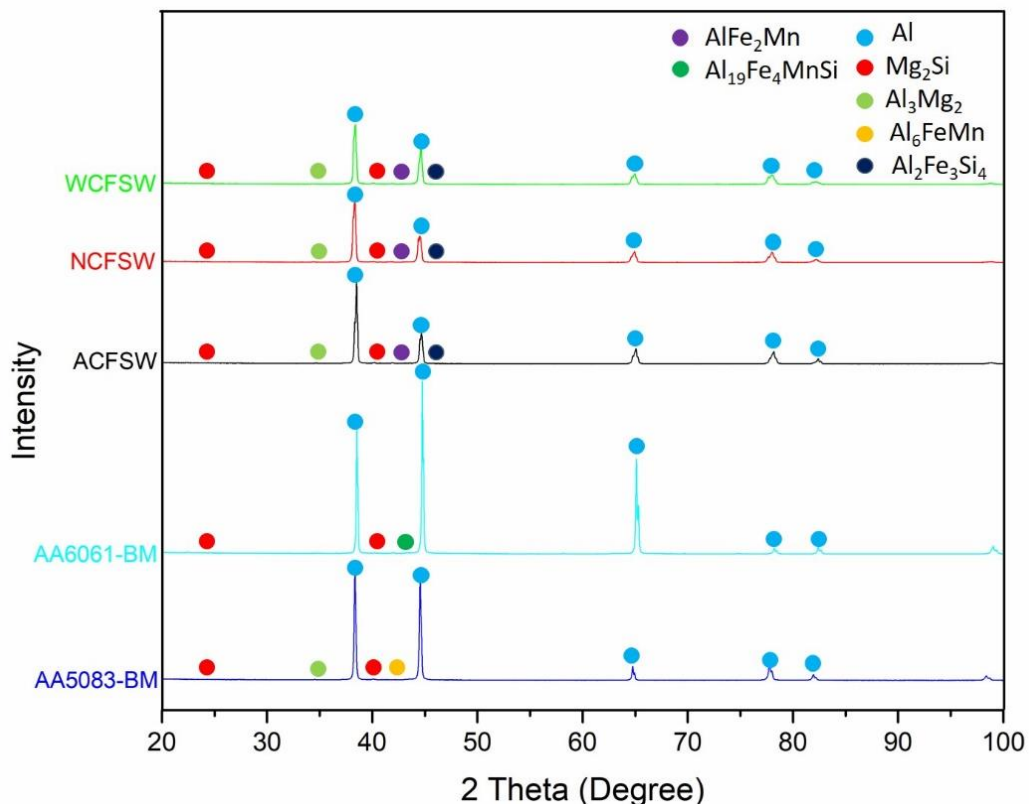


Figure 4.39: XRD results of base materials and FSWed samples

4.3.5 Corrosion behavior

4.3.5.1 Potentiodynamic polarization test

Figure 4.40 shows the PDP curves of the base materials and FSWed samples. The data extracted from PDP curves such as corrosion potential (E_{corr}) and corrosion current (i_{corr}) are represented in Table 4.9. From the results, it was observed that AA5083-BM possessed the most positive corrosion potential of -804 mV and while the most negative E_{corr} of -948 mV was reported for AA6061-BM. The (E_{corr}) of SZ of all of the FSWed conditions lay between AA5083-BM and AA6061-BM, supporting the mixed potential hypothesis of corrosion. In general, E_{corr} signifies the corrosion tendency of the sample, and i_{corr} values quantify the corrosion rate. From Table 4.9, it is observed that both base materials have lower i_{corr} values than FSWed samples. The lower i_{corr} signifies better corrosion resistance.

The corrosion resistance of FSWed aluminum alloys is affected by the existence of intermetallics. They are critical in localized corrosion processes, and they can also be the primary cause [Davoodi et al., (2016)]. As discussed earlier, the intermetallic phases precipitated in FSW of dissimilar AA5083-6061 include Al (Fe, Mn), Al-Fe-Si, and Al-Mg-Si while the intermetallic particles detected from XRD are Al_3Mg_2 , Mg_2Si , $AlFe_2Mn$ and $Al_2Fe_3Si_4$. Intermetallic particles containing iron, such as $AlFe_2Mn$ and $Al_2Fe_3Si_4$, constitute cathode. The localized corrosion of aluminium is mainly due to the galvanic coupling between micro cathodes and micro anode distributed over the metal surface [Bocchi et al., (2018) and [Davoodi et al., (2016)]. In FSWed dissimilar AA5083-6061 joint, the E_{corr} of intermetallics is nobler (acts as a cathode) compared to aluminium matrix (acts as an anode). During the corrosion phase, the aluminium matrix surrounding the intermetallics dissolves, resulting in pit formation. Also, the presence of a precipitate-free zone hastens the corrosion process. The galvanic coupling also occurred as a result of the large potential gap between PFZ and neighboring precipitates, which increased metal corrosion [Sinhmar et al., (2017)]. Some precipitates like Mg_2Si , which start to dissolve quickly during ACFSW were observed in the joints using cooling media. The presence of the precipitates was confirmed by XRD in NCFSW and WCFSW joints (Figure 4.39). Within FSWed samples, the joint made with WCFSW yielded better corrosion resistance compared to ACFSW and NCFSW joints, which is attributed to the difference in intermetallics characteristics. The coarse intermetallic particles, in contrast to fine intermetallics, are more likely to form galvanic cells with Al matrix. Furthermore, the average grain size of WCFSW was lower than NCFSW and ACFSW. The broad grain boundary area was formed by fine grains. The joint's corrosion resistance improved with large grain

boundaries being attributed to the active site for the formation of oxide films. As a result, WCFSW stir zone showed higher corrosion resistance than other joints.

The exposed surface of the base material and FSWed samples were examined after the PDP test as shown in **Figure 4.41**. The fewer pits were evenly distributed on the surface of both AA6061-T6 and AA5083-H111 base materials as shown in **Figure 4.41a and b** respectively. The corrosion propagation in AA6061 and AA5083 was intergranular for both materials. It is interesting to note that the number of pits was more in the case of ACFSW (**Figure 4.41c**), whereas it decreased for NCFSW and WCFSW samples (**Figure 4.41d and e**). This is explained by the fact that WCFSW sample has fine intermetallics and was protected during galvanic coupling.

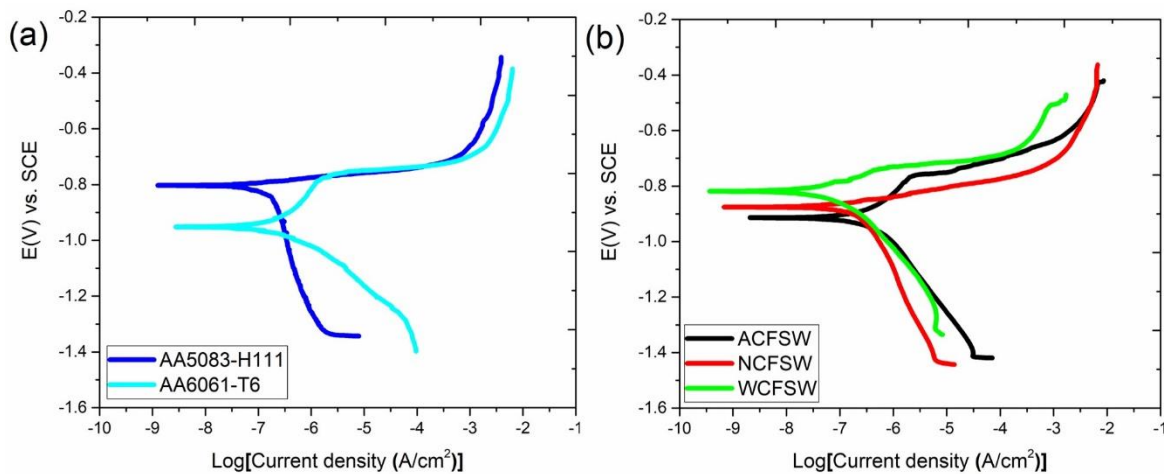


Figure 4.40: Tafel curves of BM and FSWed samples.

Table 4.9: Corrosion potentials and corrosion current density of the base materials and dissimilar FSWed AA5083-AA6061 sample conditions.

Sample conditions	Corrosion potential E_{corr} (mV (SCE))	Current density i_{corr} (A/cm^2)
AA5083-BM	-804	0.12×10^{-6}
AA6061-BM	-948	0.76×10^{-6}
ACFSW	-911	0.94×10^{-6}
NCFSW	-876	0.72×10^{-6}
WCFSW	-813	0.45×10^{-6}

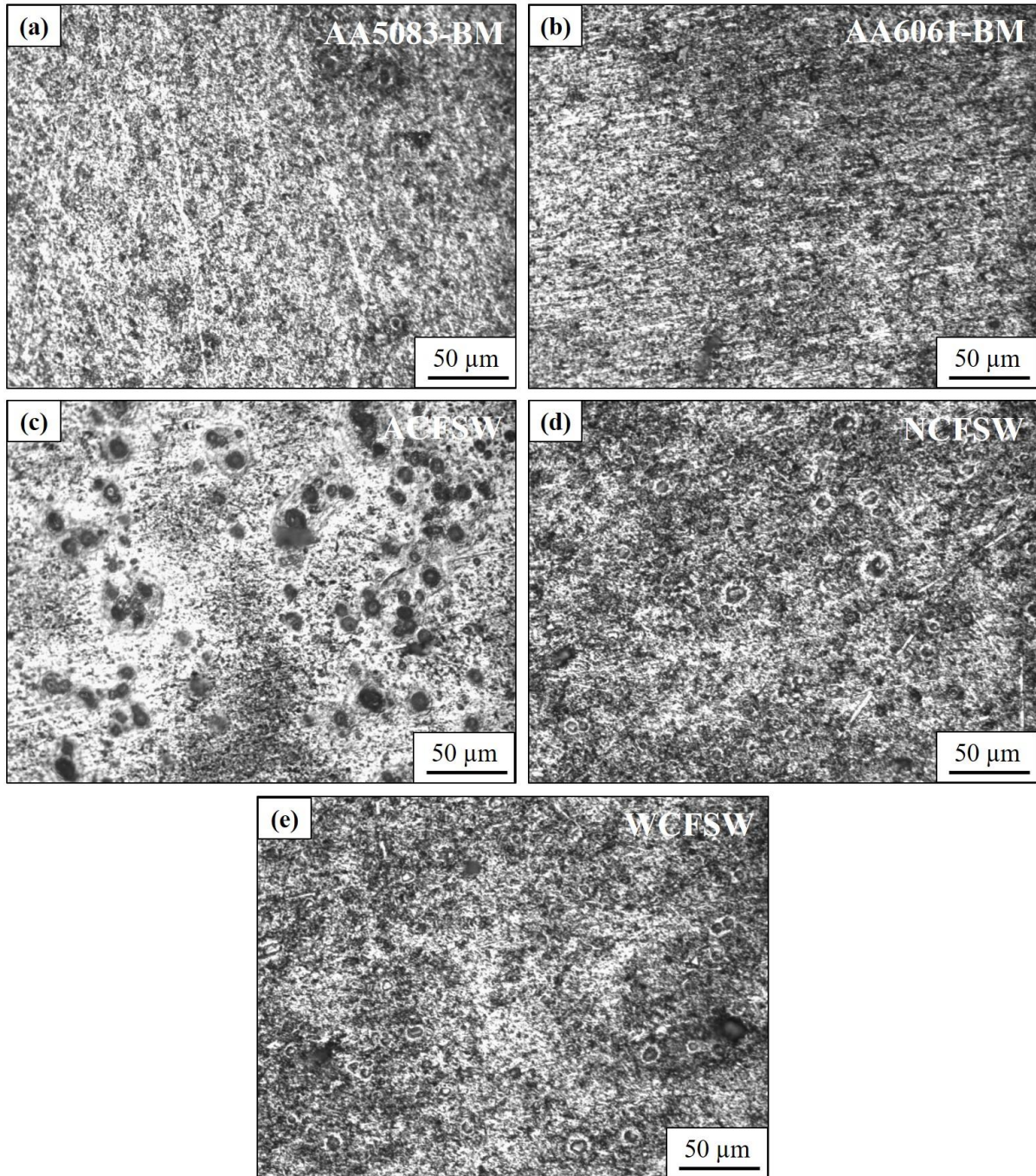


Figure 4.41: Optical micrograph images of: (a) AA5083-BM (b) AA6061-BM, (c) ACFSW, (d) NCFSW and (e) WCFSW

4.3.5.2 Electrochemical impedance spectroscopy test

The EIS findings, which were obtained at OCP after 30 minutes of submersion in test solution are shown in **Figure 4.42a**. The equivalent circuit as shown in Figure 4.42b was used to fit the results. The values fitted are represented in **Table 4.10**. In the equivalent circuit model, constant phase elements (CPE) were used. The findings of CPE are expressed in terms of solution resistance (R_s), polarization resistance (R_p), admittance (Y_0), and a number of variables (n), Where n values show the deviation of a capacitor from the ideal capacitor.

Admittance behaves like an inductor, resistor and capacitor at $n = -1, 0, 1$ respectively. For all-welded joints, the solution resistance (R_s) obtained from EIS fitting were almost equal under all conditions because of changing the solution for each sample. All the curves in **Figure 4.42a** presented similar shapes suggesting similar mechanisms for all the samples, with differences only in terms of the magnitude of impedance. The diameter of the loop represents the corrosion resistance of FSWed joints welded under various cooling conditions. The greater the loop's diameter, the higher the impedance and thus the higher the corrosion resistance [Sinhmar et al., (2018)]. WCFSW joint showed a larger loop compared to ACFSW and NCFSW joints. Thus, the corrosion resistance of WCFSW joint is higher than that of other joins. Also, the higher the polarization resistance, the greater the corrosion resistance. Polarization resistance was higher in the case of WCFSW joint and lowest in the case of ACFSW joint. As a result, the EIS fitting values match the Tafel polarization measure.

Table 4.10: The fitting results of the EIS data at SZ of dissimilar AA5083-AA6061 FSWed joints

Sample conditions	R_s (Ω)	R_p ($k\Omega \cdot \text{cm}^2$)	Y_o ($\Omega^{-1} \text{cm}^{-2} \text{s}^n \times 10^{-5}$)	n
ACFSW	4.545	24.17	1.37	0.878
NCFSW	4.723	27.25	1.23	0.892
WCFSW	5.063	34.51	1.14	0.923

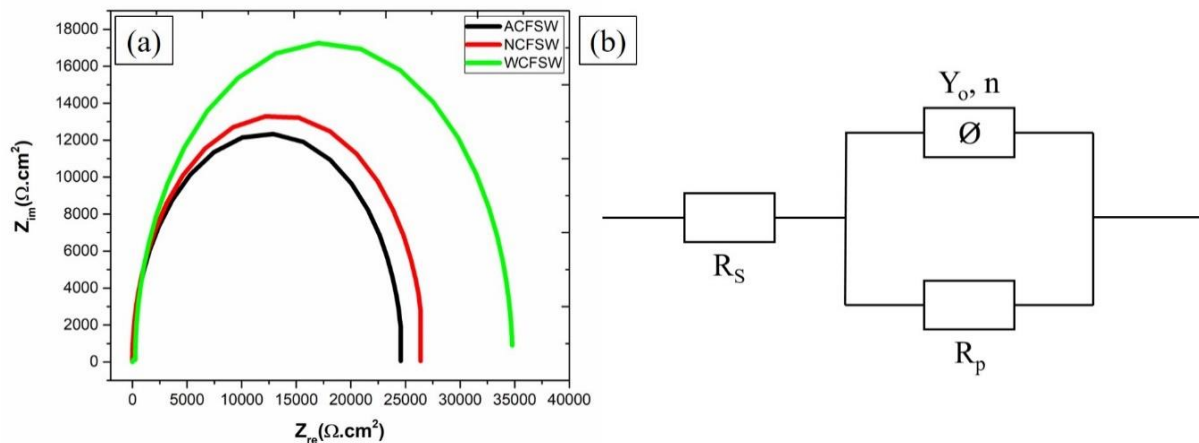


Figure 4.42: (a) EIS plot of FSWed samples and (b) Equivalent circuit used for fitting of the curves obtained from EIS test.

4.3.6 Mechanical testing

4.3.6.1 Microhardness

The hardness at the mid-section in the transverse cross-section of the FSWed joints was measured, with the microhardness distribution across welded zones of all conditions shown in **Figure 4.43**. Under different conditions of operation, the SZ and adjacent zones of FSWed joints showed lower hardness than that of base materials but the extent of softening was more severe in HAZ of the retreating side. This drop-in HAZ hardness in the case of ACFSW was the result of weld thermal heating, which was then mitigated by applying an external cooling environment. In the water-cooled weld and air-cooled weld, the maximum and minimum hardness values were recorded across the joint, respectively. The temperature generated during FSW ($\sim 480^{\circ}\text{C}$) was high enough to coarsen or dissolve strengthening precipitates in SZ and HAZ [Peel et al., (2006)]. However, when external cooling media were used, the optimal temperature was much lower ($140\text{-}380^{\circ}\text{C}$), minimizing coarsening and dissolution of strengthening precipitates [Ghetiya et al., (2017)]. According to the microhardness test results, using external cooling decreased the peak temperature of the weld nugget and increasing the rate of heat extraction as a result, there was an improvement in the hardness at SZ and HAZ. Besides, the cooling environment decreased the peak temperature hold time, decreased post-weld grain growth even further. The use of a cooling environment increases the hardness of HAZ by reducing the degree of grain coarsening (as discussed in **section 4.3.3**). WCFSW samples have the highest hardness in HAZ, whereas air-cooled welds have the lowest. Meanwhile, slightly lower hardness values were measured for NCFSW as compared with WCFSW. This is due to the different grain sizes, changes in the amount of peak temperature increase and peak temperature hold time affecting the local hardness of HAZ.

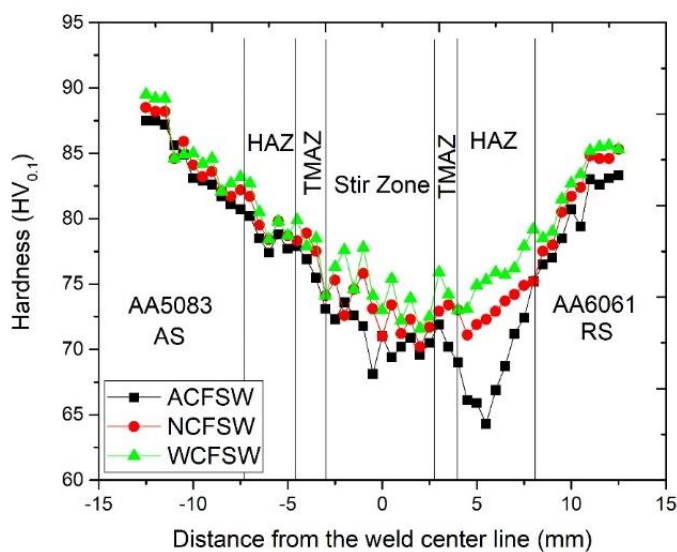


Figure 4.43: Hardness distribution across the FSWed joints.

4.3.6.2 Tensile properties

The stress-strain graph obtained by tensile testing of base material and FSWed joints is shown in **Figure 4.44a** while the **Figure 4.44b** shows the fractured specimens. The results obtained from the stress-strain graph of each sample are represented in **Table 4.11**. The tensile strength and elongation were lowered in all FSWed joints compared to that of base materials. The tensile strength tends to increase in WCFSW and NCFSW compared to ACFSW, whereas marginal reduction in elongation was observed with the use of cooling media (**Figure 4.44**). In WCFSW, a joint efficiency (ratio of the yield strength of joint to the yield strength of AA6061 base material) of 96.00% was achieved. The lowest joint efficiency of 85.71% resulted in the case of ACFSW joint. In general, the hardness distribution across the joint is used to predict tensile strength, and joints with higher hardness have better tensile strength [Rajakumar et al., (2012)]. The enhancement in hardness at SZ and HAZ in WCFSW is due to the lowering of peak temperature of joint compared to ACFSW and the reduced peak temperature resulted with increase in the tensile strength of the joint [Derazkola et al., (2019)]. According to the tensile results of the welded joints, the YS and UTS of the joint improved by regulating the weld temperature distribution with external cooling. However, excessive prior cooling by liquid nitrogen produced lower strength than WCFSW, which may be attributed to lower heat input to the weld that resulted in inadequate consolidation of the material at the SZ (as discussed in **section 4.3.3.2**).

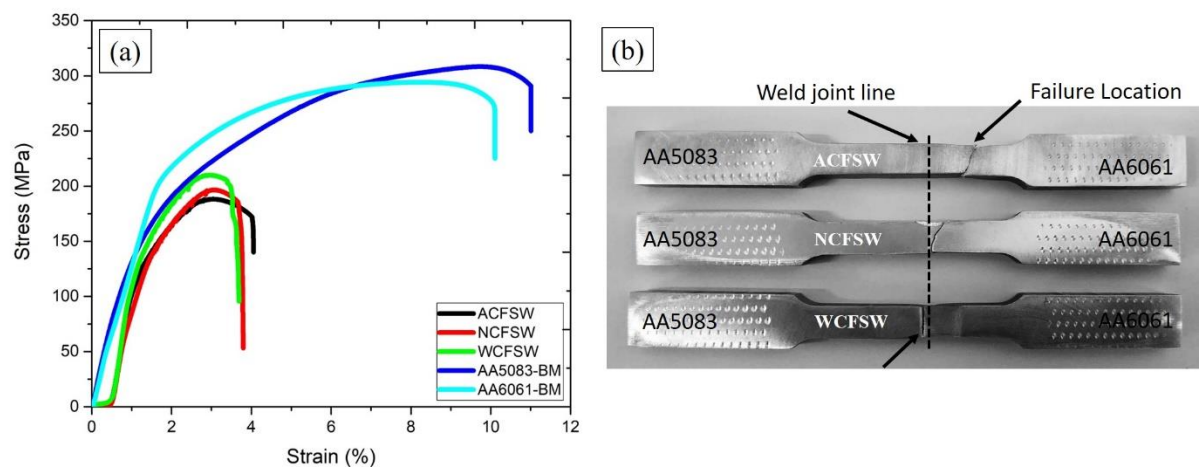


Figure 4.44: (a) Stress-strain curves of base materials and FSWed samples and (b) Appearance of the failed tensile samples.

Table 4.11: Tensile properties of the base materials and dissimilar FSWed AA5083-AA6061 sample conditions.

Sample condition	Yield strength (MPa)	Ultimate tensile strength (MPa)	Tensile elongation (%)	Joint efficiency (%)	Fracture Location
AA5083-BM	175 \pm 4	311 \pm 5	11.7 \pm 0.4	-	-
AA6061-BM	226 \pm 5	294 \pm 3	10.1 \pm 0.5	-	-
ACFSW	150 \pm 2	188 \pm 2	4.3 \pm 0.2	85.71	RS (HAZ)
NCFSW	157 \pm 1	201 \pm 1	3.8 \pm 0.2	89.71	SZ
WCFSW	168 \pm 3	212 \pm 3	3.5 \pm 0.3	96.00	SZ

Figure 4.45 depicts the fractography images of the base materials and FSWed samples. All the samples revealed the presence of dimples with varying shape and size indicating a ductile mode of fracture. The fracture surface of base metal (**Figure 4.45a and b**) showed large and deep dimples indicating a ductile-dominated fracture. The fracture surface of the ACFSW sample (**Figure 4.45c**) showed similar fracture morphology of fewer and shallow dimples than the AA6061 base material. The results agree well with that of tensile results showing more elongation in base materials than FSWed joints. The fractured surface of NCFSW and WCFSW was found to be a mix of dimples and flat surfaces. This shows a fracture mode that exhibits both ductile and brittle nature (**Figure 4.45d and e**). The joints produced with cooling media such as WCFSW and NCFSW failed at low deformation compared with ACFSW samples. However, a large number of dimples were not produced; instead, some flat surfaces and facets appeared which could be attributed to low plastic deformation during tensile failure.

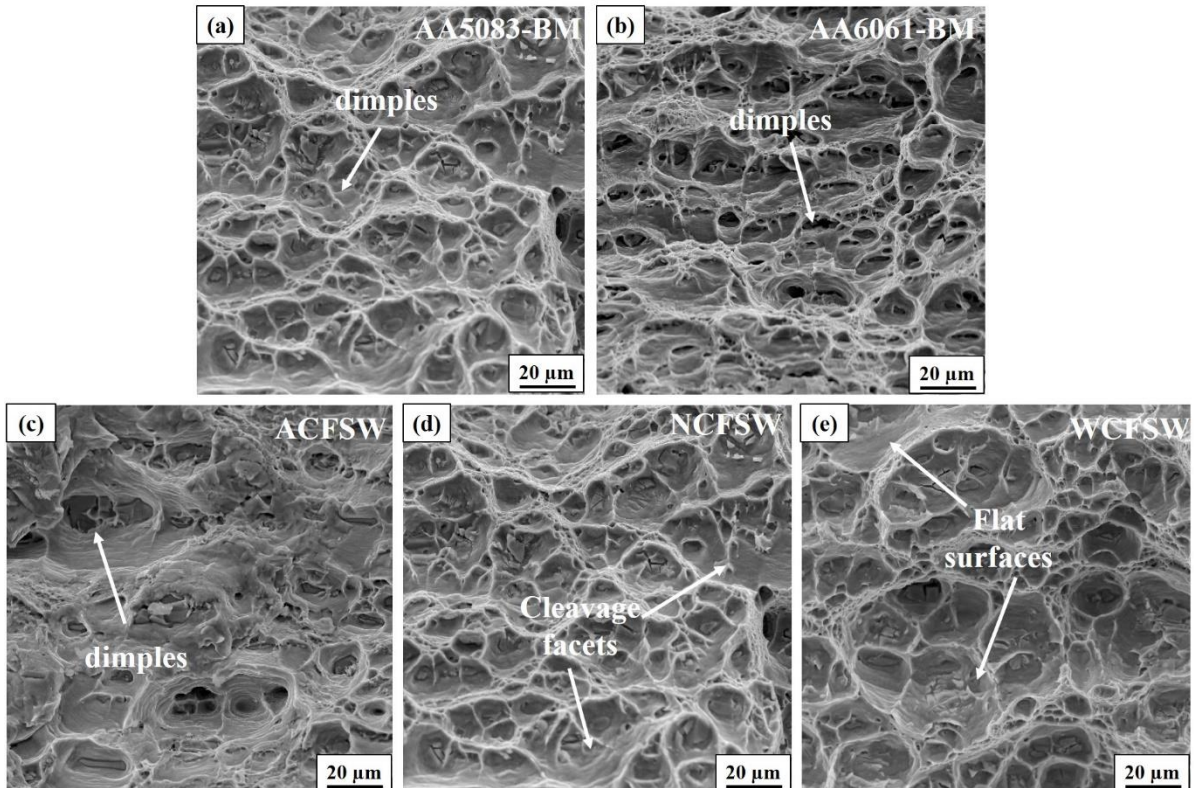


Figure 4.45: Fracture surfaces of the (a) AA5083-BM, (b) AA6061-BM, (c) ACFSW, (d) NCFSW and (e) WCFSW.

4.3.7 Summary

In the present study using FSW process, dissimilar AA5083-6061 were joined together in air, liquid nitrogen, and water cooling environment. Microstructural observations revealed that the FSW in a cooling environment reduced the width of SZ and grain size at HAZs in NCFSW and WCFSW joints relative to ACFSW joint due to rapid heat dissipation. EBSD results showed the presence of fine grain size and a large fraction of HAGBs at the SZ of the WCFSW joint compared to ACFSW due to dynamic recovery, recrystallization and grain growth. Due to the use of external cooling media, the degree of the impact of the weld thermal cycle decreased, resulting in limited post-weld grain growth and better grain refinement in WCFSW joint. From Tafel and EIS results, it was observed that the corrosion resistance of FSWed joints was lower than that of base materials. The corrosion resistance of FSWed joint prepared using a water-cooling environment improved significantly compared to that of ACFSW and NCFSW joints. The hardness values of heat affected zone were lower than that of the base metals. The minimum hardness zone in the ACFSW joint was located at RS-HAZ, which shifted to SZ in the case of NCFSW and WCFSW joints. YS and UTS of the welded joints were found to be lower than that of base materials. However, the water-cooled joint produced the highest joint efficiency of 96% in comparison to ACFSW and NCFSW joints.

4.4 Analysing microstructure, texture evolution and tensile behavior of dissimilar 5083-6061 aluminium alloys welded using air and water-cooled friction stir welding

4.4.1 Introduction

Further to the previous study on understanding the effect of cooling environment on resulting corrosion resistance and mechanical properties, it was felt to investigate the tensile behavior along the SZ and at the HAZs. Frictional and adiabatic heating cause heat to be generated during FSW to soften the material around the tool. The mechanical mixing of plasticized material surrounding the pin causes joint formation. Severe plastic deformation combined with exposure to high temperatures is responsible for local microstructural alterations and material properties modifications during FSW. Stir zone (SZ), heat affected zone (HAZ), thermomechanically affected zone (TMAZ), and base material (BM) are four different microstructural zones that evolved during FSW. This variation in microstructure is more pronounced while welding AA2xxx, AA5xxx, AA6xxx and AA7xxx type aluminium alloys. Predominantly, the heat generated during FSW alters the weld zone's microstructure and the region surrounding the weld zone in aluminium alloys. Although no melting occurs due to the heat generated during FSW, the mechanical characteristics of the material nevertheless deteriorate. Therefore, it is critical to extract excess heat generated at the weld to limit mechanical property degradation. There has been a lot of research on microstructure and mechanical properties of FSWed dissimilar aluminium alloys, with such research using different welding parameters and cooling media. Some researchers also studied the different tensile properties of FSWed aluminium alloys from the viewpoint of strain hardening behavior. As-received base materials AA5083 and AA6061 have varying mechanical properties (strength/hardness, ductility and deformation) and thermophysical properties. Moreover, very little attention was given to tensile properties and strain hardening behavior on the different zones of the FSWed joints. Therefore, the effect of air and water cooling FSW dissimilar 5083-6061 aluminium alloys on microstructure characteristics (EBSD maps, texture evolution) and mechanical behavior (such as tensile strength, strain hardening exponent, strain hardening rate) was studied in the present investigation.

4.4.2 Experimental methodology

A numerically controlled FSW machine was used to weld AA5083-H111 and AA6061-T6 of 300 x 70 x 6 mm dimensions along the rolling direction in butt joint configuration. **Figure 4.46a** shows a schematic diagram of the FSW process. The tool rotational speed of 1400 rpm and traverse speed of 60 mm/min of the FSW process were kept constant. A tool made of H13

tool steel of tapered threaded conical pin profile and with 3° concavity at the shoulder was used. Throughout the experiments, a tool plunge depth of 0.2 mm and 1° tilt angle were maintained.

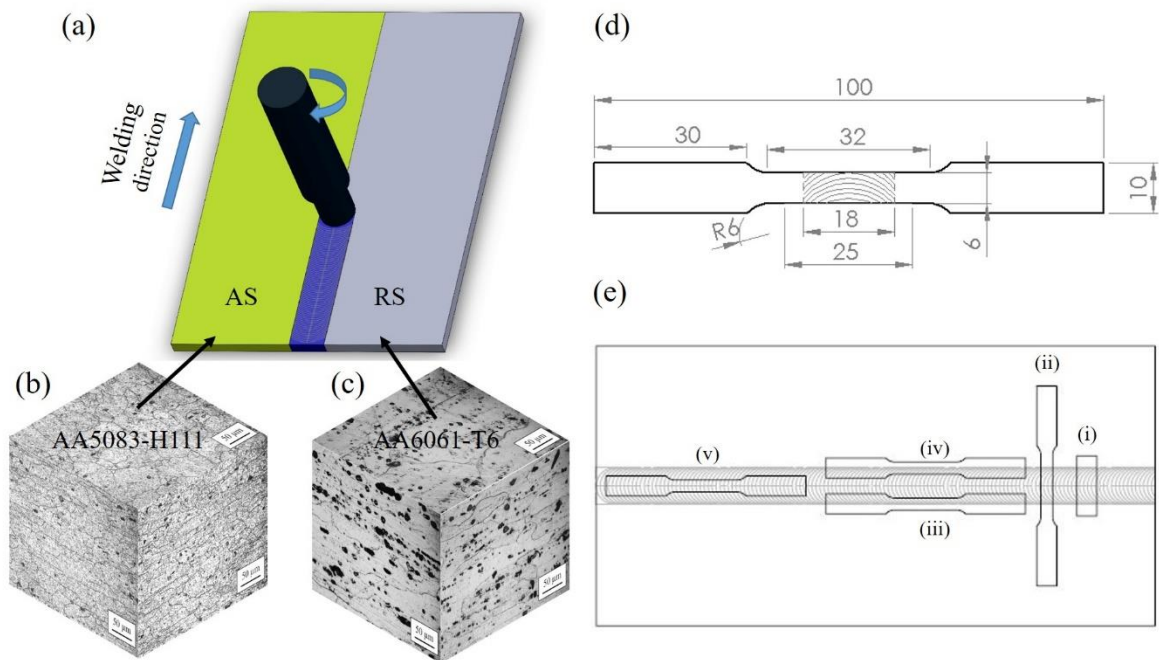


Figure 4.46: (a) Schematic illustration of FSW process, (b) Pseudo-3D optical micrograph of AA5083-H111 (c) Pseudo-3D optical micrograph of AA6061-T6, (d) Schematic with dimensions of a tensile test specimen and (e) Schematic diagram for sample preparation.

Figure 4.46a illustrates the schematic representation of the FSW experiment. The samples were labeled according to the cooling condition. Friction stir welding was done in ambient air-cooled (ACFSW) and water-cooled (WCFSW) conditions. For microstructural analysis, samples were sliced in perpendicularly/traverse direction to the weld direction as shown in **Figure 4.46e** (i). The pseudo-3D optical microstructural pictures of base metals are shown in **Figure 4.46b** and c. Microstructure testing was conducted using optical microscopy (OM) and Scanning electron microscope (SEM) with energy dispersion spectroscopy (EDS) and EBSD. Tensile specimens were prepared according to ASTM E8 specifications, as shown in **Figure 4.46d**. As shown in **Figure 4.46e**, the tensile specimens were extracted from four different locations of the welded joints such as the transverse (ii), longitudinal heat-affected zones (advancing (iii) and retreating side (iv)) location and longitudinal of stir zone (v), to welding direction from both conditions (ACFSW and WCFSW) of FSWed process conditions as shown. Tensile tests were performed using a 100 kN capacity universal testing machine (UTM) displacement-controlled mode with a crosshead speed of 0.5 mm/min. SEM was used to examine the fracture characteristics.

4.4.3 Microstructure observation

4.4.3.1 Optical Microscopy

Figure 4.47 and **Figure 4.48** illustrate the microstructures derived from ACFSW and WCFSW joints at various positions. **Figure 4.47a** depicts the ACFSW joint's cross-sectional macrostructure. The heat generated by changing cooling conditions during FSW has a considerable effect on HAZ and SZ alteration, as seen in the macrographs. The HAZ-AS and HAZ-RS are shown in **Figure 4.47b** and **c**, respectively. Grain coarsening was experienced at the AA5083-BM and AA6061-BM side HAZ because of the prolonged thermal cycle created during the FSW process. TMAZ is also created simultaneously due to heating caused by friction and mechanical deformation, which resulted in grains being slightly refined and extending upwards (**Figure 4.47d**). The SZ has a refined grain structure as a result of dynamic recrystallization (DRX) induced by severe plastic deformation (SPD) (**Figure 4.47e**).

Similar qualitative observations may be made from the ACFSW joint (see **Figure 4.47**). One main noticeable difference in WCFSW (**Figure 4.48a** shows the macrostructure) is the smaller grain size at HAZs and SZ. The macrostructure of the WCFSW joint also showed narrowed SZ and HAZ widths. In **Figure 4.48b-e**, such a change in microstructure is visible. The heat input in HAZ determines grain size, which is monitored by available cooling conditions during FSW. **Table 4.12** shows the average grain size measured at the HAZ-AS, HAZ-RS, and SZ of ACFSW and WCFSW conditions. As illustrated in **Figure 4.48**, the grain size of the WCFSW joint was determined to be the smallest at HAZ-AS, HAZ-RS, and SZ locations than different locations of ACFSW joint. Grain size varies due to changes in cooling rates. The cooling rate accelerates with the application of external coolant, resulting in shorter peak temperature holding after the weld. The external coolant during welding lowers the maximum temperature generated, which impacts grain alterations during post-weld recovery. EBSD is used to explain in-depth microstructural study at SZ in the subsequent sections.

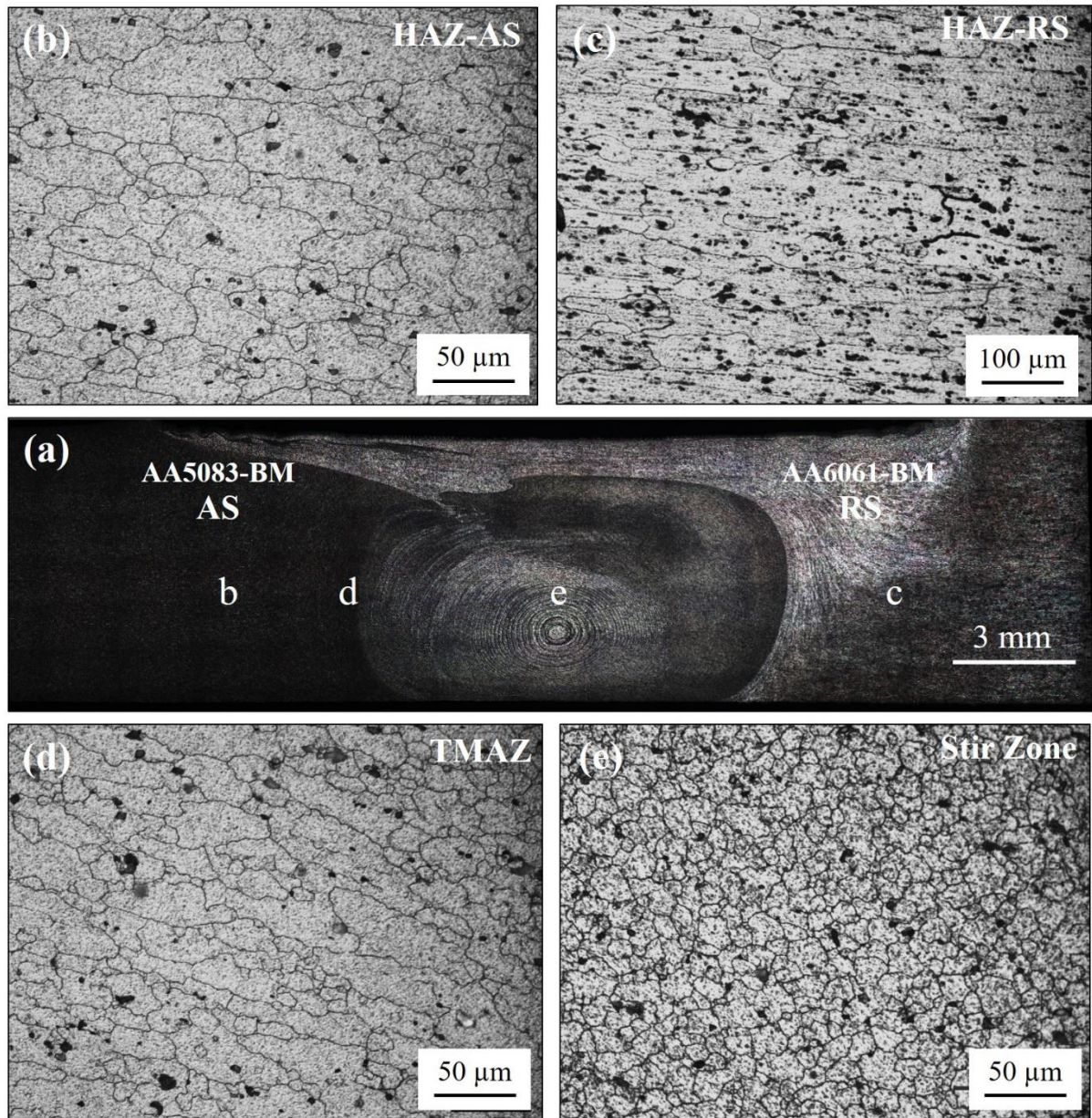


Figure 4.47: Optical images of ACFSW: (a) Macrostructure of ACFSW, (b) HAZ-AS, (c) HAZ-RS, (d) TMAZ-AS, and (e) SZ.

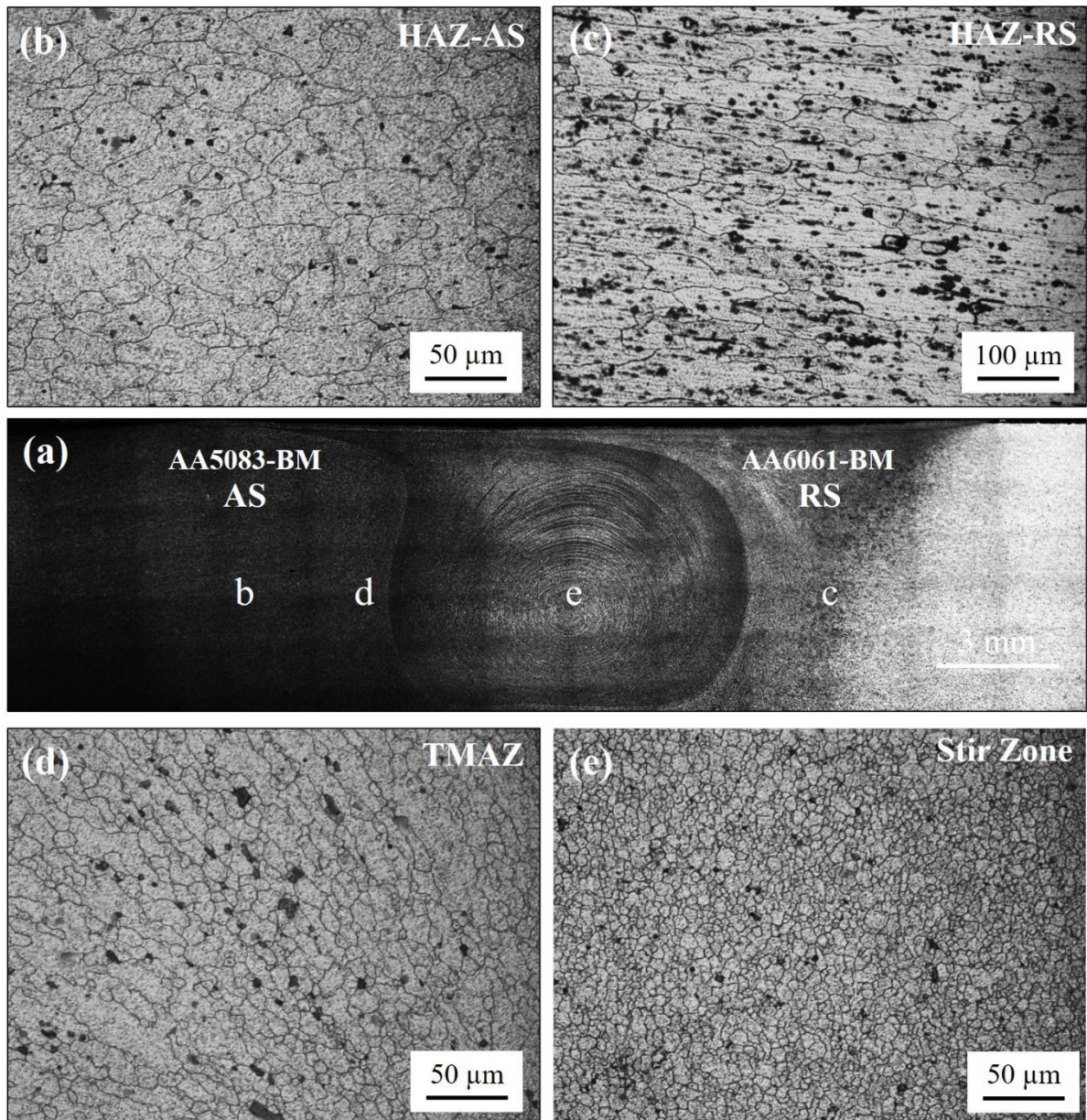


Figure 4.48: Optical images of WCFSW: (a) Macrostructure of WCFSW, (b) HAZ-AS, (c) HAZ-RS, (d) TMAZ, and (e) SZ.

Table 4.12: Average grain size at HAZ-AS, HAZ-RS and SZ of FSWed sample conditions.

Sample conditions	HAZ-AS (μm)	HAZ-RS (μm)	SZ (μm)
ACFSW	39 ± 3	121 ± 18	8.1 ± 3.5
WCFSW	32 ± 4	108 ± 17	3.4 ± 1.2

4.4.3.2 Electron Back Scattered Diffraction

Figure 4.49 illustrates EBSD maps and grain boundary misorientation angles of both BMs and SZs of FSWed joints. The crystallographic orientation of the grains was explained using the microstructure seen with different colors. The rolling process is believed to be responsible for the elongated shape of AA5083 and AA6061 grains (**Figure 4.49a and b**). While SZ is subjected to significant heat input during FSW, simultaneous strong mechanical stirring results in recrystallized grains with fine size at the SZ of the FSWed joint. Abnormal grain growth happens after the recrystallization process due to the availability of extra heat that results from the FSW process. Because grain refining happened only as a result of DRX, the grain size was maximum in ACFSW. This is a result of the phenomena of unrestrained grain expansion (**Figure 4.49c**). During FSW, however, cooling conditions were used to remove excess heat accumulated post recrystallization. Homogeneous heat draining was achieved due to the welded zone's total submersion in the cooling medium. As a result, the smallest grain size was obtained in WCFSW (**Figure 4.49d**).

It is worth noting that the two base materials have a large fraction of LAGBS, which suggests that the BMs are in a severely deformed state, as demonstrated by the results (Figure 4.49e and f). Besides creating fine grains during FSW, the misorientation of grain boundaries is also governed by the amount of heat supplied. From the misorientation angle distributions from **Figure 4.49g and h**, it is apparent that with utilizing water cooling, the fraction of HAGBs increased (**Figure 4.49g**). This is due to minimum heat holding time due to the use of water cooling, which eliminated the formation of substructure, resulting in an increase in the volume percentage of HAGBs in the sample (**Figure 4.49h**).

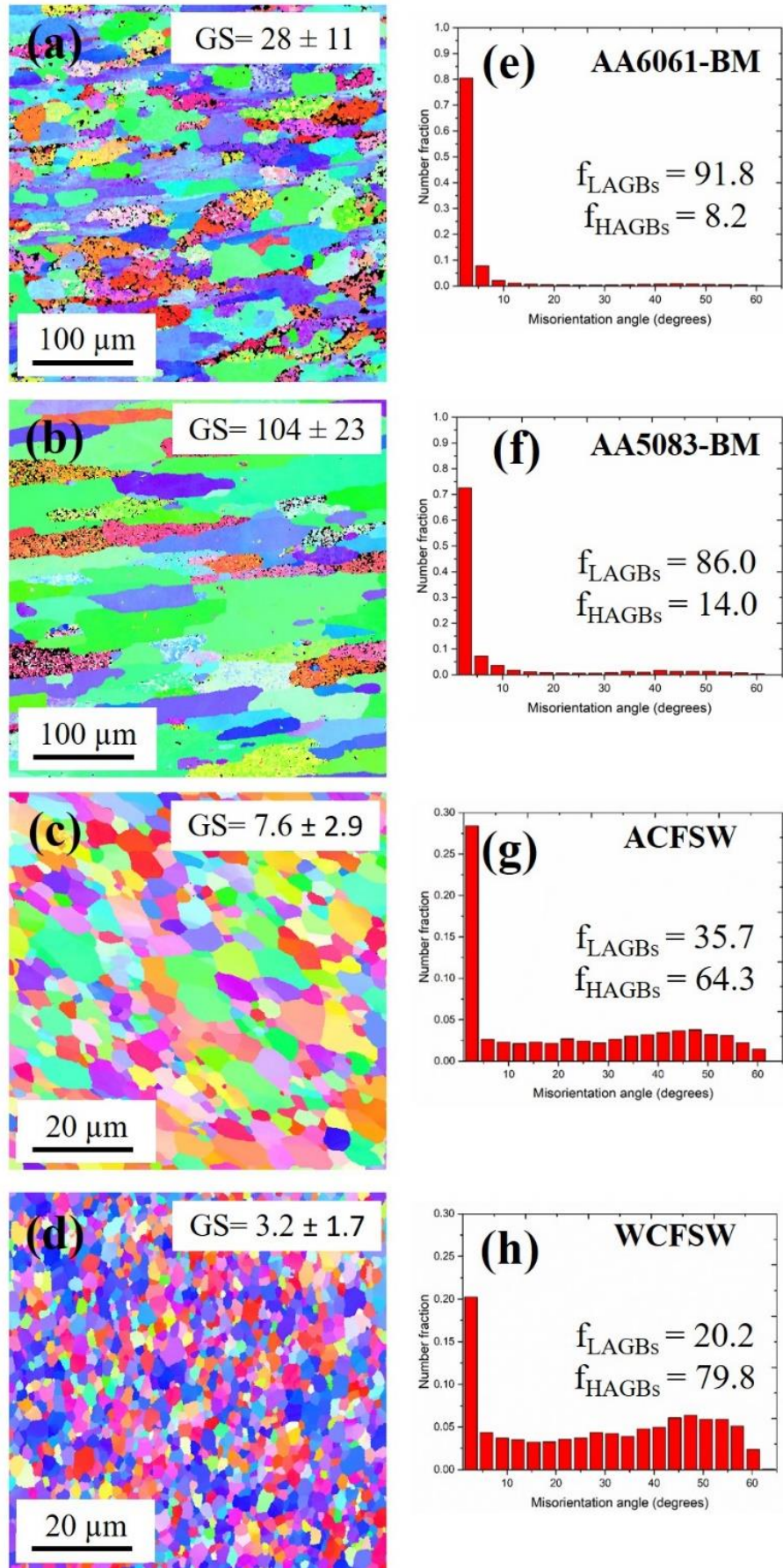


Figure 4.49: EBSD images and Misorientation angle distributions: (a) 5083-BM, (b) 6061-BM, (c) ACFSW-SZ, and (d) WCFSW-SZ.

4.4.3.3 Scanning electron microscopy

Figure 4.50 and **Figure 4.51** show the SEM images along with EDS analysis of as-received BMs and at SZ of FSWed joints. The EDS results from **Figure 4.50a** show that AA5083-BM has Al (Fe, Mn, Mg/Si) and Al-Mg intermetallic phase. AA6061-T6 alloys (**Figure 4.50b**) contained Al (Fe, Mn, Si) and Mg-Si phases. The coarser size precipitates observed in the base metals of AA5083 and AA6061 were dispersed in SZ due to vigorous stirring action (Figure 4.51a). Three distinct intermetallic compounds (IMC) are observed at ACFSW joints, such as Al (Fe, Mn), Al-Fe-Si, and Al-Mg, as shown in **Figure 4.51** due to inter-diffusion of existing precipitates. This shows that Precipitation, re-precipitation and dissolution occur during FSW of dissimilar aluminium alloys. The strengthening precipitate β'' phase (Mg_2Si) generally seen in AA6061-T6 alloy was unable to be detected using SEM analysis [Salih et al., (2020)]. Moreover, coarsening of existing precipitates or the formation of new IMCs occurs due to the thermal cycle caused during FSW [Guo et al., (2014)]. The coarsening of IMC is mainly seen in ACFSW (**Figure 4.51a**) due to excess accumulation of heat. In contrast, additional cooling with water prevented IMC growth by taking away heat, resulting in fine IMC distribution in SZ (**Figure 4.51b**). Therefore, the generation of heat and cooling cycles during FSW are critical conditions for IMC formation dissolution, precipitation, and re-precipitation.

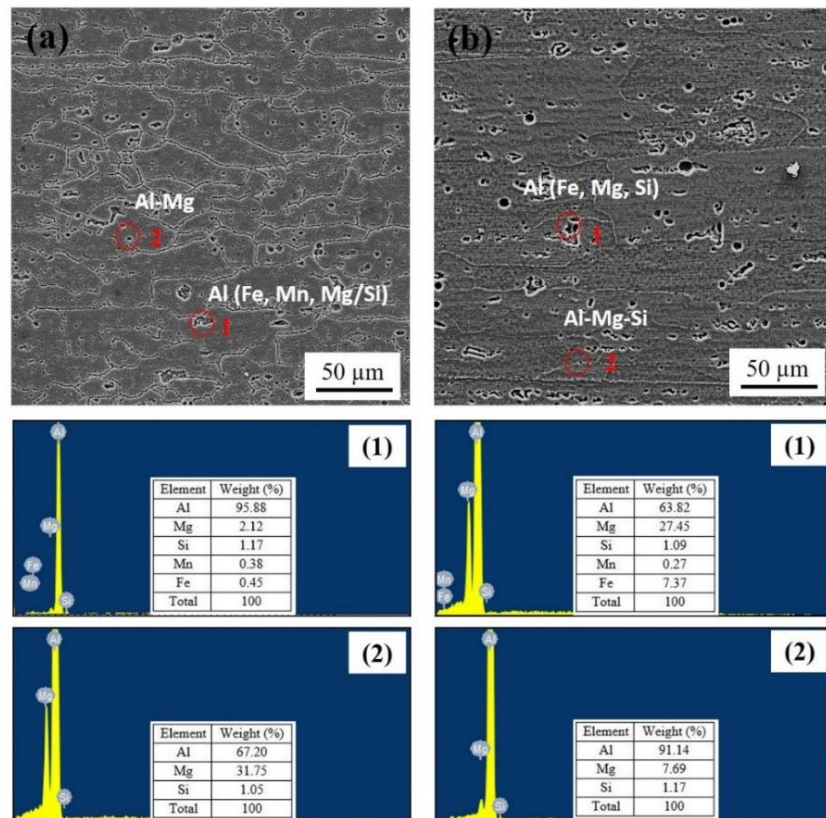


Figure 4.50: SEM images with EDS analysis of (a) AA5083-BM and (b) AA6061-BM

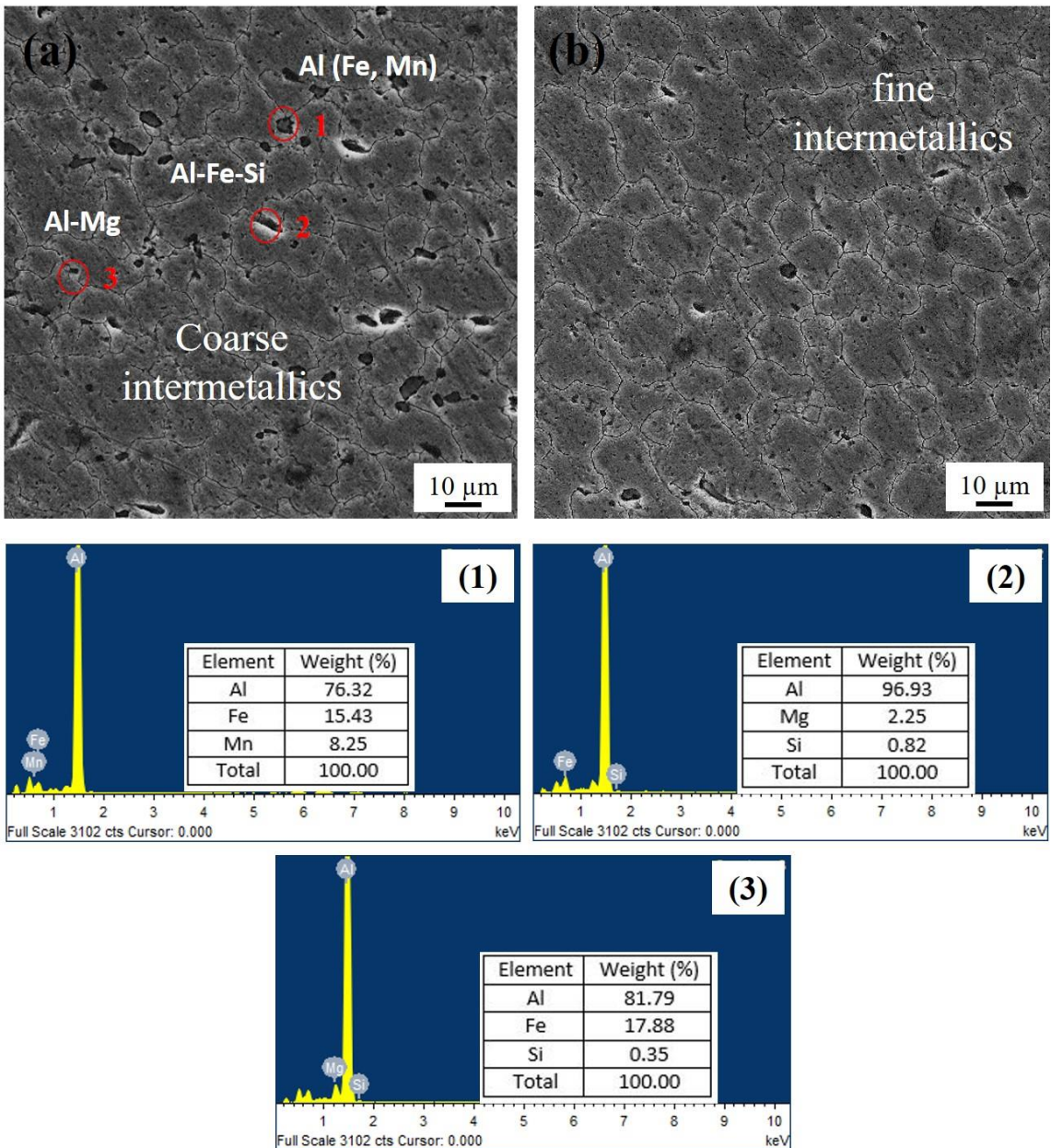


Figure 4.51: SEM images with EDS analysis of joints: (a) ACFSW and (b) WCFSW.

4.4.3.4 Texture variation

Texture evolution reveals critical details about recrystallization and plastic deformation mechanisms. Several research on the creation of crystallographic texture on aluminum alloys using FSW were identified in the literature. Therefore, we found that it is also important to study the texture of base material and that of dissimilar FSWed joints along with microstructure characteristics. To analyse texture evolutions of FSWed AA5083-AA6061 joint, pole figures at (100), (101), and (111) and orientation distribution functions (ODFs) from 0° to 90° with deviations of 5° were extracted from EBSD scans of as-received base metals and FSWed joints as shown in **Figure 4.52**. The texture components present in AA5083 base material are Cube

$[\{001\} <100>]$ and copper $[\{112\} <111>]$ components with texture intensity of 13.4, while copper $[\{112\} <111>]$ and Brass $[\{110\} <112>]$ texture components with texture intensity of 13.1 are found in AA6061-BM as shown in **Figure 4.52a and b** respectively. These textures are responsible for the poor formability of aluminium alloys by generating defects like earrings during metal forming processes [Barnwal et al., (2017)] and [Cho et al., (2020)]. When FCC metals are rolled, they produce a deformation texture common to brass and copper components. Recrystallization textures like cube textures are also typically found in FCC metals (Cho, Jae Kim, and Gil Lee 2014). The FSW joints undergo SPD at temperatures around 500 °C and the mechanisms are similar to torsion or extrusion processes [Fonda et al., (2007)]. The dynamic process can differ according to the alloying system used. Plastic deformation causes most grains to cluster in a specific orientation, resulting in grain rotation and texture production. Moradi et al., (2019) reported the texture at the SZ of AA5083-AA6082 dissimilar joint. The main orientations characterized are Rotated Cube $[\{001\} <100>$ component and Rotated Goss $[\{011\} <011>$ component. Wang et al., (2015) investigated the texture evolutions during the FSW of AA5052-AA6061. They demonstrated that Cube $[\{001\} <100>]$ and S $[\{123\} <634>]$ orientations in the BM transformed into $\{111\} 112$ shear component. According to the results of this study, the AA5083 and AA6061 samples had various combinations of deformation and recrystallization textures. Because the tool pin rotates violently, the texture distribution changes dramatically with location, especially in SZ. **Figure 4.52c and d** show the texture components of FSWed joints at different cooling environments. The pole figures demonstrate that asymmetric crystallographic textures are distributed in ACFSW and WCFSW joint due to the heterogeneous plastic flow during FSW. The main orientations in the center of the SZ of ACFSW joint are Brass $[\{110\} <112>]$ component and S $[\{123\} <346>]$ component with maximum texture intensity of 21.223, while the components changed to Copper $[\{112\} <111>]$ component and Goss $[\{110\} <001>]$ component with a maximum texture intensity of 24.128 in case of WCFSW joints. In addition, the texture intensity in SZ of the joints increases with the application of water cooling than the air-cooling FSW process. The evolution of the Goss and Brass component is responsible for excellent formability [Ghazanlou et al., (2021)]. The FSWed samples also show Goss, Rotated Goss, and Rotated Cube components, indicating recrystallization [Moghaddam et al., (2016)].

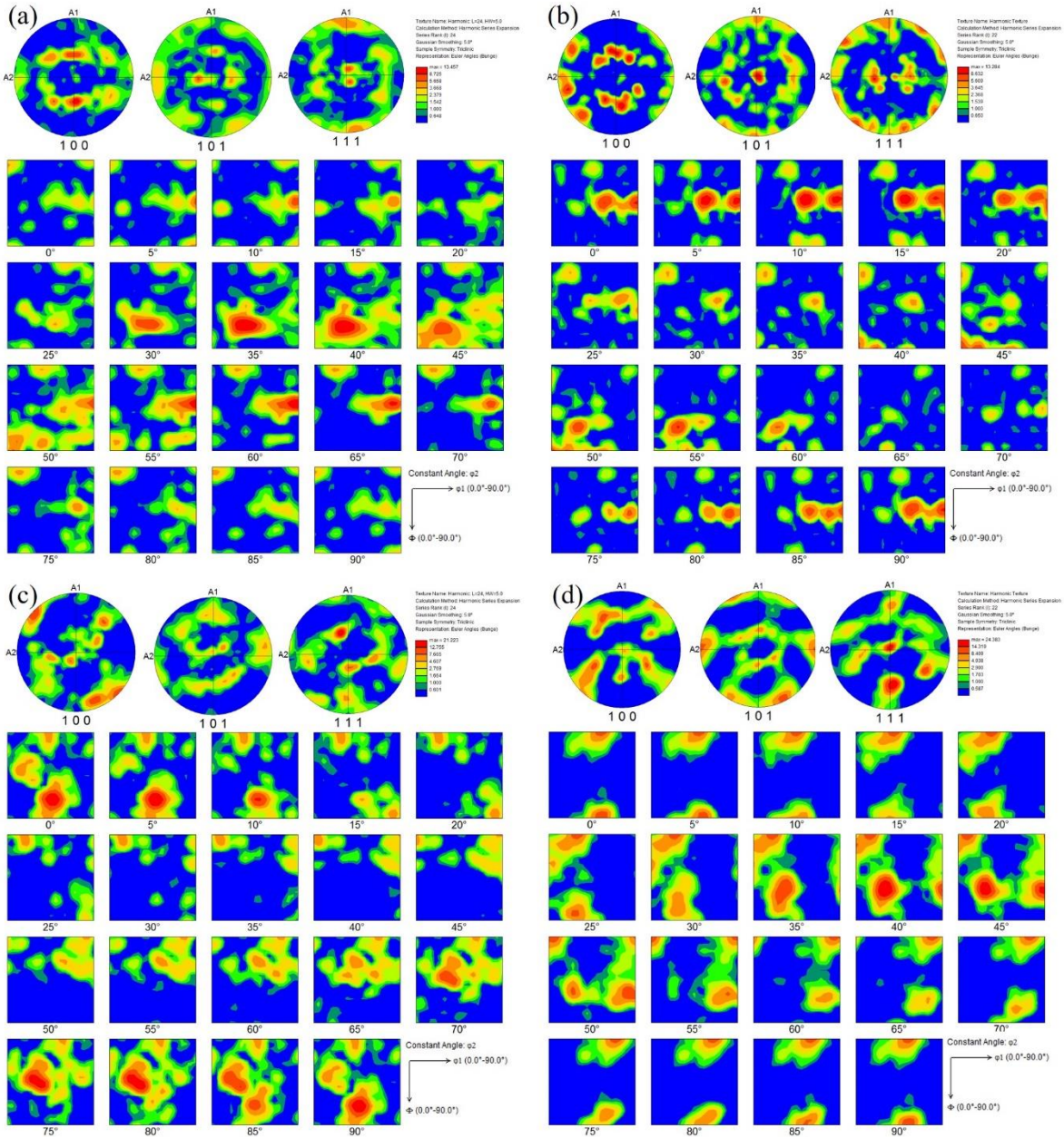


Figure 4.52: {100}, {101} and {111} PFs and ODFs: (a) 5083-BM, (b) 6061-BM, SZ of the (c) ACFSW and (d) WCFSW.

4.4.4 Mechanical study

4.4.4.1 Tensile properties

The tensile samples were extracted from four different locations (transverse to weld, longitudinal at HAZ on advancing side and longitudinal at HAZ on retreating side and longitudinal at SZ) of each condition. The tensile curves of FSWed joints (ACFSW and WCFSW) of transverse samples are shown in **Figure 4.53a**. The ultimate tensile strength (UTS), yield strength (YS) and tensile elongation (TE) were relatively lower in all FSWed joints compared to that of corresponding base materials. It is interesting to note that tensile strength increased in WCFSW compared to ACFSW (**Figure 4.53a**). In WCFSW, a joint efficiency of

72% was achieved to that of ACFSW joint, 64%. The fracture location of the ACFSW joint was in RS-HAZ while that of WCFSW was in SZ. Moreover, the cooling condition appears to be an important method governing the UTS of FSWed joints. The increased tensile strength may be attributed to a decrease in peak temperature [Derazkola et al., (2019)].

Table 4.13: Summary of tensile test results of the BMs and dissimilar FSWed samples.

Sample condition	YS (MPa)	UTS (MPa)	TE (%)
AA5083-BM	175	325	11.7
AA6061-BM	226	294	10.1
ACFSW-T	150	188	4.3
WCFSW-T	168	212	3.5
ACFSW-L	170	250	9.67
WCFSW-L	174	268	8.96
ACFSW-HAZ-AS	172	308	11.6
WCFSW-HAZ-AS	173	315	11.26
ACFSW-HAZ-RS	187	221	6.4
WCFSW-HAZ-RS	190	230	7.2

For all the FSWed joints, the stress-strain curves at SZ and HAZ were obtained through longitudinal direction tensile specimen testing and the stress-strain curves of the test are plotted as shown in **Figure 4.53b** and **c**. For comparison purposes, stress-strain curves of the as-received base materials are also included in the stress-strain plot. **Table 4.13** shows the findings of the stress-strain graph for each sample. It was observed that UTS measured in the longitudinal direction of the sample achieved a higher value than UTS measured in the transverse direction of FSW. During tensile testing, the gauge length comprised of different microstructural zones. The deformation of dissimilar welded joints was concentrated only on the weakest zone among different zones of welded joints. But the gauge length in longitudinal samples covers either SZ or HAZ fully. For the longitudinal FSW samples at SZ, the WCFSW joint showed the YS and UTS marginally higher than that of the ACFSW joint. This is due to the refined and finer grain structure of the WCFSW microstructure compared to that of ACFSW as discussed in **Sections 4.4.3.1 and 4.4.3.2**. Tensile properties at HAZ of FSWed joints were obtained through longitudinal tensile samples testing at both HAZ-AS and HAZ-RS of all the FSWed joints. From the results, it is observed that high strength was achieved using water-cooling FSW. The HAZ's heat exposure was reduced using external cooling fluid, which increases mechanical strength. Although the base material response to FSW differs slightly, the

mechanical properties of a tensile specimen extracted from HAZ-RS showed significant improvement in tensile strength in the case of the WCFSW joint.

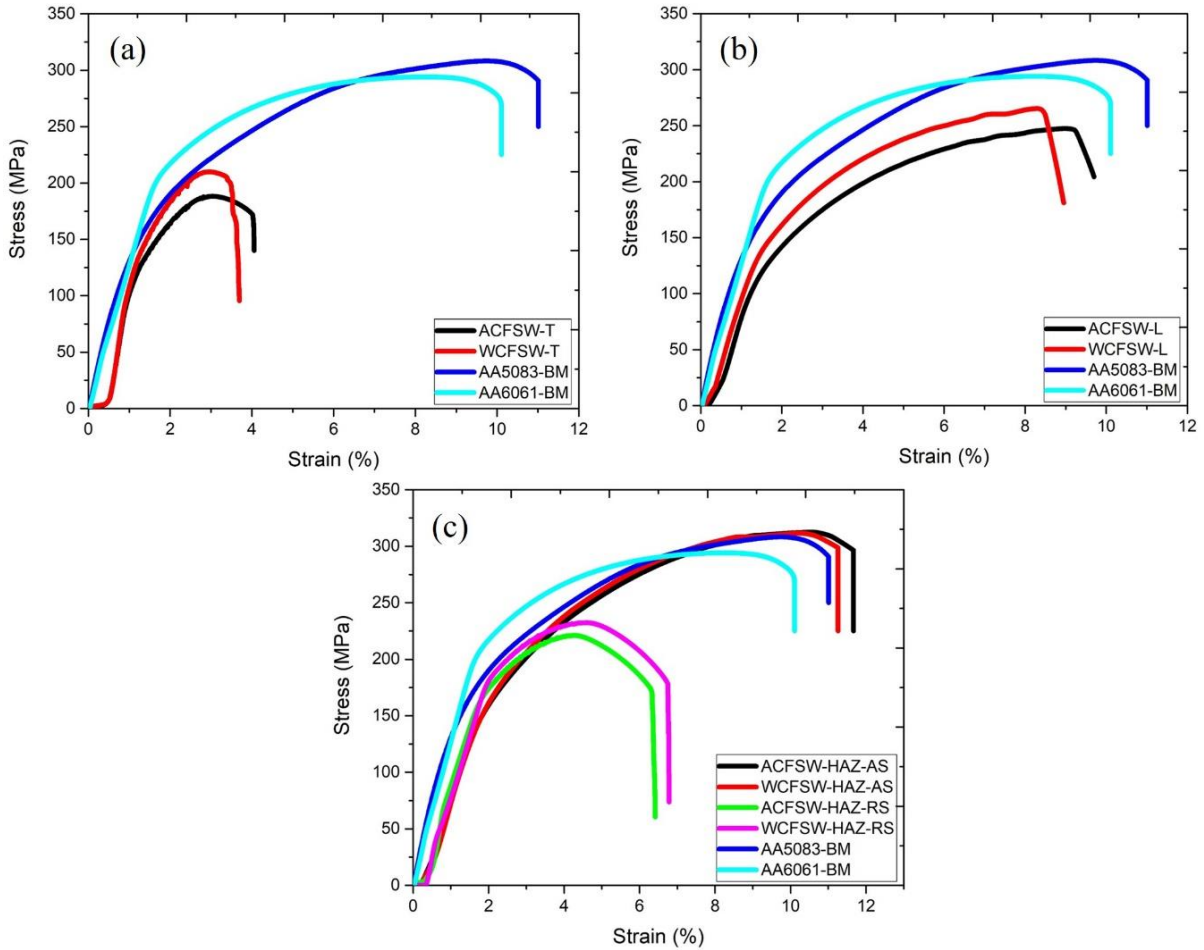


Figure 4.53: Stress-strain plots of BMs and FSWed samples: (a) Transverse tensile specimens (b) Longitudinal tested specimens at SZ (c) Longitudinal tested specimen in advancing and retreating side.

4.4.4.2 Strain hardening behavior

It is also essential to study the mechanical property that determines how a material strengthens after welding and how well it performs during the forming processes. Therefore, the strain hardening exponent (n) and strain hardening rate (θ_0) are examined for comprehending a material's behavior during the tensile test fully. If the strain hardening exponent is high, the metal can strain harden more quickly when applied a certain amount of plastic strain [Callister et al., (1991)]. According to the Holloman relationship, the material flow stress in a region of homogeneous plastic deformation can be expressed using in Eq 1 [Xu et al., (2012)].

$$\sigma = K \varepsilon^n \quad (1)$$

Where σ is true stress, ε is true strain, n is the strain hardening exponent and K is the strength coefficient. The n -value or strain hardening exponent is represented by the slope on the plot of $\log \sigma$ vs. $\log \varepsilon$ by linear fitting the curve as shown in **Figure 4.55**. The strain hardening parameters evaluated for the base metal and FSWed joints at various locations are shown in Table 4.14. Compared to the base material, the strain hardening exponent changed after FSW due to change in grain size, grain structure and precipitation behavior (sections 4.4.3.1 and 4.4.3.2). Out of all the samples, it can be seen that FSWed samples have a higher strain hardening exponent than the base metal. Moreover, the WCFSW joints exhibited a higher strain hardening exponent and tensile strength than ACFSW joints at different locations of FSWed zones. This was in agreement with the welded joints' lower grain size, texture, and higher tensile strength.

Table 4.14: Summary of strain hardening parameters.

Sample condition	Strain hardening exponent (n)	Strain hardening rate (θ_0)
AA5083-BM	0.3824	6157
AA6061-BM	0.2279	4722
ACFSW-T	0.3733	3761
WCFSW-T	0.3974	3830
ACFSW-L	0.3921	4189
WCFSW-L	0.4123	4378
ACFSW-HAZ-AS	0.4243	5534
WCFSW-HAZ-AS	0.4496	5896
ACFSW-HAZ-RS	0.2361	4026
WCFSW-HAZ-RS	0.2431	4267

Figure 4.55 illustrates a relation between $(d\sigma/d\varepsilon)$ on x-axis vs. net flow stress $(\sigma - \sigma_y)$ on y-axis known as Kocks-Mecking type plot of base metals and FSWed samples. Stage I hardening (or 'easy glide' which depended strongly on the orientation of the crystal) could be observed only in special conditions such as single crystals, where stage II hardening is due to the interaction of dislocations of primary slip systems with those in intersecting slip system, which did not appear in the present study. On the stress-strain curve, the hardening rate reduces linearly with increasing flow stress throughout stage III. This stage is sensitive to strain rate applied and highly temperature-sensitive.

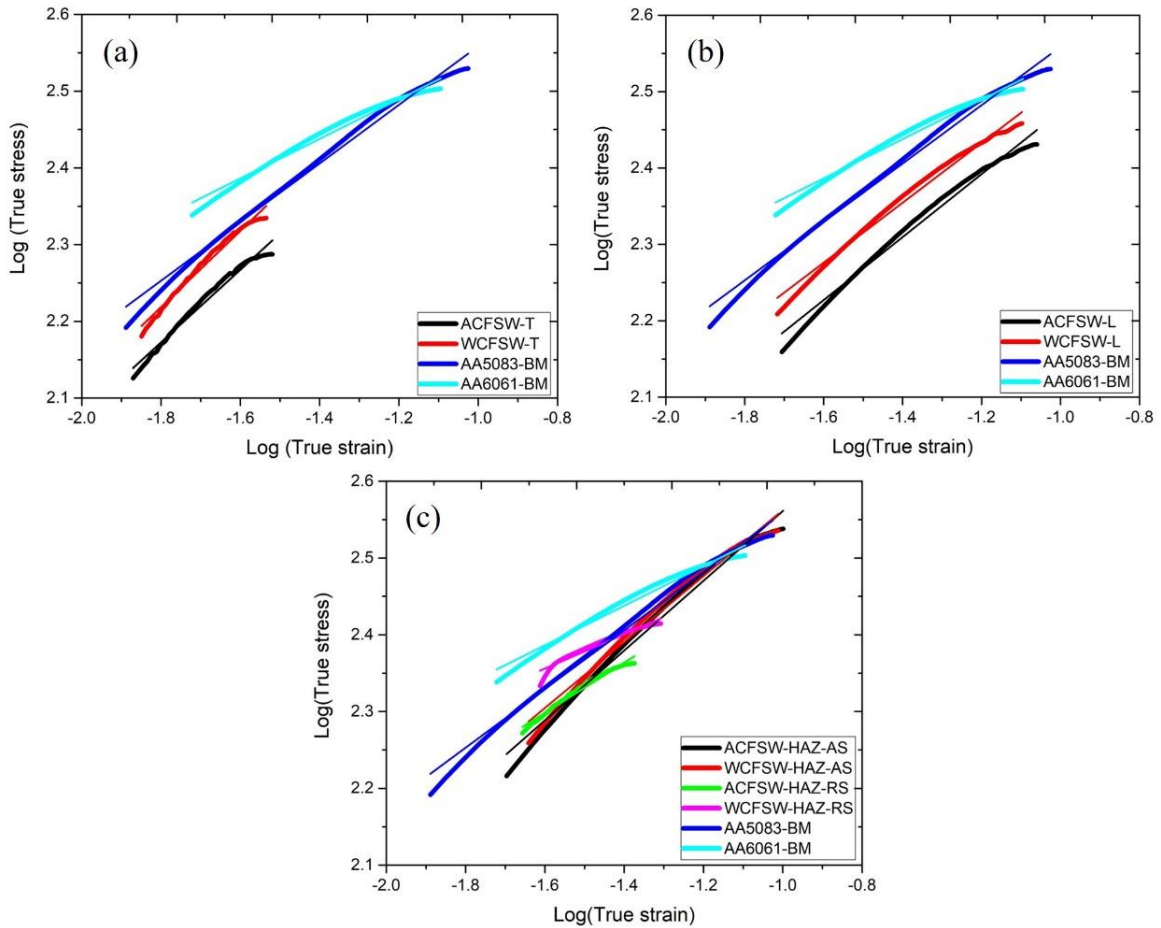


Figure 4.54: A typical plot to evaluate strain hardening exponent of FSWed samples: (a) Transverse tensile specimens (b) Transverse tested specimens (c) Longitudinal tested specimen and (d) Longitudinal at HAZ in advancing and retreating side tensile specimens.

As shown from Figure 4.55a-c, the strain hardening rate of FSWed samples is between that of both base materials. In FSWed AA5083-6061 joint for transverse tensile samples, stage III hardening finished at lower net flow stress (**Figure 4.55**). For FSWed longitudinal tensile samples at SZ, the strain hardening rate of both FSWed joints (ACFSW and WCFSW) was greater than 6061-BM, while that of the WCFSW joint was greater than ACFSW. For the longitudinal samples at HAZ, the strain hardening rate at AS was almost equal to that of AA5083-BM for both conditions, but the strain hardening at RS was much below that of AA6061-BM, while a slight improvement was observed in WCFSW condition. Strain hardening of material is sensitive to the dislocation strain field interaction and Hall Petch contribution [Chowdhury et al., (2010)]. If the number of dislocations is more, the spacing between them becomes smaller and their interactions are more repulsive, increasing resistance to deformation. [Sinclair et al., (2006)] and [Kovacs et al., (2002)] found that grain size had a significant impact on strain hardening. Still, that effect diminished as strain rates increased due to dislocation screening and dynamic recovery effects at grain boundaries. ACFSW showed

smaller grain size in SZ (**Figure 4.47e** and **Figure 4.48e**) and coarser grains at HAZ (**Figure 4.47b-c** and **Figure 4.48b-c**) than the grains at WCFSW joints. Therefore, the Hall-Petch contribution would be more strong leading to a higher strain hardening rate for WCFSW than for the ACFSW joint. Consistent with the strain hardening exponent, the strain hardening rate of WCFSW was higher than that of ACFSW joints in stages III and IV, and the strain hardening rate at HAZ in both AS and RS also increased using water cooling compared to ACFSW joints (**Figure 4.55c**).

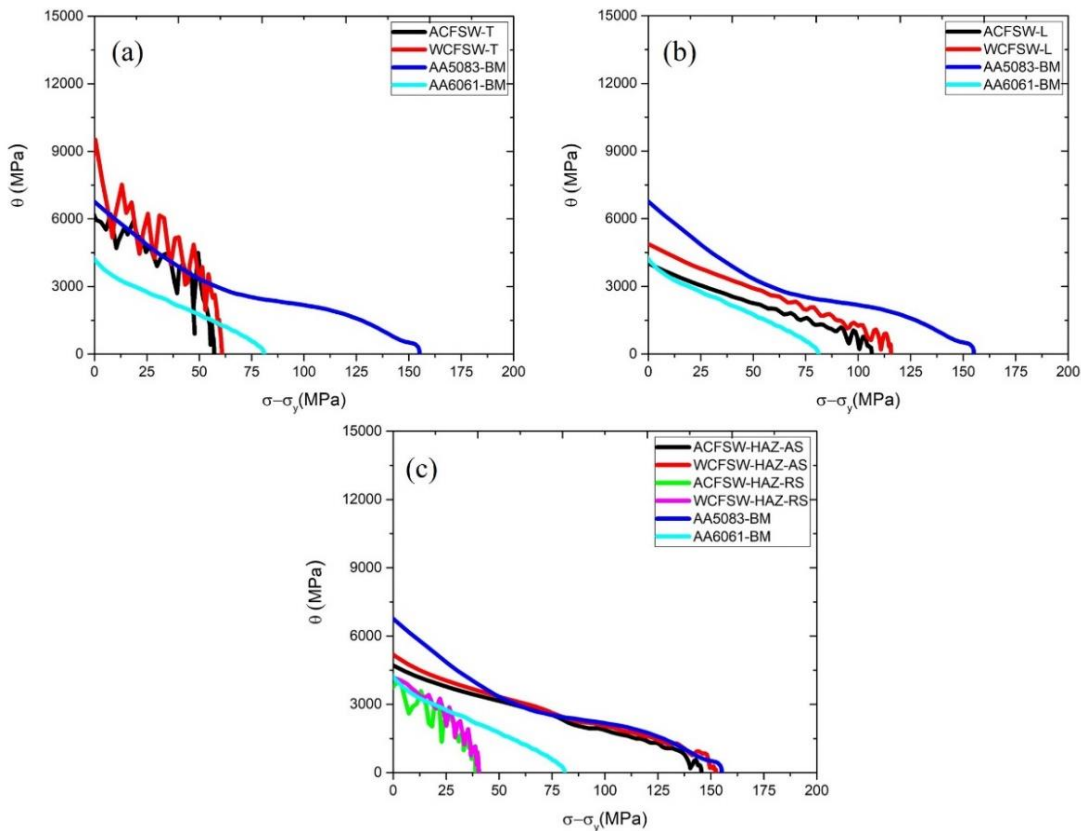


Figure 4.55: Strain hardening rate (θ) versus net flow stress ($\sigma - \sigma_y$) plots of (a) Transverse tested specimens, (b) Longitudinal tested specimens and (c) Longitudinal tested of HAZ in advancing and retreating side tensile specimens.

4.4.4.3 Fractography

Figure 4.56 depicts the fractography examination performed to analyze the fracture surface of base metals and FSWed samples. It was deduced that the base metal fracture surface (**Figure 4.56a and b**) was a ductile-dominated fracture showing large and deep dimples. The fractography of the longitudinal tensile specimen at SZ of the ACFSW joint is shown in Figure 4.56c. This consists of large size shallow dimples obtained due to severity in softening. Tensile strength was lower in the case of ACFSW-L than AA6061-BM, which is a larger size of the dimples. WCFSW-L joint at the SZ fractured surface was found to be both brittle and ductile

fracture. This is due to the occurrence of both fine dimples and flat surfaces (Figure 4.56d). The lower elongation obtained in the WCFSW-L tensile sample than at the ACFSW-L joint is due to the presence of flat surfaces, while the high strength attained is attributed to the small size of the dimples.

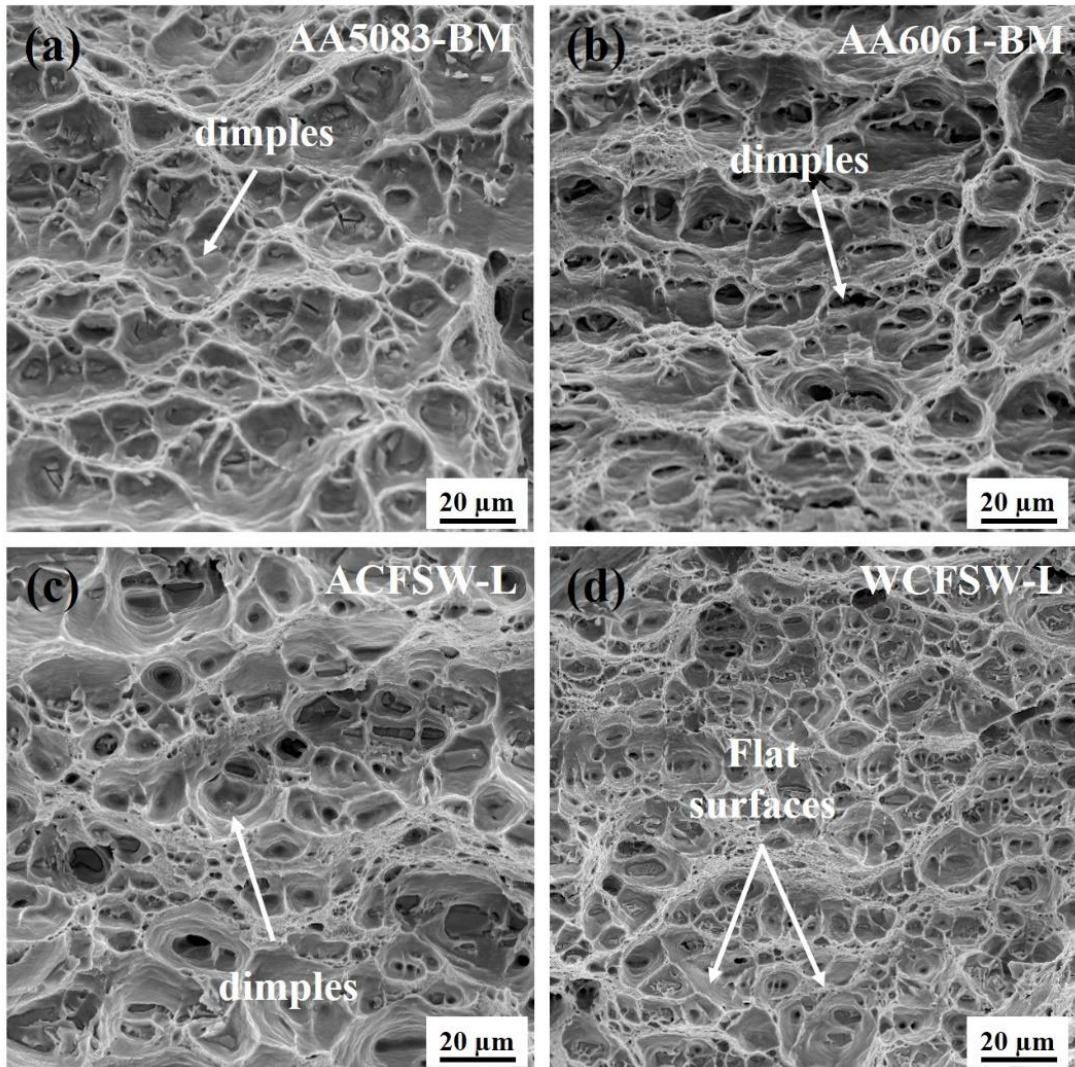


Figure 4.56: SEM images of the fracture surfaces of (a) AA5083-H111, (b) AA6061-T6, (c) ACFSW-L and (d) WCFSW-L.

4.4.5 Summary

During the welding process, significant microstructural changes contributed to the formation of four different microstructural zones. Grain coarsening occurred at HAZ of both base materials owing to the prolonged thermal cycle induced in the FSW process. Due to dynamic recrystallization by severe plastic deformation, the stir zone resulted in a refined grain structure. There were larger fractions of HAGBs in the WCFSW joint than in ACFSW. With the use of water-cooling, the influence of the heat cycle was reduced, which ensued in low post-weld grain development and greater refinement of grain structure in the WCFSW joint. The

main orientations in the center of SZ of ACFSW joint are Brass $\{110\} <112>$ component and S $\{123\} <346>$ component with a maximum texture intensity of 21.223, while the components changed to Copper $\{112\} <111>$ component and Goss $\{110\} <001>$ with a maximum texture intensity of 24.128 in case of WCFSW joints. The initial components had completely changed to base materials and some strong shear textures had formed due to severe shear deformation and rapid cooling during FSW. The strain hardening exponent and strain hardening rate enhanced slightly, while ductility decreased using water cooling of FSW. Stage III and IV hardening occurred after yielding in both base metal and FSWed samples. Lower elongation was obtained in WCFSW than ACFSW joint due to the presence of flat surfaces, while high strength attained was resulted in smaller size dimples of WCFSW joint fracture surface.

CHAPTER 5

CONCLUSIONS

5.1 Conclusions

In the present study, AA5083-H111/AA6061-T6 dissimilar friction stir butt welds of 6 mm thickness were prepared by changing the base material position and finding out the best position for the joints' high mechanical and corrosion behavior. To overcome the problems with heat generation during FSW, process conditions and the cooling environment was used and the material flow, microstructural evolution, mechanical properties and corrosion behavior were analyzed and correlated. An attempt was also made to study the effect of air and water cooling FSW dissimilar 5083-6061 aluminium alloys on the microstructure characteristics (Such as EBSD maps, texture evolution) and mechanical behavior (such as tensile strength, strain hardening exponent, strain hardening rate).

Various work elements constitute: (a) Mechanical and corrosion behavior of friction stir welded 5083-6061 aluminium alloy joints: Effect of base material position; (b) Effect of friction stir welding parameters on the material flow, mechanical properties and corrosion behavior of dissimilar AA5083-AA6061 joints; (c) Enhancing corrosion resistance and mechanical properties of dissimilar friction stir welded 5083-6061 aluminium alloys using external cooling environment; (d) Analysing microstructure, texture evolution and tensile behavior of dissimilar 5083-6061 aluminium alloys welded using air and water-cooled friction stir welding.

From the preliminary study on Mechanical and corrosion behavior of friction stir welded 5083-6061 aluminium alloy joints: Effect of base material position; following conclusions are drawn

- During the welding process, significant microstructural changes contributed to the formation of different microstructural zones. EBSD at SZ showed that sub grain

boundaries in grains collected misorientation and turned into LABs, subsequently transformed into HAB by continuous dynamic recrystallization, resulting in a fine and equiaxed microstructure.

- The materials were correctly mixed in the AA5083-AA6061 joint from AS and RS, whereas the bulk of the base metal in the AS was drawn into the stir zone and the materials were not adequately mixed in the AA6061-AA5083 joint for dissimilar aluminum alloys.
- The joint efficiency obtained by AA5083-AA5083 and AA6061-AA6061 is 61.24% and 63.94% respectively. The dissimilar joints exhibited UTS ranged between 183 and 175 MPa with joint efficiency ranging between 62.24 and 59.54% relative to the strength of AA6061-BM. It should be noted that the longitudinal strength of the dissimilar joints is comparable to the strength of the similar joint that was placed to the advancing side during the FSW.
- According to the results of polarization curves and EIS plots, the corrosion resistance of SZs is similar to that of the base material on the advancing side, which should be attributed to the fact that the majority of SZs are composed of the AS base material.

From the comprehensive study on the Effect of friction stir welding parameters on the material flow, mechanical properties and corrosion behavior of dissimilar AA5083-AA6061 joints; the following conclusions are drawn

- The stir zone microstructure of all the joints resulted in refined grains from the existing elongated microstructures of as-received base materials. Process parameters influenced the SZ and onion ring sub-structure width. The intimate intermixing of two base materials during FSW was observed at lower traverse speeds and higher rotational speeds.
- Superior tensile strength was achieved at the intermediate process conditions of 1100 rpm and 60 mm/min of the ultimate tensile strength (UTS) of around 197 MPa, with a joint efficiency of 67 % during the normal tensile test. The notch tensile strength test showed higher mechanical resistance at rotational speed of 1400 rpm and traverse speed of 60 mm/min process conditions.
- Based on the PDP and EIS test results, the corrosion resistance of welded joints was found to be lower than that of base materials. The corrosion resistance decreased with the increase in traverse speed from 40 mm/min to 80 mm/min and the corrosion resistance increased with an increase in rotational speed from 800 rpm to 1400 rpm.

- The onion ring sub-structure width was reduced at higher rotational speed and interestingly, corrosion resistance also improved with an increase in rotational speed. Tool rotational speed of 1400 rpm showed better corrosion resistance due to fragmentation and distribution of intermetallics phases, creating fewer sites for corrosion attack.

A comprehensive study was carried out on enhancing corrosion resistance and mechanical properties of dissimilar friction stir welded 5083-6061 aluminium alloys using an external cooling environment. From the analysis of the results, the following conclusions are drawn

- Microstructural observations revealed that the FSW in a cooling environment reduced the width of SZ and grain size at HAZs in NCFSW and WCFSW joints relative to ACFSW joint due to rapid heat dissipation.
- EBSD results showed the presence of fine grain size and a large fraction of HAGBs at the SZ of the WCFSW joint compared to ACFSW due to dynamic recovery, recrystallization and grain growth. Due to the use of external cooling media, the degree of the impact of the weld thermal cycle decreased, resulting in limited post-weld grain growth and better grain refinement in the WCFSW joint.
- From Tafel and EIS results, it was observed that the corrosion resistance of FSWed joints was lower than that of base materials. The corrosion resistance of the FSWed joint prepared using a water-cooling environment improved significantly compared to that of ACFSW and NCFSW joints.
- The hardness values of heat affected zone were lower than that of the base metals. The minimum hardness zone in the ACFSW joint was located at RS-HAZ, which shifted to SZ in the case of NCFSW and WCFSW joints.
- YS and UTS of the welded joints were found to be lower than that of base materials. However, the water-cooled joint produced the highest joint efficiency of 96% compared to ACFSW and NCFSW joints.

From the study on Analysing microstructure, texture evolution and tensile behavior of dissimilar 5083-6061 aluminium alloys welded using air and water-cooled friction stir welding, the following conclusions are drawn

- During the welding process, significant microstructural changes contributed to the formation of four different microstructural zones. Grain coarsening occurred at HAZ of both base materials owing to the prolonged thermal cycle induced in the FSW process.

Due to dynamic recrystallization by severe plastic deformation, the stir zone resulted in a refined grain structure.

- There were more significant fractions of HAGBs in the WCFSW joint than in ACFSW. With the use of water-cooling, the influence of the heat cycle was reduced, which ensued in low post-weld grain development and greater refinement of grain structure in the WCFSW joint.
- The main orientations in the center of SZ of ACFSW joint are Brass $\{110\} <112>$ component and S $\{123\} <346>$ component with a maximum texture intensity of 21.223, while the components changed to Copper $\{112\} <111>$ component and Goss $\{110\} <001>$ with a maximum texture intensity of 24.128 in case of WCFSW joints. The initial components had completely changed to base materials and some strong shear textures had formed due to severe shear deformation and rapid cooling during FSW.
- The strain hardening exponent and strain hardening rate enhanced slightly, while ductility decreased using water cooling of FSW. Stage III and IV hardening occurred after yielding in both base metal and FSWed samples. Lower elongation was obtained in WCFSW than ACFSW joint due to the presence of flat surfaces, while high strength attained was resulted in more minor size dimples of WCFSW joint fracture surface.

5.2 Future scope of work

Present research involves changing base material position, controlling heat input by employing different FSW process conditions, and utilizing a cooling environment for joining AA5083-AA6061 dissimilar aluminum alloys using the Friction stir welding technique. The methodology was adopted to enhance structural efficiency by improving mechanical and corrosion properties. The microstructure development process, corrosion behavior and mechanical characteristics of friction stir welded joints were investigated through the optical microscope (OM), electron backscattered diffraction (EBSD), scanning electron microscope and X-ray diffraction, electrochemical workstations as well as universal testing machine (UTM). The work also includes the effect of air and water cooling FSW dissimilar 5083-6061 aluminium alloys on the microstructure characteristics (Such as EBSD maps, texture evolution) and mechanical behavior (such as tensile strength, strain hardening exponent, strain hardening rate). Although an extensive study has been conducted in this regard, it is apparent that there are ample scopes for further work in this area.

Some suggestive directions for the possible future work are given below:

- Fatigue testing and analysis of submerged dissimilar FSWed AA5083-AA6061 dissimilar aluminium alloys can be interesting research.
- The present investigation was beneficial, but when the tool has no traverse speed (such as friction stir spot welding) for dissimilar FSWed AA5083-AA6061 can be studied extensively.
- Further microstructural analysis of FSWed joints using advanced characterization techniques like TEM to assess the influence of dislocation densities in improving the details about the microstructure.
- Dissimilar joining of Aluminium with polymers can further reduce the weight of the structures and joining these two highly dissimilar materials can be an interesting area of research.

BIBLIOGRAPHY

Afrin, N., D. L. Chen, X. Cao, and M. Jahazi. 2007. "Strain Hardening Behavior of a Friction Stir Welded Magnesium Alloy." *Scripta Materialia* 57(11):1004–7.

Azimzadegan, T. and S. Serajzadeh. 2010. "An Investigation into Microstructures and Mechanical Properties of AA7075-T6 during Friction Stir Welding at Relatively High Rotational Speeds." *Journal of Materials Engineering and Performance* 19(9):1256–63.

Bagheri Hariri, Mohiedin, Sajad Gholami Shiri, Yadollah Yaghoubinezhad, and Masoud Mohammadi Rahvard. 2013. "The Optimum Combination of Tool Rotation Rate and Traveling Speed for Obtaining the Preferable Corrosion Behavior and Mechanical Properties of Friction Stir Welded AA5052 Aluminum Alloy." *Materials and Design* 50:620–34.

Barnwal, Vivek Kumar, Rajesh Raghavan, Asim Tewari, K. Narasimhan, and Sushil K. Mishra. 2017. "Effect of Microstructure and Texture on Forming Behaviour of AA-6061 Aluminium Alloy Sheet." *Materials Science and Engineering A* 679(June 2016):56–65.

Blanc, C. and G. Mankowski. 1997. "Susceptibility to Pitting Corrosion of 6056 Aluminium Alloy." *Corrosion Science* 39(5):949–59.

Bocchi, Sara, Marina Cabrini, Gianluca D'Urso, Claudio Giardini, Sergio Lorenzi, and Tommaso Pastore. 2018. "The Influence of Process Parameters on Mechanical Properties and Corrosion Behavior of Friction Stir Welded Aluminum Joints." *Journal of Manufacturing Processes* 35(July):1–15.

Burger, G. B., A. K. Gupta, P. W. Jeffrey, and D. J. Lloyd. 1995. "Microstructural Control of Aluminum Sheet Used in Automotive Applications." *Materials Characterization* 35(1):23–39.

Callister, W. D. 1991. "Materials Science and Engineering: An Introduction (2nd Edition)." *Materials & Design* 12(1):59.

Cavaliere, P., A. Squillace, and F. Panella. 2008. "Effect of Welding Parameters on Mechanical and Microstructural Properties of AA6082 Joints Produced by Friction Stir Welding." *Journal of Materials Processing Technology* 200(1–3):364–72.

Cetkin, Edip, Y. H. Çelik, and Semsettin Temiz. 2019. "Microstructure and Mechanical Properties of AA7075/AA5182 Jointed by FSW." *Journal of Materials Processing Technology* 268(September 2018):107–16.

Chen, S. and X. Jiang. 2014. “Texture Evolution and Deformation Mechanism in Friction Stir Welding of 2219Al.” *Materials Science and Engineering A* 612:267–77.

Chen, Shujun, Xiaoxu Li, Xiaoqing Jiang, Tao Yuan, and Yazhou Hu. 2018. “The Effect of Microstructure on the Mechanical Properties of Friction Stir Welded 5A06 Al Alloy.” *Materials Science and Engineering A* 735(March):382–93.

Cho, Chang Hee, Kwang Tae Son, Jae Cheol Lee, Shae K. Kim, Young Ok Yoon, and Soong Keun Hyun. 2020. “Effect of the Mg Contents on the Annealing Mechanism and Shear Texture of Al–Mg Alloys.” *Materials Science and Engineering A* 786(March):139471.

Cho, J. H., S. H. Kang, H. N. Han, and K. H. Oh. 2008. “Modeling Friction Stir Welding Process of Aluminum Alloys.” *Metals and Materials International* 14(2):247–58.

Cho, Jae Hyung, Sang Ho Han, and Chang Gil Lee. 2016. “Cooling Effect on Microstructure and Mechanical Properties during Friction Stir Welding of Al-Mg-Si Aluminum Alloys.” *Materials Letters* 180:157–61.

Cho, Jae Hyung, Won Jae Kim, and Chang Gil Lee. 2014. “Texture and Microstructure Evolution and Mechanical Properties during Friction Stir Welding of Extruded Aluminum Billets.” *Materials Science and Engineering A* 597:314–23.

Choi, Don Hyun, Byung Wook Ahn, David J. Quesnel, and Seung Boo Jung. 2013. “Behavior of β Phase (Al 3 Mg 2) in AA 5083 during Friction Stir Welding.” *Intermetallics* 35:120–27.

Chowdhury, S. M., D. L. Chen, S. D. Bhole, X. Cao, E. Powidajko, D. C. Weckman, and Y. Zhou. 2010. “Tensile Properties and Strain-Hardening Behavior of Double-Sided Arc Welded and Friction Stir Welded AZ31B Magnesium Alloy.” *Materials Science and Engineering A* 527(12):2951–61.

Colegrove, P. A. and H. R. Shercliff. 2004. “Two-Dimensional CFD Modelling of Flow Round Profiled FSW Tooling.” *Science and Technology of Welding and Joining* 9(6):483–92.

Davoodi, Ali, Zohreh Esfahani, and Majid Sarvghad. 2016. “Microstructure and Corrosion Characterization of the Interfacial Region in Dissimilar Friction Stir Welded AA5083 to AA7023.” *Corrosion Science* 107:133–44.

Derazkola, Hamed Aghajani and Farzad Khodabakhshi. 2019. “Underwater Submerged Dissimilar Friction-Stir Welding of AA5083 Aluminum Alloy and A441 AISI Steel.” *International Journal of Advanced Manufacturing Technology* 102(9–12):4383–95.

Donatus, U., G. E. Thompson, X. Zhou, J. Wang, A. Cassell, and K. Beamish. 2015. "Corrosion Susceptibility of Dissimilar Friction Stir Welds of AA5083 and AA6082 Alloys." *Materials Characterization* 107:85–97.

Dong, Jialiang. 2019. "& C Corrosion Microstructure and Properties of Underwater Friction Stir-Welded 7003-T4 / 6060-T4 Aluminum Alloys." *Journal of Materials Science* 54(16):11254–62.

Dumont, M., A. Steuwer, A. Deschamps, M. Peel, and P. J. Withers. 2006. "Microstructure Mapping in Friction Stir Welds of 7449 Aluminium Alloy Using SAXS." *Acta Materialia* 54(18):4793–4801.

Elangovan, K. and V. Balasubramanian. 2008a. "Influences of Post-Weld Heat Treatment on Tensile Properties of Friction Stir-Welded AA6061 Aluminum Alloy Joints." *Materials Characterization* 59(9):1168–77.

Elangovan, K. and V. Balasubramanian. 2008b. "Influences of Tool Pin Profile and Welding Speed on the Formation of Friction Stir Processing Zone in AA2219 Aluminium Alloy." *Journal of Materials Processing Technology* 200(1–3):163–75.

Etter, A. L., T. Baudin, N. Fredj, and R. Penelle. 2007. "Recrystallization Mechanisms in 5251 H14 and 5251 O Aluminum Friction Stir Welds." *Materials Science and Engineering A* 445–446:94–99.

Fahimpour, V., S. K. Sadrnezhaad, and F. Karimzadeh. 2012. "Corrosion Behavior of Aluminum 6061 Alloy Joined by Friction Stir Welding and Gas Tungsten Arc Welding Methods." *Materials and Design* 39:329–33.

Farahmand Nikoo, M., H. Azizi, N. Parvin, and H. Yousefpour Naghibi. 2016. "The Influence of Heat Treatment on Microstructure and Wear Properties of Friction Stir Welded AA6061-T6/Al₂O₃ Nanocomposite Joint at Four Different Traveling Speed." *Journal of Manufacturing Processes* 22:90–98.

Feng, A. H., D. L. Chen, Z. Y. Ma, W. Y. Ma, and R. J. Song. 2014. "Microstructure and Strain Hardening of a Friction Stir Welded High-Strength Al-Zn-Mg Alloy." *Acta Metallurgica Sinica (English Letters)* 27(4):723–29.

Fonda, R. W. and J. F. Bingert. 2007. "Texture Variations in an Aluminum Friction Stir Weld." *Scripta Materialia* 57(11):1052–55.

Fratini, L., G. Buffa, and R. Shivpuri. 2009. "In-Process Heat Treatments to Improve FS-

Welded Butt Joints.” *International Journal of Advanced Manufacturing Technology* 43(7–8):664–70.

Fujii, Hidetoshi, Ling Cui, Masakatsu Maeda, and Kiyoshi Nogi. 2006. “Effect of Tool Shape on Mechanical Properties and Microstructure of Friction Stir Welded Aluminum Alloys.” *Materials Science and Engineering A* 419(1–2):25–31.

Ghaffarpour, Morteza, Mohammad Kazemi, Mohammad Javad Mohammadi Sefat, Ahmad Aziz, and Kamran Dehghani. 2017. “Evaluation of Dissimilar Joints Properties of 5083-H12 and 6061-T6 Aluminum Alloys Produced by Tungsten Inert Gas and Friction Stir Welding.” *Proceedings of the Institution of Mechanical Engineers, Part L: Journal of Materials: Design and Applications* 231(3):297–308.

Ghazanlou, Siavash Imanian, Beitallah Eghbali, and Roumen Petrov. 2021. “Study on the Microstructural and Texture Evolution of Hot Rolled Al7075/ Graphene/ Carbon Nanotubes Reinforced Composites.” *Materials Chemistry and Physics* 257(June 2020):123766.

Ghetiya, Nilesh D. and Kaushik M. Patel. 2017. “Welding Speed Effect on Joint Properties in Air and Immersed Friction Stir Welding of AA2014.” *Proceedings of the Institution of Mechanical Engineers, Part B: Journal of Engineering Manufacture* 231(5):897–909.

Goswami, R., G. Spanos, P. S. Pao, and R. L. Holtz. 2010. “Precipitation Behavior of the β Phase in Al-5083.” *Materials Science and Engineering A* 527(4–5):1089–95.

Guo, J. F., H. C. Chen, C. N. Sun, G. Bi, Z. Sun, and J. Wei. 2014. “Friction Stir Welding of Dissimilar Materials between AA6061 and AA7075 Al Alloys Effects of Process Parameters.” *Materials and Design* 56:185–92.

Hassan, Kh A. A., P. B. Prangnell, A. F. Norman, D. A. Price, and S. W. Williams. 2003. “Effect of Welding Parameters on Nugget Zone Microstructure and Properties in High Strength Aluminium Alloy Friction Stir Welds.” *Science and Technology of Welding and Joining* 8(4):257–68.

Ishii, Katsuya, Ryota Ozaki, Kenji Kaneko, Hisaaki Fukushima, and Masataka Masuda. 2007. “Continuous Monitoring of Aluminum Corrosion Process in Deraerated Water.” *Corrosion Science* 49(6):2581–2601.

Jayaraman, M., R. Sivasubramanian, and V. Balasubramanian. 2010. “Establishing Relationship between the Base Metal Properties and Friction Stir Welding Process Parameters of Cast Aluminium Alloys.” *Materials and Design* 31(9):4567–76.

Kang, Ju, Rui dong Fu, Guo hong Luan, Chun lin Dong, and Miao He. 2010. “In-Situ Investigation on the Pitting Corrosion Behavior of Friction Stir Welded Joint of AA2024-T3 Aluminium Alloy.” *Corrosion Science* 52(2):620–26.

Karthikeyan, L. and V. S. Senthil Kumar. 2011. “Relationship between Process Parameters and Mechanical Properties of Friction Stir Processed AA6063-T6 Aluminum Alloy.” *Materials and Design* 32(5):3085–91.

Karthikeyan, L., V. S. Senthilkumar, and K. A. Padmanabhan. 2010. “On the Role of Process Variables in the Friction Stir Processing of Cast Aluminum A319 Alloy.” *Materials and Design* 31(2):761–71.

Kartsonakis, I. A., D. A. Dragatogiannis, E. P. Koumoulos, A. Karantonis, and C. A. Charitidis. 2016. “Corrosion Behaviour of Dissimilar Friction Stir Welded Aluminium Alloys Reinforced with Nanoadditives.” *Materials and Design* 102:56–67.

Kovács, I., N. Q. Chinh, and E. Kovács-Csetényi. 2002. “Grain Size Dependence of the Work Hardening Process in Al99.99.” *Physica Status Solidi (A) Applied Research* 194(1):3–18.

Krishnan, K. N. 2002. “On the Formation of Onion Rings in Friction Stir Welds.” *Materials Science and Engineering A* 327(2):246–51.

Kumar, K. and Satish V. Kailas. 2008a. “On the Role of Axial Load and the Effect of Interface Position on the Tensile Strength of a Friction Stir Welded Aluminium Alloy.” *Materials and Design* 29(4):791–97.

Kumar, K. and Satish V. Kailas. 2008b. “The Role of Friction Stir Welding Tool on Material Flow and Weld Formation.” *Materials Science and Engineering A* 485(1–2):367–74.

Kumar, Kethavath Kranthi, Adepu Kumar, and M. V. N. V. Satyanarayana. 2021. “Enhancing Corrosion Resistance and Mechanical Properties of Dissimilar Friction Stir Welded 5083-6061 Aluminium Alloys Using External Cooling Environment.” *Proceedings of the Institution of Mechanical Engineers, Part L: Journal of Materials: Design and Applications*.

Leitao, C., R. M. Leal, D. M. Rodrigues, A. Loureiro, and P. Vilaça. 2009. “Mechanical Behaviour of Similar and Dissimilar AA5182-H111 and AA6016-T4 Thin Friction Stir Welds.” *Materials and Design* 30(1):101–8.

Li, Na, Wenyi Li, Yaxin Xu, Xiawei Yang, and Nikolaos D. Alexopoulos. 2018. “Influence of Rotation Speed on Mechanical Properties and Corrosion Sensitivity of Friction Stir

Welded AA2024-T3 Joints.” *Materials and Corrosion* 69(8):1016–24.

Liu, G., L. E. Murr, C. S. Niou, J. C. McClure, and F. R. Vega. 1997. “Microstructural Aspects of the Friction-Stir Welding of 6061-T6 Aluminum.” *Scripta Materialia* 37(3):355–61.

Liu, Hui Jie, Hui Jie Zhang, Yong Xian Huang, and Lei Yu. 2010. “Mechanical Properties of Underwater Friction Stir Welded 2219 Aluminum Alloy.” *Transactions of Nonferrous Metals Society of China (English Edition)* 20(8):1387–91.

Liu, Huijie, Yanying Hu, Chao Dou, and Dusan P. Sekulic. 2017. “An Effect of the Rotation Speed on Microstructure and Mechanical Properties of the Friction Stir Welded 2060-T8 Al-Li Alloy.” *Materials Characterization* 123:9–19.

Liu, X. C., Y. F. Sun, T. Nagira, K. Ushioda, and H. Fujii. 2019. “Experimental Evaluation of Strain and Strain Rate during Rapid Cooling Friction Stir Welding of Pure Copper.” *Science and Technology of Welding and Joining* 24(4):352–59.

Lumley, Roger N. 2010. *Fundamentals of Aluminium Metallurgy: Production, Processing and Applications*.

Malopheyev, Sergey, Igor Vysotskiy, Vladislav Kulitskiy, Sergey Mironov, and Rustam Kaibyshev. 2016. “Optimization of Processing-Microstructure-Properties Relationship in Friction-Stir Welded 6061-T6 Aluminum Alloy.” *Materials Science and Engineering A* 662:136–43.

Mastanaiah, P., Abhay Sharma, and G. Madhusudhan Reddy. 2016. “Dissimilar Friction Stir Welds in AA2219-AA5083 Aluminium Alloys: Effect of Process Parameters on Material Inter-Mixing, Defect Formation, and Mechanical Properties.” *Transactions of the Indian Institute of Metals* 69(7):1397–1415.

Mehdizade, Maryam, Ali Reza Eivani, and Mansour Soltanieh. 2020. “Effects of Reduced Surface Grain Structure and Improved Particle Distribution on Pitting Corrosion of AA6063 Aluminum Alloy.” *Journal of Alloys and Compounds* 838:155464.

Meilinger, Akos and Imre Torok. 2013. “The Importance of Friction Stir Welding Tool.” *Production Processes and Systems* 6(1):25–34.

Mishra, R. S. and Z. Y. Ma. 2005. “Friction Stir Welding and Processing.” *Materials Science and Engineering: R: Reports* 50(1):1–78.

Mishra, Rajiv S., Murray W. Mahoney, Yutaka Sato, and Yuri Hovanski. 2016. “Friction Stir Welding and Processing VIII.” *Friction Stir Welding and Processing VIII* 50:1–300.

Mofid, Mohammad Ammar, Amir Abdollah-Zadeh, Farshid Malek Ghaini, and Cemil Hakan Gür. 2012. "Submerged Friction-Stir Welding (SFSW) Underwater and under Liquid Nitrogen: An Improved Method to Join Al Alloys to Mg Alloys." *Metallurgical and Materials Transactions A: Physical Metallurgy and Materials Science* 43(13):5106–14.

Moradi, Mohammad Mahdi, Hamed Jamshidi Aval, Roohollah Jamaati, Sajjad Amirkhanlou, and Shouxun Ji. 2019. "Effect of SiC Nanoparticles on the Microstructure and Texture of Friction Stir Welded AA2024/AA6061." *Materials Characterization* 152(April):169–79.

Moshwan, Raza, Farazila Yusof, M. A. Hassan, and S. M. Rahmat. 2015. "Effect of Tool Rotational Speed on Force Generation, Microstructure and Mechanical Properties of Friction Stir Welded Al-Mg-Cr-Mn (AA 5052-O) Alloy." *Materials and Design* 66(PA):118–28.

Nandan, R., T. DebRoy, and H. K. D. H. Bhadeshia. 2008. "Recent Advances in Friction-Stir Welding - Process, Weldment Structure and Properties." *Progress in Materials Science* 53(6):980–1023.

Ni, D. R., D. L. Chen, D. Wang, B. L. Xiao, and Z. Y. Ma. 2014. "Tensile Properties and Strain-Hardening Behaviour of Friction Stir Welded SiCp/AA2009 Composite Joints." *Materials Science and Engineering A* 608:1–10.

P., Ajay Kumar, Devinder Yadav, Chandra S. Perugu, and Satish V. Kailas. 2017. "Influence of Particulate Reinforcement on Microstructure Evolution and Tensile Properties of In-Situ Polymer Derived MMC by Friction Stir Processing." *Materials and Design* 113:99–108.

Padmanaban, G. and V. Balasubramanian. 2009. "Selection of FSW Tool Pin Profile, Shoulder Diameter and Material for Joining AZ31B Magnesium Alloy - An Experimental Approach." *Materials and Design* 30(7):2647–56.

Palanivel, R., P. Koshy Mathews, I. Dinaharan, and N. Murugan. 2014. "Mechanical and Metallurgical Properties of Dissimilar Friction Stir Welded AA5083-H111 and AA6351-T6 Aluminum Alloys." *Transactions of Nonferrous Metals Society of China (English Edition)* 24(1):58–65.

Park, S. K., S. T. Hong, J. H. Park, K. Y. Park, Y. J. Kwon, and H. J. Son. 2010. "Effect of Material Locations on Properties of Friction Stir Welding Joints of Dissimilar Aluminium Alloys." *Science and Technology of Welding and Joining* 15(4):331–36.

PARK, Sung Hyeon, Jong Shin KIM, Min Su HAN, and Seong Jong KIM. 2009. "Corrosion

and Optimum Corrosion Protection Potential of Friction Stir Welded 5083-O Al Alloy for Leisure Ship." *Transactions of Nonferrous Metals Society of China (English Edition)* 19(4):898–903.

Pashazadeh, Hamed and Jamal Teimournezhad. 2014. "Numerical Investigation on the Mechanical, Thermal, Metallurgical and Material Flow Characteristics in Friction Stir Welding of Copper Sheets with Experimental Verification." *Materials and Design* 55:619–32.

Peel, M.J. (2005) 'The friction-stir welding of dissimilar aluminium alloys', The University of Manchester, *Doctor of Philosophy Thesis*

Peel, M. J., A. Steuwer, and P. J. Withers. 2006. "Dissimilar Friction Stir Welds in AA5083-AA6082. Part II: Process Parameter Effects on Microstructure." *Metallurgical and Materials Transactions A: Physical Metallurgy and Materials Science* 37(7):2195–2206.

Peel, M. J., A. Steuwer, P. J. Withers, T. Dickerson, Q. Shi, and H. Shercliff. 2006. "Dissimilar Friction Stir Welds in AA5083-AA6082. Part I: Process Parameter Effects on Thermal History and Weld Properties." *Metallurgical and Materials Transactions A: Physical Metallurgy and Materials Science* 37(7):2183–93.

Peel, M., A. Steuwer, M. Preuss, and P. J. Withers. 2003. "Microstructure, Mechanical Properties and Residual Stresses as a Function of Welding Speed in Aluminium AA5083 Friction Stir Welds." *Acta Materialia* 51(16):4791–4801.

Polmear, I.J. 1995. "Light Alloys, Metallurgy of light metals" 3rd edition New york: Halsted Press.

Rajakumar, S. and V. Balasubramanian. 2012. "Correlation between Weld Nugget Grain Size, Weld Nugget Hardness and Tensile Strength of Friction Stir Welded Commercial Grade Aluminium Alloy Joints." *Materials and Design* 34:242–51.

Ratchev, P., B. Verlinden, and P. Van Houtte. 1995. "Effect of Preheat Temperature on the Orientation Relationship of (Mn,Fe)Al₆ Precipitates in an AA 5182 Aluminium-Magnesium Alloy." *Acta Metallurgica Et Materialia* 43(2):621–29.

Ren, S. R., Z. Y. Ma, and L. Q. Chen. 2007. "Effect of Welding Parameters on Tensile Properties and Fracture Behavior of Friction Stir Welded Al-Mg-Si Alloy." *Scripta Materialia* 56(1):69–72.

Rhodes, C. G., M. W. Mahoney, W. H. Bingel, R. A. Spurling, and C. C. Bampton. 1997.

“Effects of Friction Stir Welding on Microstructure of 7075 Aluminum.” *Scripta Materialia* 36(1):69–75.

Sabari, S. Sree, S. Malarvizhi, and V. Balasubramanian. 2016. “Influences of Tool Traverse Speed on Tensile Properties of Air Cooled and Water Cooled Friction Stir Welded AA2519-T87 Aluminium Alloy Joints.” *Journal of Materials Processing Technology* 237:286–300.

Sakthivel, T., G. S. Sengar, and J. Mukhopadhyay. 2009. “Effect of Welding Speed on Microstructure and Mechanical Properties of Friction-Stir-Welded Aluminum.” *International Journal of Advanced Manufacturing Technology* 43(5–6):468–73.

Salih, Omar S., Nigel Neate, Hengan Ou, and W. Sun. 2020. “Influence of Process Parameters on the Microstructural Evolution and Mechanical Characterisations of Friction Stir Welded Al-Mg-Si Alloy.” *Journal of Materials Processing Technology* 275(February 2019):116366.

Sato, Yutaka S., Seung Hwan C. Park, and Hiroyuki Kokawa. 2001. “Microstructural Factors Governing Hardness in Friction-Stir Welds of Solid-Solution-Hardened Al Alloys.” *Metallurgical and Materials Transactions A: Physical Metallurgy and Materials Science* 32(12):3033–42.

Schmidt, H. B. and J. H. Hattel. 2008. “Thermal Modelling of Friction Stir Welding.” *Scripta Materialia* 58(5):332–37.

Schmidt, H. and J. Hattel. 2005. “Modelling Heat Flow around Tool Probe in Friction Stir Welding.” *Science and Technology of Welding and Joining* 10(2):176–86.

Schmidt, H. N. B., T. L. Dickerson, and J. H. Hattel. 2006. “Material Flow in Butt Friction Stir Welds in AA2024-T3.” *Acta Materialia* 54(4):1199–1209.

Schneider, J. A. and A. C. Nunes. 2004. “Characterization of Plastic Flow and Resulting Microtextures in a Friction Stir Weld.” *Metallurgical and Materials Transactions B: Process Metallurgy and Materials Processing Science* 35(4):777–83.

Schneider, M., K. Kremmer, C. Lämmel, K. Sempf, and M. Herrmann. 2014. “Galvanic Corrosion of Metal/Ceramic Coupling.” *Corrosion Science* 80:191–96.

Sharma, Chaitanya, D. K. Dwivedi, and Pradeep Kumar. 2012. “Influence of In-Process Cooling on Tensile Behaviour of Friction Stir Welded Joints of AA7039.” *Materials Science and Engineering A* 556:479–87.

Sinclair, C. W., W. J. Poole, and Y. Bréchet. 2006. “A Model for the Grain Size Dependent Work Hardening of Copper.” *Scripta Materialia* 55(8):739–42.

Sinhmar, S. and D. K. Dwivedi. 2017. “Enhancement of Mechanical Properties and Corrosion Resistance of Friction Stir Welded Joint of AA2014 Using Water Cooling.” *Materials Science and Engineering A* 684(September 2016):413–22.

Sinhmar, Sunil and Dheerendra Kumar Dwivedi. 2018. “A Study on Corrosion Behavior of Friction Stir Welded and Tungsten Inert Gas Welded AA2014 Aluminium Alloy.” *Corrosion Science* 133(January):25–35.

Snyder, Benjamin and Alvin M. Strauss. 2021. “In-Process Cooling of Friction Stir Extruded Joints for Increased Weld Performance via Compressed Air , Water , Granulated Dry Ice , and Liquid Nitrogen.” *Journal of Manufacturing Processes* 68(PA):1004–17.

Su, J. Q., T. W. Nelson, R. Mishra, and M. Mahoney. 2003. “Microstructural Investigation of Friction Stir Welded 7050-T651 Aluminium.” *Acta Materialia* 51(3):713–29.

Surekha, K., B. S. Murty, and K. Prasad Rao. 2009. “Effect of Processing Parameters on the Corrosion Behaviour of Friction Stir Processed AA 2219 Aluminum Alloy.” *Solid State Sciences* 11(4):907–17.

Svensson, L. E., L. Karlsson, H. Larsson, B. Karlsson, M. Fazzini, and J. Karlsson. 2000. “Microstructure and Mechanical Properties of Friction Stir Welded Aluminium Alloys with Special Reference to AA 5083 and AA 6082.” *Science and Technology of Welding and Joining* 5(5):285–96.

Thomas, W. M. and E. D. Nicholas. 1997. “Friction Stir Welding for the Transportation Industries.” *Materials and Design* 18(4–6):269–73.

Verma, Rajesh P., K. N. Pandey, and Yogesh Sharma. 2015. “Effect of ER4043 and ER5356 Filler Wire on Mechanical Properties and Microstructure of Dissimilar Aluminium Alloys, 5083-O and 6061-T6 Joint, Welded by the Metal Inert Gas Welding.” *Proceedings of the Institution of Mechanical Engineers, Part B: Journal of Engineering Manufacture* 229(6):1021–28.

Wang, B. B., F. F. Chen, F. Liu, W. G. Wang, P. Xue, and Z. Y. Ma. 2017. “Enhanced Mechanical Properties of Friction Stir Welded 5083Al-H19 Joints with Additional Water Cooling.” *Journal of Materials Science and Technology* 33(9):1009–14.

Wang, Bin, Bo Bo Lei, Jia Xiang Zhu, Quan Feng, Liang Wang, and Deng Wu. 2015. “EBSD

Study on Microstructure and Texture of Friction Stir Welded AA5052-O and AA6061-T6 Dissimilar Joint.” *Materials and Design* 87:593–99.

Wang, Xiangbin, Yi Pan, and Diana A. Lados. 2018. “Friction Stir Welding of Dissimilar Al/Al and Al/Non-Al Alloys: A Review.” *Metallurgical and Materials Transactions B: Process Metallurgy and Materials Processing Science* 49(4):2097–2117.

Xu, Shaowen and Xiaomin Deng. 2008. “A Study of Texture Patterns in Friction Stir Welds.” *Acta Materialia* 56(6):1326–41.

Xu, W. F., J. H. Liu, D. L. Chen, G. H. Luan, and J. S. Yao. 2012. “Improvements of Strength and Ductility in Aluminum Alloy Joints via Rapid Cooling during Friction Stir Welding.” *Materials Science and Engineering A* 548:89–98.

Xu, Weifeng and Jinhe Liu. 2009. “Microstructure and Pitting Corrosion of Friction Stir Welded Joints in 2219-O Aluminum Alloy Thick Plate.” *Corrosion Science* 51(11):2743–51.

Yutaka, Sato S., Hiroyuki Hiroyuki, Keiske Ikeda, Masatoshi Enomoto, Shigetoshi Jogan, and Takenori Hashimoto. 2001. “Microtexture in the Friction-Stir Weld of an Aluminum Alloy.” *Metallurgical and Materials Transactions A: Physical Metallurgy and Materials Science* 32(4):941–48.

Zeng, X. H., P. Xue, D. Wang, D. R. Ni, B. L. Xiao, and Z. Y. Ma. 2018. “Effect of Processing Parameters on Plastic Flow and Defect Formation in Friction-Stir-Welded Aluminum Alloy.” *Metallurgical and Materials Transactions A: Physical Metallurgy and Materials Science* 49(7):2673–83.

Zhang, Chenghang, Yu Cao, Guangjie Huang, Qinghui Zeng, Yulong Zhu, Xinde Huang, Na Li, and Qing Liu. 2020. “Influence of Tool Rotational Speed on Local Microstructure, Mechanical and Corrosion Behavior of Dissimilar AA2024/7075 Joints Fabricated by Friction Stir Welding.” *Journal of Manufacturing Processes* 49(August 2019):214–26.

Zhang, Chenghang, Guangjie Huang, Yu Cao, Yulong Zhu, and Qing Liu. 2019. “On the Microstructure and Mechanical Properties of Similar and Dissimilar AA7075 and AA2024 Friction Stir Welding Joints: Effect of Rotational Speed.” *Journal of Manufacturing Processes* 37(November 2018):470–87.

Zhang, Jingqing, Yifu Shen, Bo Li, Haisheng Xu, Xin Yao, Binbin Kuang, and Jicheng Gao. 2014. “Numerical Simulation and Experimental Investigation on Friction Stir Welding of 6061-T6 Aluminum Alloy.” *Materials and Design* 60:94–101.

Zhang, Z. and H. W. Zhang. 2008. “A Fully Coupled Thermo-Mechanical Model of Friction Stir Welding.” *International Journal of Advanced Manufacturing Technology* 37(3–4):279–93.

Zhou, Nan, Dongfu Song, Wenjun Qi, Xiaohui Li, Ji Zou, and Moataz M. Attallah. 2018. “Influence of the Kissing Bond on the Mechanical Properties and Fracture Behaviour of AA5083-H112 Friction Stir Welds.” *Materials Science and Engineering A* 719(September 2017):12–20.

LIST OF PUBLICATIONS

International Journals published: 02, Under review: 02, Papers to be communicated: 01.

Publications

1. **Kethavath Kranthi Kumar**, Adepu Kumar, M.V.N.V Satyanarayana, “Effect of friction stir welding parameters on the material flow, mechanical properties and corrosion behavior of dissimilar AA5083-AA6061 joints” Proceedings of the Institution of Mechanical Engineers, Part C: Journal of Mechanical Engineering Science, (2021), **SCI**, DOI: [10.1177/09544062211036102](https://doi.org/10.1177/09544062211036102)
2. **Kethavath Kranthi Kumar**, Adepu Kumar, M.V.N.V Satyanarayana, “Enhancing corrosion resistance and mechanical properties of dissimilar friction stir welded 5083-6061 aluminium alloys using external cooling environment” Proceedings of the Institution of Mechanical Engineers, Part L: Journal of Materials: Design and Applications, (2021), **SCI**, DOI: [10.1177/14644207211032335](https://doi.org/10.1177/14644207211032335)
3. **Kethavath Kranthi Kumar**, Adepu Kumar, “Microstructure, mechanical and corrosion behavior of similar and dissimilar friction stir welded 5083-6061 aluminium alloy joints” Journal of Materials chemistry and physics, (**under review**)
4. **Kethavath Kranthi Kumar**, Adepu Kumar, “Microstructure characteristics and tensile behavior of a friction stir welded AA5083-6061 dissimilar alloys welded in a different cooling environment” Metals and Materials International, (**under review**)
5. **Kethavath Kranthi Kumar**, Adepu Kumar, “Simultaneous improvement of mechanical properties and corrosion behavior of AA5083-AA6061 submerged FSWed joints by addition of nanosize Al₂O₃ particles” (**under progress**)

NATIONAL AND INTERNATIONAL CONFERENCES

6. **K. Kranthi Kumar**, Adepu Kumar, “Effect of post weld heat treatment on microstructure characteristics, mechanical and corrosion behavior of similar and dissimilar friction stir welded AA5083-AA6061” ICPCM-2019, NIT Rourkela.
7. **K. Kranthi Kumar**, Adepu Kumar, “Microstructure characterization, mechanical properties and corrosion behaviour of Friction stir welded AA5083-AA6061 joint” ICON-BEES-2021, NIT Tiruchirappalli.

CURRICULUM VITAE

Kethavath Kranthi Kumar
Research Scholar
Department of Mechanical Engineering,
National Institute of Technology Warangal,
Hanamkonda, Telangana-506004
Email: kranthikethavath@student.nitw.ac.in



Educational Qualification

Year	Degree (Marks)	Specialization	Institute
2021	Ph.D.	Mechanical Engineering	National Institute of Technology, Warangal, Telangana
2016	M.Tech. (80.20%)	Welding Engineering	National Institute of Technology, Tiruchirappalli, Tamil Nadu
2013	B.Tech. (66.97%)	Mechanical Engineering	Osmania university, Hyderabad, Telangana
2009	12 + HS (80.2%)	Science	Narayana Jr College (TSBIE)
2007	10 + SE (69%)	General	The Hyderabad Public School, Ramanthapur (CBSE)